OPTIMISATION OF CONDENSER DESIGN ON SOLAR DESALINATORS

Master of Engineering thesis

Student: Lap Kei Leung 66433275

Primary supervisor: Dr Dirk Pons

Secondary supervisor: Dr Paul Docherty

Enrolment Date: 15 August 2016

ABSTRACT

PROBLEM Access to fresh and safe drinking water is a major challenge in many countries. A variety of solar desalination technologies exist, which range from passive to highly automated systems. The problem for third-world countries is that advanced technology is difficult to fund and to maintain. Hence passive designs are advantageous. Previous research by A. Gorrie concluded that using forced cooling of the external condenser surface, an increase in water production of 60% was observed [1].

NEED As identified, the need for keeping the external condenser surface cool is the most effective method of increasing water production, and therefore different geometric designs of the external condenser surface were looked at to enhance heat rejection from the condenser.

PURPOSE There is a need to design and optimize, build, and computationally model the heat rejection of a new condenser. This is to validate that the new design is capable of rejecting more heat than the current setup (flat plate condenser). The main variable in optimise was minimisation of material use, and manufacturing economics.

APPROACH The research project intends to (a) come up with several conceptual designs, (b) run CFD (Computational Fluid Dynamics) parametric optimisation, (c) build the optimized design candidate and collect empirical data, (d) build a transient CFD model of the optimized design, and (e) formulate a mathematical model describing the water production due to the new condenser design.

COMPLEXITY This is a complex project because of the number of parametric variables involved in the optimisation process and in the commissioning of the rig to validate the optimisation results.

ORIGINALITY The work makes several original contributions. First it provides a method to optimise the design of condensers, when there is little or no published literature in this area. Second, it provides a specific solution for a solar still, and has the potential to deployed.

Contents

NOMENCLATURE

$(P_a)_{LM}$ *log mean air partial pressure* (Pa)

$\dot{m_{ew}}$ *mass flux of the solar still* (kg)

h_{fg} *Latent heat of vaporization of water* $(J.kg^{-1})$

η_f *efficiency of a single pin fin* $(\%/_{100})$

η_o *efficiency of an entire array*

A_f *surface area of a single fin* (m^2)

A_t *total surface area of the array exposed to air flow* (m^2)

C_{P_a} *specific heat capacity of air* $(Jkg^{-1}K^{-1})$

$C_{P_{mix}}$ *specific heat capacity of water vapour to air* $(Jkg^{-1}K^{-1})$

C_1, m_1 *fitting constant to* Nu_d*, denoted m in Table* 7.5 [13]

C_p *specific heat of fluid* $(J.(kg.K)^{-1})$

D_e *hydraulic diameter of duct entrance* (m)

D_{wa} *diffusivity of water vapour in air* (m^2s^{-1})

E_{mass} *evaporation rate in* $(mm.day^{-1})$

L_c *parameter to fin efficiency,* η_f

M_1, M_3 *mass of the water in basin and distilled water collected* (kg)

M_a *molecular weight of dry air* $(kg.kgmol^{-1})$

M_{mix} *molecular weight of water vapour to air* $(kg.kgmol^{-1})$

M_w *evaporative rate of water* $(kgm^{-2}s^{-1})$

N_f *number of fin in the array, denoted N in* [13]

$\overline{Nu}$ *average Nusselt number*

Nu_d *Nusselt number for an average pin fin*

Pr Prandtl number

Pr_s *Prandlt number of air on the fin array surface*

$P_{w,g}$ *partial pressure of water, cover determined by* $P(T)$ (Pa)

Re_d *Reynolds number based on pin*

R_n *Net irradiance* $(MJ\ m^{-2}\ day)$

S_D *diagonal spacing in staggered array* (m)

S_T, S_L *transverse and longitudial spacing between fins* (m)

T_2 *internal air cavity temperature* (℃)

T_3 *internal condener surface temperature* (℃)

T_4 *evaporation surface temperature* (℃)

U_b *heat transfer coefficient between the basin and soil* $(w.(m^2.K)^{-1})$

W_b *width of the base plate*

X_T, X_L *transverse and longitudial spacing ratio*

f_N *friction factor per row* (row^{-1})

k_f *thermal conductivity of fin* $(w.(m.K)^{-1})$

k_i *heat and mass transfer coefficient,* $k_{1,2,3,7,10}(hr^{-1})$, $k_{4,8}(\%/100.(hr.K)^{-1}), k_{5,9}(kg.(hr.K)^{-1}), k_6(kg.(hr.\%/100)^{-1})$

k_{mix} *thermal conductivity of water vapour to air* $(w.(m.K)^{-1})$

m_2 *slope of saturation vapour pressure curve* $(kPaK^{-1})$

m_w *mass of water in still* (kg)

v_{axial}, u_{radial} *velocity components measured in wind tunnel* $(m.s^{-1})$

α_w *absorptivity of water* $(\%/_{100})$

δ_e *saturation vapour pressure − actual vapour pressure* $= e_s - e_a\ (kPa)$

λ_v *Latent heat of vaporization of water* $(MJ\ kg^{-1})$

ρ_{mix} *density of water vapour − air mixture* $(kg.m^{-3})$

ΔP *pressure difference between inlet and outlet* (Pa)

h *heat transfer coefficient* $(w.(m^2.K)^{-1})$

A *area of the basin* m^2

C *spacing from top of the fin to ceiling* (m)

G *solar insolation entering through the glass* $(W.m^{-2})$

H *height of the fin* (m)

Ix *turbulence percentage* (%)

L *charateristic length* (m)

Le Lewis number

N *number of rows in the fin array*

Nu Nusselt number

P, A_c *parameter to* $m = \sqrt{\frac{hP}{k_f A_c}}\ (m), (m^2)$

Re Reynolds number based on duct

Subscript e, c, r, k *evaporation, condensation, conduction, radiation*

Subscript w, g, b *water, cover, basin*

T temperature (K)

U velocity of the air flow $(m.s^{-1})$

a, b fitting constants to friction factor

d diameter or thickness of pin (m)

f friction factor

k thermal conductivity $(w.(m.K)^{-1})$

m, n fitting constant to Nu_d

$m = \sqrt{\frac{hP}{k_f A_c}}$ parameter to fin efficiency, η_f

q heat transfer term $(W.m^{-2})$

t time (s)

w length of the rectangular fin (m)

γ Psychrometric constant $(kPaK^{-1})$

ε emissivity $(^{\%}/_{100})$

μ dynamic viscosity of fluid $(kg.(s.m)^{-1})$

ρ density of fluid $(kg.m^{-3})$

σ Stefan − Boltzman constant

τ transmittance of the glass cover, found in Figure 5.3.1 $(^{\%}/_{100})$ *[25]*

ψ finning factor

1 Introduction

1.1 Solar desalination

Water is an essential resource for humans. Access to a fresh and safe drinking water supply is a major challenge in many countries. In many parts of the world fresh water sources are scarce, or the existing water is not in the form of safe drinking water, for example, sea water. The process of converting sea water to fresh water is called desalination, where reverse osmosis is the most commonly used. However, this process has many disadvantages: it is a slow process; it does not remove chemical contaminants; it requires frequent replacement of the filters; and also, it requires much energy to run the system. The problem for third-world countries is that advanced technology is difficult to fund and to maintain. However, in third-world countries there is usually an abundance of solar energy, hence passive designs driven by renewable energy are advantageous.

1.2 Project Background

A previous ME thesis student A. Gorrie, identified the importance of maximizing cooling to the condenser surface on the solar desalinator, and considered this as the main objective for future projects [1]. In part of his thesis, he proposed two conceptual designs to promote cooling to the condenser surface. The first concept was the extended cover design (Fig. 2.11.2), which works by concentrating heat in a small region at the inlet (high pressure), and because of the cavity profile, the temperature decreases as it moves towards the outlet. The temperature difference will then induce a convection effect. The second concept was about the use of extended surfaces (Fig. 2.11.1), which are commonly used in heat rejection applications. However, there are still many possibilities with using extended surfaces as there are many geometric variables involved.

1.3 Project Context

The second concept of using an extended surface on the condenser was adopted, as initially it was thought that the first concept may not be effective enough to give a meaningful improvement. An extended surface is an application that is commonly used in electronic cooling, and there are endless possibilities regarding the geometrical design of the extended surfaces, which leaves scope for research.

As a continuity of the project which was not completed by A. Gorrie, this project will still share the same context in that the new condenser design must be able to be implemented on A. Gorrie's rig, and be able to operate in tropical, third world countries (Tonga). Therefore, factors such as material cost, manufacturing process and assembly requirements will be considered, as discussed in Section 8.4. The design should ultimately remain completely passive without manual supervision, and any electricity it may require must come from a renewable source (solar). But because this new condenser rig is being built and tested indoors, electrical appliances such as an axial fan and a heating foil is needed to simulate the convection and heat experienced.

1.4 Project Outline

This project will begin by studying the number of possibilities in extended surface design, set constraints and optimize for the highest condenser heat rejection using the experimental condition of A. Gorrie's Test 17 as reference. A second objective was added that the condenser design must use as minimal an amount of aluminium as possible, because this matches the context of the project to minimise material cost if this was to be deployed in third-world countries. The main constraints in this optimisation were that the extended surface must not take a space bigger than the current condenser (1256x260mm), and a height limit of 200mm was imposed on it for structural reasons. After determining the optimal condenser design, it will be manufactured along with a flat plate condenser. The purpose of the flat plate condenser is to serve as a benchmark comparison for the condenser with the extended surface. Both would be tested and validated by CFD modelling, in order to determine whether the optimisation predictions were reliable.

2 Literature Review

2.1 Fin geometry

Fins (or pins) or a heat sink are commonly used to promote cooling on a hot surface. They usually consist of multiple extruded pins in a structured array. The pins have many different geometric profiles, and the array layout can change depending on the optimal design for the application, which is pre-determined using CFD or experiments. Experiments mentioned in the literature usually consist of two forms of convection: free laminar convection (no wind), and forced convection (wind). For this project, both methods of convection will be relevant.

2.1.1 Square and rectangular

Square and rectangular pin fins are commonly used in the literature, as the simple geometry provided can be easily used for parameterization in experiments and computations. A square pin fin array contains four parameters: edge length, pin height, and X and Y spacing between pin fins. For rectangular pin fins, an additional parameter is needed to describe the second edge length. A finite difference computation was done by [2] for rectangular fin arrays under free laminar convection. It concluded that the heat transfer coefficient, h, increases with the temperature difference between the fin's surface and ambient air, $T_f - T_a$, and the height of the fin, H. The heat transfer coefficient was also found to decrease to L, the length of the fin, and therefore tall, slender fin profiles are favoured. For spacing of the fins, S, the optimal value was found to be approximately 6-7 mm for the highest heat transfer rate.

From doing CFD on several other geometries by [3], using an inlet velocity of 3 ms^{-1}, the square pin fin was shown to leave behind large vortices compared with other profiles, which caused considerable pressure loss and thus a lower cooling rate.

Of the two profiles, [4] reported that the square pins outperformed the plate fins (rectangular), due to the greater exposed surface area present.

2.1.2 Circular

Circular pin fins are the most used profile due to only needing one parameter for their geometry, and from [4], circular pins transferred more heat than other profiles except for elliptical. This result was also agreed by [3]. There are more underlying factors that control these outcomes, related to pressure drop, Reynolds number, friction factor, Nusselt correlation and different array layouts which may benefit one geometry over another; these will be discussed in later chapters.

2.1.3 Elliptical, drop shape and NACA[1]

Two geometric comparison criteria were defined by the author [3]. The first set had the same hydraulic diameter, coverage ratio, and pin length; the second set consisted of the same blockage area, the

[1] Aerofoil shapes described by a four digit code, developed by the National Advisory Committee for Aeronautics.

distance between pins and pin length. Both criteria sets were referred to as FCC[2] and SCC[3]. The result by [3] showed that these more complex profiles outperformed the circular profiles on almost all occasions. The author of [3] explained that these profiles had a higher length to thickness ratio, making them more efficient in a staggered array arrangement. Only for FCC with the inline array layout, the circle profile outperforms all other variants [3], [4]. The author of [4] explained that this was due to the unique deflection flow that the circular pin fins exhibited in an inline array.

2.1.4 Oblique and inclined fins

Having circular fins leaning at an angle from the vertical axis is an attempt to increase the surface area exposed to convection. Two different oblique fin arrangements under forced convection were investigated by [5]. One was called the single row arrangement, where all the fins in the row are inclined in the same direction; the other was called the cross-row arrangement, where fins are inclined in opposite directions alternately. It was reported that for the single row arrangement the best angle was 0 degrees, which is equivalent to having perpendicular fins; the heat transfer for the cross-row arrangement was almost identical to perpendicular fins for inclination -30 to +30 degrees [5]. This was also supported by [6], who concluded that inclined pins have the same average heat transfer coefficient to a horizontal fin. It was also suggested that only in a low Reynolds number environment (free convection) would oblique fins be able to outperform horizontal fins due to the increased surface area [6].

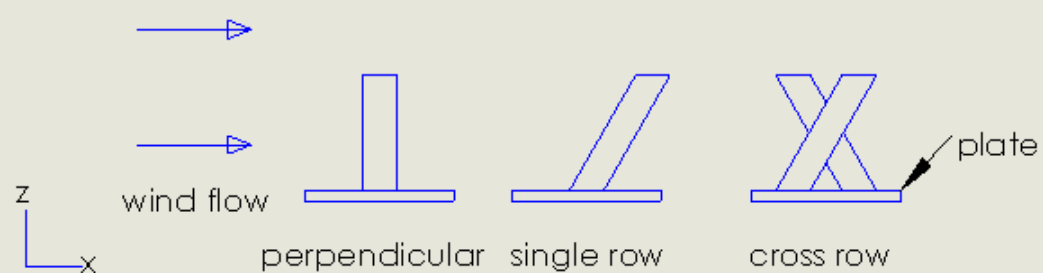

Figure 2.1.1. Different oblique fin arrangements. Image M Leung adapted from [5].

This application was also applied to rectangular fins [7], but the inclination was along the x and y planes. The experiment compared the inline array and fins facing 20 degrees from the x axis. For an input wind velocity of 15 ms^{-1}, the inclined fin array was found to have enhanced heat transfer by more than 1.5 times the inline fin array [7]. This enhancement was due to the additional formation of the longitudinal vortex for the inclined fin array, while the horseshoe vortex occurred in both experiments [7].

[2] First comparison criteria.
[3] Second comparison criteria.

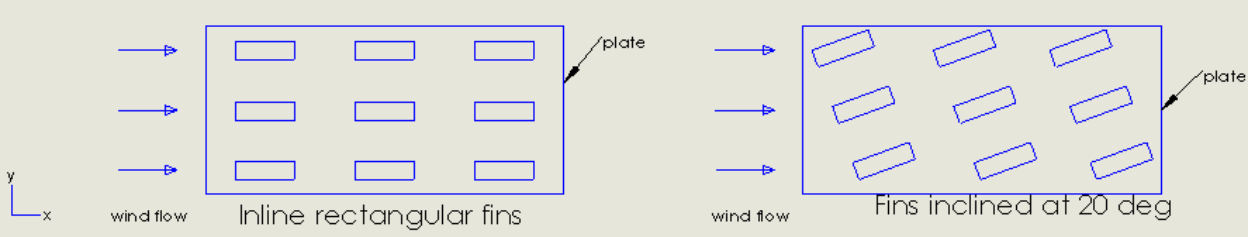

Figure 2.1.2. Inclination of rectangular fins in the xy plane. Image M Leung adapted from [7].

2.2 Fin array layout

2.2.1 Inline and staggered arrangement

There are usually two different layouts of pin fin arrays: the inline and staggered arrangements, as shown in Figure 2.1.3. This can also be applied to other geometries such as square, rectangular and elliptical. Both arrangements favour certain geometries and are also dependent on aerodynamic conditions. According to [8], inline arrays favour square fins; however, other effects, such as spacing, have not been considered. Reviewing [3] shows that staggered arrangements yield better results for all geometries, in particular for elliptical and NACA profiles. This finding from [3] disagreed with [8], but because each experiment had different criteria, it could mean that the generalized statement from [8] may not be applied to other experiments.

An explanation for this disagreement was made by [9], who concluded that while it is true that the staggered arrangement can provide a higher convective cooling rate, but only the airflow rate remains constant. This condition changes when [9] identified that the staggered arrangement induces a higher pressure drop, which decreases the actual airflow rate. Therefore, a balance must be made between how much pressure loss is acceptable so that it does not inhibit the airflow reaching the backline of the fin array.

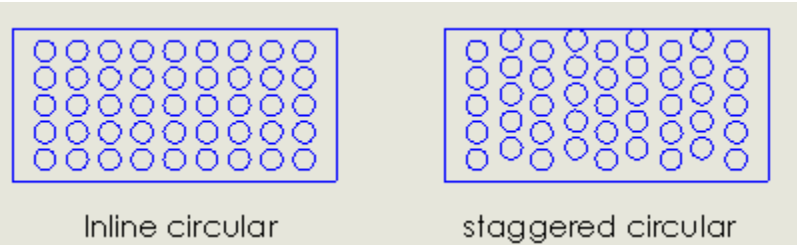

Figure 2.1.3. Inline and staggered circular pin fin arrays. Image M Leung.

2.2.2 Fin spacing

In [10], inline and staggered arrangements were compared with square pin fins, based on the highest Nusselt number and pumping power required; the optimal configuration for the square pin-fin array was under staggered condition when X_T=1.5 and X_L=1.5. As X_T and X_L increase, the performance decreases for both arrangements due to less cooling surface area available, but from X_T<2 the inline arrangement performed better than staggered. A comparison plot from [10] shows that the square array outperformed the circular array in the inline configuration at X_T=2, but for all other conditions the

circular array performed better. This concludes that there are an endless number of possibilities and that the optimal design has yet to be discovered.

$$X_T = \frac{S_T}{d} \; and \; X_L = \frac{S_L}{d},$$

2.2.3 Clearance ratio

The effect of the clearance ratio was investigated by [11]; it was found that performance increases with lower ratios. This is because taller fins have a greater surface area and also induce more turbulence, which then increases the Nusselt number [11]. The effect is more obvious in the staggered than the inline arrangement [11].

$$clearance\ ratio = \frac{C}{H}$$

Height to diameter ratio

Height to diameter ratio is defined by [11] and [12]; this is only applicable to circular fins. Pin fins with height to diameter ratio of 0.5- 4 are called short pin fins, above a ratio of 4 are called long pin fins. Short pin fins are used in turbine cooling while long pin fins are used in heat exchanger applications [12]. Pin fins with a ratio less than three have a constant heat transfer rate, while greater than three the heat transfer rate increases significantly [12]. This is due to end wall effects being dominant in short pin fins, and in long pin fins, heat transfer increases with surface area [12].

2.3 Fin array orientation

2.3.1 Flat, side and upside down

The orientation effect was investigated on square pin-fin heat sink under natural convection [8]; it was found that the downward facing heat sink had the lowest heat transfer coefficient. For the other two cases, the sideward orientation outperformed the upward one for finning factor ψ, less than 2.7, otherwise the situation is reversed. There was no information on the orientation effect for forced convection.

$$\psi = \frac{Total\ surface\ area\ exposed\ to\ air\ flow}{Base\ plate\ area}$$

2.4 Fin array aerodynamics

2.4.1 Friction factor and pressure loss

Much literature is associated with aerodynamic performance based on the amount of power required to pump air into a wind tunnel. The pumping power is measured using the Reynolds number and friction factor; these can then be correlated to the heat transfer coefficient of the array. Some correlations exist; [10] and [12] show that it can be written as:

$$f = aRe_d{}^b$$

$$Re_d = \frac{\rho_{air} d U_{avg}}{\mu_{air}}$$

In [12], it was found that the constant a is a function of X_T. Other literature has many different fitting constants based on other variables, which are only relevant to the particular experimental setup it was conducted in. To measure the friction factor of a single fin array row experimentally, [13], [5], [11] and [14]:

$$f_N = \frac{\Delta P}{{}^1/_2 \rho {U_{max}}^2 N} = \frac{measure\ pressure\ difference}{dynamic\ pressure}$$

Only by measuring the experimental friction factor can the fitting constants be determined.

2.4.2 Fin density

It is assumed that the higher the fin density, the efficiency of the heat sink will increase. However, having more fins will increase the pressure drop, and thus the pumping power required [9]. Experiments by [9] show that by removing fins from areas where airflow was congested did not affect the total cooling, while also saving the material required for manufacturing. However, as the number of fins decreases past a certain point, the ability to cool decreases as well [9].

2.5 Fin array convection

2.5.1 Nusselt correlation and Reynolds number

The Nusselt number has been used in much literature as a direct measure of performance. The definition of the Nusselt number is the total heat transfer divided by the conductive coefficient, which takes the general form:

$$Nu = \frac{hL}{k}$$

where h is the heat transfer coefficient, L is the characteristic length and k is the thermal conductivity.

As h increases, which is achieved by better heat sink design, the Nusselt number will increase. By using the Nusselt number to measure performance, correlations with the Reynolds number can be made. An empirical model was made for the average Nusselt number on a staggered square pin-fin array [11]:

$$\overline{Nu} = 2.8358 Re^{0.58} \left(1 + {}^C/_H\right)^{-0.848} \left({}^{S_T}/_d\right)^{-0.251} Pr^{1/3}$$

$$Pr = \frac{C_p \mu_{air}}{k_{air}}$$

$$Re = \frac{\rho_{air} D_e U_{max}}{\mu_{air}}$$

where C_p, μ *are the specific heat and dynamic viscosity of the fluid,*

and D_e *is the hydraulic diameter of duct entrance*

The above correlation is valid for 10000< Re <34000, 1.58<S_T/d<9.33, 0<C/H<1 [11]. The direct correlation for specific heat, dynamic viscosity and thermal conductivity [15] are given by:

$$C_p = [9.8185 + 7.7 \times 10^{-4} \frac{(T_{in} + T_{out})}{2}] \times 10^{-2} \; J/_{kgK}$$

$$\mu_{air} = [4.9934 + 4.483 \times 10^{-2} \frac{(T_{in} + T_{out})}{2}] \times 10^{-6} \; kg/_{ms}$$

$$k_{air} = [3.7415 + 7.495 \times 10^{-2}(T_{in} + T_{out})] \times 10^{-3} \; W/_{mK}$$

However, the above does not account for each pin and depends on the size of the duct used in [11]. To analyse the Nusselt correlation for an average single circular pin under inline and staggered arrangements [15]:

$$Nu_d = \begin{cases} 9.02 \times 10^{-3} \, \mathrm{Re}^{1.011} \left(S_T/W_b\right)^{0.285} \left(S_L/L\right)^{0.212} & inline \\ 7.04 \times 10^{-3} \, \mathrm{Re}^{0.953} \left(S_T/W_b\right)^{0.091} \left(S_L/L\right)^{0.052} & staggered \end{cases}$$

$$0.004 \leq \left(S_T/W_b\right) \leq 0.332$$

$$0.033 \leq \left(S_L/L\right) \leq 0.212 \; inline, 0.152 \; staggered$$

$$3.3414 \; inline, \; 3.138 \; staggered \times 10^3 \; \leq Re \leq 6.683 \; inline, 4.98 \; staggered \times 10^3$$

A generalized model was proposed for an average pin fin [10] in the form of:

$$Nu_d = m\left(\mathrm{Re}_d \frac{U_{max}}{U_{avg}}\right)^n$$

where m and n are fitting constants, which depend on pin spacing, fin geometry, their arrangement and other experimental variables, which makes it possible to compare different research in the literature.

2.5.2 Efficiency and effectiveness

To analyse the efficiency of a single square, rectangular and circular pin fin, [16] made the following statements:

$$\eta_f = \frac{\tanh mL_c}{mL_c}$$

$$m = \sqrt{\frac{hP}{k_f A_c}}$$

$$L_c = \begin{cases} H + \left({}^{t}/_{2}\right) \ t = d \ for \ square \ fin, t = thickness \ for \ rectangular \ fin \\ H + \left({}^{d}/_{4}\right) \ circular \end{cases}$$

$$P = \begin{cases} 4d \ square \\ 2w + 2t \ rectangular \ \ w \ is \ length \ of \ rectangular \ fin \\ \pi d \ circular \end{cases}$$

$$A_c = \begin{cases} d^2 \ square \\ wt \ rectangular \\ 0.25\pi d^2 \ circular \end{cases}$$

For the efficiency of an entire array, [16] showed that it could be written as:

$$\eta_o = 1 - \frac{N_f A_f}{A_t}\left(1 - \eta_f\right)$$

Using this, the theoretical efficiency of an array design can be determined; however, this does not take into account the aerodynamic effects of pin spacing and the clearance ratio mentioned in other literature.

2.5.3 Heat transfer coefficient

By rearranging the basic definition of the Nusselt number in [10], the heat transfer coefficient can be written as:

$$h = \frac{Nu_d k_{air}}{d}$$

Using the correlation for Nu_d in 2.5.1, the efficiency values in 2.5.2 can be determined.

2.6 Heat rejection optimisation

2.6.1 Least material equation

The use of orthotropic material to build heat sinks was looked at by [17] to reduce to heat rejection per mass of material. In the literature, Polyphenylene Sulphide (PPS) was compared with aluminium using the least material pin fin equation [17] for air and water under natural and forced convection:

$$d_{lm} = 1.503(hV^2k^{-1})^{0.2}$$

where d_{lm} is the optimal pin diameter, and V is the volume of the pin fin. This means that for a given volume of material available with a known heat transfer coefficient, the optimal pin fin diameter and height could be determined. It was found that for a pin fin height of less than 5cm there was no difference in the heat transfer coefficient between PPS and aluminium. Therefore, in terms of heat

rejection per mass of material, PPS is better than aluminium for pin fin height below 15cm due to its reduced density (1700kg/m^3). This meant that for small-scale heat sinks, PPS would be more ideal due to its reduced weight and easier manufacturability. However, the literature intended heat sinks to be cooled from the top and not as an inline duct flow; also, there was a lack of experimental data to validate the computational results.

2.6.2 Constant volume of material and optimal configuration

Optimization for the optimal heat rejection was done for a square inline heat sink which can vary in base size, fin height, diameter and number [18]. The model ignores the volume of the base plate and looks at finding the optimal setup by constraining the volume of material used to be $V = 0.25\pi D^2 W^2 H S^{-2}$, where D is the diameter of fin, W is the width of the square baseplate and S is the constant x and y spacing [18]. To complete the optimisation the literature, the k-epsilon turbulence model was used for 2D in FLUENT, and the problem was split into a process of three comparisons:

1. By varying the ratio between the pin diameter and spacing, ($0.25\pi D^2 S^{-2}$) for 0.2, 0.3 and 0.4.
2. Keeping the best diameter to spacing ratio and varying the dimensionless air velocity, (0.67, 1 and 1.33).
3. Looking at different pin height to base plate width ratios, (HW^{-1}) for 0.5, 1.5 and 2 while using the best diameter to spacing and air velocity.

It was found that the optimal ratio of diameter to spacing was 0.2, which meant that it favoured more slender fins that are widely spaced [18]. Air velocity did not influence the optimal design, and by fixing the diameter to spacing at 0.2, the optimal pin height to base plate width ratio was 1.5 [18]. The limitation of this literature was that it only considered flow interaction in 2D without any experimental data. However, the spacing of the pin fins would also have an effect on the airflow. The model used a constant inflow air velocity at the inlet regardless of the pressure drop induced by the heat sink; this is not true in a real system where the fan supplying the air would operate by a fan curve.

2.7 Evaporation

2.7.1 Penman-Shuttleworth equation

In the literature, the Penman-Shuttleworth equation was used in the topic of hydrology to determine the depth of water which evaporated. The equation provided in [19] was not very well understood regarding nomenclature. In [20] the equation is called the modified Penman equation by W. James Shuttleworth in 1993.

$$E_{mass} = \frac{m_2 R_n + \gamma \times 6.43(1 + 0.536 \times U)\delta_e}{\lambda_v (m_2 + \gamma)}$$

$$m_2 = \frac{4098\left(0.6108 \times \exp\left(\frac{17.27 \times (T - 273.3)}{T}\right)\right)}{(T)^2}$$

$$\gamma = \frac{0.0016286 \times P_{kPa}}{\lambda_v} (kPaK^{-1})$$

$$\delta_e = e_s - e_a \ (kPa)$$

The above equation could be applied to predict the productivity of solar stills, which also takes into account the relative humidity as proposed by [1]. In the literature review of [1], they showed two empirical correlations by [21, 22] to model solar still productivity. These correlations were based on water depth, temperature, and also variables related to the dimensions and geometry of the solar still. The limitations of these correlations were that they were only relevant to the experiment setup where it was conducted. The advantages of using the Penman-Shuttleworth equation is that it takes into account the instantaneous temperature and humidity, which are dependent on rig design, water depth, and geographic location. Therefore, it is possible to relate the performance of different solar stills without needing to know how the experiment was set up. There is no literature documenting the use of the Penman-Shuttleworth equation in passive desalination, and therefore it could be worthwhile to explore it.

2.8 Flow straightener

Due to limited resources, it is difficult to generate a stream of perfectly straight and laminar flow. Most likely the flow will be generated using an axial fan, which creates a helical flow that travels in all three dimensions, resulting in a significant pressure loss across the duct, making the ideal inline flow assumption inappropriate in calculations and adding complexity to CFD modelling. Therefore, ways of straightening the flow must be looked at.

2.8.1 Flow straightener designs

In [23, 24], three flow straightener designs were compared: the Etoile, Tube bundle, and Laws perforated plate straightener. A swirl was produced using two 90-degree bends to replicate turbulence in a wind tunnel of length 91D (D is the diameter of the straightener), and where 2D is the length of the straightener in [23, 24]. Measurements were taken at various distances down the wind tunnel for velocity ratio, turbulence, and swirl angle. The Laws perforated plate provided the best velocity profile, the Tube bundle for the least swirl angle, and Etoile for minimizing turbulence [23, 24]. A modified Etoile straightener, called the open Etoile where the centre is hollow, was found to have better performance than the closed Etoile [25]. However, the open Etoile fails to completely generate a fully developed flow; therefore, the author proposed that the open Etoile straightener could be used upstream of another flow straightener to add benefit with minimal velocity loss [25].

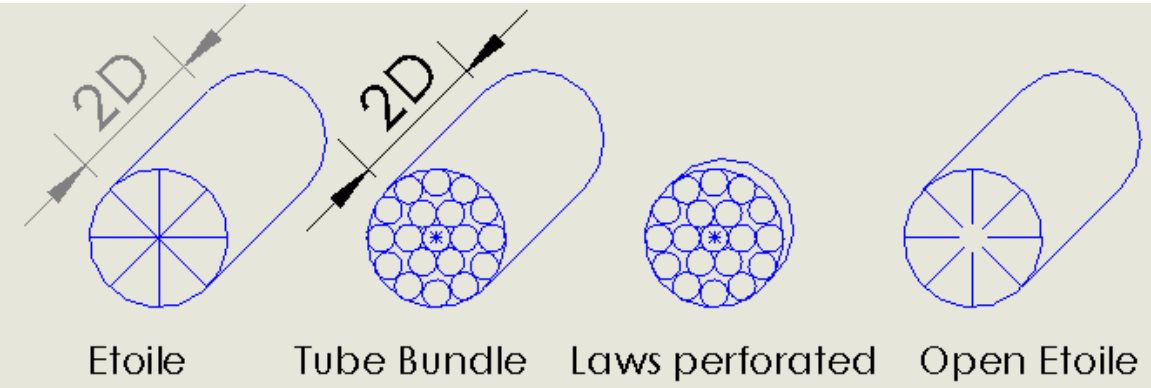

Figure 2.8.1. Etoile and tube bundle straightener. Image M Leung adapted from [23, 24], [25].

2.8.2 Velocity profile, turbulence, and swirl angle

These three parameters were defined as the following in [23, 24]:

$$velocity\ profile = \frac{U}{U_{max}}, turbulence = Ix(\%), swirl\ angle = arctg\left(\frac{v_{axial}}{u_{radial}}\right)(^\circ)$$

In the experiment setup by [23, 24], four sets of measurements were taken for these parameters at downstream distances of 6, 9, 14 and 22D. Measurements were obtained using a Laser Doppler Anemometer installed in a wind tunnel; this may be hard to apply in the limited space of the solar stills. Therefore an empirical correlation for turbulence intensity was found in [26]:

$$Ix(\%) = 0.16Re^{-1/8}$$

There is no approach to obtaining the swirl angle without proper data acquisition equipment, but to visualize the swirl angle some form of tufts may be sufficient.

2.8.3 Length of the straightener

Straighteners of length 2D have been recommended by ISO 5167 for best performance [25]. Shorter Etoile straighteners of length D/16 and D/8 have been investigated. It was concluded that the length of the Etoile straightener was not related to removing the swirl, but it does affect the axial component of the turbulence intensity [25].

2.8.4 Centrifugal fan

The viability of a centrifugal fan was discussed in [9] as it supplies a better quality inline flow than an axial fan. Centrifugal fans are more suited to high-pressure loss applications, for example, in a staggered array with a high fin density. The disadvantage of using a centrifugal fan over an axial fan is it requires more power for the same amount of airflow [9].

2.9 Dunkle's model

Dunkle's model has been widely used in passive solar desalination; however, it has the oldest correlation and it has been succeeded by a newer, more complex model.

2.9.1 Model

It has been widely accepted that the energy balance of the water in the solar still is in the form of [27], [28]:

$$\tau\alpha_w GA = (q_e + q_c + q_r + q_k)A + m_w C_{p,w}\frac{dT_w}{dt}$$

$$q_e = h_e(T_w - T_g)\ evaporation;\ q_c = h_c(T_w - T_g)\ condensation$$

$$q_k = U_b(T_w - T_b)\ conduction;\ q_r = h_r(T_w - T_g)\ radiation$$

Also, U_b can be ignored if the basin is large and well insulated [28].

The Dunkle correlation in the convective heat transfer from water to glass [29] is given by:

$$h_c = 0.884\left[T_w - T_g + \frac{(P_w - P_g)\times T_w}{268.9\times 10^3 - P_w}\right]^{\frac{1}{3}}$$

$$h_e = 16.273\times 10^{-3} h_c\left(\frac{(P_w - P_g)}{T_w - T_g}\right)$$

$$h_r = \left[\frac{1}{\varepsilon_w} + \frac{1}{\varepsilon_g} - 1\right]^{-1}\sigma\left({T_w}^2 - {T_g}^2\right)\times(T_w - T_g)$$

$$P(T) = exp\left[25.317 - \frac{5144}{T}\right] \quad T(283 - 363K)$$

The rate of water production was estimated to be based on the evaporative term [30]; however, this does not take account of the efficiency of the water collection system:

$$\dot{m} = \frac{h_e A(T_w - T_g)}{h_{fg}}\ (kg.s^{-1})$$

$$h_{fg} = 2.4935\times 10^6[1 - 9.4779\times 10^{-4}(T - 273) + 1.3132\times 10^{-7}(T - 273)^2 - 4.7974 \times 10^{-9}(T - 273)^3]\ for\ T < 343K$$

Instantaneous efficiency for the solar still is defined as [28]:

$$\eta_i = \frac{\dot{m}h_{fg}}{GA}$$

2.9.2 Limitations

To determine the limitations of the Dunkle's model, it was compared to the CFD data in [29]. It was found that the model was accurate from 17°C to 50°C. In [31], it is stated that the Dunkle's model overestimates the evaporation rate by 30%. This also agreed with [32] where it stated there was a difference of 30% in the Nusselt number between the CFD and Dunkle's model.

2.10 Chilton-Coburn

2.10.1 Model

The exact form of the Chilton-Coburn's analogy between the evaporative and condensation coefficient is [31]:

$$h_e = \frac{M_w h_{fg}}{M_{mix} C_{P_{mix}}} \frac{Le^{-2/3}}{(P_a)_{LM}} h_c$$

$$Le = \frac{k_{mix}}{\rho_{mix} C_{P_{mix}} D_{wa}}$$

$$D_{wa}\ is\ the\ diffusivity\ of\ water\ vapour\ in\ air\ (m^2 s^{-1})$$

Due to the complexity of measuring these psychrometric properties, the exact form has only been used by [31] to compare its deviation from other models and approximations. By assuming $Le = 1$ and$(P_a)_{LM} = P(T)$, the Lewis equation is derived [31].

$$h_e = \frac{h_{fg}}{M_a C_{P_a}} \frac{M_w}{P(T)} h_c$$

This approximation now ignores the effect of water vapour, and is only accurate at lower temperatures. A deviation of 58% was found for $T_w = 70$°C by using the approximation, measured by $P(T)\left(\frac{Le^{-2/3}}{(P_a)_{LM}}\right)$ [31].

2.10.2 Comparison of models

Three models were compared in [31]: the Bulk Motion, Chilton-Coburn, and Dunkle's model. The Lewis equation was only a simplification of the Chilton-Coburn and was not actually tested in [31]. It was found that the Dunkle's model will always overestimate water production, while the other two models remain relatively close to the experimental results [31]. However, it was not clear as to the instrumentation and formulation needed for these other two models, making it difficult to replicate.

2.11 Gorrie's research

2.11.1 The Gorrie model

As part of the investigation regarding the effect of relative humidity on water production, [1] found that the assumption of fully saturated air inside the solar still not to be true. This assumption was used in the Dunkle's model as there was no humidity term. More advanced models discussed earlier, like the Penman-Shuttleworth and Chilton-Coburn, did introduce humidity as a dependent variable. However, the Gorrie model also accounts for the difference in relative humidity between the brine and condenser surface, as well as three temperature differentials inside the solar still. This makes the Gorrie model to be the most detailed model of them all. However, the limitations of the Gorrie model were:

1. The model depends on the build of the solar still; [1] obtained this formulation based on the main solar still. It was also mentioned that smaller stills were made but did not obtain any water at all. Therefore, there must be a limitation on the A_e term in the formulation.
2. Internal pressure was not used in the formulation, which is one of the main variables that appears in other evaporation models. The exclusion was commented on by [1], as the pressure measurements were considered unreliable, and not suitable to be included in the formulation.
3. The Gorrie model is still an empirical correlation. It uses ten arbitrary heat and mass transfer coefficients, k_i to fit its model. Currently no one has been able to formulate a model from first principles.

Formulation of the Gorrie model, [1].

$$\dot{T_4} = -k_1 \frac{AG}{C_{p,w} M_1} - k_2 (T_4 - T_2)\ K/hr$$

$$\dot{H_1} = -k_3 H_1 - k_4 (T_4 - T_2)\ \frac{\%\ humidity}{100 \times hr}$$

$$\dot{M_1} = -k_5 (T_4 - T_2) - k_6 (1 - H_1)\ kg/hr$$

$$\dot{H_2} = -k_7 H_2 - k_8 (T_3 - T_2)\ \frac{\%\ humidity}{100 \times hr}$$

$$\dot{M_3} = -k_9 (T_3 - T_2) - k_{10} (M_1(0) - M_1)\ kg/hr$$

$H_1\ and\ H_2\ are\ the\ humidity\ at\ the\ evaporation\ and\ condensation\ surface, in\ \%/100$

2.11.2 Condenser design

The majority of this literature review focused on extended surface, as [1] proposed a future research scope of adding a fin arrangement on the condenser surface. Below are some of the basic concepts of the condenser surface, which have already been discussed in greater detail in Sections 2.1-2.5.

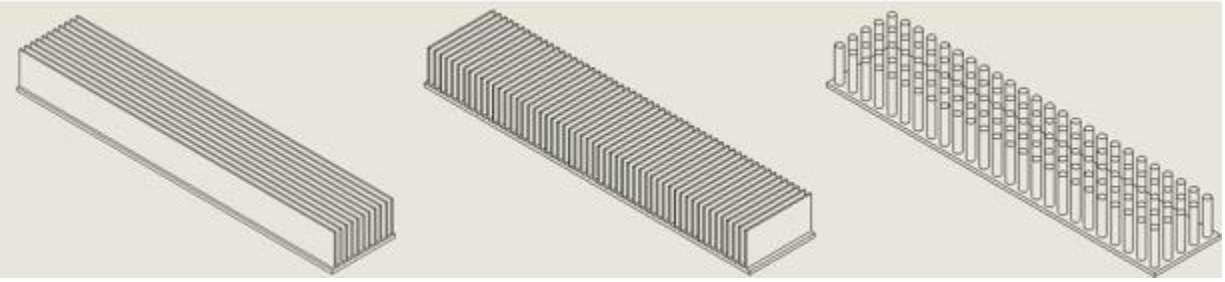

Figure 2.11.1. Conceptual design of fin arrays as proposed by A. Gorrie [1]. Image M Leung adapted from [1].

Another concept proposed by [1] was the extended cover design. The difference in cross-section width was thought to induce a pressure differential which increases the overall convective cooling. At the same time, the cover also provides shading to the condenser surface, keeping the condenser surface as cool as possible.

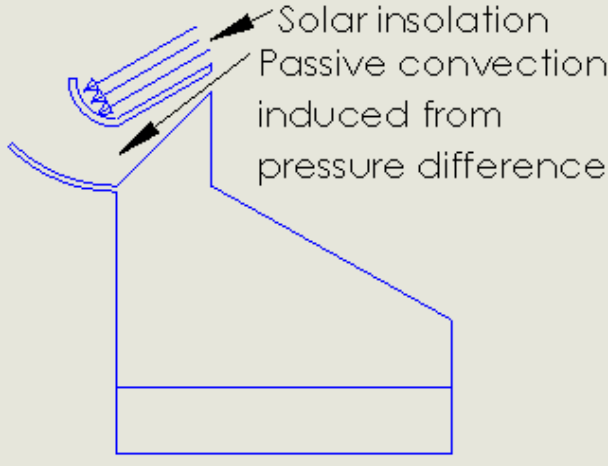

Figure 2.11.2. Extended cover surface design proposed by A. Gorrie [1]. Image M Leung adapted from [1].

2.11.3 Salinity issue

The topic of whether using actual seawater compared to fresh water in testing has been investigated by [1]. It was found that by using seawater of 3.6% salinity, it had little effect on production; looking at the results of [33], the decrease in production between 0 and 3.6% salinity is small. However, a 30% decrease in production was observed when the salinity was increased to 75% [33].

2.12 CFD modelling

2.12.1 CFD of the entire solar still

The work of [29] focused on CFD modelling the transient convective and evaporative heat transfer response for a given set of solar insolation data. This was then compared with the actual experimental data. A two-phase model (liquid and gas) was used by [29], and solved using the energy and mass equation. Internal turbulence inside the solar still was ignored, based on the assumption that the liquid remains relatively calm and the vaporization rate is low [29]. Because of the high number of time steps required to model the transient response for 14 hours, 14 stages of quasi steady state were used in [29]. Each quasi-stage required 4-12 hours of computation [29]. The result of [29] concludes that a decrease of 7.79% in production rate was reported using CFD compared to the experimental data.

A steady-state CFD analysis was performed by [32] using a fixed basin and absorber surface temperature of 300 and 350K, with an emphasis on modelling the velocity profile from convection, shear stress on absorber and basin surface, and the temperature profile at various elevations inside the solar still. The velocity profile was found to be highest in the centre of the absorber and basin surface, which was due to the high shear stress found in the same area as well [32, 34]. The paper did not model for water production but reported a 30% difference in Nusselt numbers between the experimental data (using Dunkle's model) and the CFD results.

2.12.2 Optimization methodologies and algorithm for heat sinks using CFD

Using very fine spacing, when there are many parameters, can be computationally expensive due to the combinations possible. Traditionally, optimisation of the heat sink is done using the derivative method,

but [35] commented that this method fails when the gradient does not exist. Other problems identified by [35] were:

1. The optimisation process converging to a local minima/maxima rather than the global minima/maxima. So, using an arbitrary example in Fig. 2.12.1, it can be seen that it is crucial to select the correct start point to ensure convergence to global minima.
2. Mesh instability when geometry changes.
3. The presence of discrete and continuous design parameters, like the number of fins vs fin spacing.
4. Collision constraints (e.g. the size of the pin is also governed by fin spacing).

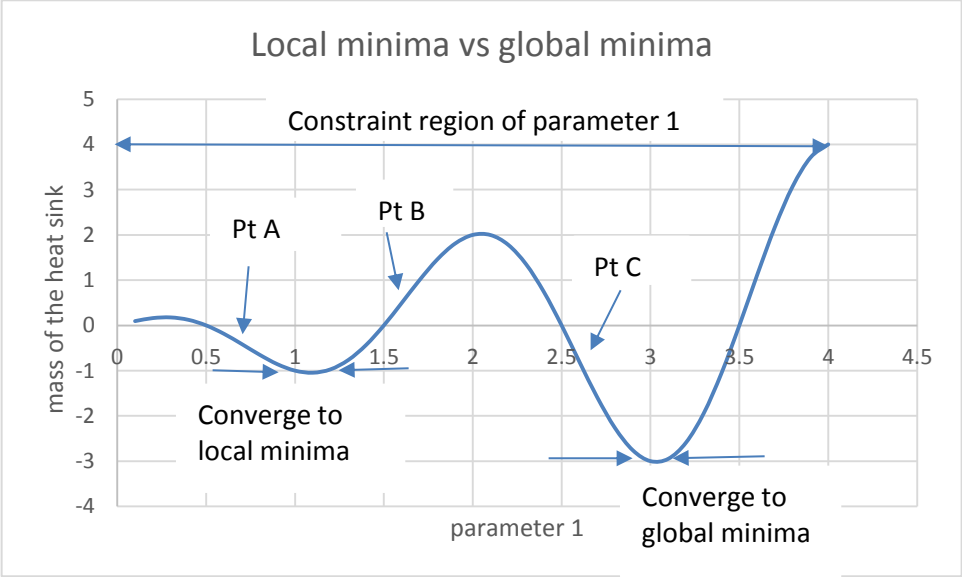

Figure 2.12.1. Illustration example of local and global minima convergence. Image M. Leung.

The approach developed by [35] consists of a mixture of two processes. They are:

1. **Local optimisation**. The process determines a *Trust region* centred on the first design point. This *Trust region* should be considered as a narrower range of the original design parameter range. For example, if the original design parameter range of the height of the pin fin is 0.5 to 4cm, and for the first design point the height of the pin fin is 1.7cm (Pt B), then the *Trust region* can be 1.5 to 2cm. If the result of the initial optimisation within the *Trust region* suggests that the local minima, the mass of the heat sink, lies to the left of the *Trust region*, then the new *Trust region* will be 1 to 1.5cm, which yields the local minima.
2. **Explorative search**. If the design point for the height of the pin fin is 0.5 to 4cm, then there will be five design points, because [35] suggested that for every design parameter there should five times the number of designs. Therefore, if the fin spacing was also a parameter, then the number of designs would be ten. The spacing of each design should be spaced as evenly as possible.

Three combinations using these two processes were experimented with by [35]:

1. Local optimisation of one single base case design (30 design points in total as there are 6 parameters).
2. Local optimisation of the best design point from the explorative search (select the best design from the 30 design points of the explorative search, then this becomes the base case design in combination 1).
3. Local optimisation for every point from the explorative search (for each of the 30 design points of the explorative search, conduct combination 1).

It was found that for the first combination, the heat sink mass was 49.1g, but for the second and third combination this decreased to 15.3 and 15g respectively. Based on the exponentially more computation required for combination 3, combination 2 was considered sufficient to provide decent optimisation. The paper also commented that the algorithm should not waste time in converging to the local optimum with high precision over other potential optima points [35].

2.12.3 Turbulence models for CFD

If the Reynolds number, Re, for an internal flow reaches above 10000, then the flow is considered fully turbulent and the flow profile will no longer be the same [16]. There are several two-equation turbulence models mentioned in [34]. The k-epsilon model is preferred due to its numerically stability and being less computationally intensive; it is formulated as:

$$\frac{\partial k}{\partial t} + u\frac{\partial k}{\partial x} + v\frac{\partial k}{\partial y} = \frac{\partial}{\partial x}\left(\frac{V_T}{\sigma_k}\frac{\partial k}{\partial x}\right) + \frac{\partial}{\partial y}\left(\frac{V_T}{\sigma_k}\frac{\partial k}{\partial y}\right) + P - D$$

$$\frac{\partial \varepsilon}{\partial t} + u\frac{\partial \varepsilon}{\partial x} + v\frac{\partial \varepsilon}{\partial y} = \frac{\partial}{\partial x}\left(\frac{V_T}{\sigma_\varepsilon}\frac{\partial \varepsilon}{\partial x}\right) + \frac{\partial}{\partial y}\left(\frac{V_T}{\sigma_\varepsilon}\frac{\partial \varepsilon}{\partial y}\right) + \frac{\varepsilon}{k}(C_{\varepsilon 1}P - C_{\varepsilon 2}D)$$

$$Where\ k\ is\ the\ kinetic\ turbulent\ energy\ and\ \varepsilon\ is\ the\ rate\ of\ dissipation\ of\ k$$

The two equations above state that the rate of change and transport of k and ε are equal to transport by diffusion, production minus destruction of k and ε [34]. Therefore, for any amount of turbulent energy, the rate of dissipation will change proportionally [34].

$$P = 2V_T\left[\left(\frac{\partial u}{\partial x}\right)^2 + \left(\frac{\partial u}{\partial y}\right)^2\right] + V_T\left(\frac{\partial u}{\partial x} + \frac{\partial u}{\partial y}\right), rate\ of\ production$$

$$V_T = \frac{C_\mu k^2}{\varepsilon}, eddy\ viscosity$$

$$C_\mu = 0.09, \sigma_k = 1, \sigma_\varepsilon = 1.3, C_{\varepsilon 1} = 1.44, C_{\varepsilon 2} = 1.92$$

However, some of the weaknesses of using this model are [34]:

1. The model uses empirical fittings which may not apply in all applications.
2. It uses wall function to scale velocities in the near wall region, which is less accurate if the flow in the near wall region is important.
3. Flow separation, reattachment and recovery.

Despite these weaknesses, the k-epsilon model is still widely used in industrial applications [34]. A variant of the k-epsilon model is the k-omega model, where ω stands for the frequency of k, described as $\omega = \frac{k}{V_T}$. This model is better suited in computing near the wall region, and flows with strong curvature [34]. Another model is the SST (Shear stress transfer) which uses the k-epsilon model when computing in the free stream and k-omega for near wall, but it is weak at computing regions after flow separation [34]. The SST model requires an initial condition close to the final result in order to converge, and, therefore, the simulation must first be run by either k-epsilon or k-omega to obtain the initial condition.

2.12.4 Wall functions

Wall functions are used in CFD packages to estimate the turbulent boundary layer as to computing them. In order to apply wall functions, the absolute distance from the wall y and fluid velocity at a distance of y away from the wall U, must be expressed in dimensionless groups. The dimensionless wall distance $y^+$and velocity U^+ are equal to $\frac{y\rho U_\tau}{\mu}$ and $\frac{U}{U_\tau}$ respectively, where U_τ is the wall friction velocity and is equal to $\sqrt{\frac{\tau_w}{\rho}}$ [34]. In order to determine the wall shear stress τ_w, U_τ must first be solved numerically, which will be mentioned in detail below.

The turbulent boundary layer is categorized into three separate regions. When $y^+ < 5$ the flow is considered to be in the viscous sublayer. In this layer the fluid velocity is proportional to the distance away from the wall, $U^+ = y^+$. As $5 < y^+ < 30$ the flow transition into the log layer, the previous relationship between U^+ and y^+ deviates slightly; this effect can be seen experimentally but it is usually treated as the viscous sublayer when using the wall function. In the log law region where $30 < y^+ < 500$, the velocity profile is modelled as [34]:

$$\frac{U}{U_\tau} = \frac{1}{k_1}\ln(Ey^+)$$

where $k_1\ is\ the\ Von\ Karman\ constant = 0.4, E = 9.8$

But before applying this equation, an initial condition of the fluid velocity U and distance away from the wall y must be known. By substituting in the expression for y^+, the above equation becomes:

$$\frac{U}{U_\tau} = \frac{1}{k_1}\ln(E\frac{y\rho U_\tau}{\mu})$$

After solving for U_τ numerically, τ_w can be determined using $U_\tau = \sqrt{\frac{\tau_w}{\rho}}$.

2.12.5 Turbulence intensity and entrance length

Turbulence intensity, which is a measure of the amount of velocity fluctuation from the mean velocity of the flow, can be defined as [36]:

$$I = \frac{U'_{rms}}{\overline{U}}$$

$$\overline{U}\ is\ the\ average\ velocity\ of\ the\ flow = \sqrt{\overline{U_x}^2 + \overline{U_y}^2 + \overline{U_z}^2}$$

$$where\ U'_{rms}\ is\ the\ root\ mean\ squre\ of\ velocity\ fluctuation = \sqrt{\frac{1}{3}\left(U'_x{}^2 + U'_y{}^2 + U'_z{}^2\right)}$$

The turbulent kinetic energy can be computed as [36]:

$$k = \frac{3}{2}U'_{rms}{}^2$$

To account for each velocity fluctuation component with respect to time, it is defined as [37]:

$$U'(t) = U - \overline{U}$$

$$U\ and\ U'\ are\ the\ instantaneous\ velocity\ and\ velocity\ fluctuation$$

$$U(t) = \sqrt{\left(U_x(t)^2 + U_y(t)^2 + U_z(t)^2\right)}$$

These quantities can be measured using a tri-axial hot wire anemometer, where sufficient sample time would give a better time average of the flow. For heat rejection applications, it is important to know the turbulent intensity at the inlet, as this would affect how much mixing occurs. Another useful quantity is the entrance length, which defines the length before an internal flow becomes fully developed. For laminar and turbulent flow, the correlation is as follows [37]:

$$L_e = 0.06 D_e Re = 0.06 \frac{\rho_{air} D_e{}^2 U_{max}}{\mu_{air}} \quad for\ Re < 2300$$

$$L_e = 1.6 D_e Re^{1/4} = 1.6 D_e \left(\frac{\rho_{air} D_e U_{max}}{\mu_{air}}\right)^{1/4}\ for\ 2300 < Re < 10^7$$

It is important to account for the entrance length provided that there is sufficient space in the design, so that the flow can be predicted and be comparable to empirical correlations.

2.12.6 Flat plate Nusselt correlation

To determine the convective coefficient, h, the Nusselt number must first be determined. Correlation exists for constant plate temperature or heat flux, provided by [38]; the local Nusselt number at x from the start of the plate is given by:

$$Nu_x = 0.3387 Re_x{}^{0.5} Pr^{1/3} \left(1 + \left({}^{0.0468}/_{Pr}\right)^{2/3}\right)^{-0.25}\ for\ isothermal\ plate\ and\ Re_x < 5 \times 10^5$$

$$Nu_x = 0.886{Re_x}^{0.5}Pr^{1/2}\left(1+\left({Pr}/{0.0207}\right)^{2/3}\right)^{-0.25} \quad for\ isoflux\ plate\ and\ Re_x < 5\times10^5$$

$$Re_x = \frac{\rho_{air} x U_{max}}{\mu_{air}}$$

The average Nusselt number along the plate for isothermal, laminar flow[38] is:

$$\overline{Nu_L} = 2Nu_x$$

For turbulent flow, the correlation is as follows [38],[39]:

$$Nu_x = 0.0296{Re_x}^{4/5}Pr^{1/3}\ for\ isothermal\ plate\ and\ 5\times10^5 < Re_x < 10^7$$

$$Nu_x = 0.0308{Re_x}^{0.8}Pr^{1/3}\ for\ isoflux\ plate\ and\ 5\times10^5 < Re_x < 10^7$$

The average Nusselt number along the plate for isothermal, turbulent flow[38] is:

$$\overline{Nu_L} = \left(0.037{Re_x}^{4/5} - 871\right)Pr^{1/3}$$

There is no correlation for the average Nusselt number for isoflux plate, as the temperature is constantly changing, but [39] commented that if the plate temperature is relatively uniform, the average correlation for isothermal could be used to approximate for isoflux conditions.

2.13 Glass absorber enhancement

The properties that describe a transparent surface are: transmissivity (the portion of radiation energy that can pass through the surface), emissivity (the portion of radiant energy that gets rejected after entering the surface), reflectivity (the portion of radiation energy that gets reflected before entering the surface) and absorptivity (the portion of radiation energy that gets absorbed by the surface).

2.13.1 Coating

By coating the glass with a monodispersed silica anti-reflective coating, a transmittance as high as 99.2%-99.5% was achieved [40]. The paper also discussed the effect of baking the glass sample, which was found to shift the transmittance towards lower wavelengths [40]. The effects of applying a low emissivity coating (aluminium-doped zinc oxide (AZO) and tin-doped indium oxide (ITO)) were discussed in [41]. When used in combination with the anti-reflective coating on the opposite side of the glass surface, a decrease of emissivity from 0.84 (low iron glass) to 0.20 was reported, with a small loss in transmittance (<0.1) [41].

2.13.2 Etching

Vapour phase etching was used by [42] to obtain a transmittance as high as 99.2%. The paper then experimented with different etching times and temperatures, and it was found that T=100°C and t=7min provided the optimal outcome. However, this research was intended for photovoltaic applications.

2.13.3 Iron content

Standard glass involves the addition of iron oxide to increase the stability in the manufacturing process; however, this causes absorption in the infrared and ultra-violet spectrum [43]. The absorption in the ultra-violet spectrum is due to ferric ion (Fe_2O_3), and the absorption in the infrared spectrum is due to ferrous ion (FeO). Because it is impossible to eliminate iron completely, the best outcome proposed by [43] is to maximize ferric ion in the total iron content; therefore absorption loss will only be in the ultra-violet spectrum. This ratio of ferric ion to total iron was defined as ferric efficiency; for 3mm thick glass and ferric efficiency of 1, the transmittance was 92% [43].

2.14 Condenser inner surface coating

The formation of dropwise condensation (DWC) and film wise condensation (FWC) is governed by surface energy. DWC is favoured in the condensation process as it has a higher heat transfer coefficient than FWC. To achieve DWC the surface must have a low surface energy. Several papers [44-47] have stated that to do this, there are three options:

1. The use of an organic promoter; [46] commented that this does not produce a permanent hydrophobic surface, and is not recommended.
2. The use of noble metals, such as gold, silver and chromium.
3. The use of low surface energy polymeric film, polytetrafluoroethylene (PTFE) film.

2.14.1 Ion implanted surfaces

Ion plating on a copper surface using Cr, Fe, Al, N, Bi, Sb, Sn, Se and In ions was reviewed in [44]. The paper concluded that only a Cr (chromium) surface was able to continuously promote DWC. Another technology, ion implantation, where doses of F, He, Ar, N and H were implanted on individual copper surfaces. Experiments showed that the copper surface implanted with F (Fluorite) ion promoted DWC the best, but later it was found that the surface was prone to oxidisation, and therefore [44] proposed to use a mixture of Cr and F ions for its new implantation. The paper concluded that this gave an excellent DWC surface, but gave no numerical quantities to describe the performance.

Another paper discussed the effect of the amount of N ion (10^{16} and 10^{15} cm^{-2}) as well as the implantation energy (20 and 60 keV) when implanting a titanium surface [45]. The paper found that an N ion dose of 10^{16} cm^{-2} with either 20 or 60 keV managed to produce a stable DWC; also [45] reported that the implantation energy had little effect on the result as both samples were similar.

2.14.2 Polymeric film

The processing condition of dynamic ion-beam mixed implantation (DIMI) technology to prepare a PTFE film on various metallic surfaces (brass, stainless steel, carbon steel and copper) were discussed in [46]. The DIMI technique consists of sputtering a PTFE plate using the Ar ion beam so that PTFE particles can be deposited on the metallic surface; then the N ion beam can be used to fix the PTFE particles so that a film is formed. The paper reported that the sample with the brass surface, using an Ar ion beam of 1.3 keV, 26mA, and an N ion beam of 32keV, 1.4×10^{14} cm^{-2} gave the best DWC surface [46]. A high energy Ar

ion beam was found to break down the PTFE surface, thus changing the properties of the coated film [46]. The heat transfer coefficient increased between 1.6 and 28.6 times for various samples [46].

Different thicknesses of polyvinylidene chloride (PVDC) coating (0.05, 0.10, 0.25 and 0.50μm) were tested in [47]. The paper found that there was a negative relationship between coating thickness and heat transfer coefficient [47]. Endurance tests were conducted for a 10μm sample and showed little sign of change after two years and five months in the presence of steam at atmospheric pressure [47].

2.15 Mixing devices inside pipes

Due to the thermal stratification problem experienced in the flat plate experiment in Section 5, which made it difficult to apply the integral approach shown in Figs. 4.6.13 and 4.6.14 to obtain the rejection value, as the layer of hot air is relatively thinner than the sampling grid. The approach was to introduce an additional length of piping either before or after the fan to mix the air evenly without causing a huge pressure loss or flow stratification that would make air velocity or temperature measurements more difficult. Other factors to take account of are adiabatic compression and energy from the fan if the pipe is placed after the fan; both these factors will increase the air temperature reading. The literature was mostly on industrial mixing where the fluid is mainly water and chemical compounds, but the concept should be able to be applied to thermally stratified air. If only using an empty pipe, 100 diameters of pipe length is needed for complete mixing of chemical species [48]. However, this was referring to liquids and it was not known what the concentration or distribution of the chemical was.

2.15.1 Air blender

In HVAC applications, thermal stratification can cause the building to be improperly air conditioned due to the variation in temperature measurements depending on where the thermal sensor is located [49]. To overcome this problem an Air Blender patented by [49] was tested to determine whether this would reduce the error on the averaging bulb sensor. By comparing the error between the average temperature verses the mixture temperature, as air velocity was not uniformly distributed, it was defined as:

$$T_{avg} = {}^{1}\!/_{n} \sum_{i=1}^{n} T_i \qquad T_{mix} = {}^{\sum_{i=1}^{n} T_i V_i}\!/_{\sum_{i=1}^{n} V_i} \qquad Error = T_{avg} - T_{mix}$$

where n is the number of grids in the measuring cross-section, i is the grid number, and T_i and V_i are the temperature and velocity measurement at each grid.

It was found that, for the same flow rate and similar incoming air temperature distribution, the system with the Air Blender had an error of 0.05°C as to 4.3°C [49]. This shows the Air Blender's effectiveness in mixing the thermal stratified air while also rebalanced the non-uniform incoming flow. To measure the mixing effectiveness of a mixing device, [49] considered the following:

$$E_{RdT} = 1 - \left({}^{Range_{DS}}\!/_{dT}\right)$$

where $Range_{DS}$ is the range of the temperature at the measuring cross-section, downstream of the mixer device and dT is the range of the temperature at the inlet.

However, this equation does not consider the ratio of hot to cold air entering the system; therefore, the earlier approach, where minimizing the error between the average temperature and mixture temperature, should be used as a measure of mixing effectiveness.

2.15.2 Static mixer

There are many different designs of industrial static mixer as discussed in [50]; comparison was made between the standard Kenics mixer and the newer Sulzer SMX designs, where the SMX(1,1,4, Ø=135°) was found to provide a higher mixing to pressure drop ratio than the Kenics RL 180° [50]. There were other more compact designs that would provide more mixing, but at the cost of a higher pressure drop [50]. Optimisation was done for the Kenics mixer alone in [51], where it looked at the twist angle and the arrangement of the blades. Given the fix parameter that the blade must fit in a 60mm pipe, each blade is 115mm long and 2mm thick, the Kenics RL 140° was found to have the most efficient mixing. In [50] it was commented that the SMX(1,1,4, Ø=135°) had similar performance to the Kenics RL 140°. The limitations of these two studies is that this had been only studied for laminar mixing where Re=100 at max [51]; it is not known how this would perform in turbulent flow.

Another study found that only the twist angle affects mixing at low Re, but at high Re the aspect ratio of the blades was also relevant [52]. Turbulent conditions of up to Re=10^5 had been studied by [53] for one unit of the Kenics RL 180° with different aspect ratios; after dimensional study and CFD modelling, [53] was able to derive the following correlation:

$$C_f AR^{2.04} = K\left({Re}/{AR^{2.15}}\right)^n \quad K \text{ and } n \text{ are fitting constants}$$

$$AR = {L_e}/{D_e} \quad L_e \text{ is the length of the Kenics unit}$$

$$\text{where } C_f \text{ is the dimensionless friction factor} = \frac{2\Delta P D_e}{\rho U^2 L_p}$$

$$L_p = \text{number of mixer units} \times L_e$$

$$K = \begin{cases} 320 & 0 < {Re}/{AR^{2.15}} < 100 \\ 32 & 100 < {Re}/{AR^{2.15}} < 1000 \\ 2.66 & 1000 < {Re}/{AR^{2.15}} \end{cases}$$

$$n = \begin{cases} -0.86 & 0 < {Re}/{AR^{2.15}} < 100 \\ -0.36 & 100 < {Re}/{AR^{2.15}} < 1000 \\ 0 & 1000 < {Re}/{AR^{2.15}} \end{cases}$$

By using this correlation, the pressure loss for a Kenics RL 180° mixer of any size or aspect ratio can be determined, making it useful in sizing the fan or pump delivering the fluid. However, this study is only valid for one unit of this particular variant of mixer; it is not known whether ΔP could be scaled proportional to the number of mixer units. In [54] the interpretation for pressure loss due to additional mixer units is as follows:

$$\Delta P = \frac{C_f \rho U^2}{D_e} N_u L_e \; where \; N_u \; is \; the \; number \; of \; mixer \; units$$

This meant the earlier expression of L_p from [53] can be interpreted as $N_u L_e$ and the assumption with proportional scaling according to the number of mixer units is correct.

To account for the amount of mixing by the static mixers, G values are used based on the amount of pressure loss by the mixer [55].

$$G = \sqrt{{Q\Delta P}/{\mu V_m}} = \sqrt{{\Delta P}/{\mu N_u L_e}}$$

where the volumetric flow rate, $Q = 0.25\pi {D_e}^2 U$ and the mixer volume, $V_m = 0.25\pi {D_e}^2 N_u L_e$.

However, the G values do not take into account the effectiveness of the mixer design, as in the literature some designs were shown to mix more effectively than others. To evaluate how well a mixer is mixing, the following approach is used [54]:

$$\bar{c}_1 = {1}/{n} \sum_{i=1}^{n} \bar{c}_{1,i} = \frac{Q_1}{Q_1 + Q_2}$$

The average concentration of the first chemical species inside the mixture assuming full mixing, $\bar{c}_1$ has to be equal to the ratio of flow rate of both species, Q_1 and Q_2. To measure the homogeneity of the mixture, the coefficient of variance is used where S_1 is the standard deviation of the mixture concentration [54]:

$$COV = \frac{S_1}{\bar{c}_1} \qquad {S_1}^2 = {1}/{n-1} \sum_{i=1}^{n} \left(\bar{c}_{1,i} - \bar{c}_1\right)$$

A general form of empirical correlation has been developed for COV for one mixer unit [54]:

$$COV = b.exp\left(\frac{-Z' L_e}{D_e}\right)$$

where b and Z' are fitting constants, b depends on $\bar{c}_1$ values and Z' is related to mixer geometry. For the Kenics mixer only, the following fitting constant exists for $\bar{c}_1$ =0.1 [54]:

$$COV = 3.04.exp\left(\frac{-0.171' L_e}{D_e}\right)$$

The application of this empirical correlation is limited to $\bar{c}_1$ =0.1, but $Z' = 0.171$ is still valid for all Kenics mixers. Therefore, more work will need to be done to correlate $\bar{c}_1$ for a range of b values.

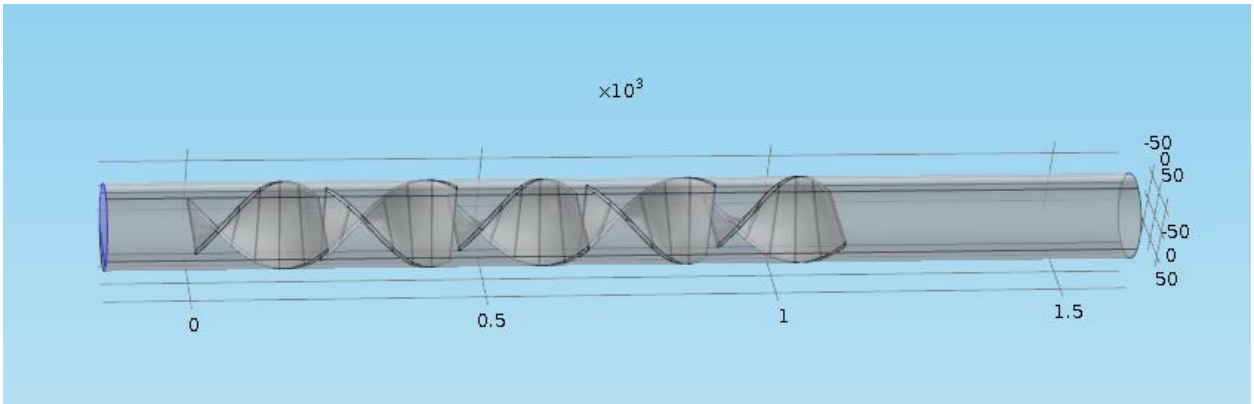

Figure 2.15.1. A schematic representation of the Kenics RL 180° mixer comprising five units.

2.16 Key findings and limitations

A fishbone diagram was used to illustrate the topics that were relevant in solar still condenser design on Fig. 2.16.1. Limitations or topics that were desired but was not found in the literature were shown in red. Topics that were looked at in the literature review are shown in black, topics that were in the literature and involved in this research were shown in blue.

2.16.1 Use and limitations of mathematical models for passive solar stills

There are four mathematical models discussed in the literature review, each of which varies regarding complexity and approach. The more complex models will require more setup and data processing, while the simpler models are only limited to certain operating conditions due to empirical fittings. Some models rely on humidity, while others depend on the different modes of heat transfer in convection, evaporation, radiation, and condensation.

The use and limitations of the four mathematical models are:

1. The Chilton-Coburn provides the most in-depth yet most complex approach, as it requires many psychrometric measurements.
2. The Dunkle's model has been widely used in much of the literature, and it only requires several temperature measurements; it has been found to overestimate production by 30% [32]. This is due to its reliance on empirical fittings, which only works for a certain temperature range, 17℃ to 50℃ [29]. It also ignores the partial pressure of the water vapour as it does not have a humidity term anywhere in its formulation; this assumption causes the model to fail at a higher temperature when the internal air becomes more humid.
3. There has been no literature documenting the use of the Penman-Shuttleworth equation to model passive solar still performance. It is not known whether evaporation in hydrology can be compared to the inside of a solar still.

4. The Gorrie model was derived from the rig that he had used. It is one of the few models that takes humidity into account. Unlike the Dunkle's model, this model has not been verified by other researchers yet. Limitations of the Gorrie model are: absence of the pressure term in its formulation, as pressure will change with temperature; the model uses arbitrary heat and mass transfer coefficients with non-homogenous dimensions, which hides the information of how the other variables (for example drop backs, re-evaporation) affect the overall water production rate; and absence of heat transfer coefficient terms, as in the Chilton-Coburn the effects of humidity are linked with the heat transfer coefficient.

2.16.2 Findings and limitations regarding condenser design and operational factors

Inner condenser surface coating

The literature also suggested the use of ion implantation techniques to induce dropwise condensation, so that the heat transfer coefficient is increased. Some types of coatings are unstable and will degrade over time, particularly for polymeric film. Some degrade slower due to a higher ion count and implantation energy, but this will accelerate if there is friction. The only permanent solution would be to use a noble metal (gold, silver) surface, but that would be a costly application.

Extended surfaces

A topic like extended surfaces has been applied to heat exchangers and computer cooling but has not been applied directly to heat rejection in solar stills. For heat sink pin-fin geometry it was found that circular and elliptical pin-fins are superior to square and rectangular pin-fins in forced convection [3]. As for the pin-fin arrangement, a staggered alignment was found to have a greater heat transfer coefficient than inline, provided that there is sufficient airflow to reach to the back rows of the array.

There are also many other possible pin-fin geometries that were not considered, like introducing multiple pin-fin geometries on the same pin-fin array might give better results. However, this will increase the level of complexity in setting up the optimisation problem, which is not effective for just a small increase in heat rejection. Also, it is not yet known as to whether adding an extended surface will have an impact on the overall water production.

For free convection, little is known about how different pin-fin geometries will perform. Therefore, the optimal design solution for forced convection may not be applicable when there is no airflow. It could be that pin-fin array with the maximum surface area is the optimal design regardless of the pin geometry.

Rig Geometry

Research on solar still scalability, height and inclination of the condenser surface have not been covered in the literature. In most journal papers only one rig is designed and built with no emphasis on rig geometry. The only studies regarding rig geometry are about the effects of single slope stills (SSS) and double slope stills (DSS). Without knowing the effects of these parameters, it is not known whether the

mathematical models are still valid when the rig geometries change as none of them contain variables describing them at all.

Airflow management

Flow straighteners are found to reduce the vortices in airflow, which can then provide a smoother flow for experimental measurement purposes. However, there will be some pressure loss associated with it depending on the amount of additional surface area the airflow has to come into contact with. Unless exact measurements are required on each pin-fin, taking the average of the heat rejected across the entire array is sufficient when comparing with the results from CFD.

As for the air flowing through the pin-fin array, the formation of vortices is useful in heat rejection as long as it does not result in a significant pressure drop across the system. A pin-fin array with square fins and staggered alignment is an example of this.

Least material optimisation

Both papers were discussed using mathematical and computational methods to determine the optimal fin height and diameter on a duct flow/top flow heat sink. The paper that looked at duct flow heat sink considered the model as a slice in 2D, and the size/number of fins was only changed with a constant volume of material. Therefore, the flow interaction from the side of the fin and possibilities with a different volume of material was not considered. Another paper primarily looked at using PPS as to aluminium for top flow heat sinks to achieve better heat rejection to mass ratio, and also comparing with several different heights, spacing, and diameter of fins using the least material equation. However, this equation requires a constant convective coefficient which is not suitable to be used in duct flow heat sink when the air temperature gets hotter as it travels through the heat sink.

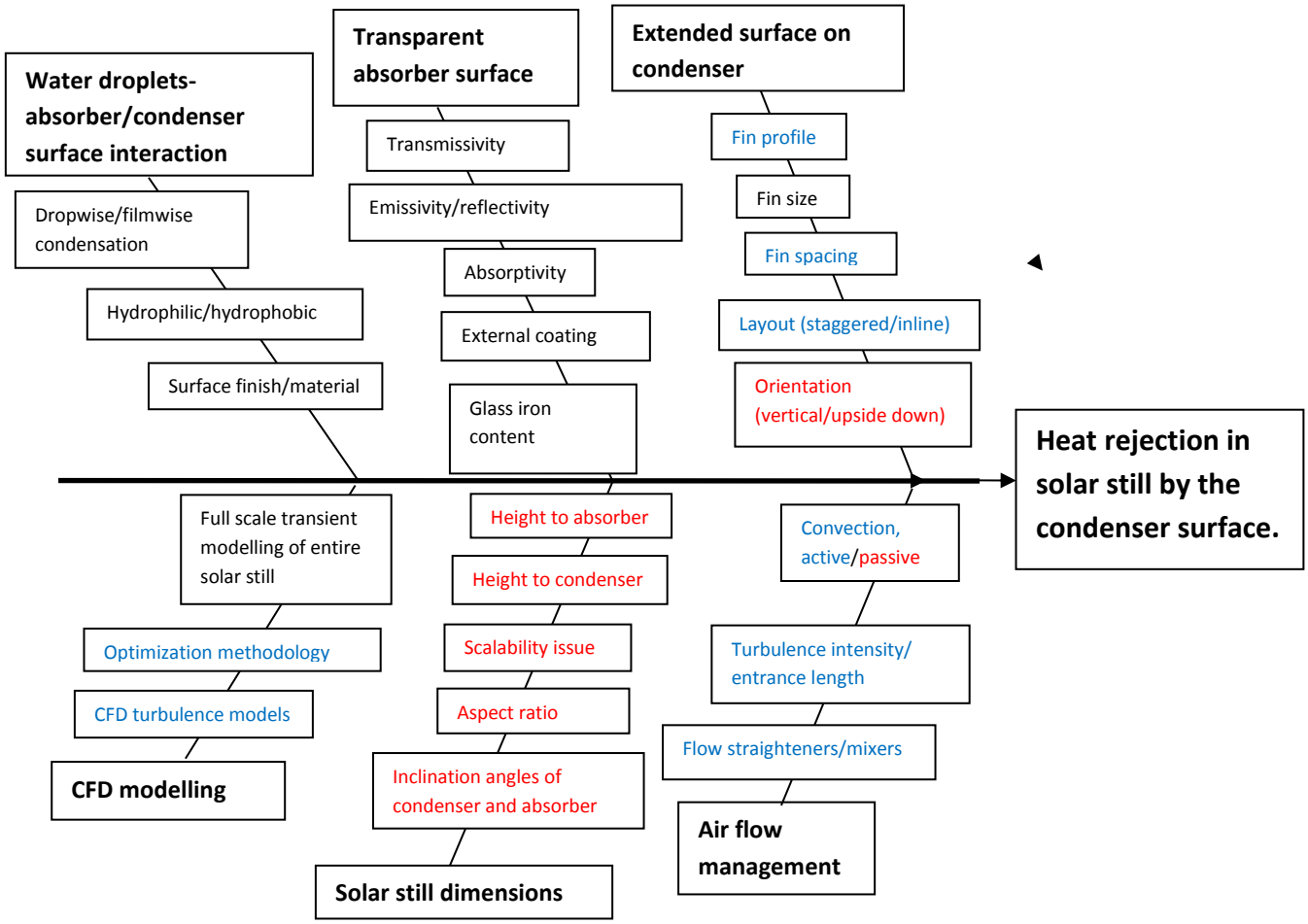

Figure 2.16.1. Summary of topics that are relevant to the heat rejection ability of the condenser: black= topics covered in the literature review; blue=topics that were covered in both the literature review and in this research; red = unknown content (research needed).

3 Method

3.1 Purpose

The purpose of this research is to optimise the geometric design of the external condenser surface, to maximise heat rejection per volume of aluminium used.

There are many studies regarding optimisation on passive solar still designs and methods of modelling. However, none has looked at optimising the condenser surface. Gorrie identified that by forced cooling of the condenser surface, an increase of 60% in water production was achieved. The intended outcome of this project is to use CFD and experimental data to validate the heat rejection of the new condenser design.

3.2 Approach

The goal of this project was to find ways to increase heat rejection by the condenser surface. This was achieved by CFD and experimentation.

The project consists of four phases: the first phase was devising with possible geometric designs of the condenser surface, and also considering the design of the rig to test the chosen condensers. The second phase was about conducting CFD to determine the optimal condenser design that matches the purpose statement. In the third phase, experimental data were collected for the optimal condenser design. Along with the experimental data, a fully detailed CFD was done for the optimal condenser design dedicated to the experiment setup and environment, so that the findings can be validated.

3.2.1 Phase 1: Defining the scope of the optimisation problem

This phase considered the possible geometric designs of the external condenser surface and the rig needed to test the new design. It was decided that the geometric design would be in the form of extended surfaces to improve heat rejection, and the objective was to determine which geometric design would satisfy the purpose statement. The basic design of the condenser was based on the dimension of the flat plate condenser used in Gorrie's experiment, and any geometric improvement would be done by adding material on top of the existing flat plate. Also, the manufacturability of the design was also considered based on the resources given in this project.

1.1 Geometric design variants

Pin-fins were chosen as the optimal extended surface to be installed on the condenser surface, as they could provide a large amount of additional surface area to improve heat rejection and be parametrized for CFD optimisation. Based on the literature review, there were four basic pin-fin geometries: square, rectangular, circular and ellipsoidal. Along with these basic pin-fin geometries, other key parameters (plate thickness, pin-fin height and size, material, the number of fins and spacing), and constraints (condenser area, the allowable number of fins and spacing) were determined in Section 4.1.

3.2.2 Phase 2: Setting up the CFD parametric optimisation

As identified by [35], there is a need for a methodology to approach CFD parametric optimisation so that time is not wasted in computing for points away from the optima. The optimisation approach on Fig. 3.2.1 adopted the approach from [35] for finding the optimal geometric candidate of the pin-fin array under forced convection. There are four design parameters in total: they are the fin geometry, fin height, fin array configuration and the number of fins. An equivalent cross-sectional area of 10mm diameter was held for all pin geometries so that direct comparison can be made as to heat rejection versus aluminium used. The presence of continuous and discrete/logical parameter values pose problems for CFD programs. Therefore, the two-stage approach in Figure 3.2.2 was used to optimise for one or two variables at a time. Also, this process reduced the number of unnecessary computations on points far away from the optima. All resulting response parameters for each simulation were documented for potential future use.

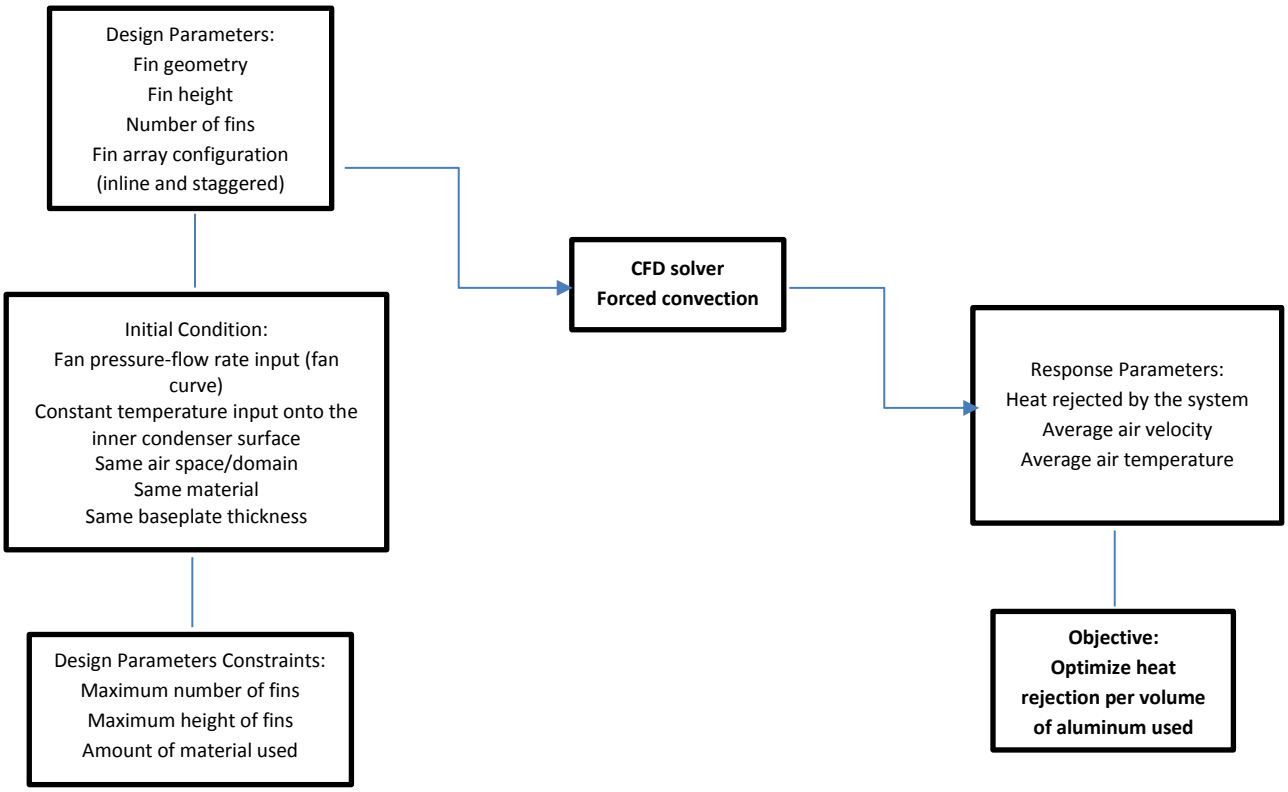

Figure 3.2.1. Following the design optimisation approach according to [35]. Modified by M. Leung.

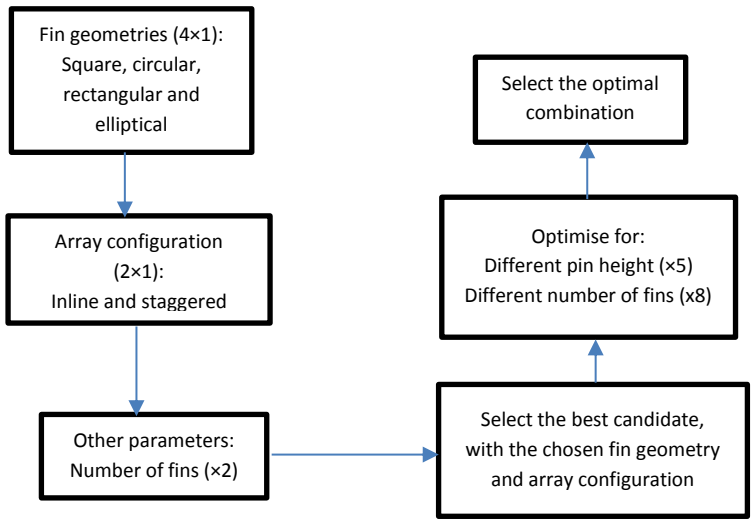

Figure 3.2.2. The two stage CFD optimisation process for determining the best geometric design of the external condenser surface for heat rejection.

This resulted in 100 simulations in total, with 16 simulations in the first stage to determine the optimal configuration and pin geometry, and 84 in the second stage to determine the optimal pin height and the exact number of fins. The combination that gives the highest heat rejection per volume of aluminium used was considered the optimal condenser design.

Phase 3: Rig design and empirical data collection

The purpose of this phase was to collect relevant experimental data so that a comparison could be made as to the heat rejection performance between a flat plate condenser and the optimal condenser design. From how well the experimental data matched the CFD, it then gave the level of confidence/uncertainty when using the heat rejection value from CFD.

1. Planned out the data acquisition setup required for the experiment, thermocouples, PID controller, pressure transducer etc. Produced manufacturing drawings for the rig and both condenser designs (flat plate and optimal condenser design), shown in Section 11.2.
2. Finalized the manufacturing options when fabricating the rig and condenser plates, such as whether to manufacture the water container from bending a single piece of Perspex or assembling several pieces of Perspex to form the container, see Section 4.6.
3. Purchased and gathered relevant resources and equipment, including ducting, heating element, axial fan, aluminium sheets and bars, Perspex sheets and data acquisition probes.
4. Manufactured the rig and both condenser designs, as per Section 5.1-5.3.
5. Gathered experimental data for the heat rejection and also the velocity and temperature profiles at the inlet and outlet of the main duct for both the flat plate and optimal condenser design.

Phase 4: Refined CFD to validate the experimental result

Refined CFD analyses were done for both the flat plate and the optimised pin-fin condenser after the experiment had taken place. The purpose of this refined CFD study was to include the experimental conditions of each test run, which were measured during the experiment. Experimental conditions, such as ambient temperature and inner condenser temperature, need to be entered back into the refined CFD, so that the outcome of the modelling could be compared directly with the data collected during the experiment. The disagreement between the refined CFD and the experimental results were discussed in Sections 6, 7 and in the Discussion. Also, updates on the rig geometry were also included in the refined CFD analysis.

4 CFD optimisation of the condenser design

4.1 Parametric design variants and fixed constraints

In the first part of the optimisation, all four fin geometries (square, circular, rectangular and elliptical) were considered, as mentioned in Section 3.2.2, as well as different fin array configurations (inline and staggered). Fins were fixed at 100mm high in the first part to give a better understanding of how other design parameters affected heat rejection, and varied in the second part. The number of fins were fixed at 18, 21, 90 and 100 fins in the first part, depending on the array configuration. To restrict the number of combinations, all four pin geometries had the same cross-sectional area equivalent to 10mm diameter. After the best fin geometry and array configuration were determined from the first part of the optimisation, a more refined search was done to determine the exact optimal number and height of the fins.

4.1.1 Fin geometries, layout, and parametric constraints

From the initial parameterization below, which considers all possible combinations achievable with the inline/staggered arrangement and all four different pin geometries and number of fins in the x and y directions. The parameterization was used to create the pattern on COMSOL, which could then be used for automated optimisation purposes. In the first and second part of the optimisation, more constraints were added, such as the height and number of pin-fins.

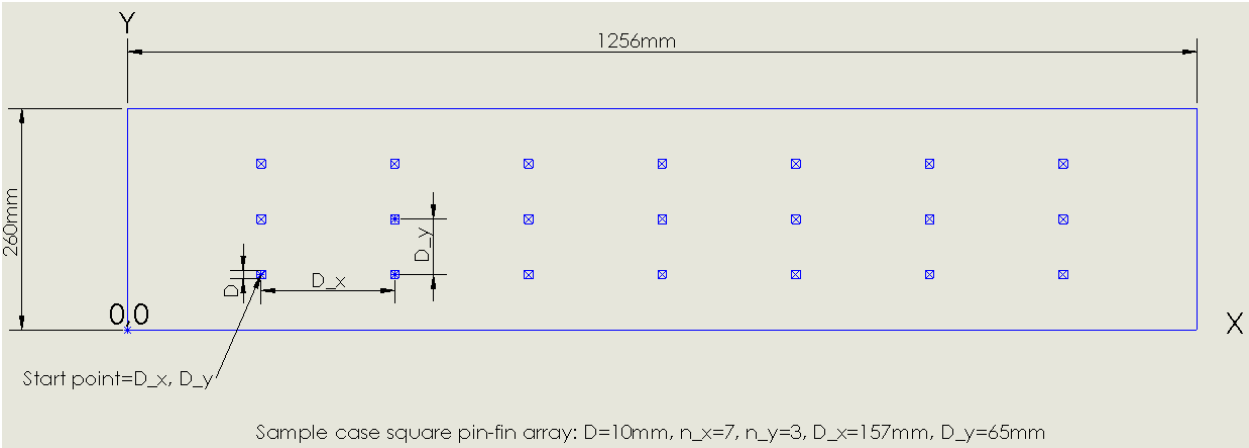

Figure 4.1.1. Parametrisation for the square pin-fin array inline on COMSOL.

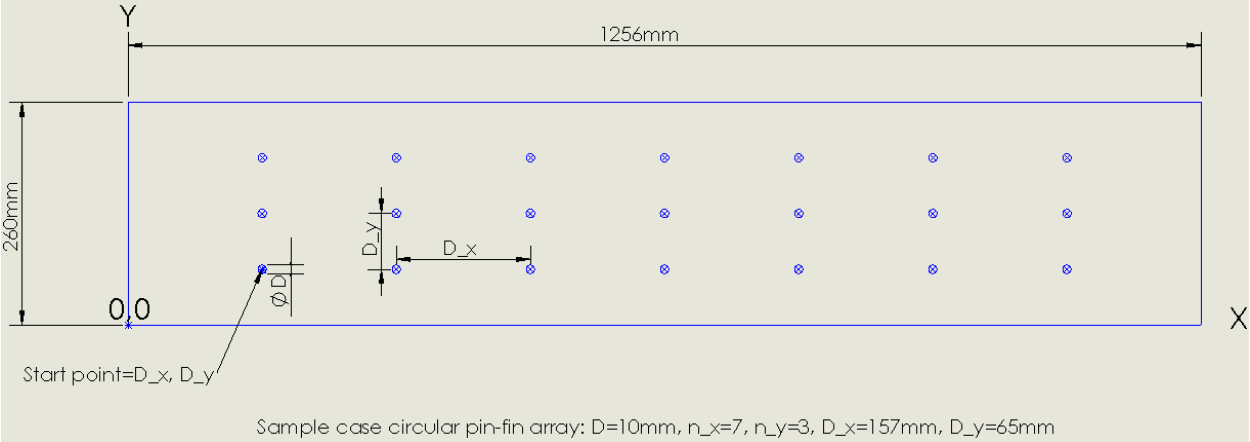

Figure 4.1.2. Parametrisation for the circular pin-fin array inline on COMSOL.

Definition of parameters for square and circular inline pin-fin arrays:

D=Edge length for square pin-fins and diameter for circular pin-fins.
n_x=Number of pin-fins in the x-direction.
n_y=Number of pin-fins in the y-direction.
D_x=Spacing of pin-fins in the x-direction, centre to centre.
D_y=Spacing of pin-fins in the y-direction, centre to centre.
$Plate\_x$=Length of the plate=1256mm
$Plate\_y$=Width of the plate=260mm
P_h=Height of the pin-fin

Parametrisation for square and circular inline pin-fin arrays:

$$D = \sqrt{0.25 \times \pi \times 10mm^2} = 8.86mm\ (square), 10mm\ (cirucular)$$

$$n_x = rounddown\left(\frac{Plate\_x}{2D}\right);\ integers\ only$$

$$n_y = rounddown\left(\frac{Plate\_y}{2D}\right);\ integers\ only$$

$$D\_x = \frac{Plate\_x}{n\_x + 1}$$

$$D\_y = \frac{Plate\_x}{n\_y + 1}$$

$$0mm < P\_h < 200mm$$

Definition of parameters for rectangular and elliptical inline pin-fin arrays:

$D1$=X dimension of the pin-fin geometry.
$D2$=Y dimension of the pin-fin geometry
n_x=Number of pin-fins in the x-direction.

n_y=Number of pin-fins in the y-direction.
D_x=Spacing of pin-fins in the x-direction, centre to centre.
D_y=Spacing of pin-fins in the y-direction, centre to centre.
$Plate\_x$=Length of the plate=1256mm
$Plate\_y$=Width of the plate=260mm
P_h=Height of the pin-fin
Parametrisation for rectangular and elliptical inline pin-fin arrays:

$$D1 = 2 \times \sqrt{0.25 \times \pi \times 10mm^2} = 17.73mm\ (rectangular), 20mm\ (elliptical)$$

$$D2 = 0.5 \times \sqrt{0.25 \times \pi \times 10mm^2} = 4.43mm, 5mm\ (elliptical)$$

$$n_x = rounddown\left(\frac{Plate\_x}{2D1}\right);\ integers\ only$$

$$n_y = rounddown\left(\frac{Plate\_y}{2D2}\right);\ integers\ only$$

$$D\_x = \frac{Plate\_x}{n\_x + 1}$$

$$D\_y = \frac{Plate\_x}{n\_y + 1}$$

$$0mm < P\_h < 200mm$$

Using a similar approach to the square and circular pin-fin, but now with an additional parameter to describe the pin-fin geometry.

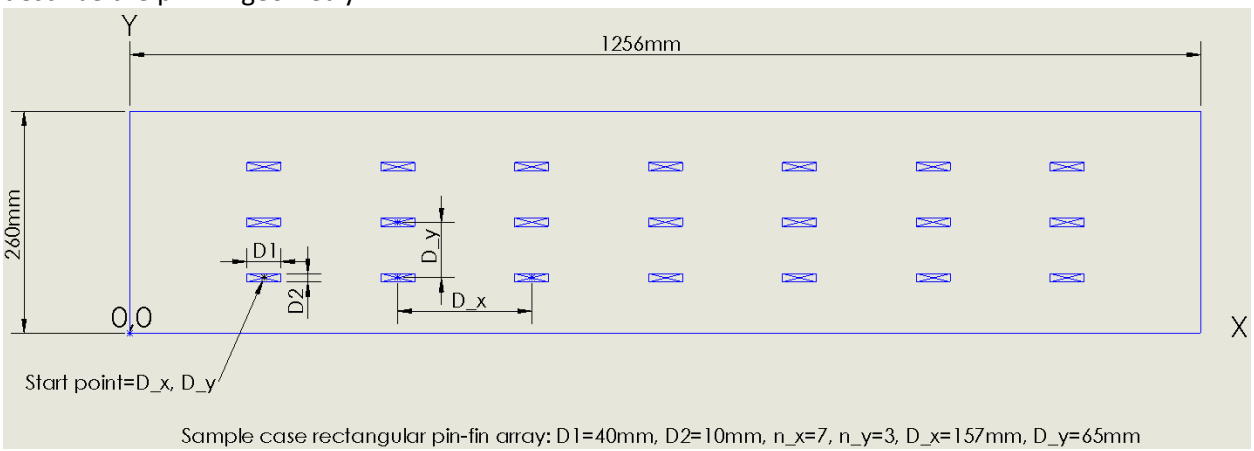

Figure 4.1.3. Parametrisation for the rectangular pin-fin array inline on COMSOL.

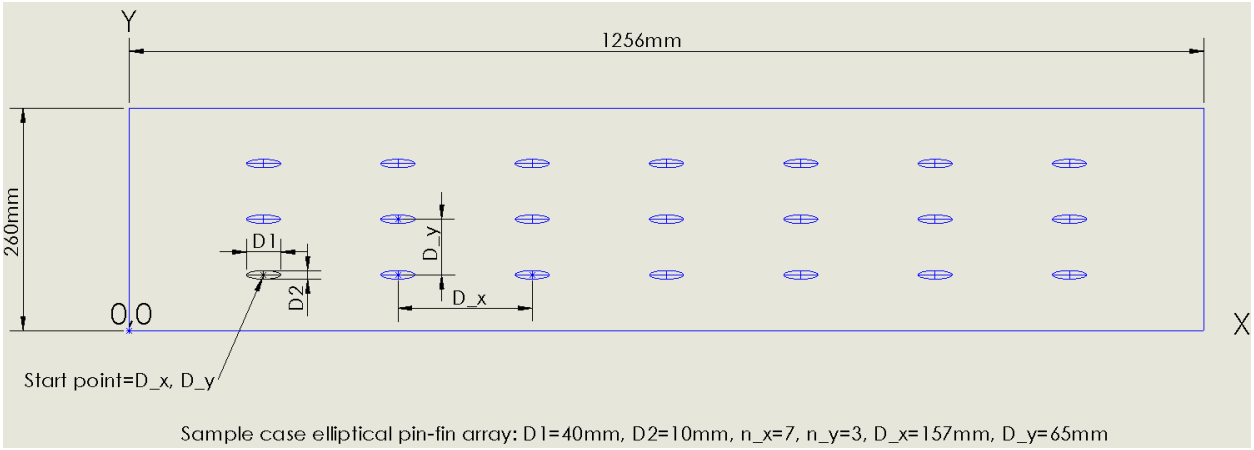

Figure 4.1.4. Parametrisation for the elliptical pin-fin array inline on COMSOL.

Definition of parameters for square and circular staggered pin-fin arrays:

D=Edge length for square pin-fins and diameter for circular pin-fins.
n_x=Number of pin-fins in the x-direction.
n_y=Number of pin-fins in the y-direction.
n_xlong=Number of columns with number of pin-fins equal to n_y.
n_xshort=Number of columns with number of pin-fins equal to $n\_y - 1$.
n_ywide=Number of pin-fins in the y-direction for n_xlong columns, also equal to n_y.
$n\_ynarrow$=Number of pin-fins in the y-direction for n_xshort columns, also equal to $n\_y - 1$.
D_x=Spacing of pin-fins in the x-direction, centre to centre.
D_y=Spacing of pin-fins in the y-direction, centre to centre.
$Plate\_x$=Length of the plate=1256mm
$Plate\_y$=Width of the plate=260mm
P_h=Height of the pin-fin

Parametrisation for square and circular staggered pin-fin arrays:

$$D = \sqrt{0.25 \times \pi \times 10mm^2} = 8.86mm\ (square), 10mm\ (cirucular)$$

$$n_x = rounddown\left(\frac{Plate\_x}{2D}\right);\ integers\ only$$

$$n_y = rounddown\left(\frac{Plate\_y}{2D}\right);\ integers\ only$$

$$n\_xlong = rounddown(0.5n\_x + 0.5);\ integers\ only$$

$$n\_xshort = rounddown(0.5n\_x);\ integers\ only$$

$$n\_ynarrow = n\_y - 1$$

$$n\_ywide = n\_y$$

$$D\_x = \frac{Plate\_x}{n\_x + 1}$$

$$D\_y = \frac{Plate\_x}{n\_y + 1}$$

$$0mm < P\_h < 200mm$$

The situation is the same as for square and circular inline arrangement but with one less fin every second column. n_xlong, n_xshort, $n\_ynarrow$ and n_ywide are dummy variables to help with generating the overall array on COMSOL, by counting the number of wide and narrow columns based on the total number of pin-fins in the x-direction, n_x. The first column must always be the wide column. If n_x is odd then the number of wide columns, determined by n_xlong, will be one greater than the number of short columns, termed n_xshort. If n_x is even then $n\_xlong = n\_xshort$, and $n\_xlong + n\_xshort = n\_x$.

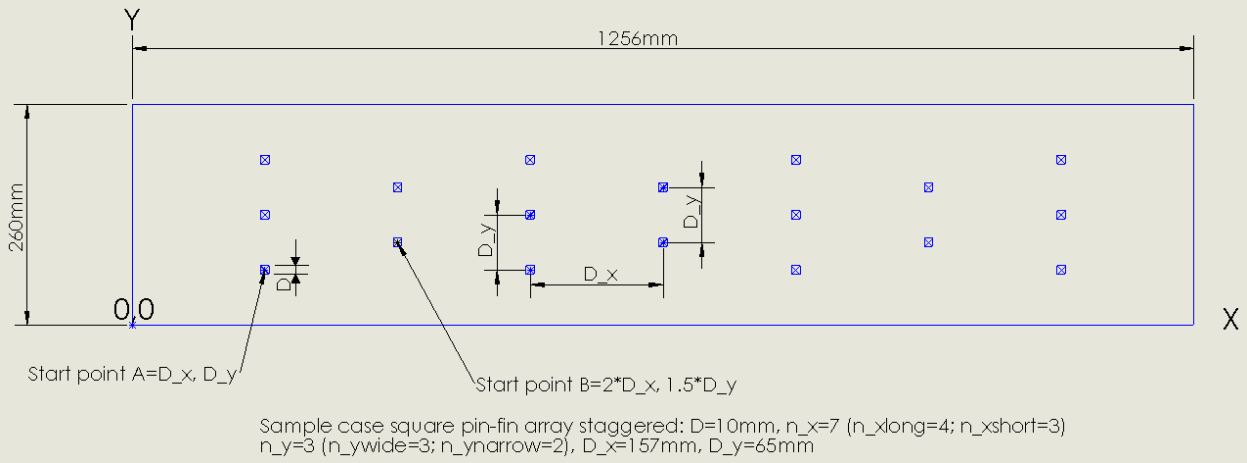

Figure 4.1.5. Parametrisation for the square pin-fin array staggered on COMSOL.

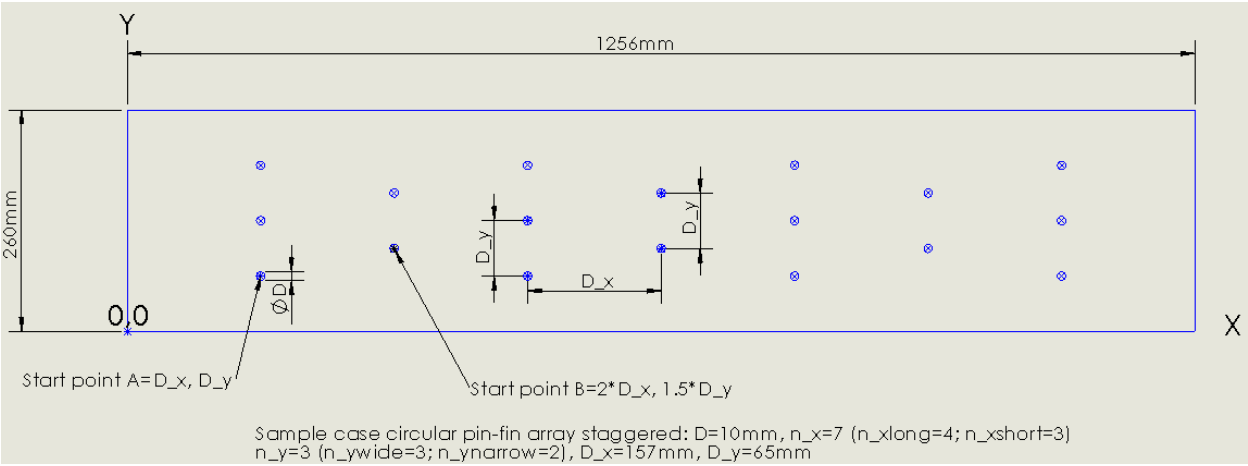

Figure 4.1.6. Parametrisation for the circular pin-fin array staggered on COMSOL.

Definition of parameters for rectangular and elliptical staggered pin-fin arrays:

$D1$=X dimension of the pin-fin geometry.
$D2$=Y dimension of the pin-fin geometry
n_x=Number of pin-fins in the x-direction.
n_y=Number of pin-fins in the y-direction.
n_xlong=Number of columns with number of pin-fins equal to n_y.
n_xshort=Number of columns with number of pin-fins equal to $n\_y - 1$.
n_ywide=Number of pin-fins in the y-direction for n_xlong columns, also equal to n_y.
$n\_ynarrow$=Number of pin-fins in the y-direction for n_xshort columns, also equal to $n\_y - 1$.
D_x=Spacing of pin-fins in the x-direction, centre to centre.
D_y=Spacing of pin-fins in the y-direction, centre to centre.
$Plate\_x$=Length of the plate=1256mm
$Plate\_y$=Width of the plate=260mm
P_h=Height of the pin-fin

Parametrisation for rectangular and elliptical inline pin-fin arrays:

$$D1 = 2 \times \sqrt{0.25 \times \pi \times 10mm^2} = 17.73mm\ (rectangular), 20mm\ (elliptical)$$

$$D2 = 0.5 \times \sqrt{0.25 \times \pi \times 10mm^2} = 4.43mm, 5mm\ (elliptical)$$

$$n_x = rounddown\left(\frac{Plate\_x}{2D1}\right);\ integers\ only$$

$$n_y = rounddown\left(\frac{Plate\_y}{2D2}\right);\ integers\ only$$

$$n\_xlong = rounddown(0.5n\_x + 0.5);\ integers\ only$$

$$n\_xshort = rounddown(0.5n\_x);\ integers\ only$$

$$n\_ynarrow = n\_y - 1$$

$$n\_ywide = n\_y$$

$$D\_x = \frac{Plate\_x}{n\_x + 1}$$

$$D\_y = \frac{Plate\_x}{n\_y + 1}$$

$$0mm < P\_h < 200mm$$

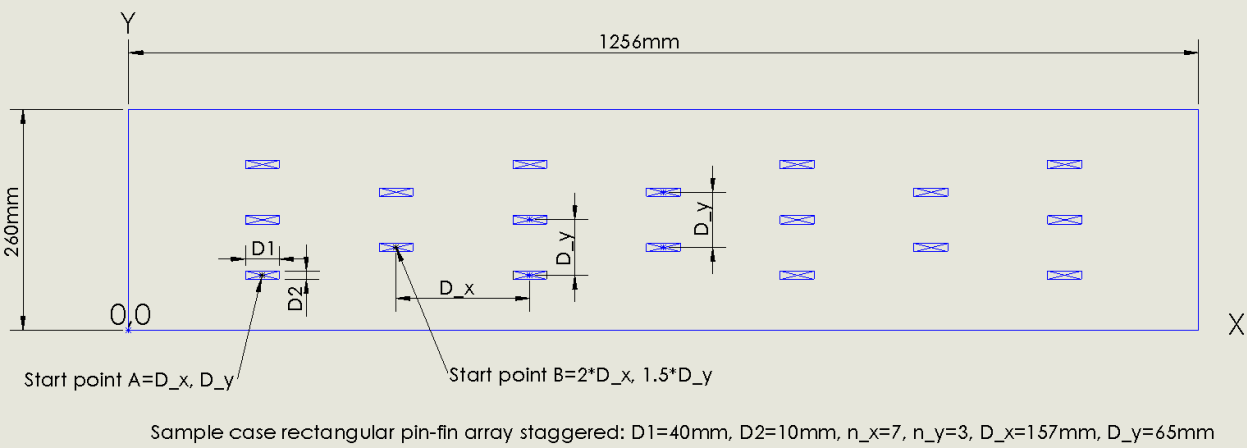

Figure 4.1.7. Parametrisation for the rectangular pin-fin array staggered on COMSOL.

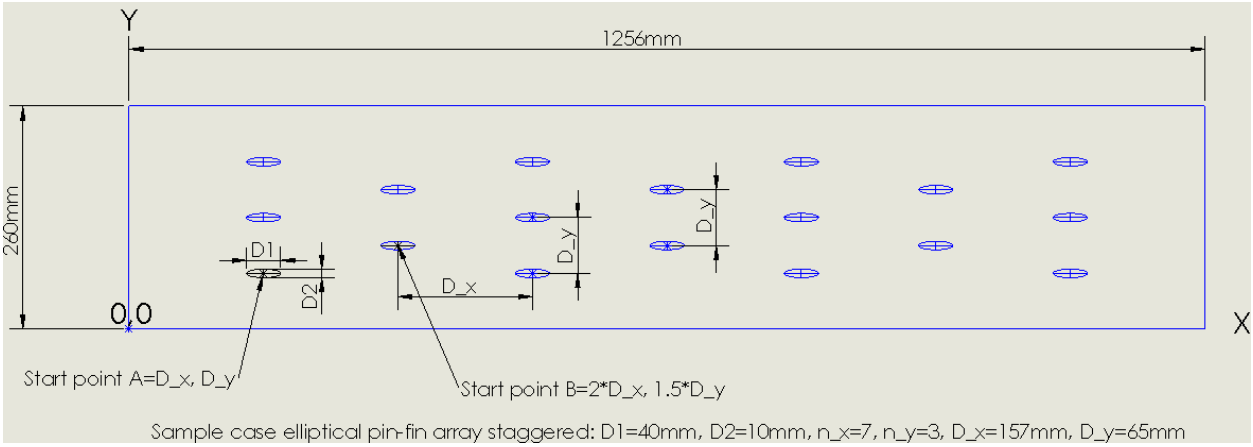

Figure 4.1.8. Parametrisation for the elliptical pin-fin array inline on COMSOL.

4.2 Collecting and calculating relevant response parameters from CFD results

Apart from determining the heat rejection on each CFD for the different condenser designs, information like average air temperature and air velocity were also collected in Section 4.5.5 to give further insight on the heat rejection characteristics that was found in Figs. 4.5.4 and 4.5.8.

4.2.1 Calculating heat rejection with the integral approach

Airflows from the inlet to the outlet at a uniform mass flow rate, assuming no change in air density; therefore, by determining the temperature difference between the inlet and outlet of the duct, and applying first principle thermodynamics, the heat rejected by the air can be computed as:

$$\dot{Q} = \dot{m} C_p (T_{Outlet} - T_{Inlet}) \; (W)$$

$$C_p \; of \; air = 1.005 kJ.(kg.K)^{-1} \; Specfic \; heat \; capacity \; of \; air$$

However, the mass flow rate and temperature coming out of the outlet will not be consistent along the z axis due to the pin-fins blocking and pushing some portion of air towards the ceiling. Therefore, the

complete approach would be to integrate the product of velocity, air density and temperature for both the inlet and outlet, and then subtracting it.

$$\dot{Q} = C_p \left(\sum_{0}^{mesh_{i=n1}} \rho_{i\ outlet} v_{i\ outlet} T_{i\ outlet}\ A_{i\ mesh} - \sum_{0}^{mesh_{i=n2}} \rho_{i\ inlet} v_{i\ inlet} T_{i\ inlet}\ A_{i\ mesh} \right) (W)$$

By visualising the inlet and outlet cross-section being made up of multiple tetrahedral mesh with an area of $A_{i\ mesh}$. Each mesh domain has its own data on air density, velocity and temperature, which was then multiplied by the mesh area and specific heat capacity of air to obtain the energy at the inlet and outlet.

4.2.2 Importance of other output parameters given by CFD

Air velocity and air temperature were also needed to be interrogated from the CFD as it also correlates to the amount of heat rejection by a fin array. This was done in Section 4.5 to explain for the heat rejection demonstrated by different fin array density and fin height. Because the fan was modelled using a fan curve, it has already accounted for the losses in flow rate due to the pressure induced by the fin array.

Average air velocity experienced by the fins determines how much air is flowing towards each fin. If the air velocity is higher due to compression by the fin array, this suggests it is more likely for there to be heat transfer by convection. However, a higher air velocity may not necessarily mean higher heat transfer as it also depends on the temperature difference between the external fin surface and incoming air. These details are discussed in detail using evidence from CFD in Section 4.5.

4.3 COMSOL optimisation setup for part 1 of optimisation

4.3.1 Steady state modelling

Steady state modelling was considered sufficient for determining the final heat rejection of a condenser surface given the same amount of heat gets inputted onto the system at any given time. Therefore, there was no need in doing transient modelling as the rate at which the system heats up from initial condition was of no interest. The input parameters for the steady state condition were chosen in Section 4.3.3 to best reflect on the condition experienced by the inner condenser surface in Test 17 of Gorrie's experiment.

4.3.2 Assumptions made

It was assumed that the optimal condenser design found will continue to reject heat better than other condenser design candidates for different heat load onto the inner condenser surface, as long as the other parameters remained the same. Therefore, several inner condenser temperatures were tested during the experiment to validate this assumption.

The RIL-150 fan, selected from Fig. 4.6.19, was to be modelled on CFD using the pressure-flow curve given. It was assumed that the flow inside the ducted space is linear. As to modelling, the profile of the

air generated by the axial fan, the helical flow effect, was assumed negligible as the air entering and leaving the duct is the same.

Mesh convergence will not be included in the CFD optimisation due to the amount of time required to repeat this process for each design point. If a mesh setting is showing a clear trend between the different optimisation parameters, and computes in a reasonable time (under one day per design point), then this mesh setting will be used for the remainder of the optimisation.

4.3.3 Relevant input conditions

The input conditions were selected based on the continuous measurements from Test 17 by Gorrie; they were the inner condenser surface temperature and the ambient air temperature shown in Figs. 4.3.3 and 4.3.6. Because this CFD optimisation was done in steady state, therefore only the average measurements from Test 17 were needed. No information can be found regarding the fan used in Test 17, therefore, the RIL-150 was purchased, shown in Fig. 4.6.19.

Heat source: Inner condenser surface temperature

It was decided to model the heat source onto the inner condenser surface; a constant temperature is better than heat flux as it was easier to control accurately during an experiment. An inner condenser temperature of 29.81℃ was used for the first part of the optimisation, as it was the average temperature on the inner condenser surface from Test 17 by Gorrie, shown in Fig. 4.3.3. The inner condenser temperature was a response to the heat flux experienced by the inner condenser surface, which was approximately 100W.m^{-2} for Test 17 shown in Fig. 4.3.4.

In Section 4.5.3, using the condition in Gorrie's Test 17, ambient, the inner condenser plate temperature of 18.33°C and 29.81°C gave a heat rejection value of 39.46W. This equates to a heat flux input of 120.8W.m^{-2}, which was higher than the average of 100W.m^{-2} in Test 17. The difference could come from the error in the measured pyrometer value, as it was not placed directly under the inner condenser plate but at the basin of the rig. However, by assuming that the heat onto the plate is equivalent to the pyrometer value, it still gave a close estimate.

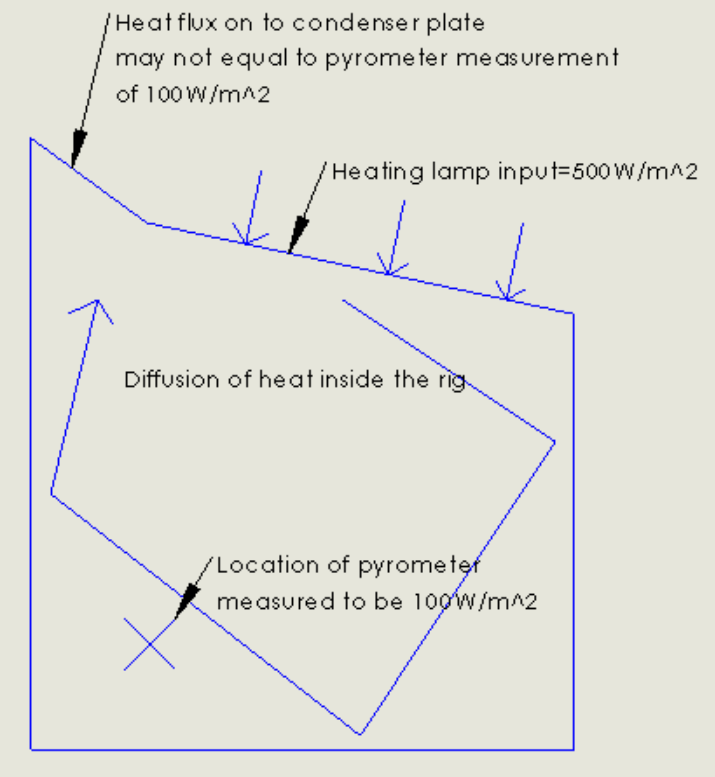

Figure 4.3.1. Difference in pyrometer measurement and actual heat reaching the condenser plate on Gorrie's rig.

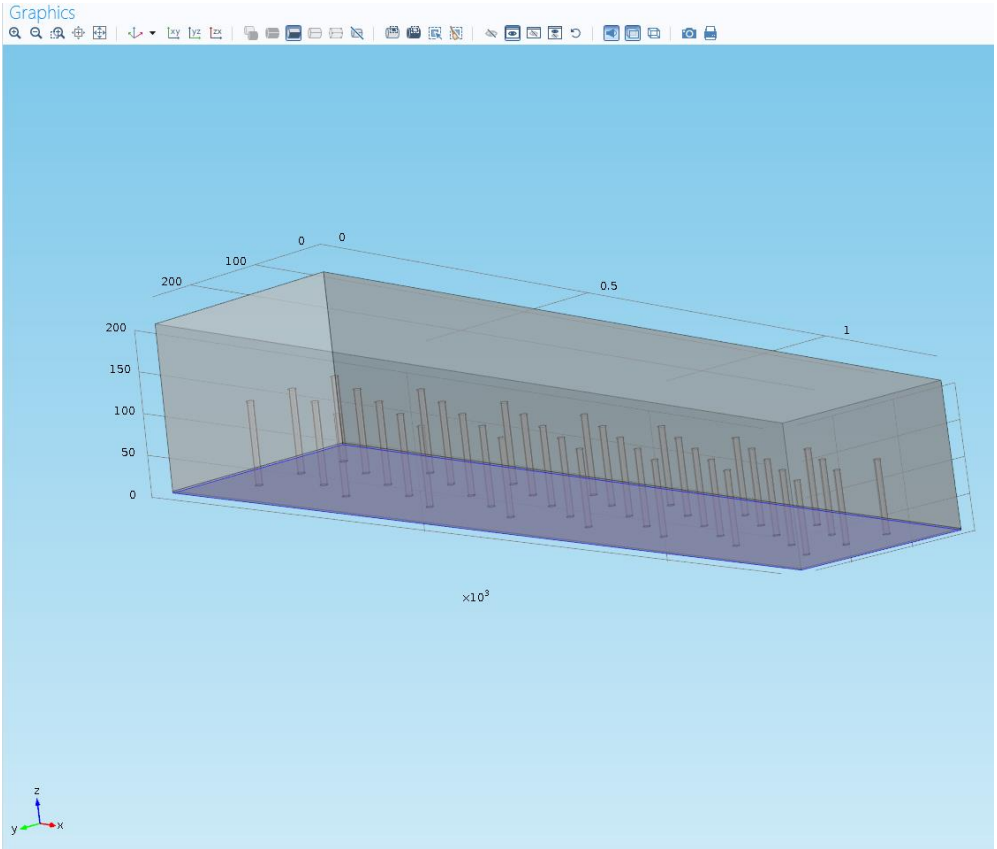

Figure 4.3.2. Prescribing the inner condenser temperature on COMSOL.

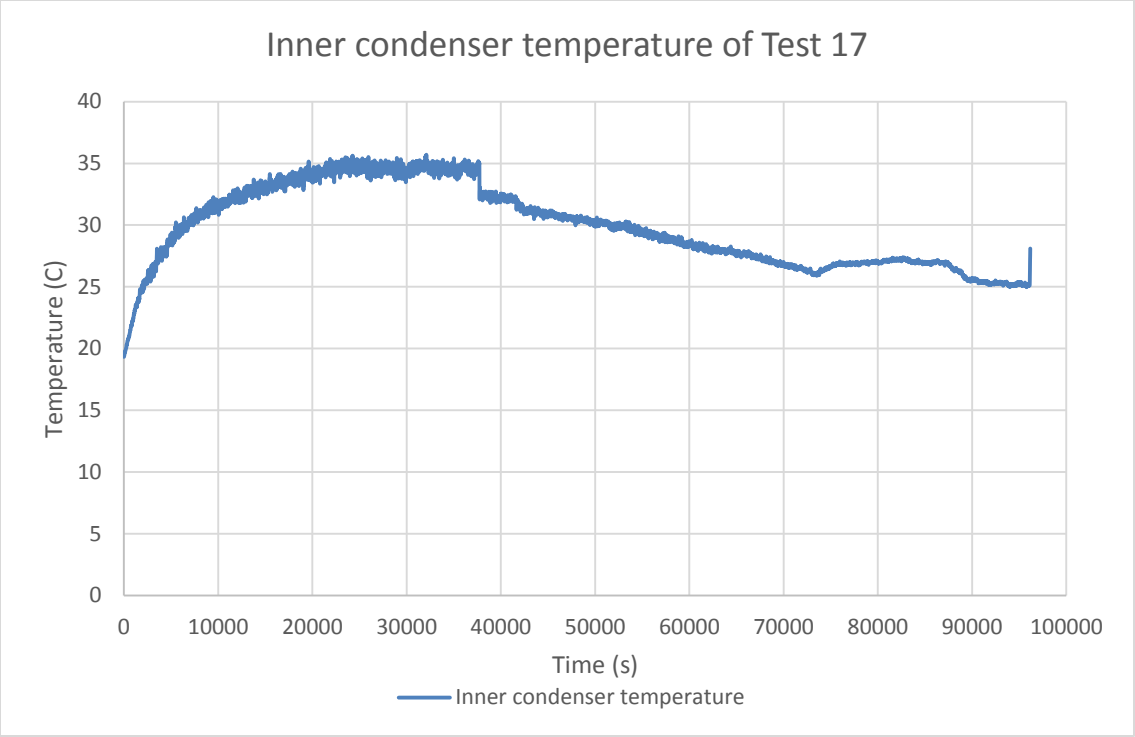

Figure 4.3.3. Inner condenser temperature profile during Test 17 by A. Gorrie [1].

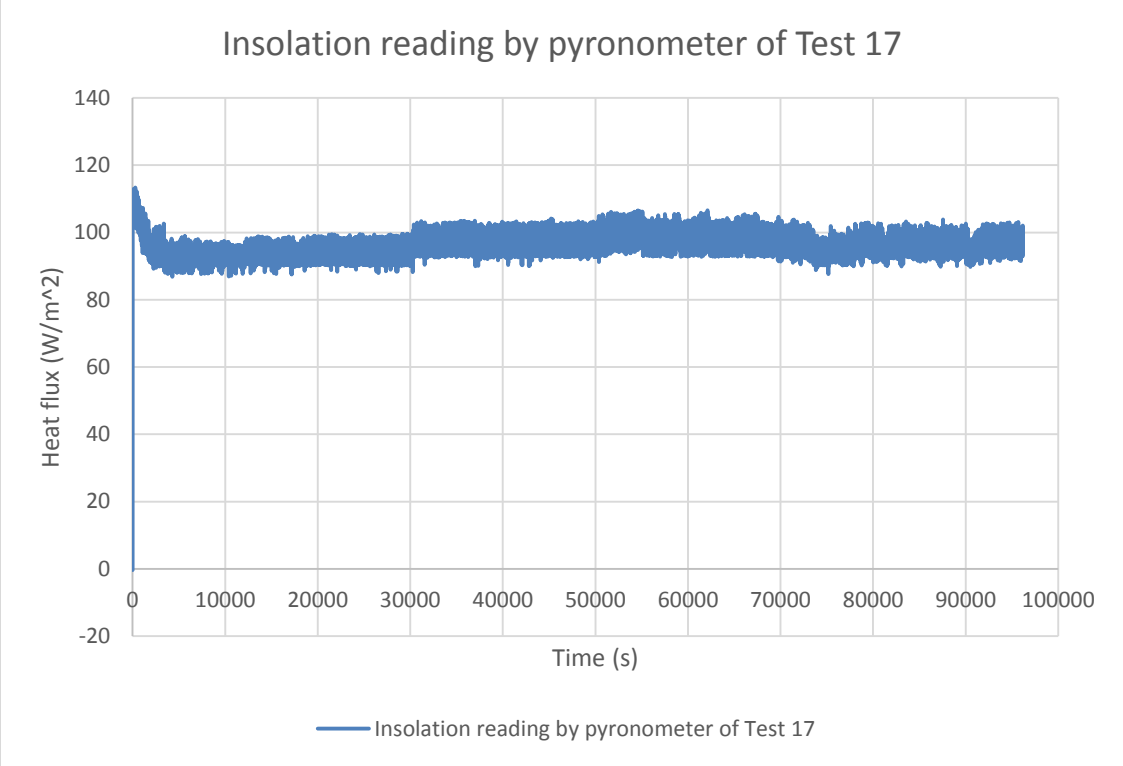

Figure 4.3.4. Heat flux experienced on the inner condenser surface during Test 17 by A. Gorrie [1].

Initial and inlet temperature

An initial temperature of 18.33℃ was applied to the entire system as this was the average ambient temperature from Test 17 by Gorrie, shown in Fig. 4.3.6. This will also be used as the temperature of air supplied by the axial fan.

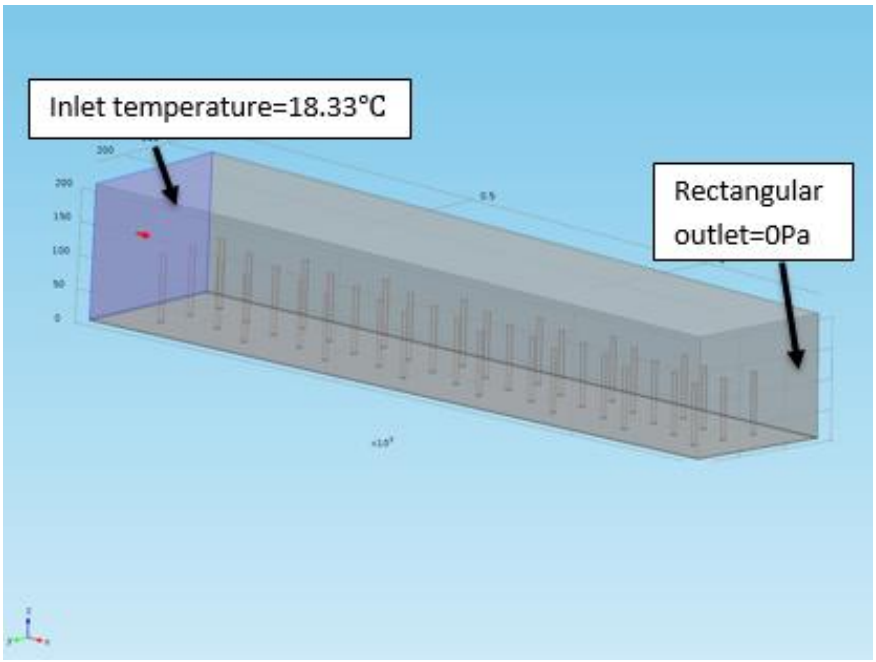

Figure 4.3.5. Prescribing the inlet temperature on COMSOL.

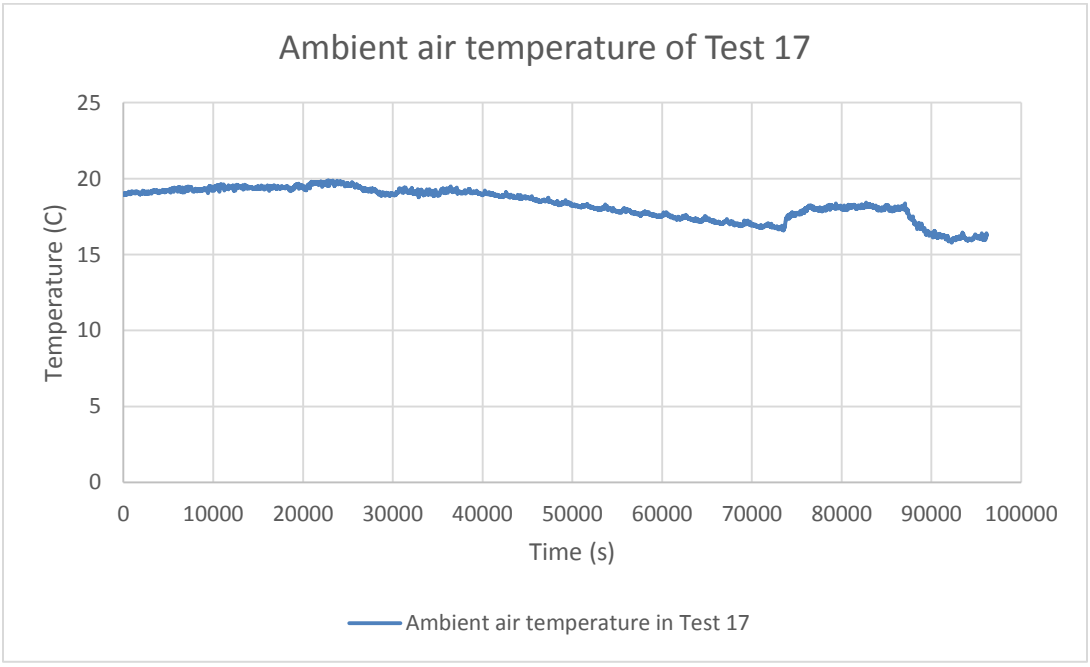

Figure 4.3.6. Ambient air temperature during Test 17 by A. Gorrie [1].

Airflow characteristic

The fan static pressure data points were generated from the low-speed line of Fig. 4.3.7. This was then inputted onto COMSOL shown in Fig. 4.3.8. Each design variant will generate a different pressure drop inside the duct, which is related to the amount of obstruction (number of fins). The software uses this information and scales down the flow rate accordingly.

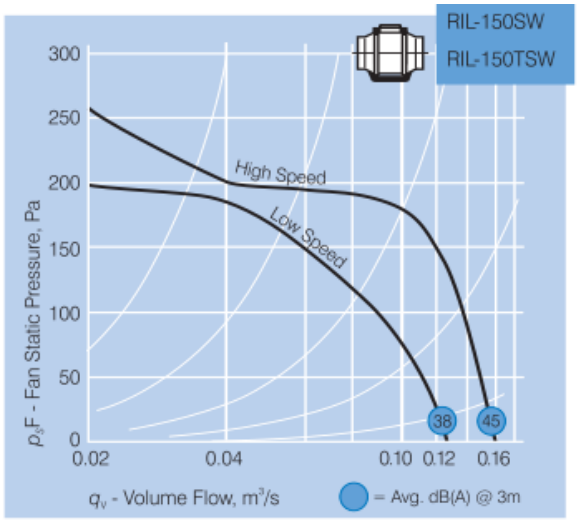

Figure 4.3.7. Fan curve based on the low speed line. [http://www.fantech.com.au/images/PDF/Catalogue/provent.pdf] Reproduced on the assumption of fair use.

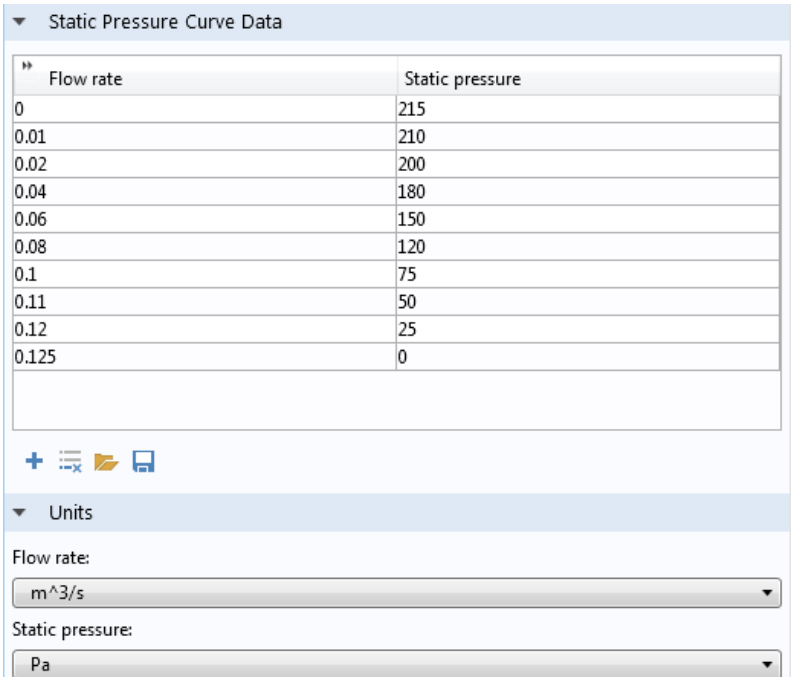

Figure 4.3.8. COMSOL input to represent the fan's flow characteristic.

Rectangular outlet condition

In the model, it was assumed that the pressure at the outlet was zero, and that there was no backflow into the system.

Wall boundaries

The wall boundaries in the system are surfaces that are exposed to the airflow, which are the three side walls of the duct, the outer condenser surface and the pin fin surfaces. This is important as it will indicate to the software where the walls are, so air velocities are scaled down accordingly.

Defining domains and material properties

By defining volume domains, it indicates to the software to treat them as a single group, which can be convenient when selecting a large number of repetitive geometries (pin-fins). In every model, there are three domains: the inside air envelope, base plate and the pin-fins. The thermal conductivity of air will be calculated by the model based on the temperature by COMSOL; for the pin-fins and base plate, it will use the built-in thermal conductivity of $238 Wm^{-1}K^{-1}$ for aluminium.

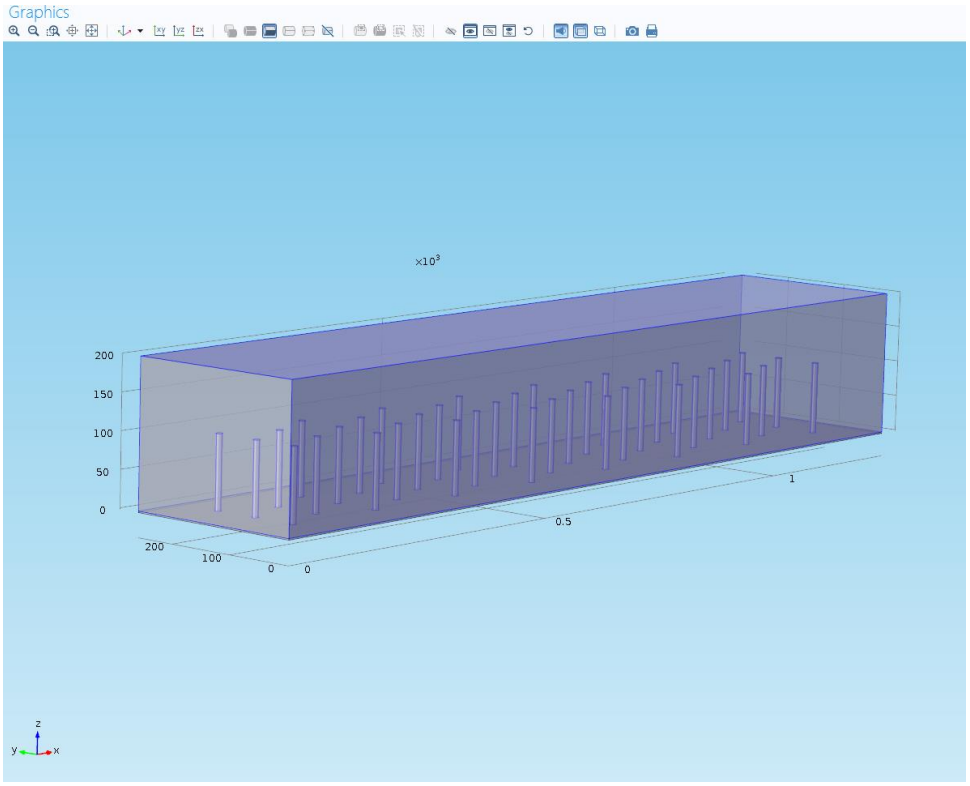

Figure 4.3.9. Wall boundaries on the model.

4.3.4 CFD model used

The initial calculation of the air entering into the duct was found to be turbulent. Using the definition of the Reynolds number, the dimension of the duct (200×260mm) and the maximum volumetric flow rate of the fan, 0.125m^3/s, the calculation becomes:

$$Re = \frac{\rho v D}{\mu}, where\ v = \frac{volumetric\ flow\ rate}{duct\ inlet\ area} = 2.4m.s^{-1},$$

$$D\ is\ the\ hydraulic\ diameter\ of\ the\ duct = \frac{2 \times base \times height}{base + height} = 0.23m$$

$$\rho\ and\ \mu = 1.225kgm^{-3}\ and\ 1.983 \times 10^{-5}Pa.s\ for\ air$$

$$Re = \frac{1.225kgm^{-3} \times 2.4m.s^{-1} \times 0.23m}{1.983 \times 10^{-5}Pa.s} = 34000\ (turbulent)$$

This means that to model the given airflow input, a turbulent model must be chosen instead of laminar flow. The literature already showed that the k-epsilon model is preferred due to its numerical stability and computation time. The limitation of this model is it will not compute flow in the viscous and transition boundary layer, which leaves behind a non-zero velocity.

4.3.5 Heat transfer validation with analytical solutions

Heat transfer along a single pin was modelled on COMSOL to check whether it matches with the analytical solution. By doing this, it will give confidence that the heat transfer component of the CFD module is working as intended. The analytical equation that it is being compared to is taken from [16]. This equation was originally used for predicting at which height the pin will have the same temperature as the ambient air; therefore, anywhere after this height the material will not be rejecting any heat and thus is not needed. For this equation to work, the pin must be assumed to be infinitely long. Therefore, a length of 5m was chosen:

$$T(x) = T_\infty + (T_b - T_\infty)e^{-mx}$$

With:

$$m = \sqrt{\frac{4h}{kD}}$$

$$T(x)\ is\ the\ temperature\ at\ pin\ height\ of\ x, T_\infty\ is\ the\ ambient\ air\ temperature,$$

$$T_b\ is\ the\ temperature\ at\ the\ base\ of\ the\ pin$$

Given parameters, chosen arbitrarily:

$$D = 10mm, k = 238W.(m.K)^{-1}, h = 100W.m^{-2}.K^{-1}, T_b = 302.8K \; and \; T_\infty = 291.33K$$

x (m)	0	0.050505	0.10101	0.151515	0.20202	0.252525	0.30303	0.353535	0.40404	0.454545	0.50505	0.555555
Analytical T(x) (K)	302.8	297.2895	294.4264	292.9388	292.1659	291.7643	291.5557	291.4472	291.3909	291.3616	291.3464	291.3385
FEA T(x) (K)	302.8	297.2936	294.4291	292.9405	292.1669	291.7649	291.556	291.4474	291.391	291.3617	291.3465	291.3386
x (m)	0.60606	0.656565	0.70707	0.757575	0.80808	0.858585	0.90909	0.959595	1.0101	1.060605	1.11111	1.161615
Analytical T(x) (K)	291.3344	291.3323	291.3312	291.3306	291.3303	291.3302	291.3301	291.33	291.33	291.33	291.33	291.33
FEA T(x) (K)	291.3345	291.3323	291.3312	291.3306	291.3303	291.3302	291.3301	291.33	291.33	291.33	291.33	291.33

Figure 4.3.9. Comparison between analytical and FEA temperature profile along the length of the pin.

An extremely fine mesh setting was used on COMSOL, where the maximum and minimum element size were 0.1, 0.001m respectively. There seems to be, at the most, a magnitude 10^{-3} error from the analytical solution, both converging to the redundant height of 0.959595m.

4.3.6 Mesh settings

The free tetrahedral mesh setting was preferred on COMSOL, as it was able to automatically set the default mesh settings for a given mesh refinement size; for example, extremely coarse, extra coarse, coarser, coarse, normal, extremely fine. In the first phase of optimisation for the optimal pin geometry and layout, the extremely coarse mesh was selected on COMSOL. However, some adjustments were made to the minimum element size of the pin-fins and base plate domain, due to the presence of narrow regions in the geometry. Trials have been done on adjusting the mesh settings from COMSOL's default setting so that it could provide consistent results while computing in a reasonable time. It was found that the mesh size of each domain will also affect other domains. Therefore, it is recommended to use similar mesh sizes in all domains. There are cases where a particular mesh setting did not work for some of the design points due to the huge variation in geometry, most notably the number of fins, and their size and height. Below were the general mesh settings used throughout the optimisation for all design combinations shown in Table 4.3.1. There were cases where the minimum element size on the pin-fins had to be refined, as the mesh did not transition well to the air domain, which caused COMSOL not to recognize the internal boundary between the two domains.

Table 4.3.1. Mesh size settings for each domain; only the base plate domain was refined to minimum element size=1mm.

Mesh size settings	**Air domain**	**Pin-fins**	**Base plate**
Max element size (mm)	126	126	126
Min element size (mm)	22.6	22.6	1
Max element growth rate	1.5	1.5	1.5
Curvature factor	0.6	0.6	0.6
Resolution of narrow regions	0.5	0.5	0.5

Table 4.3.2. Mesh settings for wall boundary layers.

Boundary layer properties	Value
Number of boundary layers	5
Boundary layer stretching factor	1.2
Thickness of first layer	Automatic
Thickness adjustment factor	2.5

The minimum element size for the base plate was changed to 1mm as the thickness of the base plate was 2mm. To compute flow in the turbulent boundary layer, several layers of boundary mesh were needed for every wall surface that is exposed to the airflow. This includes all three side walls of the duct, the top surface of the condenser and the exposed fin surfaces.

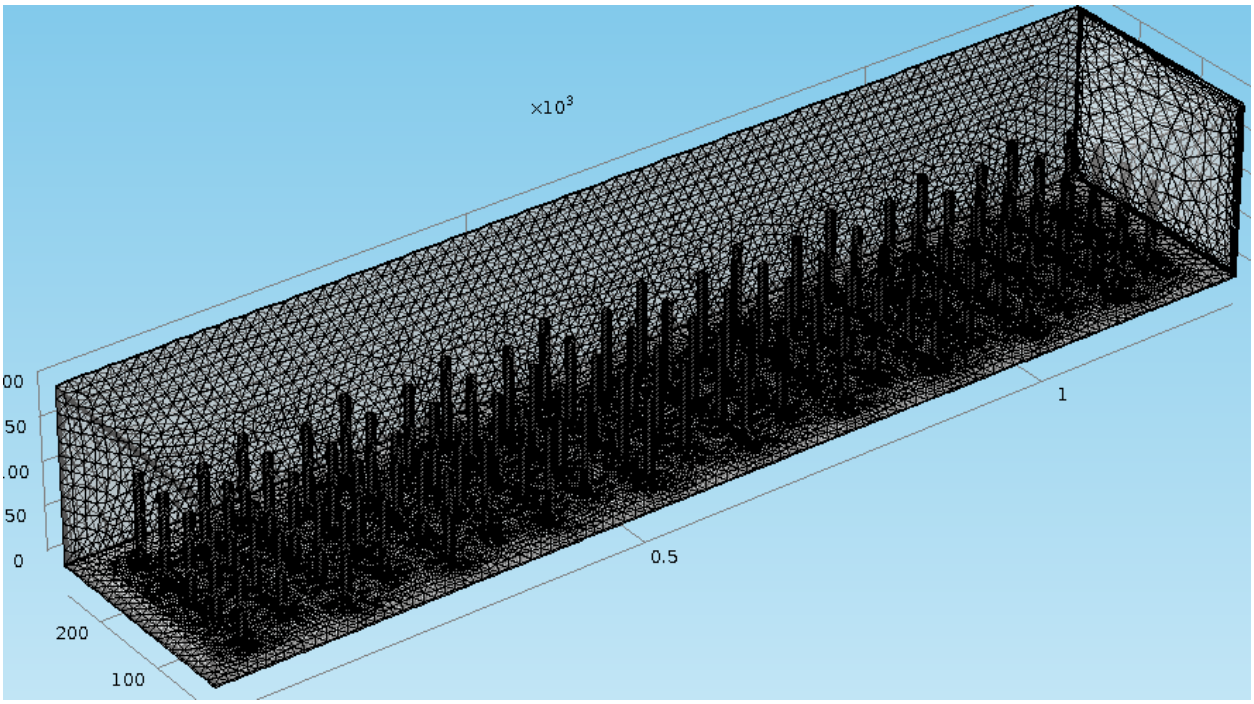

Figure 4.3.10. Complete mesh for all three domains (ducted air space, pin-fins and the condenser); the boundary layer mesh can be seen on the edge of the air space to compute near wall velocities.

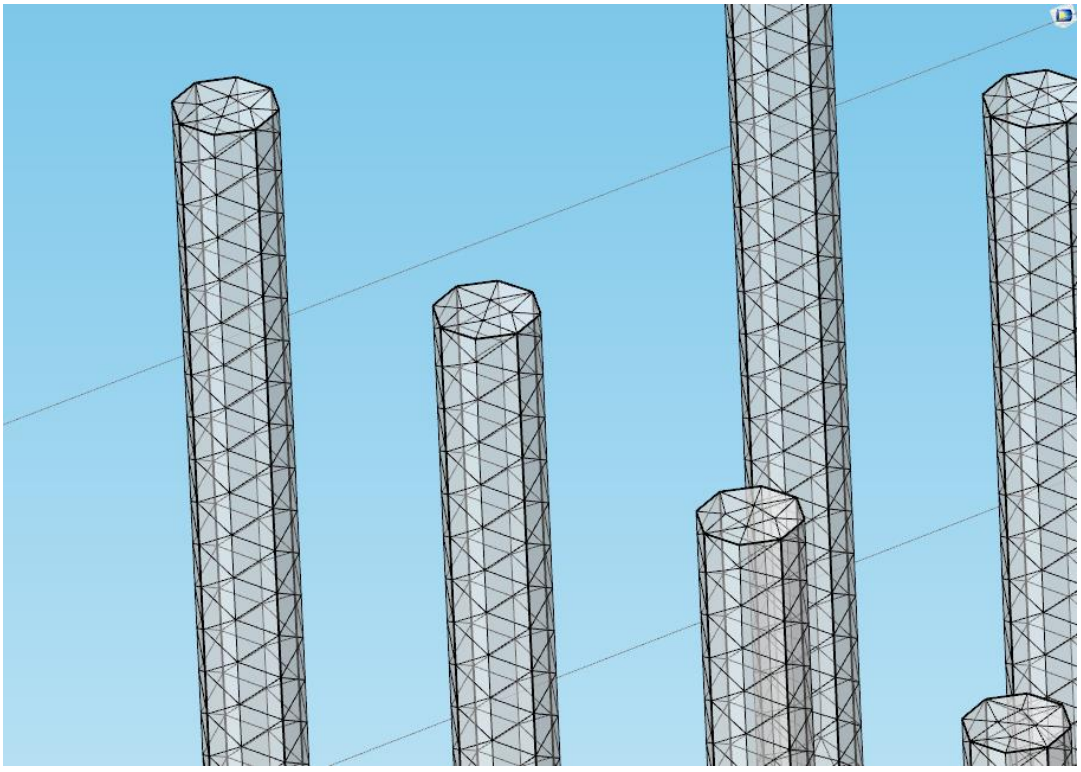

Figure 4.3.11. The mesh generated for the circular pins; note the rough edging of forming the circle with tetrahedral mesh; and a finer mesh setting was used in part 2 and refined the CFD later.

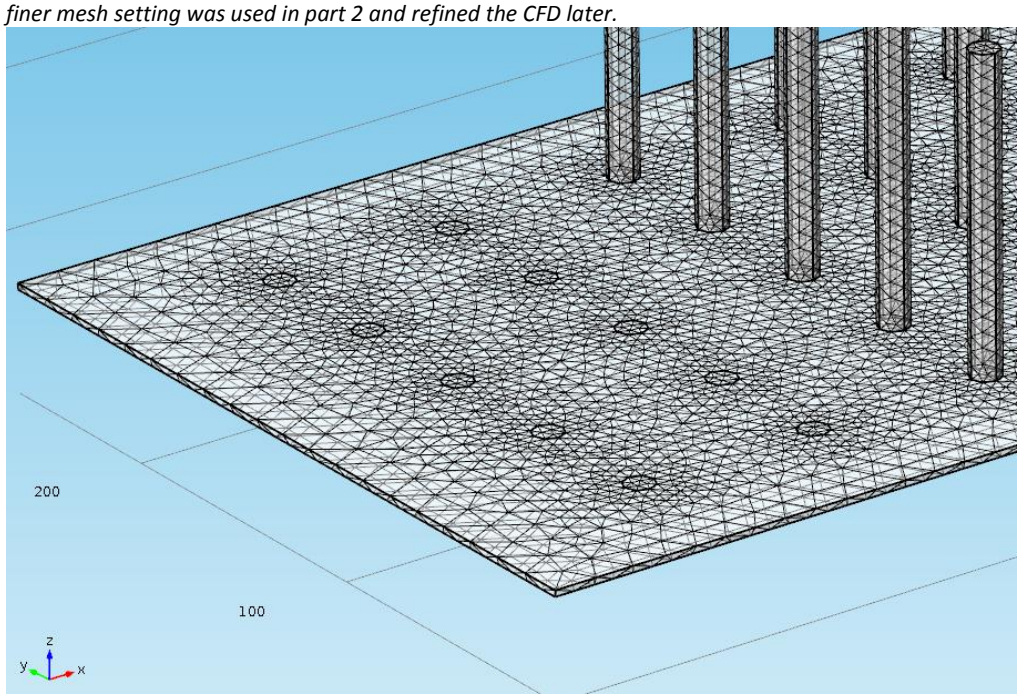

Figure 4.3.12. Thin edges on the base plate and mesh refinement between the pin-fins and base plate top surface. Note the growth rate of mesh size further away from the pin's base was determined by COMSOL's meshing algorithm.

4.4 Optimization part 1

4.4.1 Optimal fin geometry and layout

The number of fins in the x and y directions were set to follow the 7:3 and 20:5 ratios, as illustrated in Table 4.4.1, to determine the effects of sparse and denser pin-fins arrays; these ratios were chosen arbitrarily for convenience. Note that the equivalent pin-fins ratio in staggered arrangement give one less pin-fin per every second column.

Table 4.4.1. Result table for optimising between different numbers of pin-fins, fin geometries (square, circular, rectangular and elliptical) and arrangements (inline and staggered). The total heat removed from the fin array is measured in W; performance is measured in the total heat removal/volume of aluminium used, measured in kW/m^3.

Type	Plan view	Heat removal, Performance W, (kW/m^3)	No of fins
Square inline 7x3 fins; 0.1m high	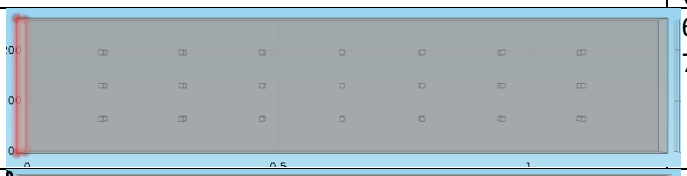	6.35 7.77	21
Square staggered 7x3 fins; 0.1m high		5.09 6.41	18
Square inline 20x5 fins; 0.1m high		15.36 10.68	100
Square staggered 20x5 fins; 0.1m high	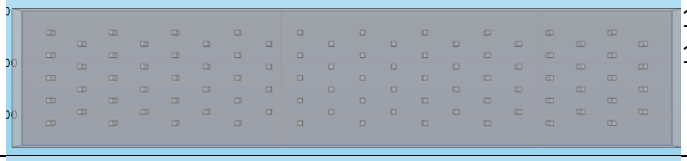	14.34 10.54	90
Circular inline 7x3 fins; 0.1m high		10.23 12.50	21
Circular staggered 7x3 fins; 0.1m high	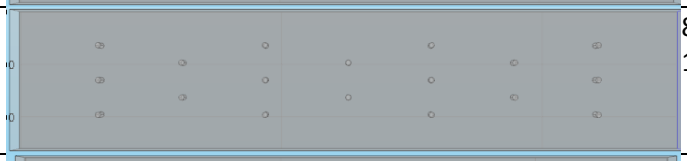	8.76 11.03	18
Circular inline 20x5 fins; 0.1m high	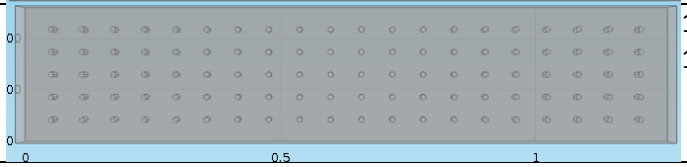	19.69 13.69	100

Circular staggered 20x5 fins; 0.1m high	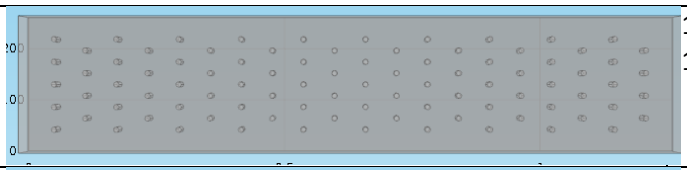	19.19 14.11	90
Rec-tangular inline 7x3 fins; 0.1m high	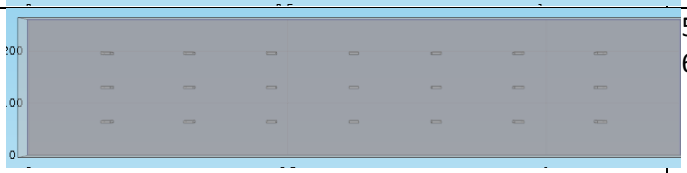	5.01 6.12	21
Rec-tangular staggered 7x3 fins; 0.1m high	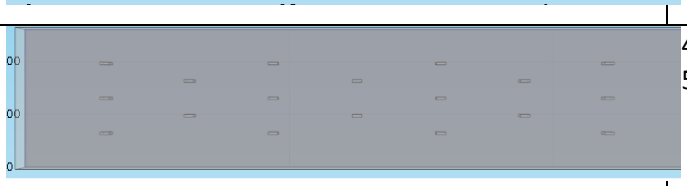	4.19 5.27	18
Rec-tangular inline 20x5 fins; 0.1m high	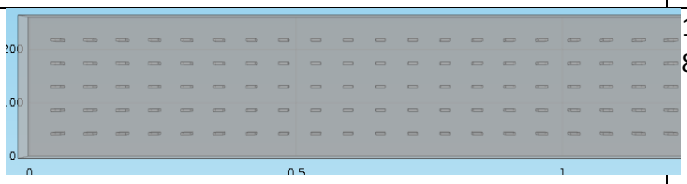	12.91 8.98	100
Rec-tangular staggered 20x5 fins; 0.1m high	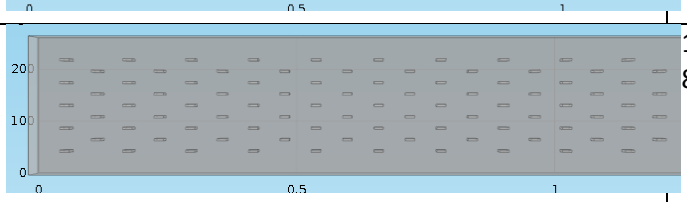	11.81 8.68	90
Elliptical inline 7x3 fins; 0.1m high	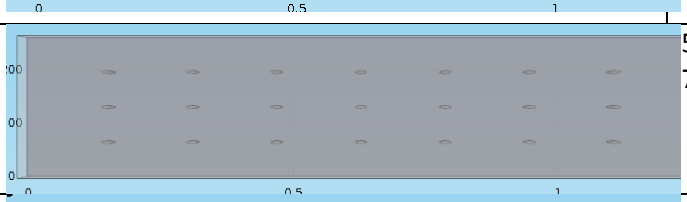	5.90 7.21	21
Elliptical staggered 7x3 fins; 0.1m high	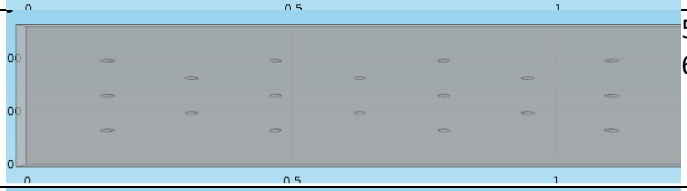	5.08 6.39	18
Elliptical inline 20x5 fins; 0.1m high	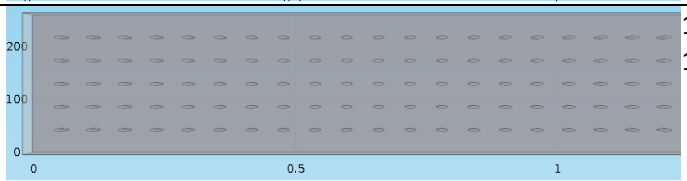	15.87 11.03	100
Elliptical staggered 20x5 fins; 0.1m high	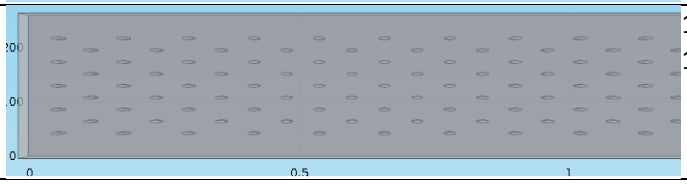	15.12 11.12	90

Table 4.4.2. Summary table for the best case of each arrangement.

Best case for:	fin geometry	Performance (kW/m^3)	No fins
7x3 inline	Circular	12.50	21
7x3 staggered	Circular	11.03	18
20x5 inline	Circular	13.69	100
20x5 staggered	Circular	14.11	90

The inline configuration was better in arrays with less fins, as the additional cooling effect of having that extra fin per every second column was significant. In denser fin arrays, the inline configuration falls behind the staggered configuration in both heat removal and performance, due to having more fins slowing down the airflow for the entire system. Regarding the optimal fin geometry, it was found that the circular pins performed better in sparser fin arrays due to a higher frontal surface area exposed to the airflow, $\pi \times 10mm = 31.42mm$ for circular, compared to $D = 8.86mm$ for square pins. It was originally thought that due to the rectangular and elliptical pins having the biggest total exposed surface area, it will have the highest heat rejection, but because its frontal area faces the airflow, it was significantly smaller than the other two geometries, and both had the lowest heat rejection and performance. Because of this, it could be of interest to model the heat rejection if the rectangular and elliptical pins were rotated by 90° to expose their wider face to the airflow, but due to time constraints, this was not considered.

Later studies show that the mesh used in this set of optimisations were too coarse and did not give mesh convergence. The heat rejection for the flat plate result in Section 4.5.3 was 39.46W, which was higher than any of the results in Table 4.4.1. Despite these uncertainties, in the manufacturing phase, it was decided that the circular pin was the only feasible pin geometry, given the limitations in manufacturing complexity. In the literature findings in Sections 2.1.2 and 2.2.1, it was mentioned that circular pins with a staggered arrangement usually perform better than other configurations, except for other complex pin geometry designs, such as the aerofoil shape.

4.5 Optimization part 2

4.5.1 Optimization for pin height and number of fins

From this part onwards, the plate thickness was changed to 6mm from 2mm due to new manufacturing requirements, while the inner condenser temperature remained the same. Eight different fin densities were modelled, with the 1950 fins being an extreme case to determine the effects of overcrowded fins. Each fin density was tested using five different pin heights of 40, 80, 120, 160 and 200mm. For the 300 fins, an 80mm high candidate did not converge on COMSOL. Therefore, the pin height was moved to 85mm to complete the trend. Apart from determining the heat rejection per volume of aluminium used (performance), other information such as air velocity and temperature profiles were studied as they directly contribute to heat rejection.

4.5.2 Model simplification and modifications

In this study, the coarser mesh setting was selected on COMSOL with further refinements on the pins and the base plate. Due to a large amount of optimisation and the level of mesh size precision required, ways of simplifying the model were looked at. A simplified sliced model was used to approximate the full-size model shown in Fig. 4.5.1. To simulate the effects of staggered flow, a minimum of three rows of pin-fins were used. The fan flow rate from Fig. 4.3.8 was down-scaled proportionally according to the slice width while maintaining the same pressure characteristic. The same inner condenser temperature was prescribed on the slice model as heat transfer was expected to occur mainly in the upwards direction. The width of the slice was changed according to the number of fins, which equals D_y. After obtaining the heat rejection from the integral approach in 4.2.1, this value was then scaled up in proportion to the slice width to obtain the total heat rejection as for the full model. However, this overestimated the heat rejection value, as it does not take into account the viscous effects from the side walls, and also the overhang airspace shown in Fig. 4.5.2. A visual explanation of how the overhang caused the heat rejection to be overestimated can be found in Figs. 8.5.1 and 8.5.2. A comparison of the slice and full-size model, using the same mesh settings will be discussed in Table 4.5.3. The slice model computed in 13 hours while the full-size model took 69 hours for the 165 fins, 200mm high pin-fin model.

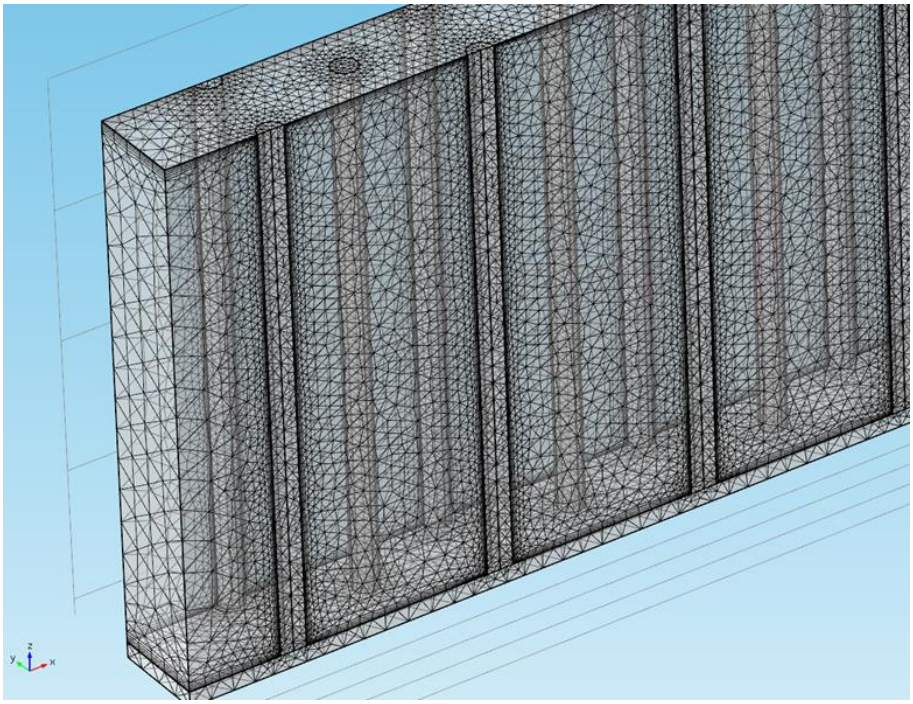

Figure 4.5.1. Simplified slice model for 165 fins, the coarser mesh setting was used instead of the extremely coarse.

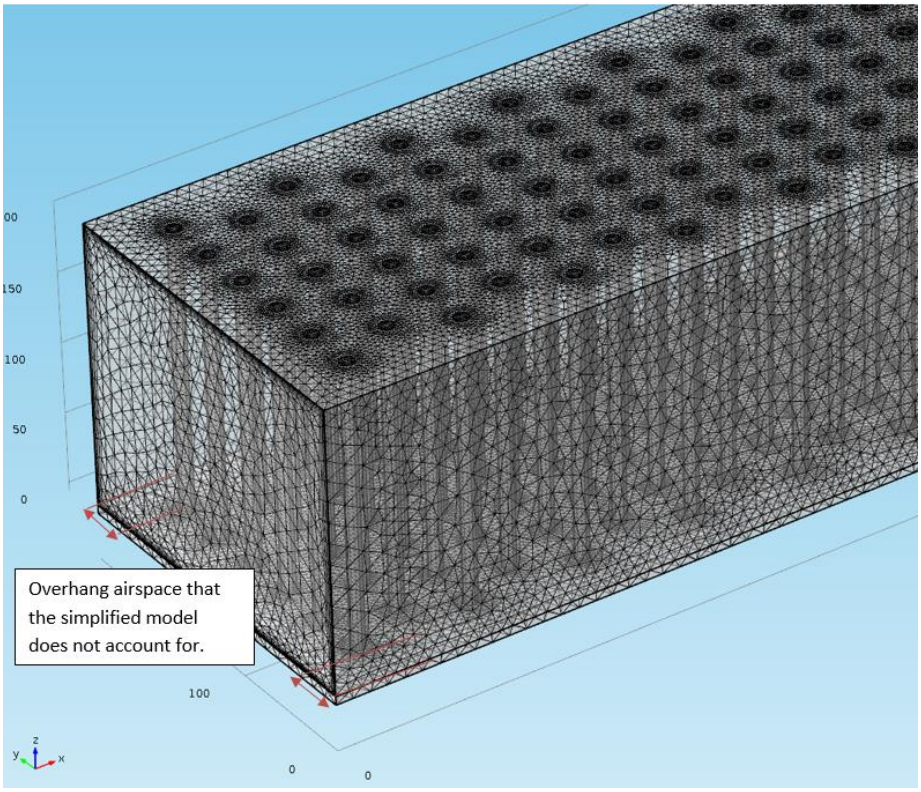

Figure 4.5.2. Mesh of the full scale 165 fins 200mm tall condenser.

Table 4.5.1. Mesh settings for the simplified model and the full scale as shown in Figs. 4.5.1 and 4.5.2.

Mesh size settings	**Air domain**	**Pin-fins**	**Base plate**
Max element size (mm)	126	126	126
Min element size (mm)	1	1	1
Max element growth rate	1.5	1.5	1.5
Curvature factor	0.6	0.6	0.6
Resolution of narrow regions	0.5	0.5	0.5

Table 4.5.2. Mesh settings for wall boundary layers.

Boundary layer properties	Value
Number of boundary layers	5
Boundary layer stretching factor	1.2
Thickness of the first layer	Automatic
Thickness adjustment factor	2.5

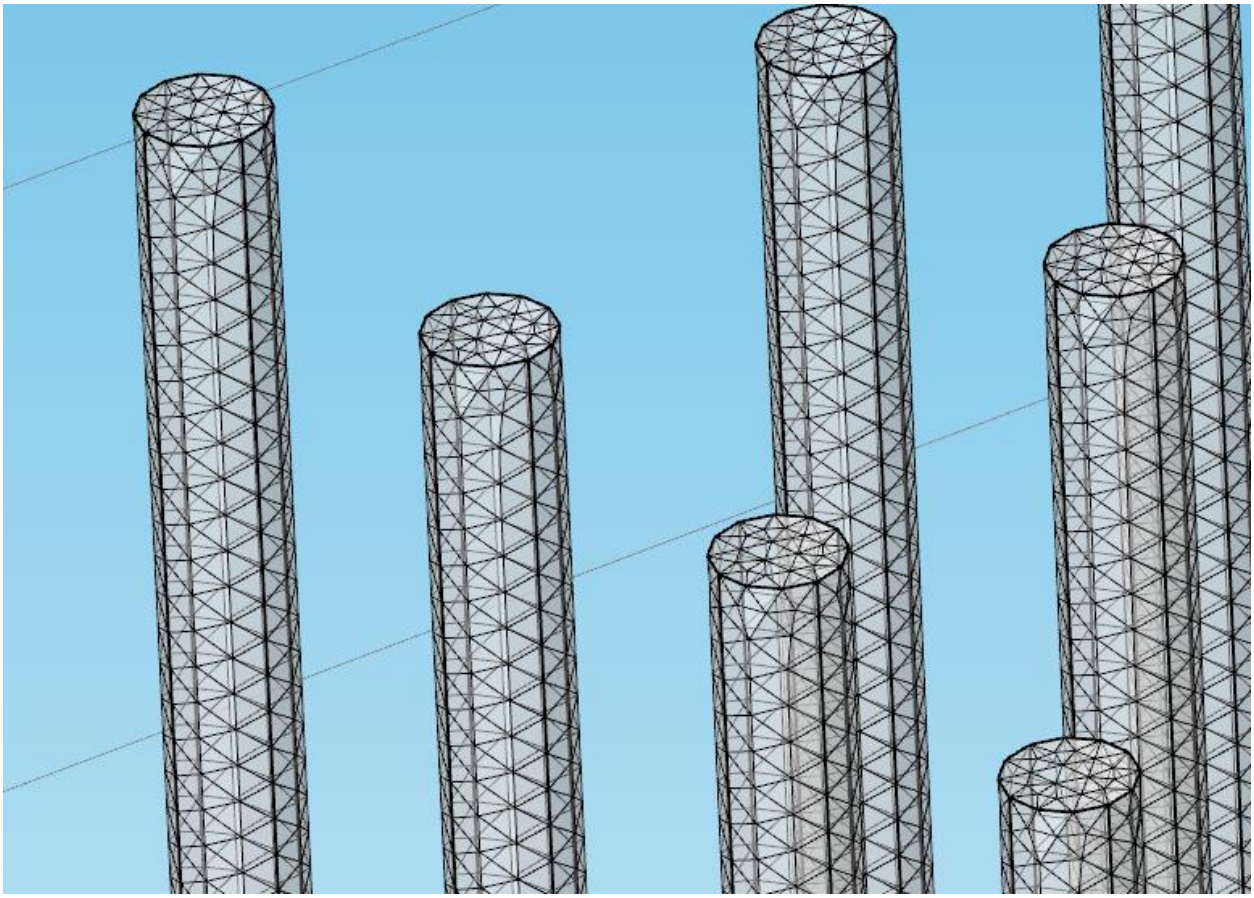

Figure 4.5.3. A finer mesh setting was used on the pin-fins as for part one of the optimisation.

The input conditions for the inner condenser plate temperature was 29.81℃, while the fan curve was scaled down proportionally accordingly for the simplified model. It was assumed that the full-scale model was more accurate than the simplified model due to the overhang issue illustrated in Fig. 4.5.2; therefore, it was used as the reference for this comparison. A relative error of 33% was found for total heat rejection on Table 4.5.3 by using the width scaling method to determine the full-scale heat rejection for the simplified model; this was due to the simplified slice model not taking account that the overhang region will provide less heat rejection as there are no fins (see Fig. 4.5.2). Also, the viscous effect from the side walls were not taken into account in the simplified model, which would have increased the amount of airflow and made the heat rejection higher.

The heat rejection per volume of aluminium value was more conservative as it does not accumulate more error from width scaling, but it still overestimates by 15%. After this comparison, it was decided that this amount of overestimation was acceptable for the purposes of design optimisation, which comes in Section 4.5.5.

Table 4.5.3. Validation of the simplified slice approach.

	Simplified Table 4.5.1-4.5.2 settings	Full-scale, Table 4.5.1-4.5.2 settings	Relative error %
Full-scale heat rejection (W)	338.94	254.81	33.0165
Heat rejection per volume of Al (kW/m^3)	64.46	55.99	15.13456

4.5.3 Flat plate model

To set the benchmark for the optimisation, a case with the 6mm flat plate was considered. Using the same ambient, inner condenser plate temperature (18.33°C and 29.81°C) and mesh setting as in Tables 4.5.1 and 4.5.2, except without the section on the pin-fin. It was found that the heat rejection and heat rejection per volume of aluminium values were 39.46W and 20.14kW.m^{-3}.

4.5.4 Limitation in part one results

It was observed that the heat rejection values in part one were smaller than the value for flat plate. This was a cause for concern as theoretically the pin-fin condenser should reject more heat than the flat plate given sufficient air passing through it. This inconsistency was due to the different mesh settings used in Tables 4.3.1 and 4.5.1. To repeat all 16 runs in part one using Table 4.5.1 setting would require as much as 69 hours for models with higher fin density, which was already carried out once for the 165 fins 200mm model in full scale. Therefore, the results for part one would be accepted knowing that there is a limitation whether the circular pin was the best geometry of the four and whether the stagger layout was better than inline. Due to manufacturing limitations, circular pins were used in constructing the rig. In the future the simplified approach could have been adopted in part one, but this simplification technique was not known at the time.

4.5.5 Part two results

Optima and chosen optimal candidate for experiment

The optimal performance of 65.14 kW.m^{-3} was found to be at 228 fins, 200mm tall. There was no sign of a point of inflexion for the height of the fins as it gets better for taller fins except for the 1950 fins series. For the number of fins, it was found that the 228 fins performed the best at 200mm tall followed closely behind by 165 fins with a difference of 0.67kW.m^{-3}. Therefore, it was decided that the 165 fins at 200mm tall should be manufactured instead as the optimal design due to a reduction in time and material cost for this project. This design was estimated to produce 338.94W of heat rejection at the ambient, inner condenser plate temperature of 18.33°C and 29.81°C using the simplified slice approach, as shown in Fig. 4.5.8.

Implication of airflow experience by the pins

Heat rejection performance increased as the pin-fins got taller, except for the 1950 fins series, see Fig. 4.5.4. This was due to the compression of airflow caused by continuity, and more air is forced to travel between the fins and above the fins. The air velocity on to the fins was found to decrease with the number of fins in Fig. 4.5.6, which meant that it was better to have fewer but taller fins for the same

amount of material. However, with taller and less fins the heat needs to travel further in order to be rejected, as to shorter and more fins; therefore, there exists an optima at 228 fins, 200mm high and not at 38 fins. For 1950 fins, the sharp decrease in air velocity after 160mm showed that the effect of pressure drop was significant enough (207 Pa in 1950 fins, 200 mm; 83.4 Pa in 228 fins, 200mm) as evidential from checking the low-speed fan curve from Fig . 4.3.7. This drop in airflow directly correlated to the drop in heat rejection per volume material after the pin height of 160mm for the 1950 fins in Fig. 4.5.4.

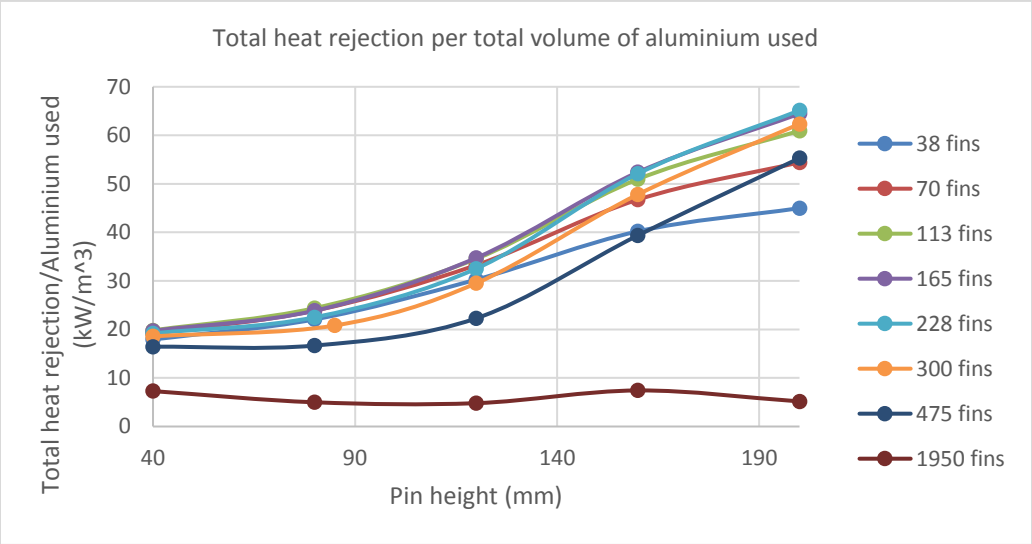

Figure 4.5.4. The overall plot of the optimisation, with the objective being the maximum heat rejection per volume of aluminium.

Implication of temperature profile

The temperature difference between the air and pin-fins was an important factor in predicting heat rejection, as shown in Fig. 4.5.7, because if the pin-fins were tall or slender enough to have a portion of its height at the same temperature as the flowing air, then there would be no heat transfer occurring for that portion. This effect was not seen in 38-475 fins between 40-200mm high pins. Therefore, the heat rejection per volume of aluminium value gets higher as the pin height increased. As for the 1950 fins 200mm high, the temperature of the pin-fins and air were almost identical, causing total full-scale heat rejection to fall after 160mm (see Fig. 4.5.4).

Explanation of the performance trend

Due to the given constraint parameters, this was the resulting optima. However, if factors such as the fan, height of the air space and diameter of the fins were to be changed, the optima would not be the same. Looking at the trend in Fig. 4.5.4, if the ceiling were to be higher than 200mm, then there would be a point where the 475 fins would overtake the 228 and 300 fins line, judging from the steepness of the gradient. At a pin height of 200mm, the top surface of the pin would be touching the roof of the duct. Therefore, the loss of this top surface would cause a penalty in convective heat transfer, which slowed down the rate of increase in heat rejection per volume material for most fin numbers, as shown in Fig. 4.5.4. Looking at Fig. 4.5.5 for the lowest pin height value of 40mm, the samples with high pin

densities had the lowest performance. These pins were dense enough that the air was treating the top surface of the pin as a single flat surface. Therefore, the airflow gets pushed upwards, resulting in a loss in convection to the fins. Samples with low pin densities, from 38-70 fins have a lower performance at 40mm high because the amount of additional performance the pins were able to provide was small in comparison to the plate (flat plate condenser at 6mm thick has a performance of 20.14kW.m^{-3}). At 113 and 165 fins, the amount of available pin surface area was able to provide more heat rejection while sufficient air was able to travel through the pins.

Conclusion

There were two modes of heat transfer involved in this problem: conduction and convection. Heat transfer by conduction occurs from the inner condenser surface to the tip of the fins, while convection occurs on the fin surface area exposed to the airflow. Too much conduction but not enough convection, as shown in the 1950 fins, 200mm pin height sample, would not allow enough cool air to pass through for convection to occur. Not enough conduction, but a high amount of convection, such as the 38 fins, 40mm pin height sample and the flat plate condenser, do not make good use of the cool air that is available. Therefore, the goal of obtaining the optimal design is to maintain the balance between conduction and convection.

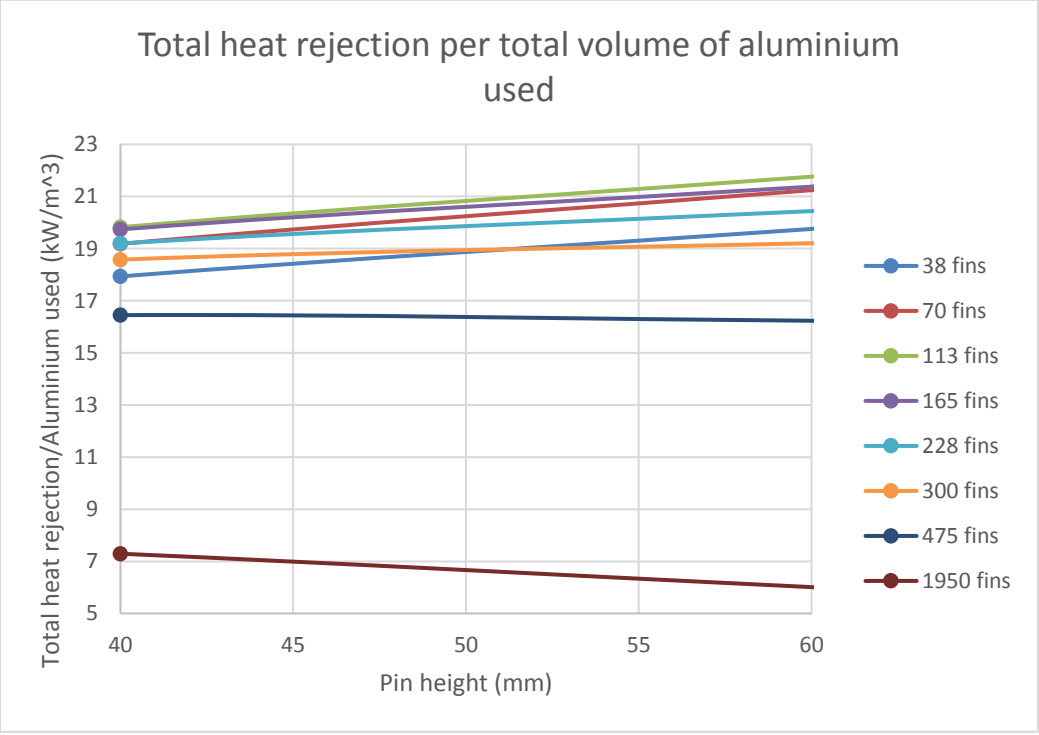

Figure 4.5.5. The enlarged plot of the overall plot above for pin height of 40-60mm.

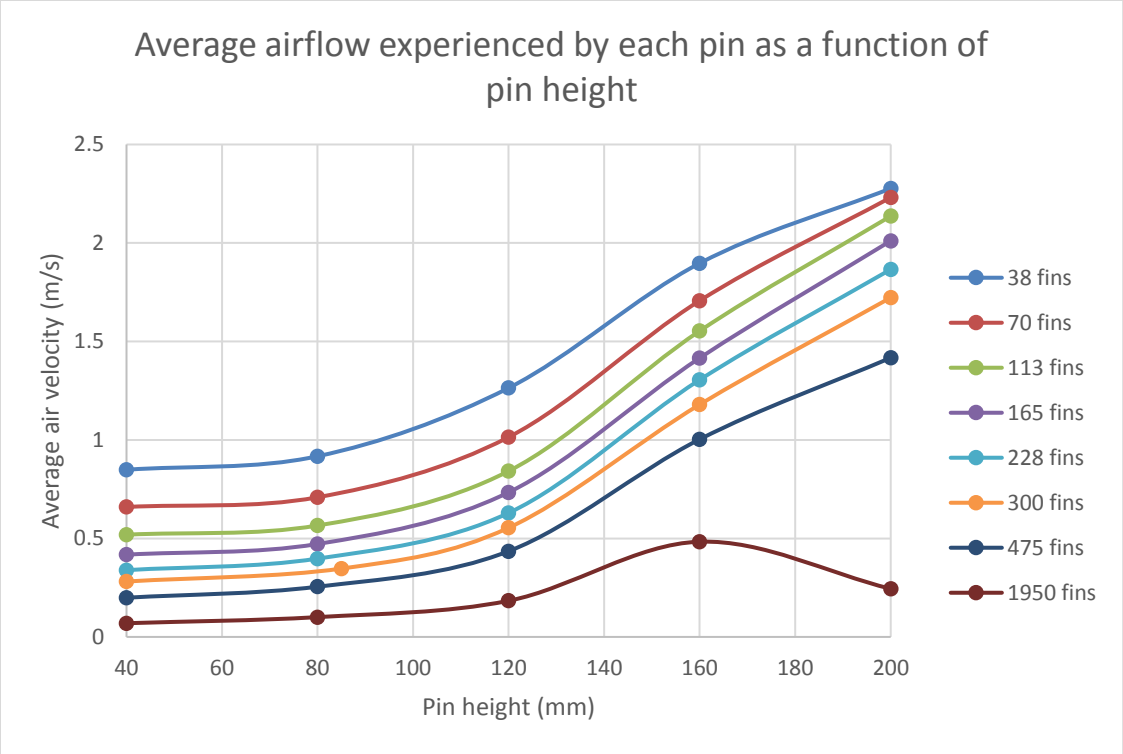

Figure 4.5.6. Average air velocity along the height of the pin fin, measured at the outlet.

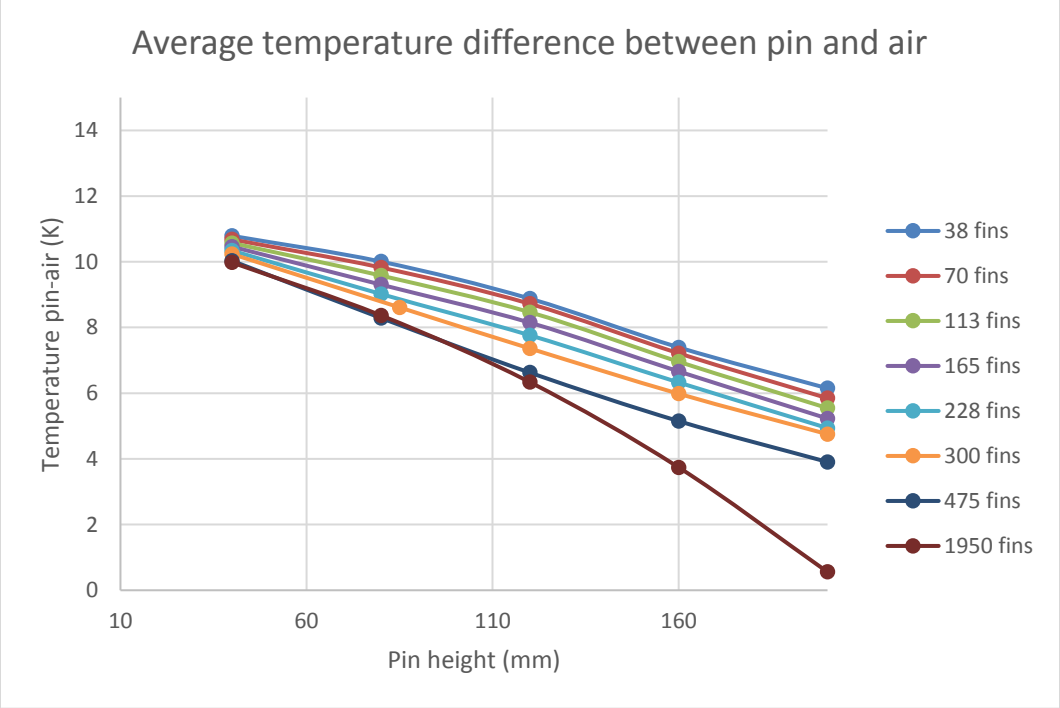

Figure 4.5.7. The difference between the average temperature of the pins in the heat sink and the average temperature of the air in the domain.

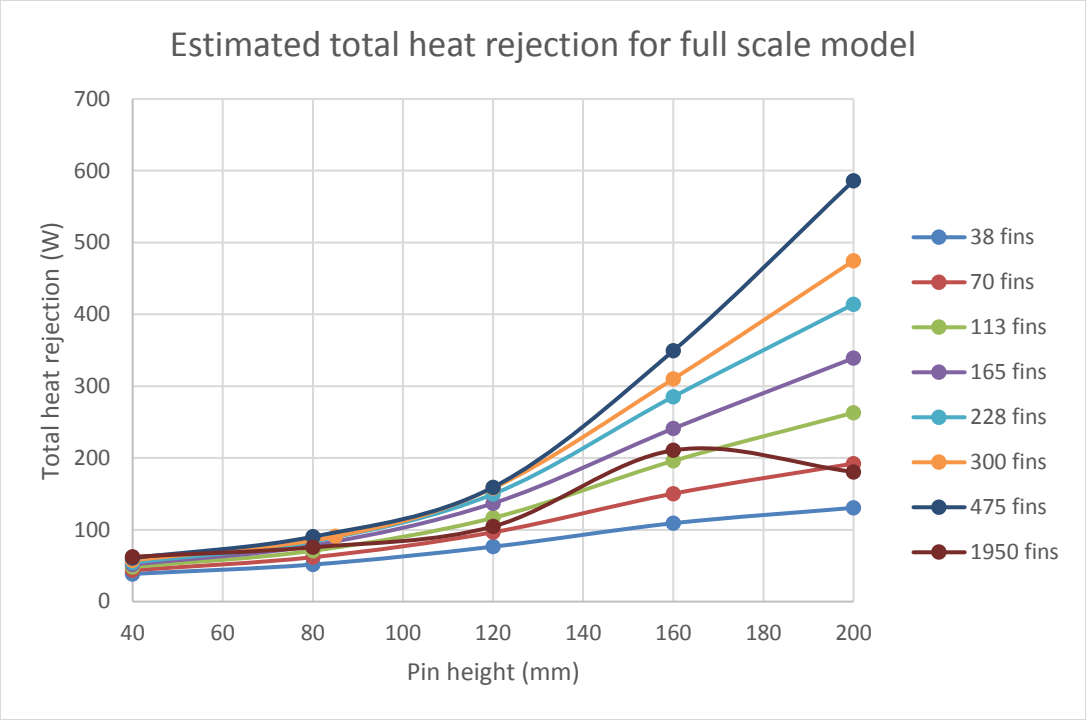

Figure 4.5.8. Estimated full-scaled heat rejection based on the ratio of the simplified slice width versus the width of the full-scale model (260mm).

By comparing the 3D velocity profile from COMSOL, in Fig 4.5.9 and 4.5.10 for two extremity in fin densities (38 and 1950 fins), Fig 4.5.9 shows that there is airflow being compressed thus causing a higher amount of air on to the fins, and in Fig 4.5.10 there was little airflow as the pressure loss caused the fan to stall.

Looking at the 3D temperature profile of the two fin densities, the fins in the 38 fins array was hotter than the air, which meant there was heat transfer, as shown in Fig 4.5.11. In Fig 4.5.12, the fins and the air was almost the same temperature, which meant that the heat was not being rejected due to congestion in airflow.

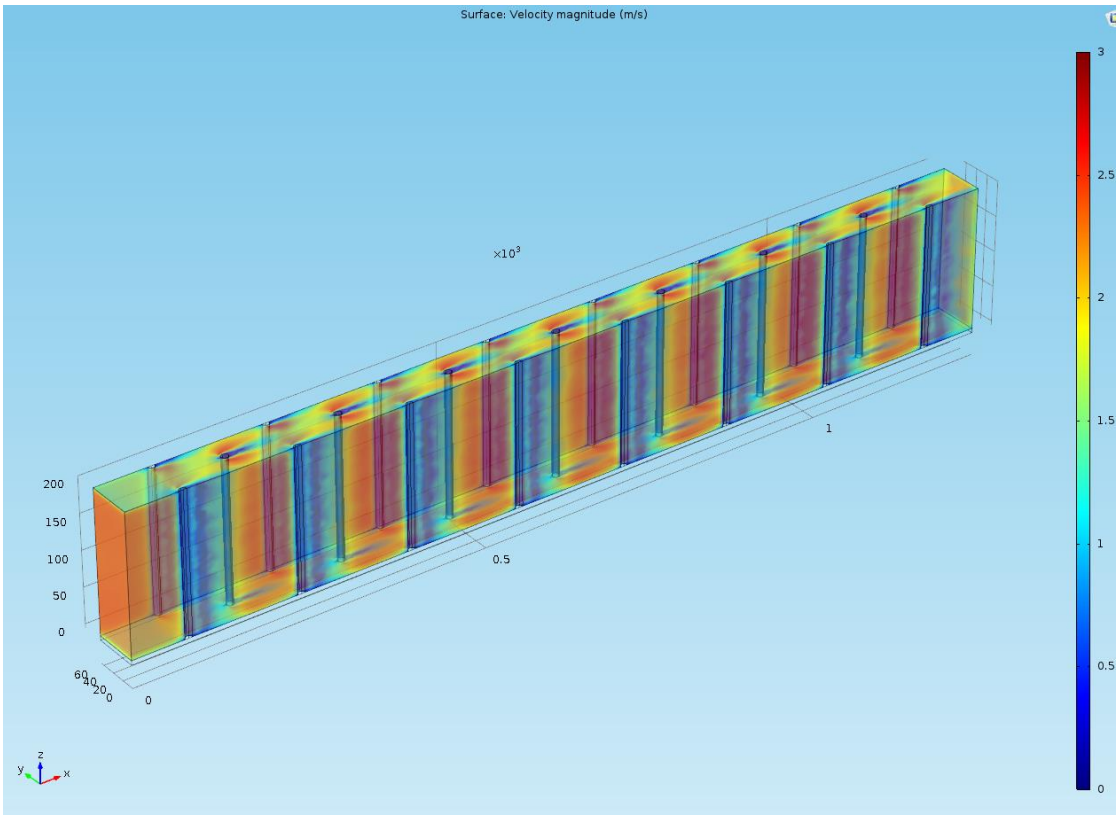

Figure 4.5.9. Velocity profile of the 38 fins, 200mm high simplified model.

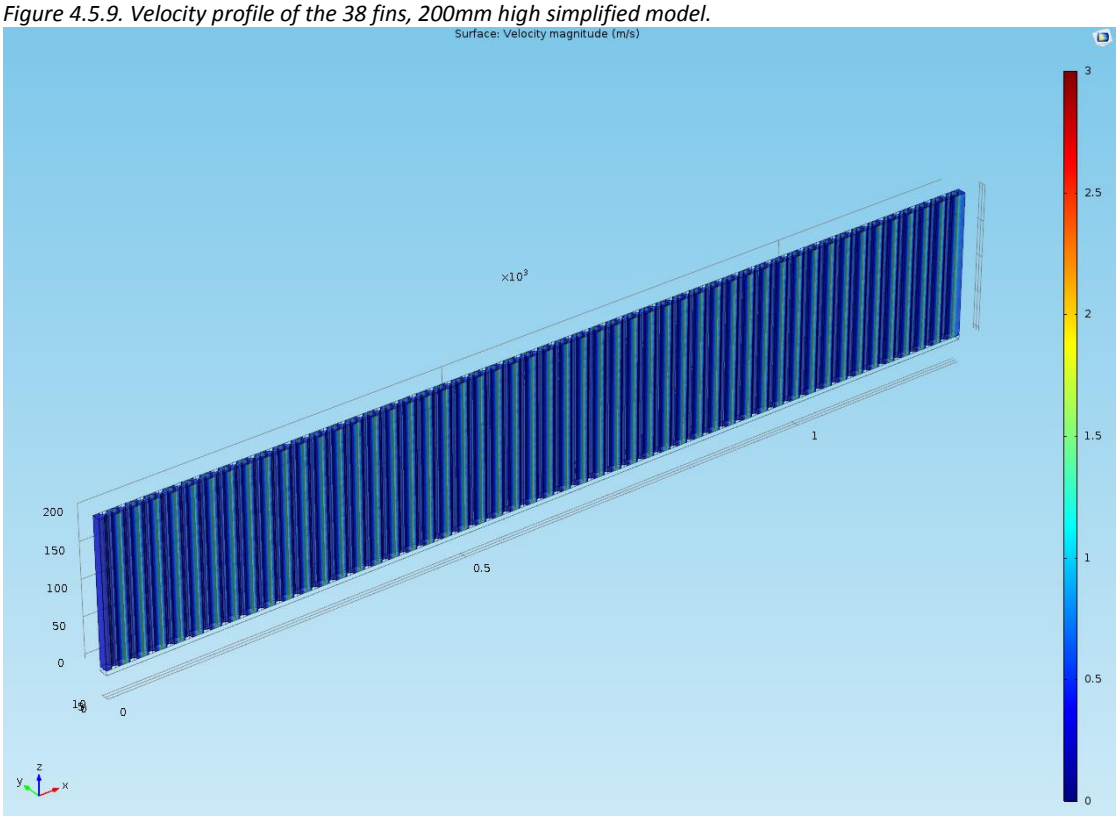

Figure 4.5.10. Velocity profile of the 1950 fins, 200mm high simplified model.

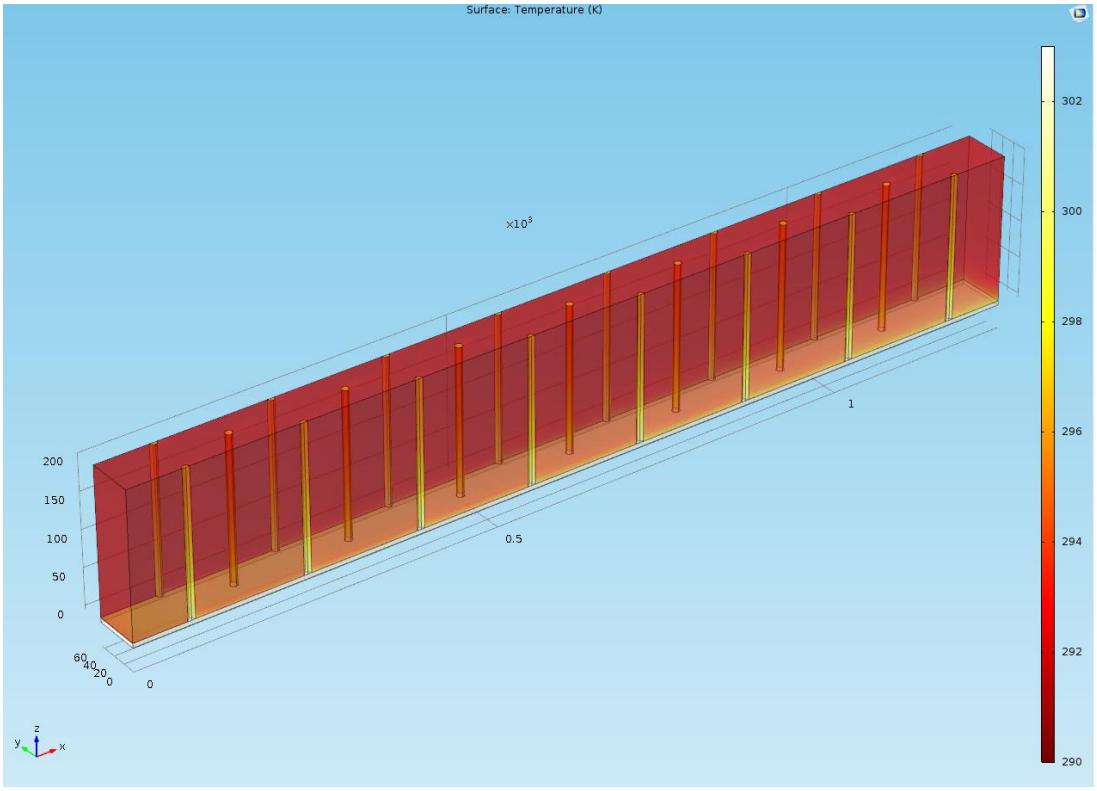

Figure 4.5.11. The temperature profile of the 38 fins, 200mm high simplified model. Notice the temperature difference between the pins and air.

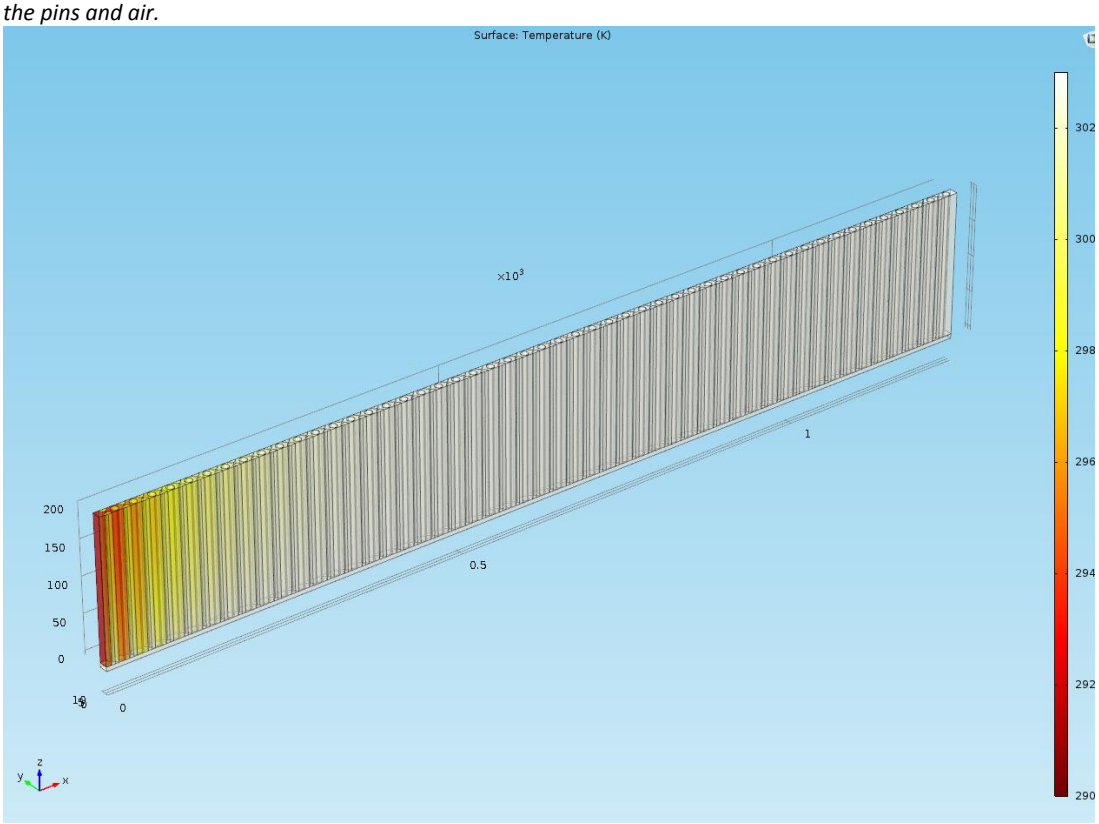

Figure 4.5.12. The temperature profile of the 1950 fins, 200mm high simplified model. Notice the temperature between the pins and air are nearly identical due to insufficient air convection.

4.6 Test rig design and manufacture of the condenser

In this section, the fabrication of the test rig will be discussed to best match the conditions modelled in the CFD optimisation. Though it was understood that not all conditions could be met due to limitations in equipment, some assumptions were made and a final fully detailed CFD was done after the experiment to account for it. The main deliverables of the test rig were to provide a constant temperature input on the inner condenser surface, a ducted airflow along the condenser and a mean of measuring the air velocity and temperature profile inside the duct such that it was comparable to the detailed CFD results. Using the data collected, heat rejection was evaluated using the integral approach in Section 4.2.1.

Due to the size and specific design of the condenser, it was not feasible to manufacture it from a single piece of aluminium due to wastage. Therefore, the condenser was manufactured by attaching the pin-fins onto the plate. It was accepted that there would be thermal contact losses between the fins and the plate. To minimise this loss in heat transfer, thermal grease was used between the aluminium surfaces.

4.6.1 Finalised design of the condenser plate and pin-fin arrangement

From Section 4.5.5 the optima was found to be at 228 fins each at 200mm tall. However to reduce manufacturing time the 165 fins, 200mm tall variant was built instead, as the difference in performance was found to be small. The optima would then be validated by on the basis that the experimental results of the 165 fins condenser matches the refined CFD study.

Therefore, there are 15 long and short columns according to the formulation of Section 4.1.1. Each pin-fin is 9.5mm in diameter as no supplier could source 10mm rods and a plate 6mm thick. The exact dimensions of the condenser are described in Fig. 4.6.1. In this model, the aluminium was considered to have a thermal conductivity of 238W.(m.K)$^{-1}$, but this cannot be ensured in the experiment as there are many grades of aluminium. This problem was accounted for in the fully detailed CFD.

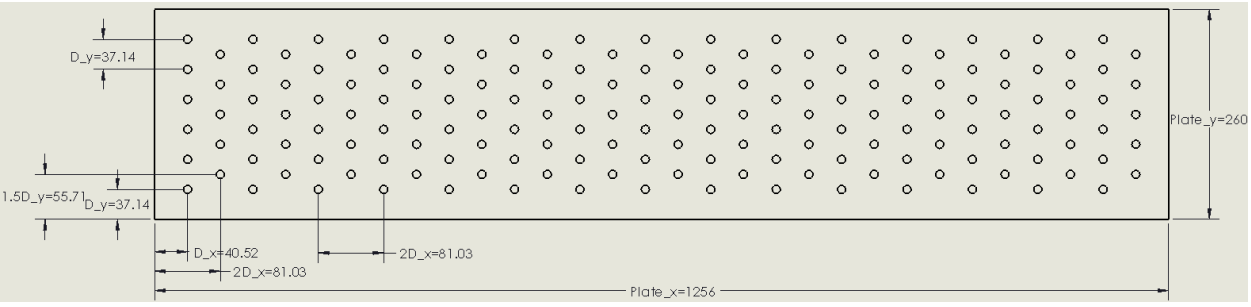

Figure 4.6.1. Layout view of the optimal condenser at 165 fins, each fin 200mm tall.

4.6.2 Manufacturing options for the condenser

In all three options considered, thermal grease would be used to enhance thermal contact; they were:

1. Bolting the pin-fin on to the base plate using a 3mm bolt.
2. Machining 4mm blind holes on the 6mm plate, and letting the fins sit on the blind holes assuming the pin-fins do not become loose due to the airflow.
3. Gluing or welding the pin-fins onto the plate.

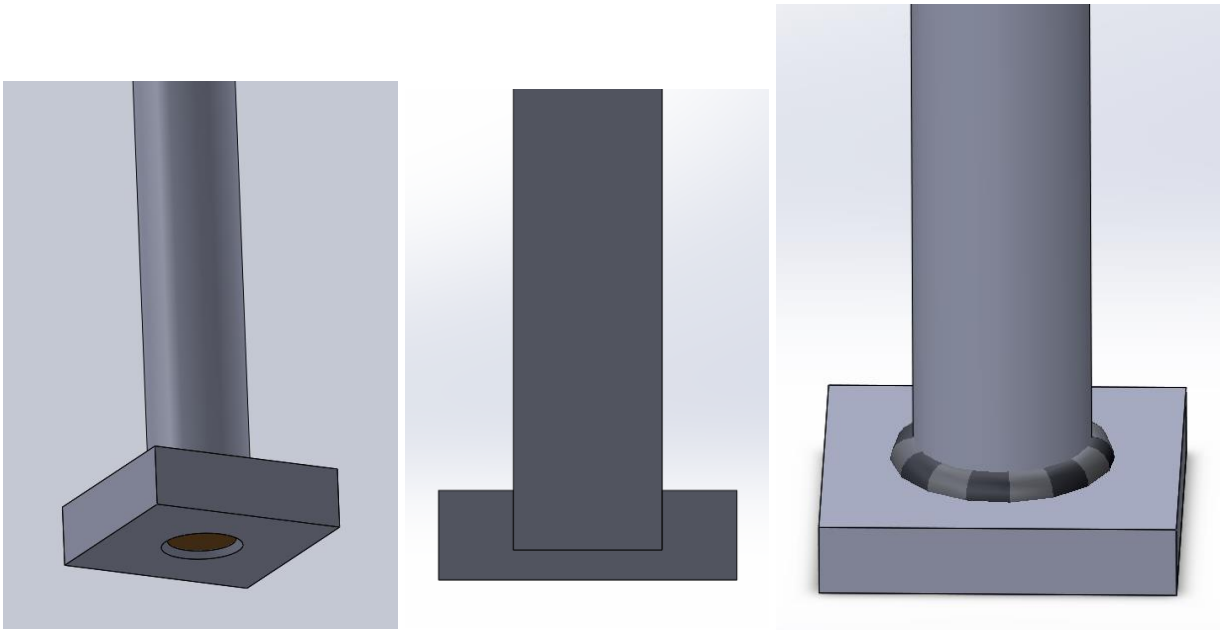

Figure 4.6.2. From left to right, bolting, blind holes and adhesive were considered as potential options to join the pin-fins on to the condenser. Image M. Leung.

Considerations of the three fastening options

For the first option, a 4mm countersink screw was the minimum possible fastener that could be drilled and taped reliably. Still, this would change the overall thermal conductivity as the bolts are made of steel. Though this difference in thermal conductivity can be accounted for in the fully detailed CFD. The advantage of this option is it would maintain a tight connection between the two surfaces under airflow and can be easily removed. The second option considered is sitting the pin-fins on a 4mm blind hole; it was not known whether the airflow would be strong enough to make the pin-fins fall over, but if it is enough to make the pin-fins tilt slightly, then thermal contact between the two surfaces is lost. Of the three options, this would require the most machining and time due to the amount of precision to ensure the pin-fins are perfectly in contact with the blind hole. The merits of adopting this option would be that it does not need any foreign material to fasten the two objects and it would be easy to assemble. Some form of adhesive, such as glue or soldering around the edge of the pin-fins was considered. The downside of this approach was that there was no means of making sure the pin-fins are attached in the exact location during the fastening process; also the adhesive material would block some of the airflow

intended for the plate and pin-fin surface. Advantages of this approach would be minimal manufacturing process required.

Chosen pin-fin fastening option

Flathead countersunk screws were used as they could provide a strong, accurate attachment with the plate while also being convenient to install. Other options had various advantages, but it could not be ensured that the pin-fins would remain intact with the plate under airflow or whether the pin-fins were perpendicular to the plate. The first option had flaws that could be resolved in the fully detailed CFD, whereas the other options could introduce undesirable errors that cannot be accounted for if they did occur.

4.6.3 Specific requirements for data acquisition

To obtain experimental data that was comparable to the detailed CFD, the rig must be designed in such a way that allows temperature and air velocity measurements to be carried out inside the cavity of the airflow. Temperature measurements must be within ±0.5°C and velocity measurements ±0.2m/s to be relevant to the CFD results.

4.6.4 Conceptual design for the test rig

Water container module

The initial concept for supplying constant heat was via heating a volume of water with a water heater. Therefore, the design must be able to provide a watertight seal between the condenser and container, and be structurally stable when supporting the load of the condenser unit (about 10 to 15kg). Also, the designs must have a mechanism to allow water to be refilled and air bubbles to escape, and a place for a stirring device to evenly mix the water.

The first design consists of only a sheet metal form from 1mm stainless steel, in which the edges would be welded. A design feature of this concept is that it has an overlap on three sides to support the weight of the condenser module. The overhangs would be such that the open space area exposed to the water would be equivalent to 1256×260mm, which is the heating domain that was modelled in the CFD. Therefore, the condenser plate must be bigger to allow for this overhang. Another feature is the flat sheet on the side to ensure water does not enter into the condenser module from the water inlet side.

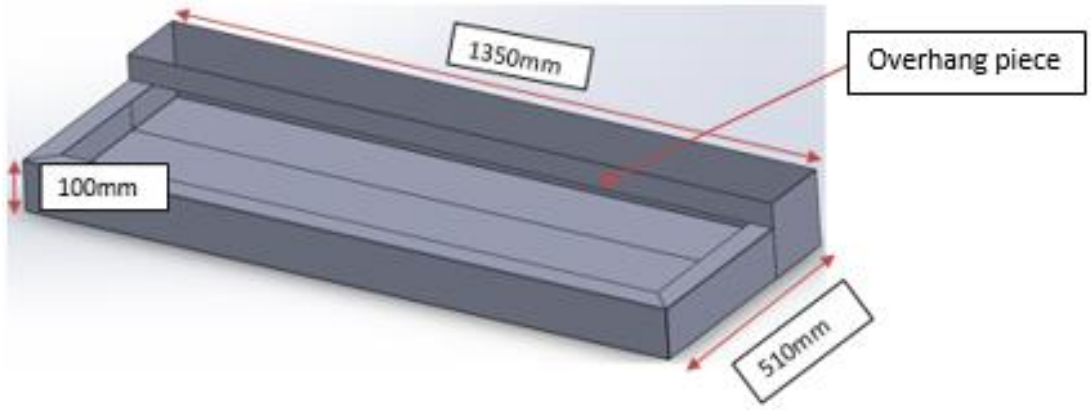

Figure 4.6.3. First concept for the water container: a sheet metal water container.

By replacing the overhangs with a wooden support reduces the volume of water that needs to be heated. The potential problem of this design is the electrical wiring coming out of the heating element may become a fire hazard if the support is made from wood. This problem can be resolved if both ends are supported by an external piece of metal instead.

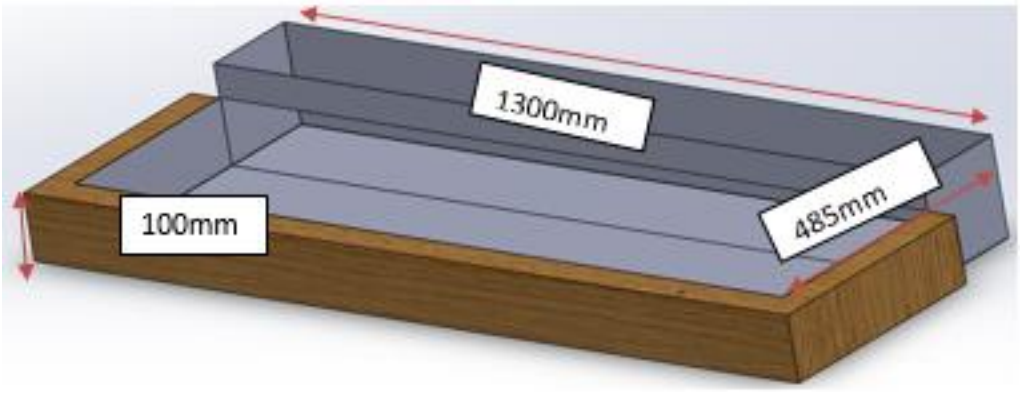

Figure 4.6.4. The second concept for the water container: the use of supports to hold up both ends of the condenser module.

Instead of using sheet metal as the container material, Perspex was used in this design to insulate the water so that the temperature controller would need less effort to maintain constant water temperature. Acyclic glue and waterproof tape would be used to seal up any gaps on the side of the container. Silicone glue would be used to seal between the condenser and the container unit as it needs to be removed at least once for the flat condenser and pin-fin condenser testing. The overhang piece was omitted in this design as the watertight mechanism would be incorporated into the condenser module instead (see the third concept of the condenser module). By doing so, less gluing is needed to seal the condenser and the water container.

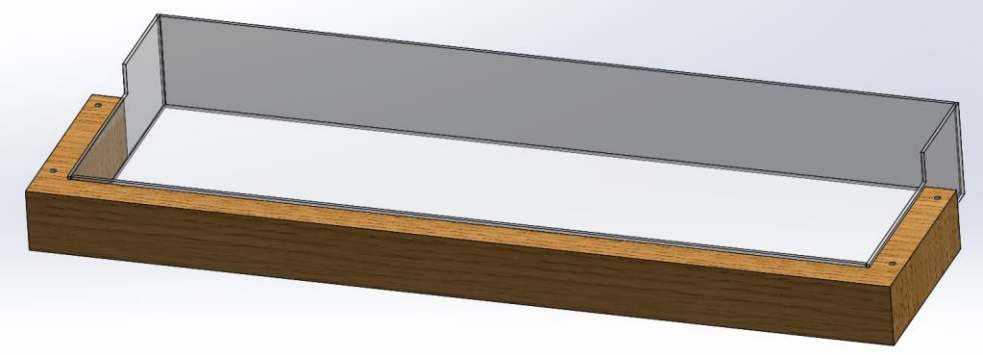

Figure 4.6.5. The third concept for the water container: a Perspex container.

Condenser module

The first concept consists of three pieces of Perspex as the duct, which would be held straight by two wooden frames bolted onto the edge of the extended condenser plate. A 4mm deep channel would be machined on both sides of the plate to ensure that no water enters the ducted cavity. The Perspex pieces would be glued using acrylic glue, and the connection between the Perspex duct and silicone glue would be used to seal the edge between the Perspex and the condenser plate.

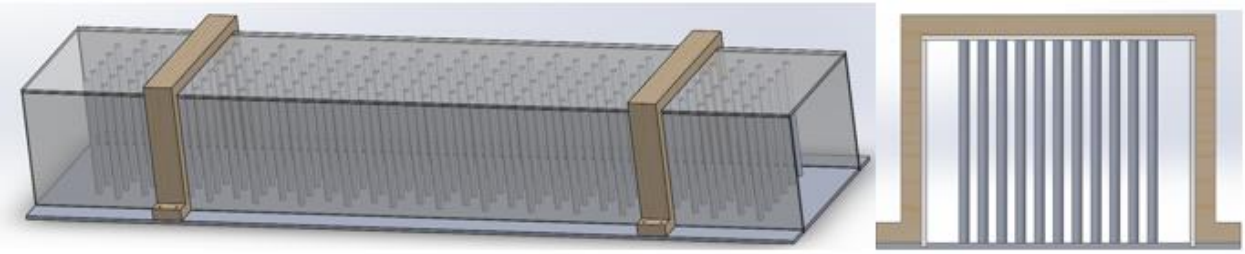

Figure 4.6.6. The first concept of the condenser cover: fastening the walls with two wooden frames.

The second concept uses a single piece of Perspex that is heat folded, which can be fastened onto the condenser plate. Two lengths of waterproof tape would be used to seal the edge between the Perspex cover and the condenser plate. This concept eliminates the need for an aligning mechanism, though the resulting radius of the bend may affect airflow.

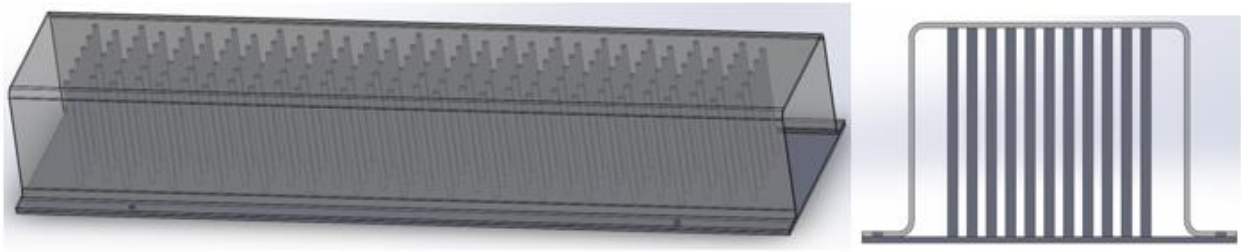

Figure 4.6.7. The second concept of the condenser cover: a single-piece Perspex cover formed by heat folding.

This is similar to the first concept for the Perspex ducting, but this also has an in-built water sealing mechanism. The rails on both sides are of different heights, and the higher piece would be used to barricade water from infiltrating into the condenser cavity. Two bars are welded onto each end of the

rail; this could be used as a point of support from an external object, such as the wooden supports in the second and third water container concepts.

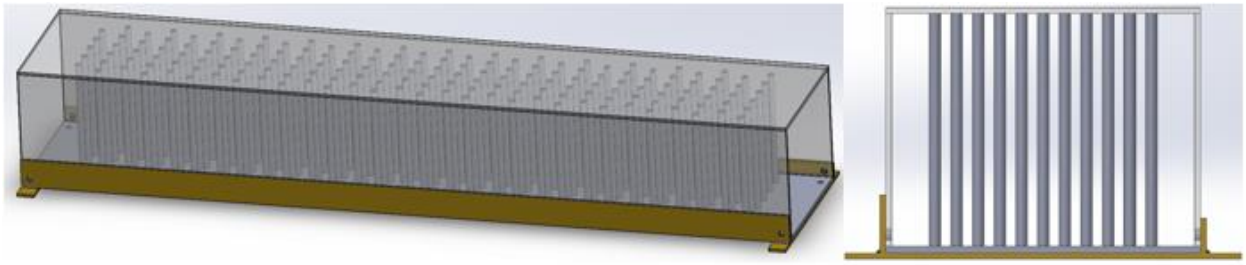

Figure 4.6.8. The third concept of the condenser cover: fastening the walls with a metal frame made from a flat bar.

Heating element specifications

If water was selected as the heating media, a submerged water heating element was considered. Due to the long aspect ratio of the condenser, one heating source would not be sufficient to provide even heating of the water. Therefore, the heating element was based on a 2.4kW, 1069mm long water heater. Based on the container dimensions in Fig. 4.6.3, the volume of water was determined to be $0.033m^3$=33kg. To heat up this volume of water from 18°C to 29.81°C would take 11 minutes assuming no heat loss. The water temperature of 29.81°C was selected as explained in Section 4.3.3, and a PID controller was used to maintain constant water temperature. To ensure even heating along the container, a paint mixer was used to stir the water at the inlet.

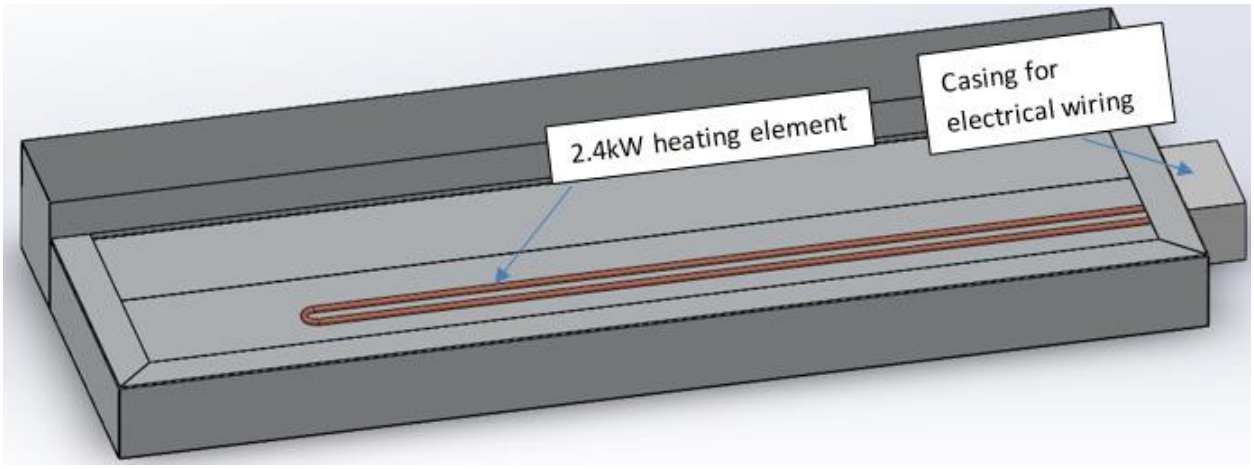

Figure 4.6.9. Heating element layout inside the water container.

Temperature controller

Because there was a need to maintain constant water temperature to ±1°C, a PID controller was used. The PID controller was connected to a K-type thermocouple which was bonded to the inner condenser surface. Depending on the response time of the system from factors, such as thermal mass and heat transfer rate to the surroundings, the PID system was calibrated to reduce the amount of fluctuation in the power output.

Figure 4.6.10. Digital PID controller used to maintain constant water temperature. Photo M.Leung.

Limitations of the water container design and the heating foil concept

It was originally thought that water would be the most suitable heating medium due to its high thermal mass. Due to the amount of manufacturing complications with the water container for ensuring water tightness, the heating foil option was considered instead. The new concept was to use a 2000W.m^{-2} heating foil to apply heat to the condenser, and use the same PID controller to regulate the power going into the heating foil so that a constant inner condenser temperature could be achieved. The disadvantage of this was that the foil was made out of arrays of heating wires spaced at 23.8mm, which could create cold spots on the condenser plate. To dampen out this effect a 6mm heating plate was added between the condenser and heating foil.

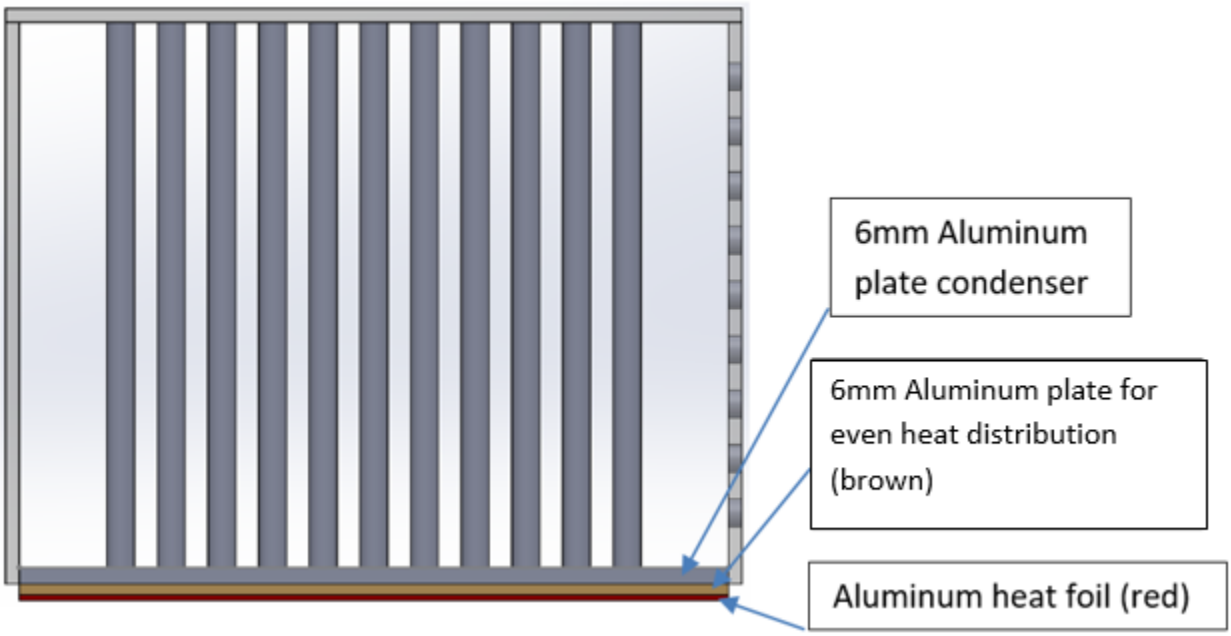

Figure 4.6.11. Cross-section layout of the heating foil/condenser plate layer.

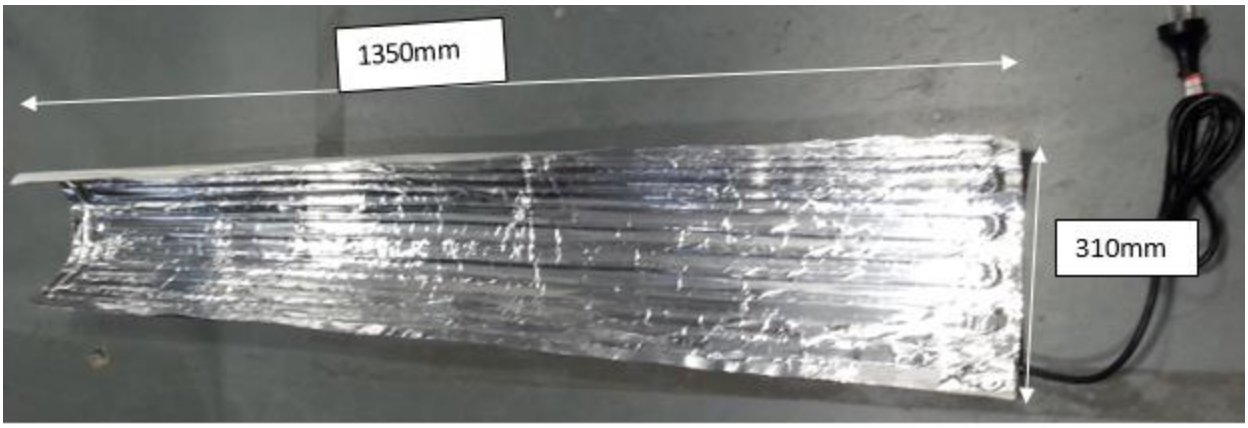

Figure 4.6.12. The adhesive heat foil with the three-pin plug.

Chosen rig concept

Based on the convenience in manufacture and operation, the heating foil concept was used. An extra layer of 6mm aluminium plate was needed to spread the heat more evenly before reaching the condenser. Rig concepts that use water as the heating source were dropped due to:

1. The difficulty in ensuring the container is watertight; any leakage may cause fire hazards if in contact with the electronics.
2. The container would be difficult to carry when filled with water due to its mass (>33kg including the condenser); it would also be inconvenient to drain the water without incorporating a draining mechanism at the bottom of the container.
3. Due to the large volume of water, it would take significantly longer to heat the inner condenser up to the correct temperature compared to the heating foil.
4. Originally, it was thought that water could provide more even heat distribution than heating foil, but because the heat rod did not cover the aspect ratio of the condenser plate fully, so a stirring device would be needed throughout the experiment. This would be inconvenient when taking measurements, and it was not known whether the stirring would introduce noise to the data.
5. Any air bubbles caused by the stirring or when refilling the container with water would have a significant impact on heat transfer onto the condenser surface.

Measuring heat rejection using the airflow

To calculate the heat rejection of the condenser, an array of air velocity and temperature measurements were needed at the outlet and inlet, as taking the average across the cross-section was not sufficient to provide the level of accuracy, due to the influence of the wall viscous effects. Therefore, 77 measurements of air velocities and air temperature were needed at the inlet and outlet of the flat plate and pin-fin condenser, as shown in Fig. 4.6.14. To achieve this, 11 holes would be needed to be drilled on the side of the duct wall so that the pitot probe can enter the air space. When not taking measurements, the holes were sealed with tape to avoid disturbance to the airflow. Because of symmetry, only half of the inlet and outlet were needed.

To determine the energy rejected on each square grid, the four nodes would be averaged to give $\overline{V}$ and $\overline{T}$. For example, using the notation illustrated in Fig. 4.6.13, the average velocity in grid 1, $\overline{V}_1 = 0.25(V_{1,1} + V_{1,2} + V_{2,1} + V_{2,2})$. This process would be repeated for temperature and every grid at the inlet and outlet. Then the corresponding grid between the inlet and outlet would be matched, such that:

$$\dot{Q}_1 = C_p LW(\rho_{1\ outlet}\overline{V}_{1\ outlet}\overline{T}_{1\ outlet} - \rho_{1\ inlet}\overline{V}_{1\ inlet}\overline{T}_{1\ inlet})(W)$$

By summing every corresponding product of each grid pair between the inlet and outlet, the total energy rejected would be this sum multiplied by two.

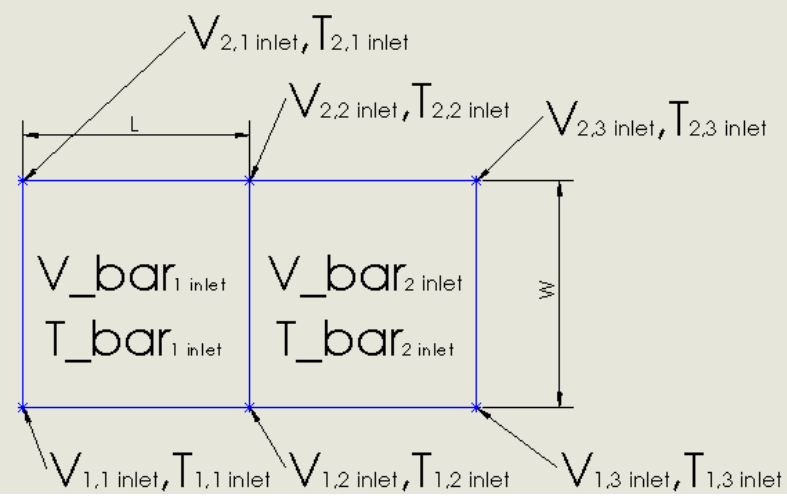

Figure 4.6.13. Defining the velocity and temperature notation for each node.

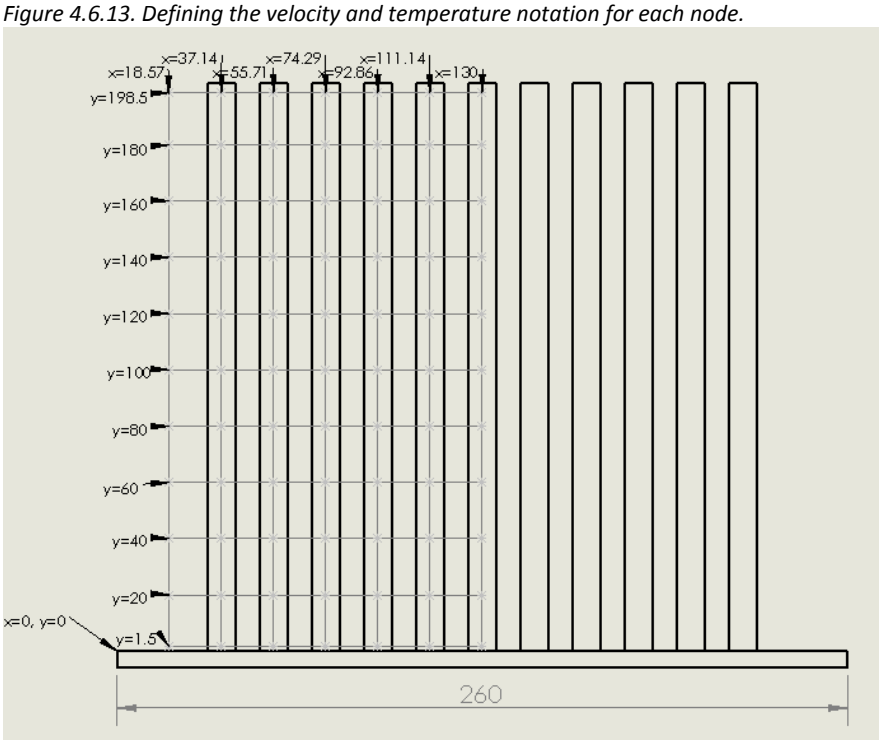

Figure 4.6.14. Grid showing the 77 coordinates where the air velocity measurements were taken for the flat plate and pin-fin condenser. This was done at the inlet and outlet.

Condenser plate temperature control

Ten 2x5mm deep holes were drilled on the edge of the condenser plate, each connected with a T-type thermocouple. The hole at the inlet was used to control the power output of the heating foil so that the inner condenser temperature was constant at 30°C, another hole was placed 4.5mm away to ensure the DAQ reading was close to 30°C. The other eight holes on the lengthwise edge were connected with the DAQ (data acquisition) to monitor any temperature change along the length of the condenser plate, so that this information could be accounted for in the refined CFD model.

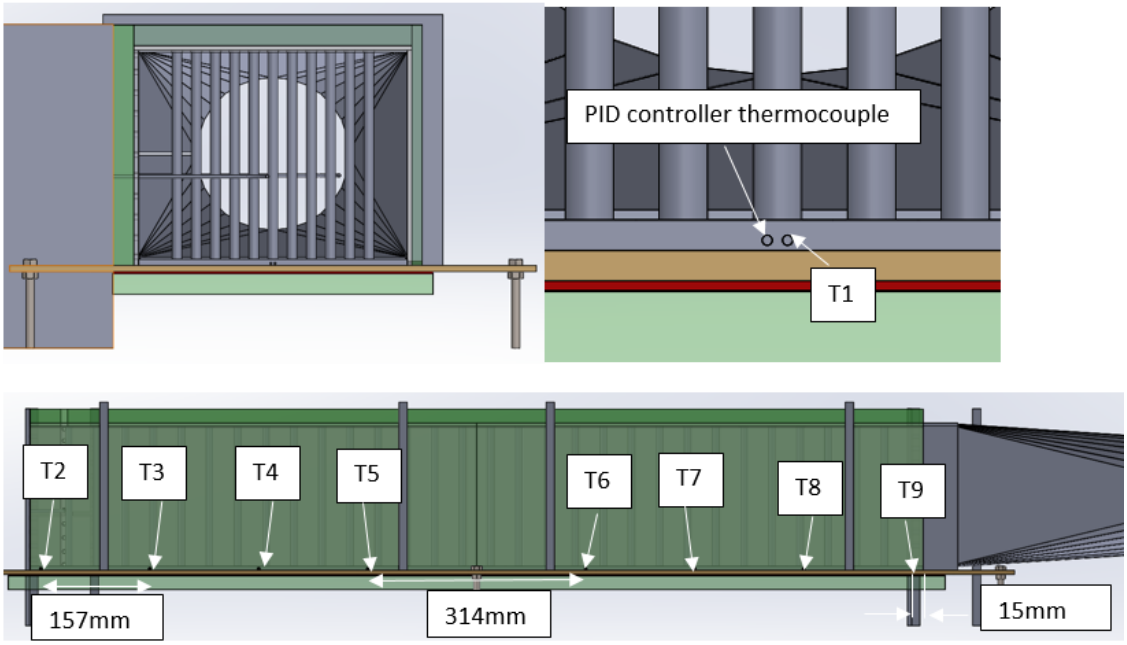

Figure 4.6.15. Location of side holes to control and measure the condenser plate temperature.

Measuring heat rejection with power meter

A METEC power meter was used to measure the energy supplied to the heating foil, but because the dial reading on the power meter was only accurate to 0.1kWhr, it was connected to a BK Precision 175MHz counter which was capable of displaying at 10^{-4}kWhr. To obtain the power of the heating foil, the energy value would have to be divided by the accumulative measurement time, which was set at 30 minutes. This heat foil power value would then be compared with the CFD heat rejection value, assuming all the energy entering the foil is rejected by the airflow.

Figure 4.6.16. The METEC power meter was connected to the BK Precision 175MHz counter, where one tick corresponds to 10^{-4} KWhr.

Data acquisition equipment

Pitot tube

By measuring the difference between the static and dynamic pressure using the pitot tube, the air velocity can be determined using the Bernoulli equation. Due to the geometry of the probe being a right angle bend, the rig would need to be adjusted, so the head of the probe measures at the point of interest. Also, the pitot tube is only capable of measuring 1D flow in the incoming direction, and it was assumed that most of the flow measured would be parallel to the inline direction.

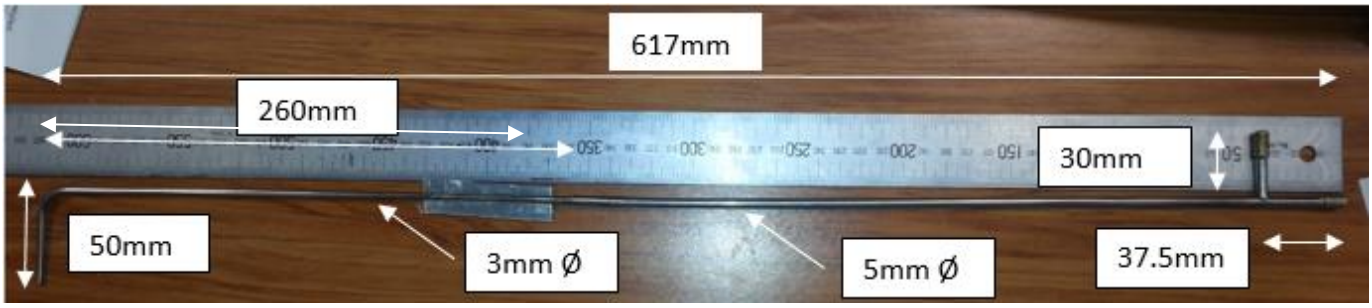

Figure 4.6.17. Dimensions of the pitot tube used.

Air temperature measurements

A handheld T-type temperature probe was used to measure temperature profile along the cross-section of the duct, which would then be read off the DAQ. From the specifications, these probes are accurate to ±0.5K.

Noise in DAQ measurements

Because of the unstable nature of the airflow and heat transfer, it was not possible to obtain a stable reading from the DAQ equipment. To account for this problem, each measurement should be taken as time averages over 30 seconds.

Airflow management

Transitional ducting

Due to the circular outlet of the fan and the rectangular profile of the duct, a 400mm circular to rectangle transition was needed. It was expected that there would be some pressure loss associated with the transition, which was included in the fully detailed CFD after the experiment. The duct development would be folded using the cardboard pattern shown in Fig. 4.6.18.

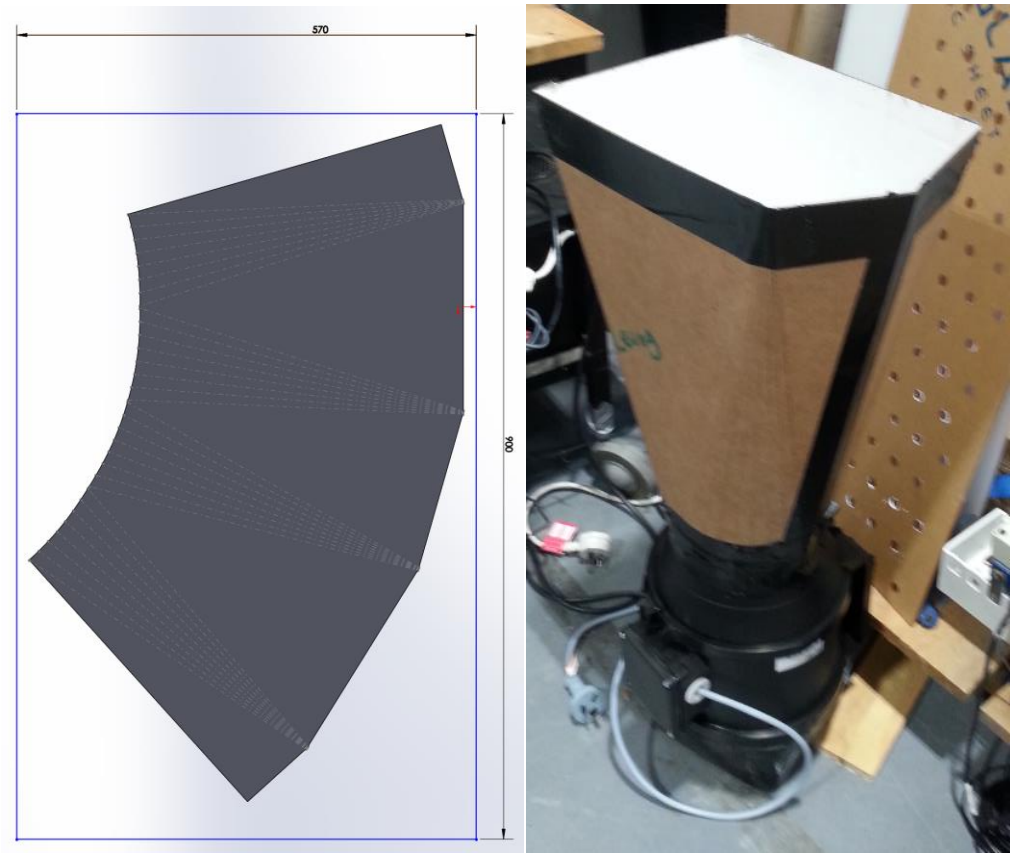

Figure 4.6.18 Left: laser-cutting pattern for forming the transitional duct. Right: the transitional duct connected to the fan.

Fan selection

As the RIL-150 fan was used in the initial CFD optimisation, therefore it must be used in the experiment for consistency purposes. The fan was originally selected due to its fan outlet diameter (147mm) being similar to the size of the main duct (260mm by 200mm high). An axial fan was preferred over a centrifugal fan due to cost, and axial fans can generate more flow given the same power. The disadvantage of using an axial fan is it will generate an omnidirectional flow compared to a consistent, straight flow. Flow straighteners were considered, but it was not known how much additional pressure loss could be introduced. Therefore, in both the optimisation and fully detailed CFD, the flow at the duct inlet was assumed to be uniform.

Figure 4.6.19. PROVENT RIL-150 SW axial fan, rated at 38W.

Manufacturing considerations and constraints

Pin-fins

Due to the 10mm aluminium rods not being available, only 9.5mm aluminium rods could be purchased. These came in 5m lengths, which could be cut by a drop saw to 205mm to account for the turning process to smooth out the surface. Also, it was noted that 3mm was lost for every drop saw cut, so seven lengths of the aluminium rod were purchased. After turning both sides of every pin-fin to 202mm, a 20mm deep 2.5mm diameter blind hole was drilled to allow for the 3mm tap to be made.

Drilling holes onto the pin-fin condenser plate

It was identified that the plate would need to be 1286mm long due to the 15mm needed to account for the probe entry at the inlet and outlet. Because the digital milling machine could only reach 1m, it was decided to obtain two pieces of 643x260mm instead to allow easier management and transport. To avoid the drill from bending the work piece, smaller pilot holes were drilled before making the 4mm hole. Also, because the precision of the digital mill would only be 0.01mm, and by definition the x and y spacings are irrational, there would be an error of 0.02mm for the final hole in the x-direction. More errors were introduced when the work piece was rotated or moved during the session, but the hole locations were accurate to 0.5mm.

Side walls, top wall and pin straightener of the duct

The side walls of the main duct consist of four pieces of polycarbonate, each 643x208x4.5mm. This was because if it were a single piece it would be 1286x208mm and it would not fit inside the laser cutter. The top wall of the duct was split into two 643x209x4.5mm pieces, so that the main duct could be split into two pieces for better handling. Another two 643x200x2mm pieces of polycarbonate were also laser cut to be used as the pin straightener on the top wall of the main duct.

Foil heater and plate

Because the heating wires do not cover the edge of the heating foil, a bigger heating foil was needed to provide constant heat to the condenser region. The heating foil sourced was 1350x310mm so that the wires in the heating element could directly cover the 1276x260 region at a constant temperature. An

additional 1550x510x6mm plate was used so that the adhesive foil could be attached to this plate instead of the condenser plate, as there was a need to test two condenser plate variants (flat plate and pin-fin condenser) because the adhesive foil could not be removed.

5 Rig commissioning and data collection

5.1 Finalized design

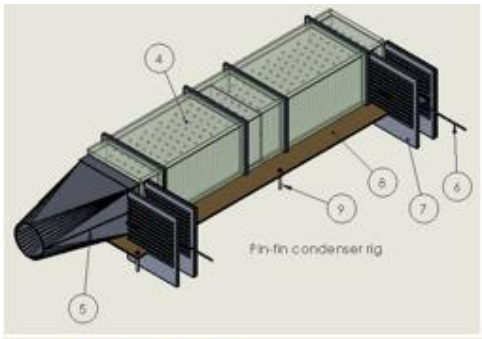

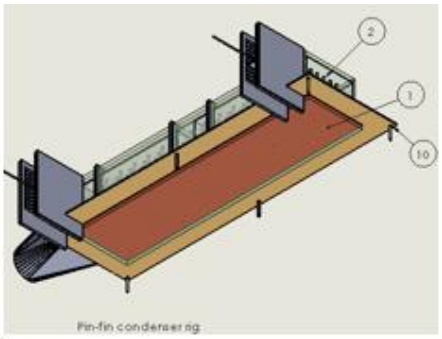

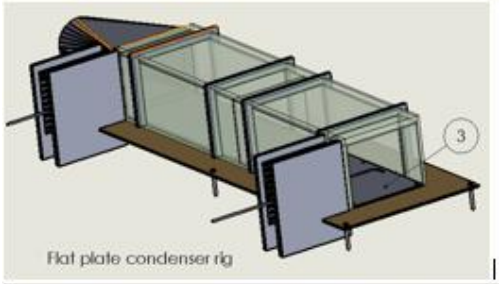

ITEM NO.	PART NUMBER	DESCRIPTION	QTY.
1	Heating Foil	2000W/m^2 adhesive heating foil	1
2	Pin-fin Condenser	165 fins, 200mm high 9.5mm dia	1
3	Flat Plate Condenser	1286x260x6mm	1
4	Main Ductmodule	See main duct assembly drawings	1
2	Transistional Duct	Rectangular to round 260x200 to 147dia	1
6	Pitot probe	Pitot tube	1
7	Pitot Stand	Laser cut from 4.5mm MDF	
8	heat bufferplate	1550x510x6mm 5005 Aluminum	1
9	M8x80 bolt		6
10	M8 nut		6

Figure 5.1.1. Overview of the components in the flat plate and pin-fin condenser rig.

The final design consists of one rig with two condenser plates (flat plate/pin-fin) that can be installed or removed via unscrewing the 14 M4 countersink screws, as shown in Figs. 11.2.2 and 11.2.3. The rig consists of three modules: the main duct assembly, the condenser plate heating module, and the air extraction assembly with some differences for the flat plate and pin-fin condenser, as shown in Figs. 11.2.2-11.2.5. To allow for the pitot tube to measure the airflow inside the rig, 11 holes were drilled on the side wall of the main duct at the inlet and outlet location. A pitot stand was made so that the pitot tube would always enter in at the same angle for each hole.

5.1.1 Flat plate condenser

A single piece of 5005 aluminium plate, 1286x260x6mm, was chosen to be the flat plate condenser. Ten 2mm holes were drilled on the edge of the plate for the thermocouples T1-T9 to record the temperature, according to Fig. 4.6.15. Thermal grease was added to maximise heat transfer between the heating plate (brown) to the condenser plate, which was also bolted down by M4 countersunk screws with 1mm of under flush to minimise its effect on the airflow.

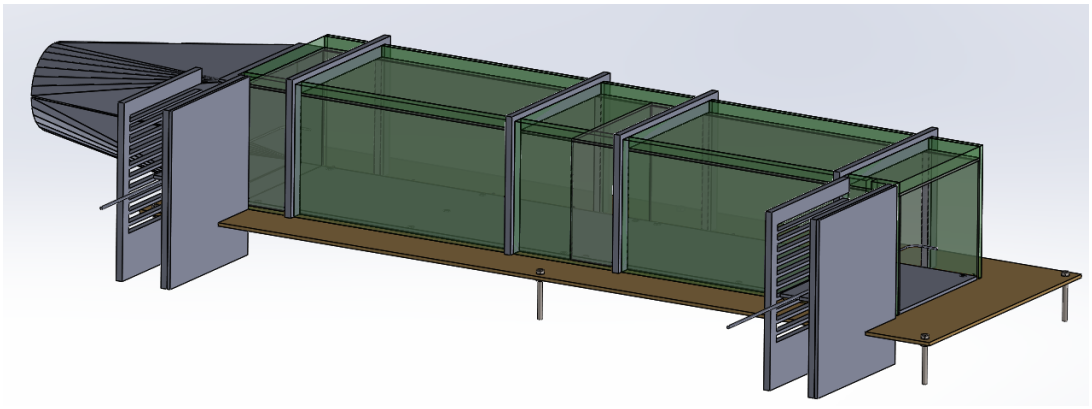

Figure 5.1.2. SolidWorks model of the flat plate condenser rig with polystyrene insulation (green).

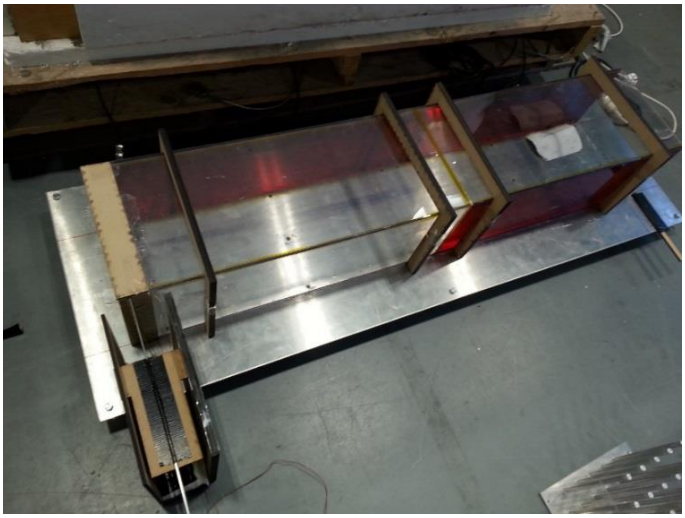

Figure 5.1.3. Perspex side walls of the main duct and the pitot stand. Length of rig is 1550mm.

5.1.2 Pin-fin condenser

Two separate pieces of 5005 aluminium was used instead to give the same condenser plate area due to manufacturing constraints. The pin-fins were attached to the plate with 165 M4 countersunk screws in the bottom of the condenser plate, and the bottom of each pin-fin was coated with thermal grease to help the plate-pin heat transfer. As mentioned in Section 4.6.4, only 9.5mm 6060 aluminium rods were available. For a better description of the assembly, see Fig. 11.2.3.

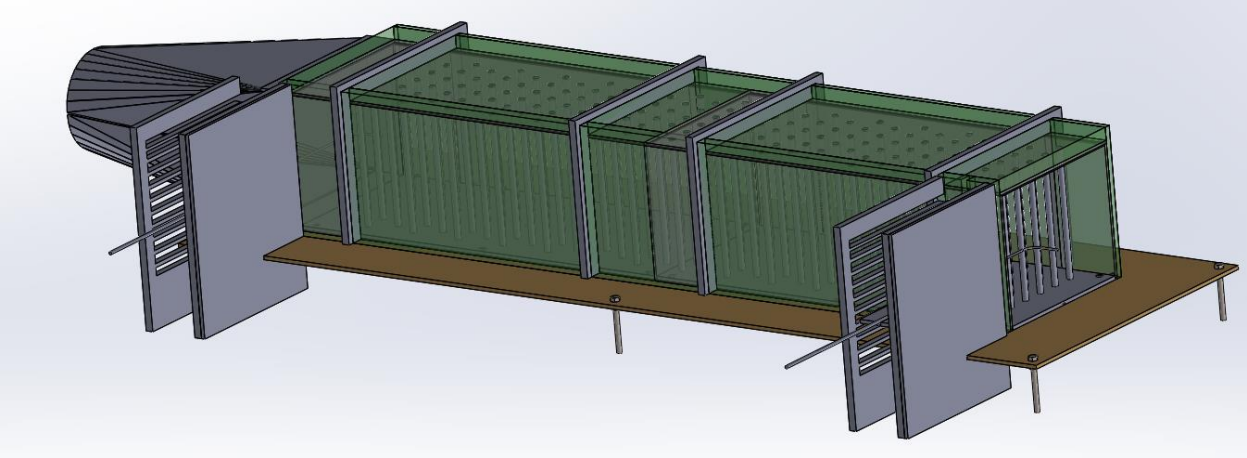

Figure 5.1.4. SolidWorks model of the pin-fin condenser with polystyrene insulation (green).

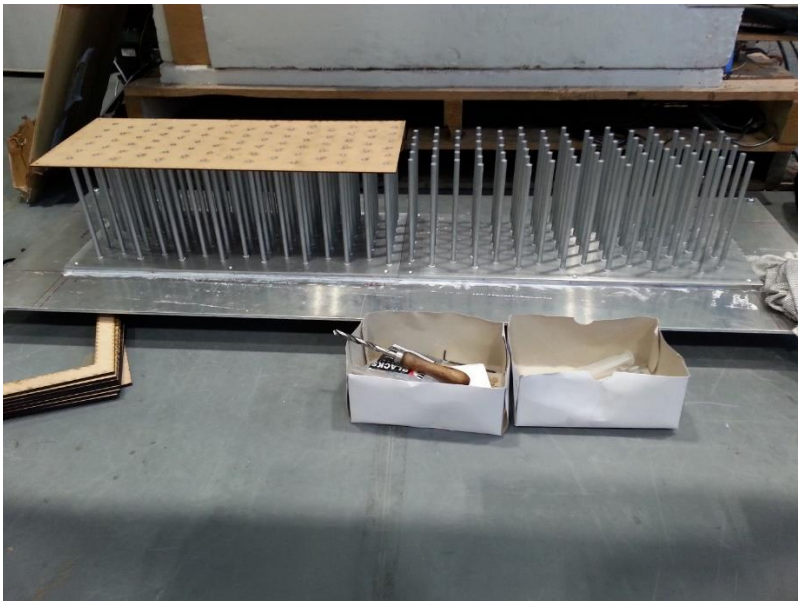

Figure 5.1.5. Pin-fin condenser in construction, without the main duct and fan.

5.2 Design modification

5.2.1 Pitot tube

Due to the hot wire anemometer being too fragile to be implemented in this rig, a pitot tube was chosen instead. The velocity expected from the CFD optimisation in Sections 4.4 and 4.5 were between 0.5-2m/s within the rectangular duct section. Using Bernoulli's theorem: $P_{dynamic} - P_{static} = 0.5\rho U^2$, so the range of pressure difference=0.15 to 2.4Pa. However, the fan outlet was much faster due to transitioning to a smaller cross-section, from using conservation of mass flow rate the velocity at the fan outlet would be 7.37m/s assuming no pressure loss from the transitional duct, which equates to 32.6Pa.

Figure 5.2.1 Left: The 100Pa pressure transducer rated at ±0.75% of reading. Right: The fixing mechanism to keep the head of the pitot tube parallel to the airflow.

Figure 5.2.2. Left: Close-up of the pitot stand and pitot tube; the pitot stand was designed to align with the 11 pitot holes on the side wall of the main duct. Right: Markers on the pitot tube to show each depth at which measurements would be taken; this was to be repeated for all 11 pitot holes, as demonstrated in Fig. 4.6.14.

5.2.2 Change in inlet location

Due to the 50mm bend in the pitot tube colliding with the first row of pin-fins, the original inlet position that was defined in the previous CFD optimisation had to be moved 15mm to the front, and, as a consequence, the plate and rectangular duct were extended by 15mm. An additional 50mm portion of the rectangular duct was added at the outlet so that the probe could reach the defined outlet line.

Because of this change, the geometric model in the refined CFD simulations was also updated.

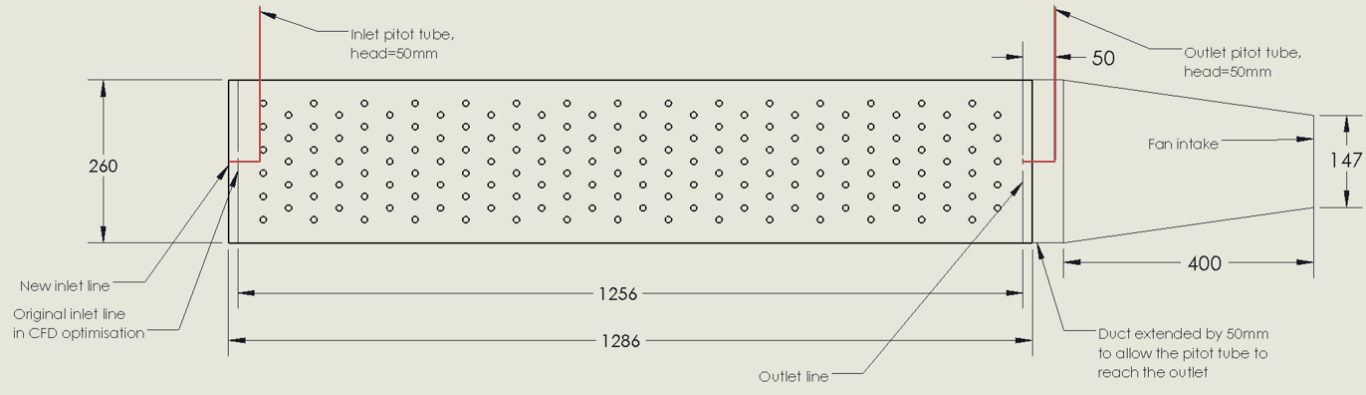

Figure 5.2.3. Location of the new inlet position due to the length of the pitot tube head; the pitot tube is shown in red.

5.2.3 Thermal insulation

10mm of S-grade polystyrene foam was needed to seal the main duct to ensure minimal heat loss, as this would greatly improve the relevance of the power meter measurement.

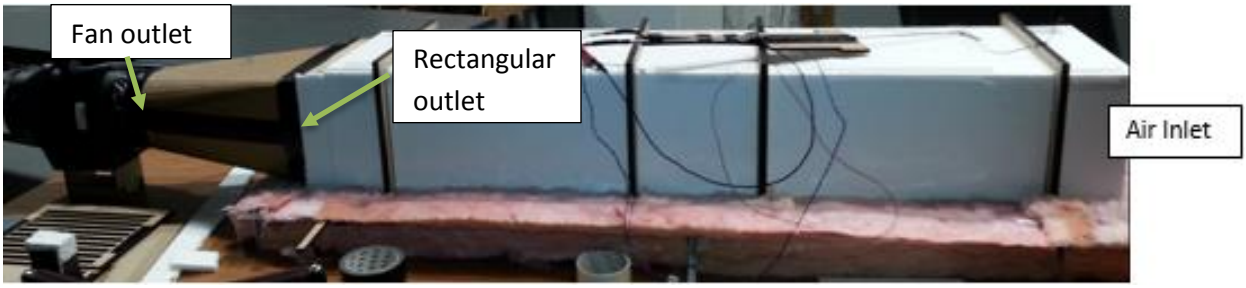

Figure 5.2.4. The complete rig setup with polystyrene and glass wool insulation.

Glass wool was used underneath the heating foil and on the heating plate to prevent heat from escaping underneath. While not flammable, the heating foil could get above 100°C should the PID temperature controller fail.

5.2.4 Orientation of the fan

It was found that the flow was not delivered evenly across the empty rectangular duct due to the hub of the fan generating less flow at the flow centre. Therefore, the fan was reversed so that the flow was being extracted from the condenser instead. By doing this, the amount of airflow would theoretically remain the same due to continuity, but in the experiment, this would produce a much more laminar flow entering the main duct.

Figure 5.2.5. The transitional duct and the fan, designed to extract air from the main duct.

5.3 Reliability of data acquisition and experimental equipment

A Type T thermocouple was used for temperature measurements and temperature control. It has an error of ±0.5K; therefore, the experiments measuring temperature differences of less than 2K was not recommended assuming 20% accuracy. To minimize this problem, the measuring temperature should be much higher than the ambient temperature. The pressure transducer was determined to be suitable for the expected operating range of 0.15-32.6Pa, but the connecting rubber tubes must not be blocked when taking measurements. There was no information given for the pitot tube; it was obtained from the Mechanical department and it has a tolerance of ±2%. This should not cause more error unless the tube is bent such that the tube no longer allows air to pass through it. Regarding the axial fan, a pressure-flow rate curve was provided and was used in the CFD optimisation, but whether the existing fan operates according to this curve had not been tested. Assuming the difference between the actual fan and the curve is small, the flow rate would be measured in the experiment and compared with the CFD assuming the same pressure-flow rate curve. For determining the reliability of the power meter and counter unit, a measurement was taken at maximum heating foil power during test 5 of the pin-fin condenser experiment. This was found to be 657.4W, which is reasonable as the supplier stated a value of 666W.

Table 5.3.1. Reliability of the sensors and equipment used in the rig and DAQ.

Name of equipment	Specification	Precision
Axial fan	RIL-150	Measured in experiment
Pitot tube	Unknown	±2% of measurement
First sensor 100Pa Pressure transducer	LDES100UF6S	±0.75% of reading
T1-T9	Type T thermocouple	±0.5K

PID controller thermocouple	Type T thermocouple	±0.5K
Pitot probe thermocouple	Type T thermocouple	±0.5K
PID controller	Type T thermocouple	±0.5K
Power meter	METEC IEC 1036	10000 impluse/KWhr
Universal counter	BK Precision 175MHz	10^{-4} KWhr

6 Results for Flat plate condenser

6.1 Heating foil power output

Originally, it was thought that the same inner condenser temperature and the ambient temperature according to Test 17 by Gorrie could be achieved in the experiment. However, the ambient temperature was found to fluctuate during the entire 30 minutes measurement; also, the inner condenser did not have a constant temperature profile as originally expected. To account for these issues, the ambient temperature and all nine thermocouple measurements along the condenser plate were recorded every second for 30 minutes and averaged. Tests were repeated at various ambient and inner condenser plate temperatures to determine whether this had any correlation with heat rejection. The average inner condenser plate temperatures for each test was obtained using the process described in Section 6.3. After six tests, it was found that there was a linear correlation between heating foil power and the difference between the ambient and average inner condenser plate temperatures, as shown in Fig. 6.1.2. A summary table of the heating foil power for each test is in Fig. 6.1.1.

	Average ambient T (degC)	Average inner condenser (degC)	Condenser-Ambient (degC)	Measured heating foil power (W)
Test 1	23.19	26.58	3.39	24.60
Test 2	22.53	38.08	15.55	96.00
Test 3	22.14	49.89	27.75	169.00
Test 4	21.33	61.77	40.44	239.00
Test 5	20.99	73.12	52.13	309.40
Test 6	22.96	77.66	54.70	329.00

Figure 6.1.1. Summary of the ambient and inner condenser temperature of each test and the heating foil power.

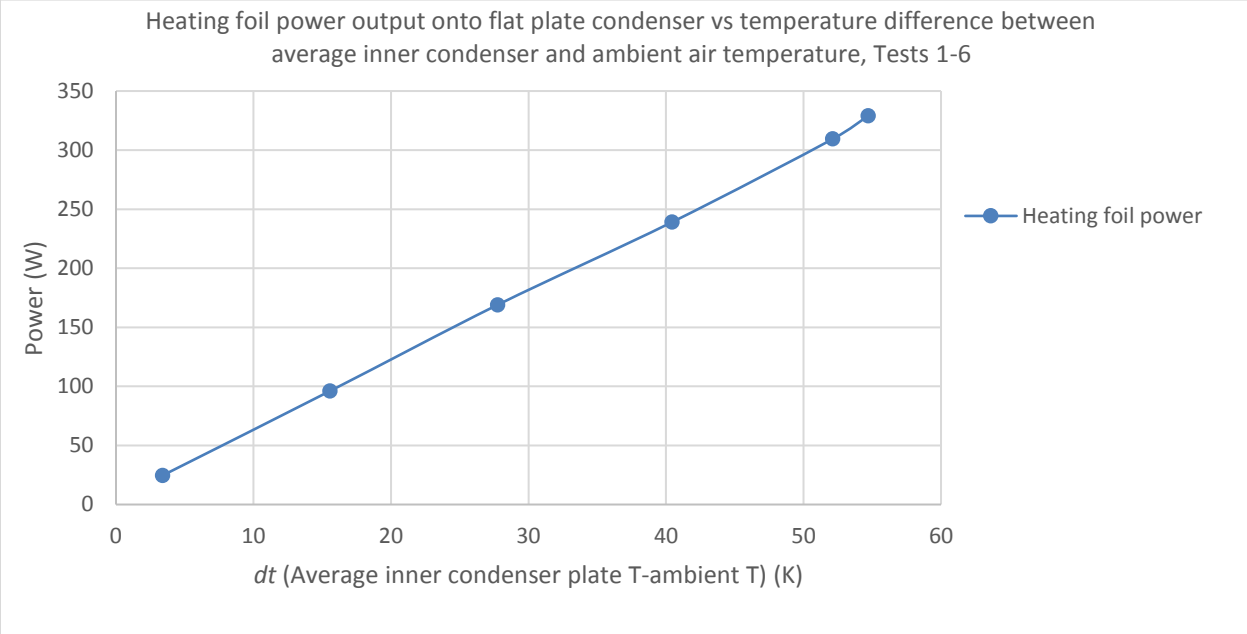

Figure 6.1.2. Plot of the heating foil power at different dt=average inner condenser plate-ambient temperatures.

6.2 Temperature profile of the inner condenser plate

The temperature profile was important, because it was needed to determine the average inner condenser plate temperature, but also to study its heat rejection characteristic. All temperature profiles from Tests 1-6 were plotted in Fig. 6.2.1. It was observed that T1 was the coolest, as it corresponds to the inlet of the air. The plate gets hotter as it gets further away from the inlet; this is because the air also gets hotter as it travels through the length of the plate. After T7, there was a slight drop in plate temperature; this was thought to be due to the additional heat rejected due to the flow beginning to transit from uniform to swirl flow as it enters the fan.

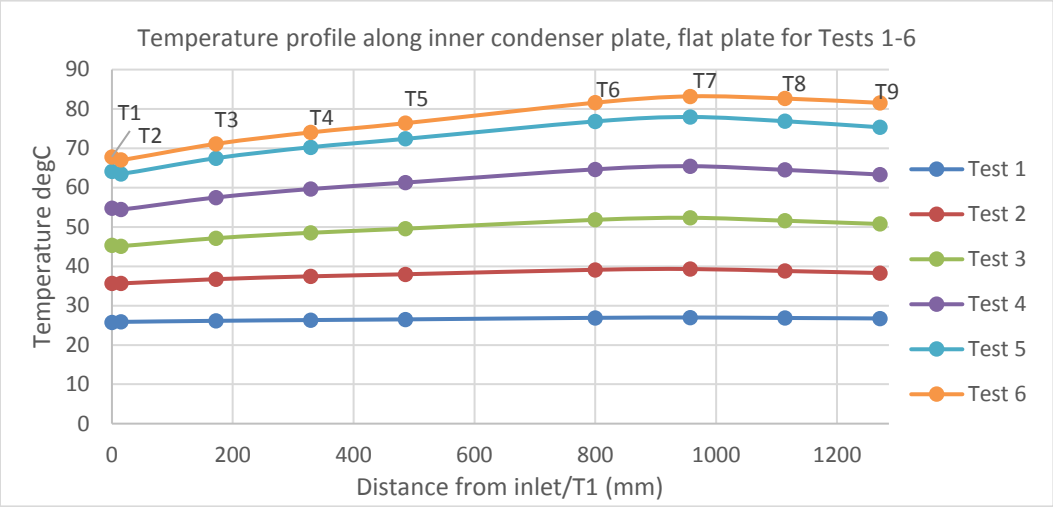

Figure 6.2.1. Temperature profile along the inner condenser plate for a different experimental run.

6.3 Obtaining average inner condenser temperature

Averaged inner condenser temperatures were obtained using the weighted average method, where the area under the temperature profile curve for each test run, shown in Fig. 6.2.1, were evaluated using the trapezoidal method. This was then divided by 1286mm, as this was the length of the condenser plate, to give the average inner condenser plate temperature.

$$Average\ inner\ condenser\ temperature = \sum_{i=1}^{8} 0.5(x_{i+1} - x_i)\,(T_{i+1} - T_i) \Big/ 1286$$

where x_i corresponds to the distance away from the inlet/T1 in mm.

6.4 Refined CFD setup and data processing for the flat plate condenser

The main purpose of making a refined CFD model for the flat plate rig was to include the experimental factors that were not considered in Section 4.5.3. In the manufacturing of the rig, there were some changes made to the geometry and the layout of the rig, such as changing the direction of the flow to extract, and the addition of a transitional duct to connect the rig with the fan. These geometry changes were then included in the refined CFD model. During the experiment in Section 6.1, it was found that the ambient temperature could not be controlled, and the inner condenser temperature was not

constant along the length of the plate, as shown in Section 6.2. To model these variations, each experimental run was modelled according to its ambient temperature and the inner condenser temperature profile that was measured during the experiment.

To save computational time and allow for higher mesh density, only half of the rig was modelled, as shown in Fig. 6.4.1. The transitional duct was included as well, to account for the pressure drop associated with it, which was found to be 27.5Pa. At the fan outlet, the airflow was extracted out by the same pressure curve used in Fig. 4.3.8, but the airflow was halved as only half of the rig was modelled. The flow was assumed to be extracted uniformly with no swirl motion, as this would require modelling the fan blade itself and it would be unreasonable in this timeframe. All the walls were assumed to be fully insulated except for the inlet, outlet and sliced area. Heat rejection was calculated using the integral approach in 4.2.1 but multiplied by two to obtain the full heat rejection for a single rig.

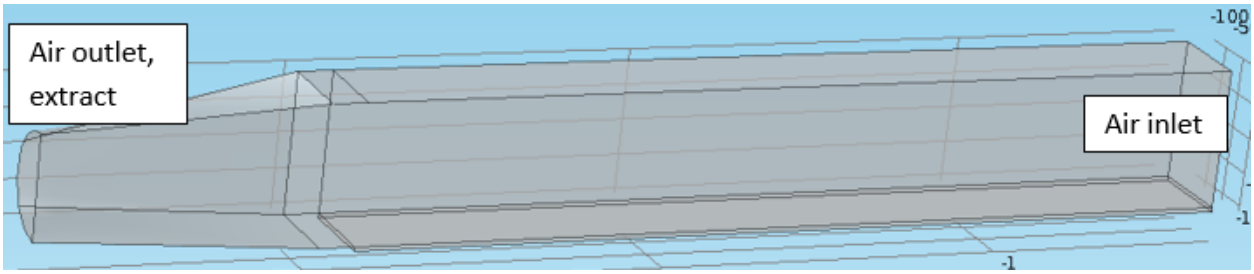

Figure 6.4.1. The geometry of the rig for the flat plate condenser rig in COMSOL, which is composed of the condenser plate, and air in the main and transitional ducts.

The normal mesh setting was selected on COMSOL; the statistics and detailed settings are shown in Fig. 6.4.2 and Table 6.4.2. This resulted in 13 hours of computation and 17GB of ram used for each run.

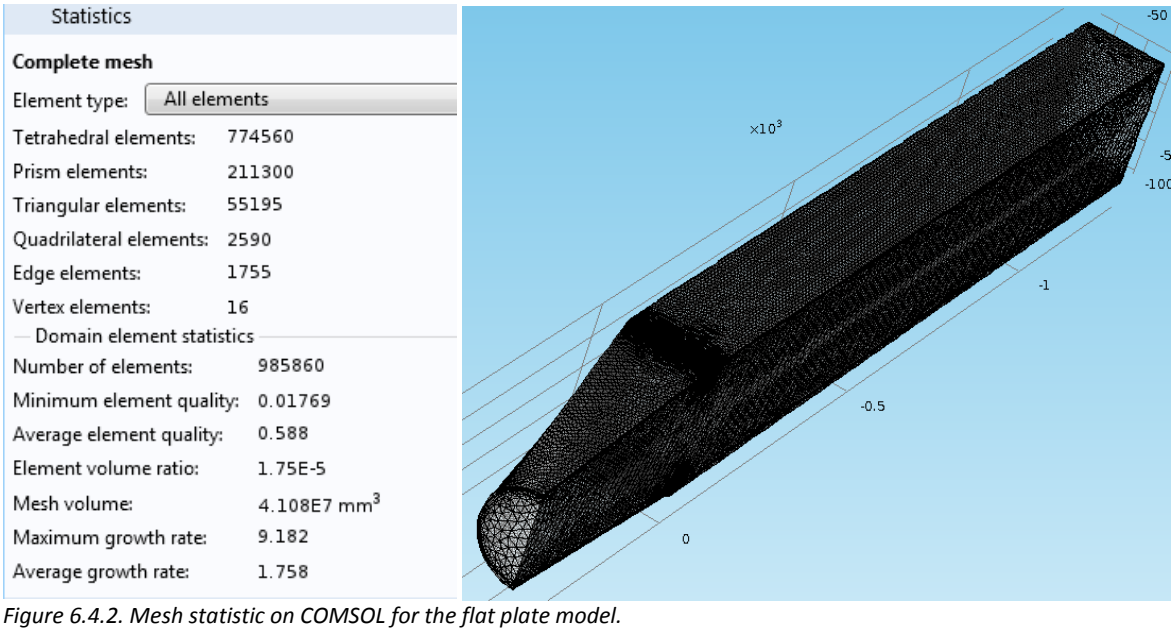

Figure 6.4.2. Mesh statistic on COMSOL for the flat plate model.

Table 6.4.1. Mesh settings for each domain. Note the 1mm minimum element size refinement applies to all domains.

Mesh size settings	**Air domain**	**Pin-fins**	**Base plate**
Max element size (mm)	169	169	169
Min element size (mm)	1	1	1
Max element growth rate	1.5	1.5	1.5
Curvature factor	0.6	0.6	0.6
Resolution of narrow regions	0.5	0.5	0.5

Table 6.4.2. Mesh settings for wall boundary layers.

Boundary layer properties	Value
Number of boundary layers	5
Boundary layer stretching factor	1.2
Thickness of the first layer	Automatic
Thickness adjustment factor	2.5

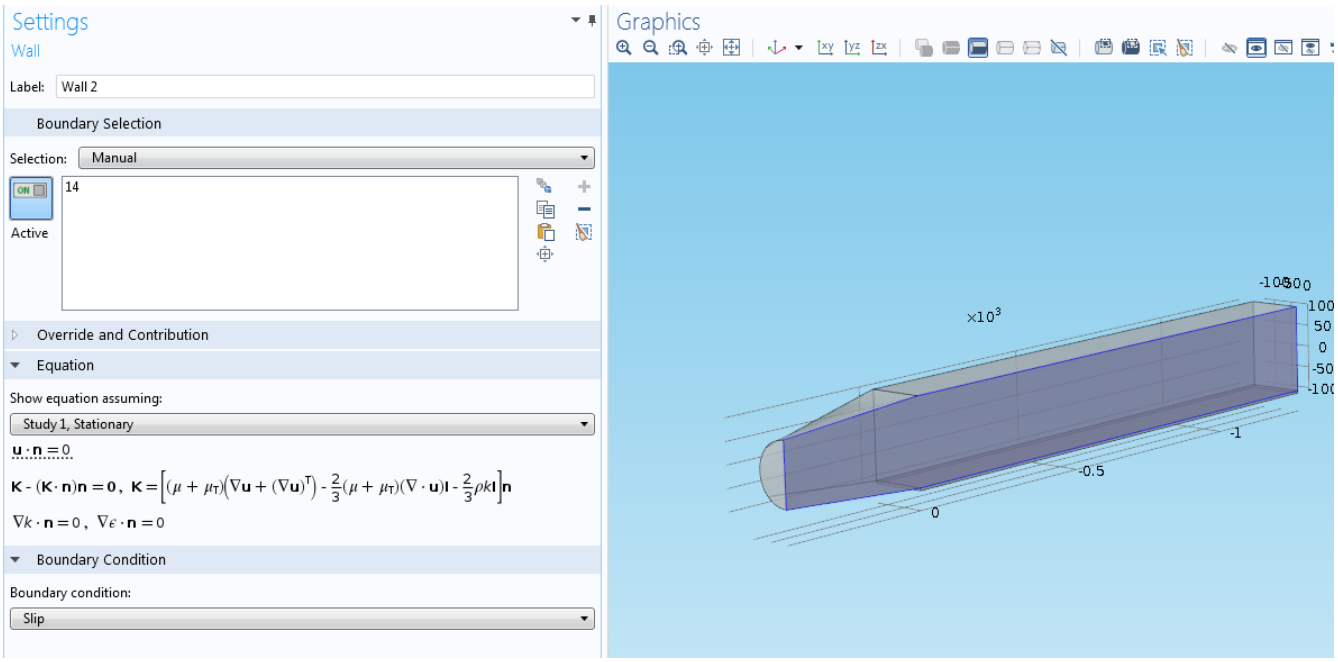

Figure 6.4.3. Slip flow condition applied to the sliced surface.

The temperature profile along the condenser plate was non-uniform, which was the result of factors that cannot be considered in this refined CFD model, such as the swirl intensity at the outlet or heat loss by the rig to the surroundings. If this effect were to be included in the CFD, then the heating plate, heating foil, and heat paste in the contact region and surrounding air would have to be included on COMSOL. Therefore, the temperature profile polynomial was inputted onto the inner condenser surface instead, to represent the result of all these external factors, which are shown in Figs. 6.4.4 and 6.4.5.

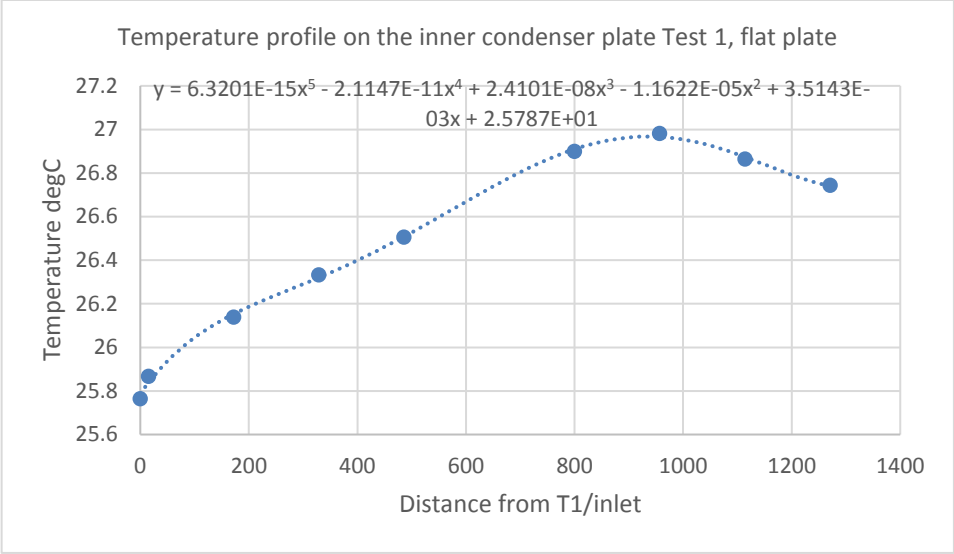

Figure 6.4.4. The temperature profile for the condenser plate in Test 1 with its fifth order polynomial.

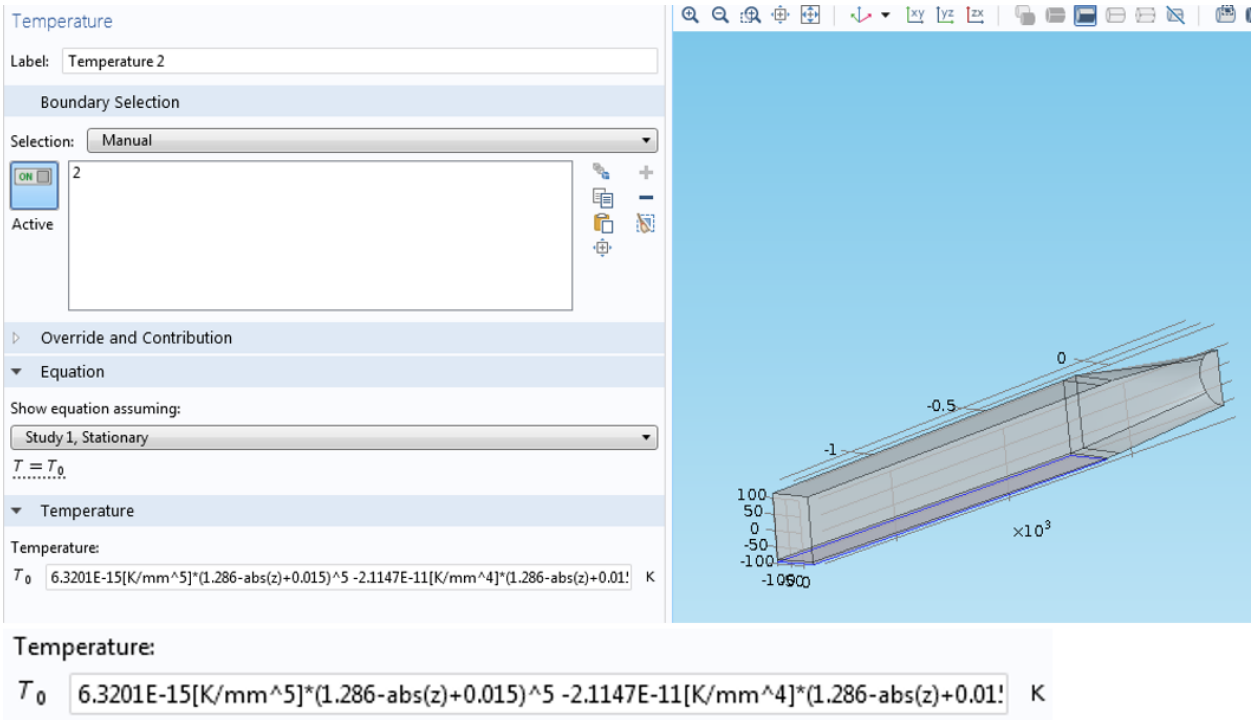

Figure 6.4.5. Inputting the temperature profile onto the inner condenser surface on COMSOL.

Because originally using the default inlet turbulence intensity value of 0.05 gave a heat rejection nearly half that of the experimental value (refer to Fig. 6.7.1), it was not known whether the actual turbulence intensity in the experiment was higher as it was not measured. Therefore, refined CFD models with an inlet turbulence intensity of 0.05 (default), 0.2 and 1 were all computed. From the literature, a turbulence intensity of 0.2 was considered to only occur in a high turbulence application, such as rotating machinery [56], which is comparable to the axial fan used in the experiment. A turbulence intensity of 1 would not be possible unless the flow was unstable, but this model gave an extreme

comparison. For the full result of the refined CFD modelling with different inlet turbulence intensity values, see Section 6.7.

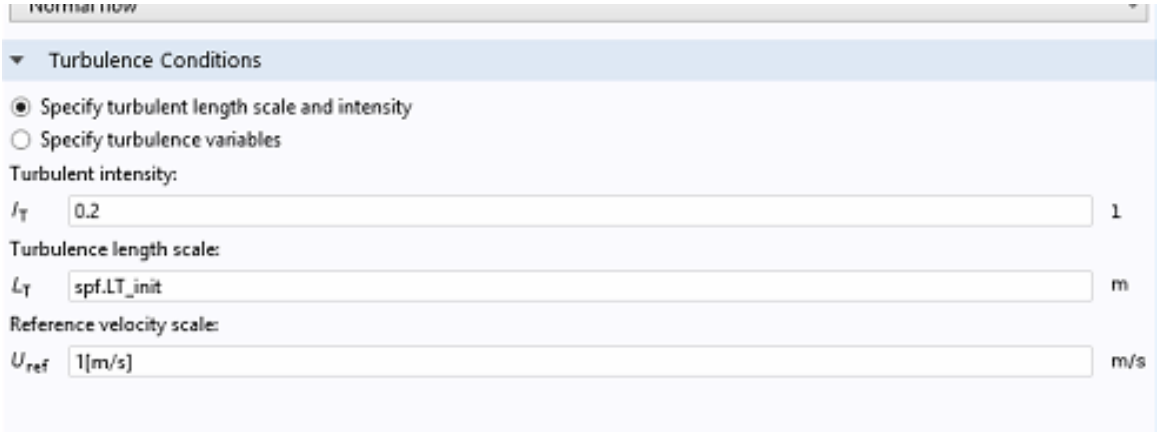

Figure 6.4.6. Inputting inlet turbulence intensity onto the refined CFD model.

6.5 Velocity profile of the rectangular inlet and outlet

The x-directional velocity measurements were taken at the inlet and outlet using the same grid in Fig. 4.6.14. Each measurement was averaged over 30 seconds, as there were fluctuations in the air velocity. This was then compared with the x-direction velocity interrogated from the refined CFD using the same grid. Fig. 6.5.1 shows how the grid in Fig. 4.6.14 was measured, and how the terminology was used in the air velocity plots in Figs. 6.5.2 and 6.5.5.

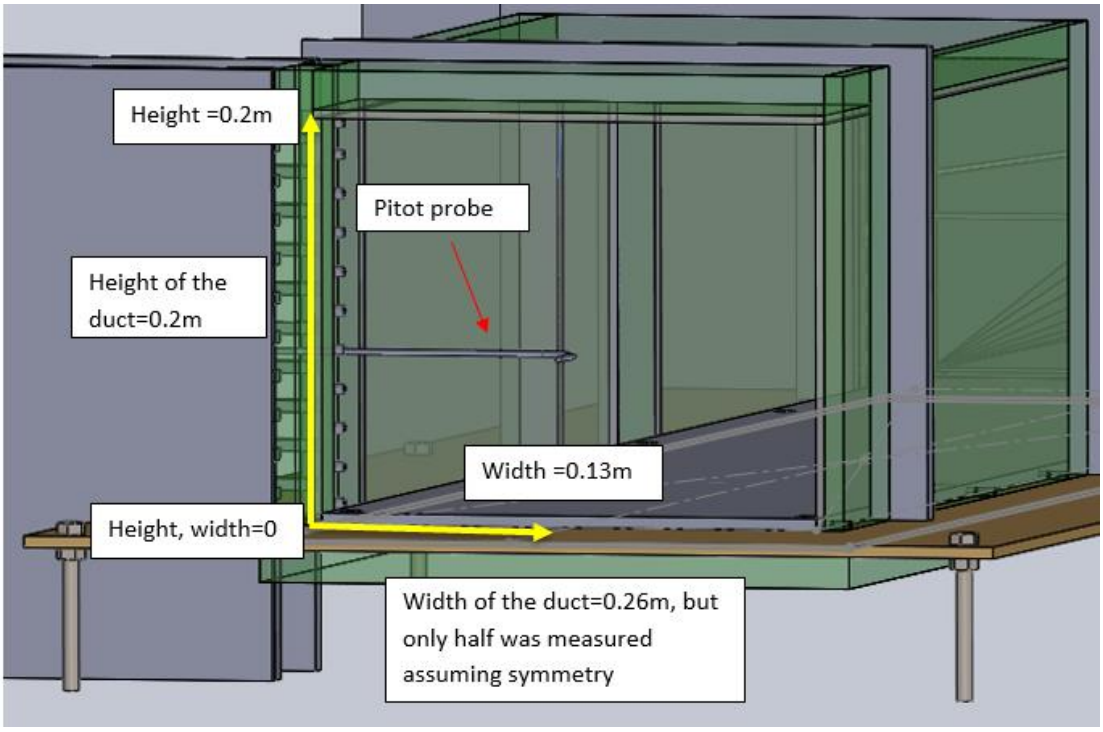

Figure 6.5.1. Description of the duct height and width, corresponding to the air velocity profile plots.

Looking at Fig. 6.5.2, the experimental velocity profile at the inlet was higher at the three edges but lower at the flow centre and the bottom edge. This difference was due to the different flow entry conditions between the experiment and the refined CFD model, which is illustrated in Fig. 6.5.3. In the experiment, the air was allowed to bend around the upper and side walls, which meant the air velocity was higher near those walls. However, at the bottom surface, the air velocity was lower due to the viscous effect from the protruding bottom plate, which can be seen in Fig. 6.5.1. In the refined CFD, the air was only allowed to enter through the rectangular profile and the viscous effect applied to all four sides, creating the parabolic flow profile.

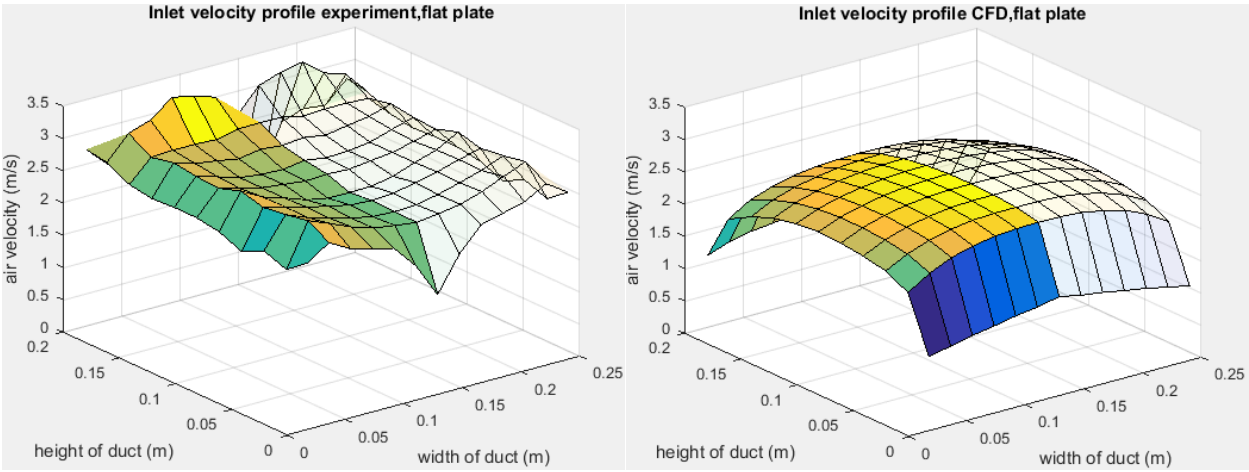

Figure 6.5.2. Experimental and refined CFD inlet air velocity profile; the solid half represents the half that was measured while the other half was mirrored assuming symmetry. Note that air velocities were not measured at the wall, and the refined CFD shows only the same location that was measured in the experiment.

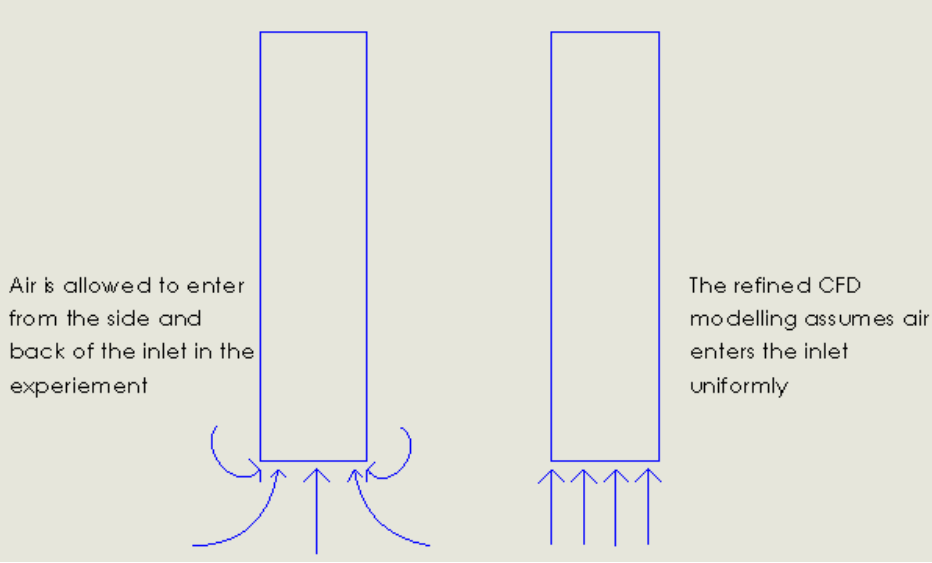

Figure 6.5.3. Top view of the rig, showing the different flow entry behaviour at the inlet, between the experiment (left) and refined CFD (right).

To graphically show the difference between the experiment and the refined CFD air velocity plot, the experimental air velocity profile was subtracted from the refined CFD profile to create an error plot. In

Fig. 6.5.4, the contours showed that there was a larger difference at the edges, which was due to the flow bending around the three walls causing a higher air velocity than what the refined CFD model suggests. At the flow centre, the experimental air velocity was lower, as a higher portion of the flow entered through the side walls, and the fan can only generate the same amount of flow.

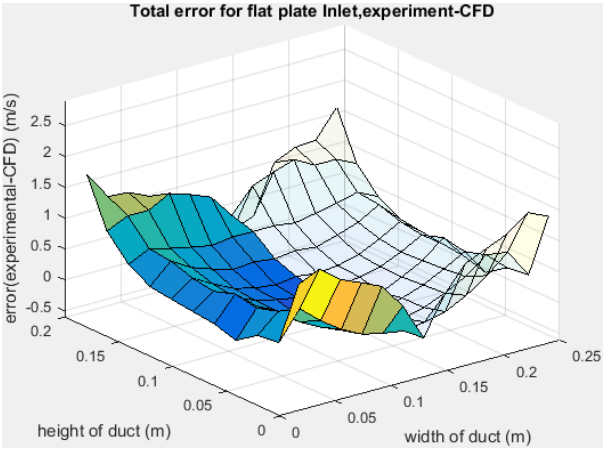

Figure 6.5.4. Total error between the experimental and the refined CFD data for the inlet of the flat plate rig.

At the outlet, the experimental flow profile had transitioned to the parabolic flow profile due to the viscous effect the flow experienced as it travels through the rectangular duct. Due to no measurements taken at the wall surfaces, the boundary viscous effect cannot be captured properly, as shown in Fig. 6.5.5 when the velocity measurements did not reach zero. The closest measurements taken were 1.5mm from the wall, but there were limitations in these measurements as the head of the pitot probe was bent slightly upwards. Therefore, when measuring air velocity at a height of 1.5mm it may have been measuring at 3mm, which meant that the air velocity would be higher. Near the roof of the duct it may have been measuring at 199mm instead of 198.5mm; therefore, the air velocity was lower.

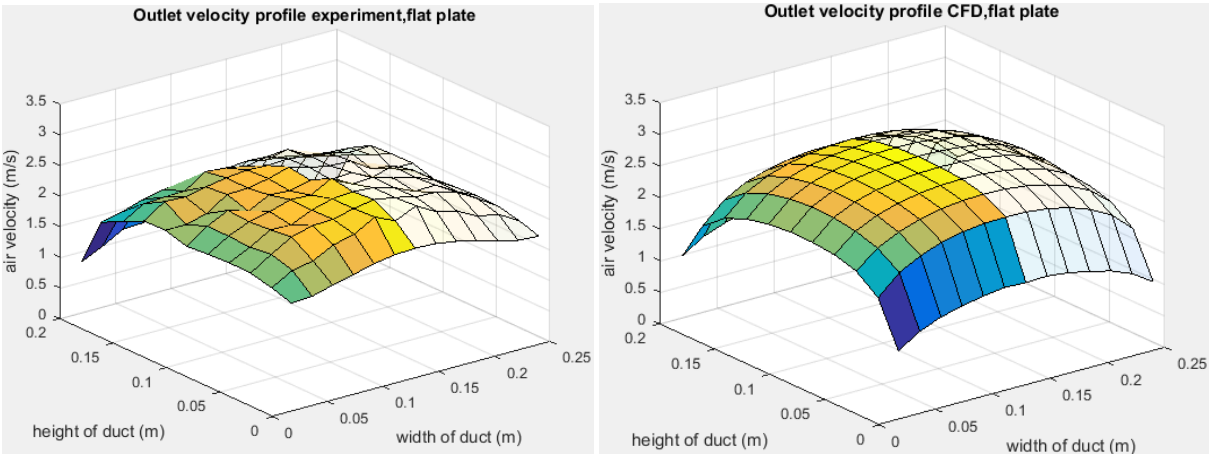

Figure 6.5.5. Experimental and refined CFD outlet air velocity profile; the solid half represents the half that was measured, while the other half was mirrored assuming symmetry. Note that air velocities were not measured at the wall and the refined CFD only shows the same location that was measured in the experiment.

The fluctuation in total error at the outlet, shown in Fig. 6.5.6, was overall less than at the inlet, as the viscous effect from all four wall surfaces was evidential from the experimental measurement. But the error was higher at the bottom of the duct due to the limitations in near wall air velocity measurements. In the experimental profile, the parabolic arcing was less, suggesting that the flow transitioned to the free stream velocity faster than what was predicted by the refined CFD model; thus it was more turbulent.

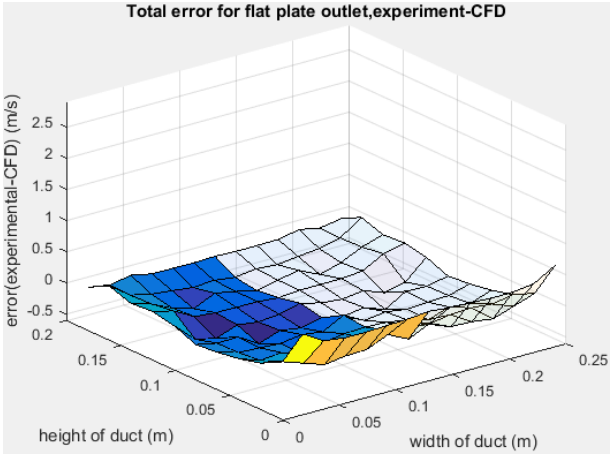

Figure 6.5.6. Total error between the experimental and the refined CFD data for the outlet of the flat plate rig.

The flow rate was then calculated by integrating the air velocity profile plots and summarised in Fig. 6.5.7. It was found that the experimental inlet flow rate was greater than the outlet profile. This problem could be due to other velocity components that were present at the outlet, thus affecting the static pressure port of the pitot tube and making the calculated air velocity to be lower. A better approach would have been to measure static pressure at the sidewall instead.

This meant that the heat rejection using the integral approach described in Section 4.6.14 cannot be calculated, as the inlet and outlet flow rates were different. Therefore, only the heating foil power and refined CFD heat rejection values were used for comparison from this point onwards. The refined CFD inlet and outlet flow rates were similar with small errors due to the coarse grid size used.

	Experiment from grid (m^3/s)	CFD from grid (m^3/s)
Inlet	0.1286	0.1129
Outlet	0.1016	0.1144

Figure 6.5.7. Flow rate obtained from integrating the velocity profile plot. It was found that the experimental outlet flow rate was smaller than the inlet.

6.6 Experimental temperature profile along rectangular cross-sections

As part of the validation between the experiment and refined CFD results, a series of temperature measurements were taken during Test 6. Experimental measurements were taken along the cross-section of the duct according to Fig. 6.6.1, and were repeated for the inlet, outlet and 547mm from the inlet. Refined CFD temperatures were interrogated in the corresponding location and were plotted from Figs. 6.6.2-6.6.6.

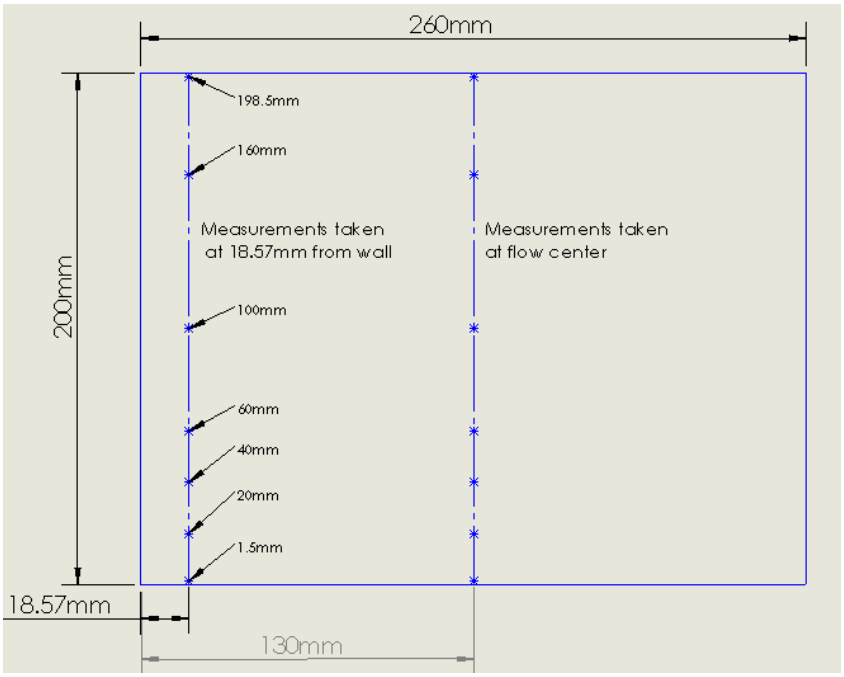

Figure 6.6.1. Measurement points along the cross-section were represented by stars; a series of measurements were taken near the wall (18.57mm) and at the flow centre.

Originally, it was intended that temperature measurements were to be taken corresponding to the entire gird shown in Fig. 4.6.14 to calculate heat rejection using the integral approach. However, this was rejected after discovering that heat rejection could not be calculated, as the flow rate at the inlet and outlet did not balance. Also, it was not feasible, as the ambient temperature would have changed significantly before all 231 measurements were taken. The new aim of the temperature measurements was to quickly validate between the refined CFD results. Therefore, a new measuring grid, illustrated in Fig. 6.6.1, was used. This ends up with 42 measurements in total, with each measurement averaged over 30 seconds.

After data collection, it was found that the ambient temperature did change by 0.4K over the entire data collection process. Therefore, the data was standardised such that the individual air measurements were subtracted from the corresponding ambient temperature at the time of measurement. These temperature difference values would be added to the overall average ambient temperature.

At the inlet, the temperature measurements were taken, as per Fig. 6.6.1. The temperature profile near the wall and at the flow centre were plotted in Fig. 6.6.2. It was found that the inlet temperature was not equal to the ambient temperature. This could be because of the error within the different thermocouples, which were rated at ±0.5K. On average, the experimental values were 0.5K greater than the ambient air. Alternatively, it could suggest pre-heating of the surrounding air; this effect was noticeable for regions closer to the plate (height from plate surface below 0.05m).

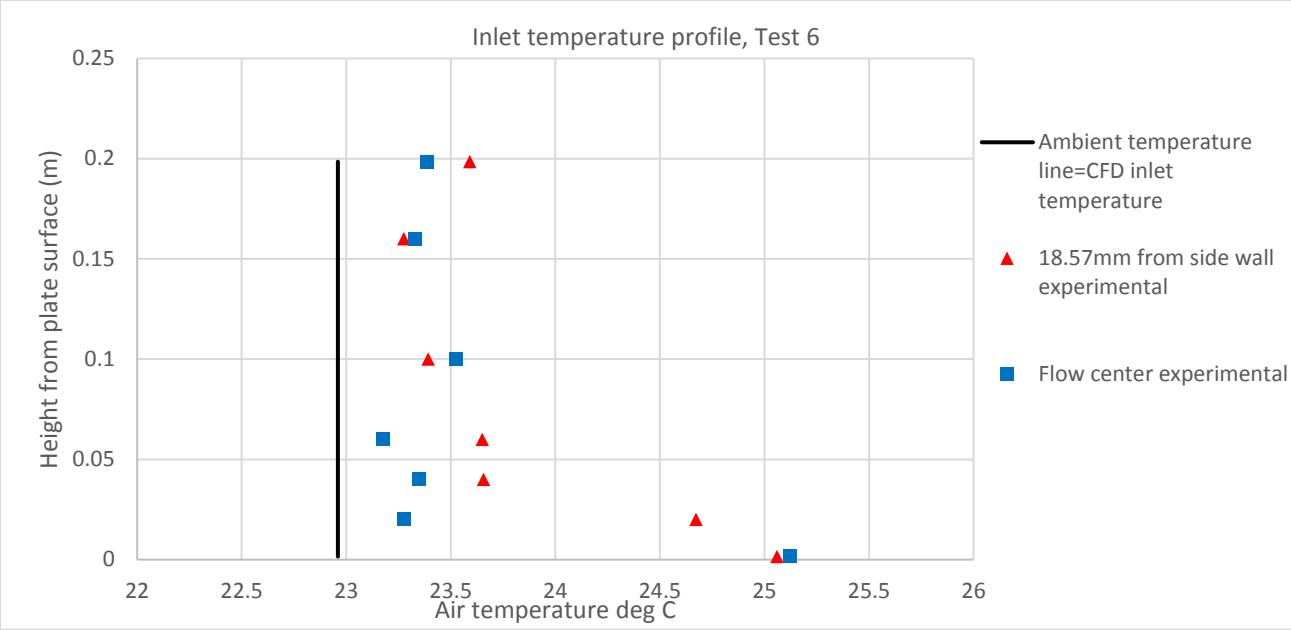

Figure 6.6.2. Temperature profile at the inlet; in the experiment it was found that the inlet air temperature was not equal to the ambient air temperature.

For the temperature profile measured at 547mm from the inlet, 18.57mm from the side wall was plotted in Fig. 6.6.3. It was found that the experiment temperature profiles were hotter than all the refined CFD profiles. As the inlet turbulence intensity increased, this matched more closely the experimental measurements. This suggests that the refined CFD models predict a smaller heat transfer near the side wall, and that the wall viscous effect was not so significant in the experiment.

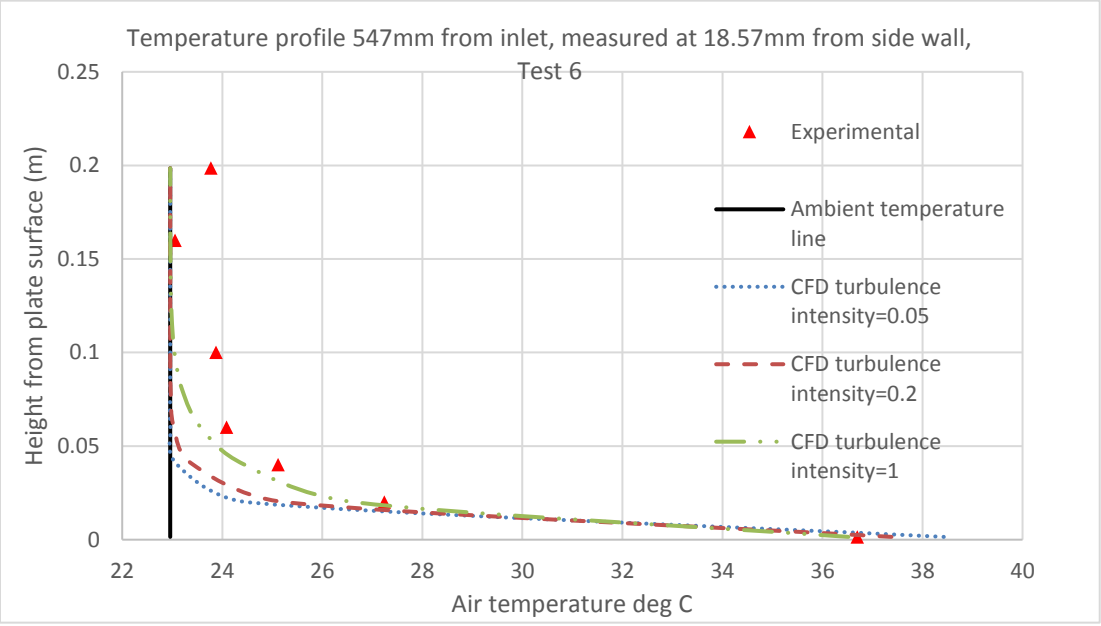

Figure 6.6.3. Temperature profile at 547mm from the inlet, measured 18.57mm from the side wall.

The temperature profile at the flow centre, 547mm from inlet, was plotted in Fig. 6.6.4. All turbulence models predicted a trend that was within the experimental profile from height 20 to 150mm, but it was difficult to determine which inlet turbulence intensity reflected the experimental trend better due to the noise in the experimental data. At a height of 1.5mm, the experimental data showed a cooler temperature than all the refined CFD models. This was due to the flow transitioning to the mainstream velocity faster from the plate surface than what the CFD predicts, as shown in Fig. 6.5.5.

Above 150mm, all the refined CFD profiles predicted the airflow to be at ambient temperature. All experimental temperature profiles shown from Figs. 6.6.2-6.6.6, found that the temperature at the roof (198.5mm) was always slightly hotter than the 160mm measurement. This could be due to the roof material emitting some of the heat it had absorbed from its contact with the heating plate, despite the material of the roof/main duct being Perspex, which was meant to have a low thermal conductivity.

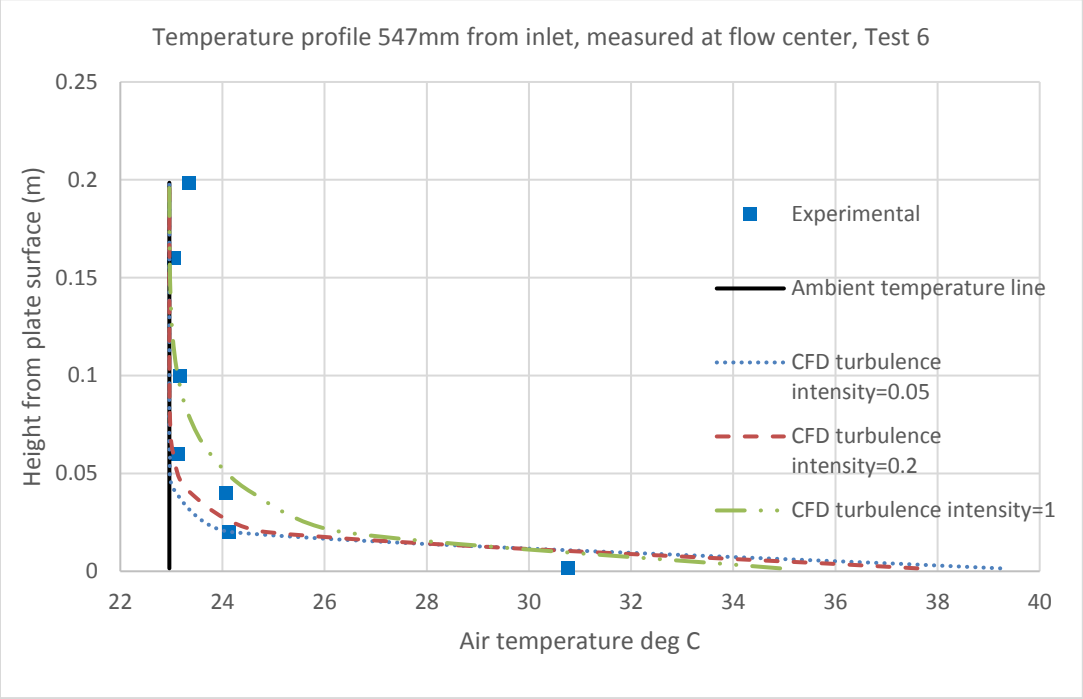

Figure 6.6.4. Temperature profile at 547mm from the inlet, measured at the flow centre.

At the outlet, a similar situation occurred that the temperature profile at 18.57mm from the side wall did not match. In Fig. 6.6.5, the experimental profile was shown to be hotter than all the refined CFD profiles except at a height of 1.5mm. This was due to the airflow transitioning to the free stream faster in the experiment than what the refined CFD model predicts, resulting in the air being more evenly mixed. At the flow centre of the outlet, shown in Fig. 6.6.6, the same fluctuation occurred at the 2nd and 3rd experimental temperature points from the plate surface similar to Fig. 6.6.4. This again made determining which inlet turbulence intensity best reflected on the actual situation difficult, as different inlet turbulence intensities fitted the experimental profile better depending on whether it was fitting through the 2nd or the 3rd experimental data point.

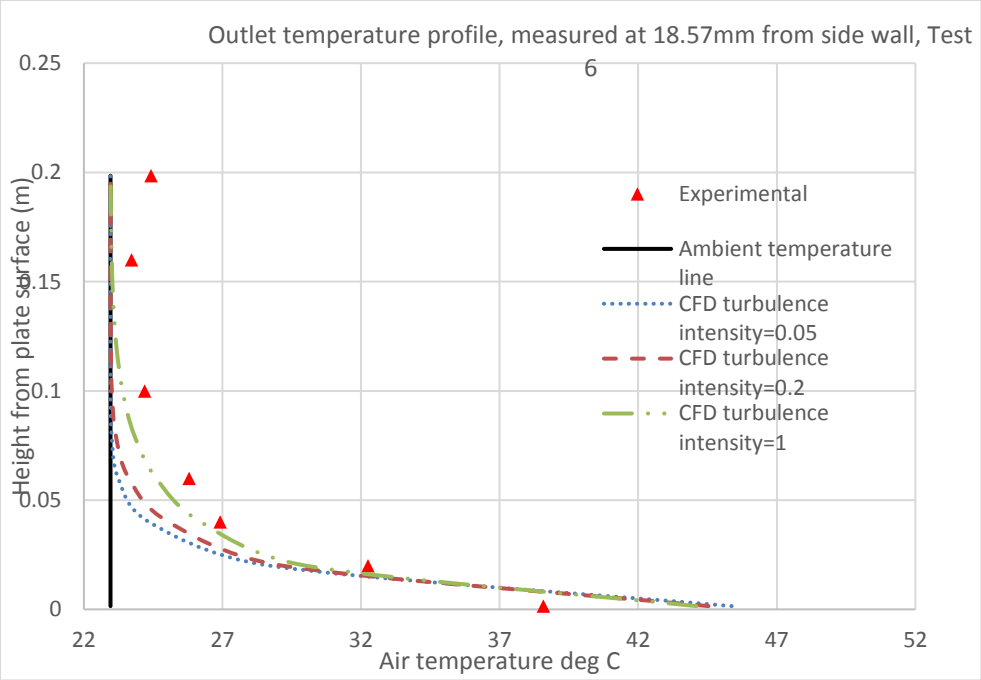

Figure 6.6.5. Temperature profile at the outlet, measured at 18.57mm from the side wall.

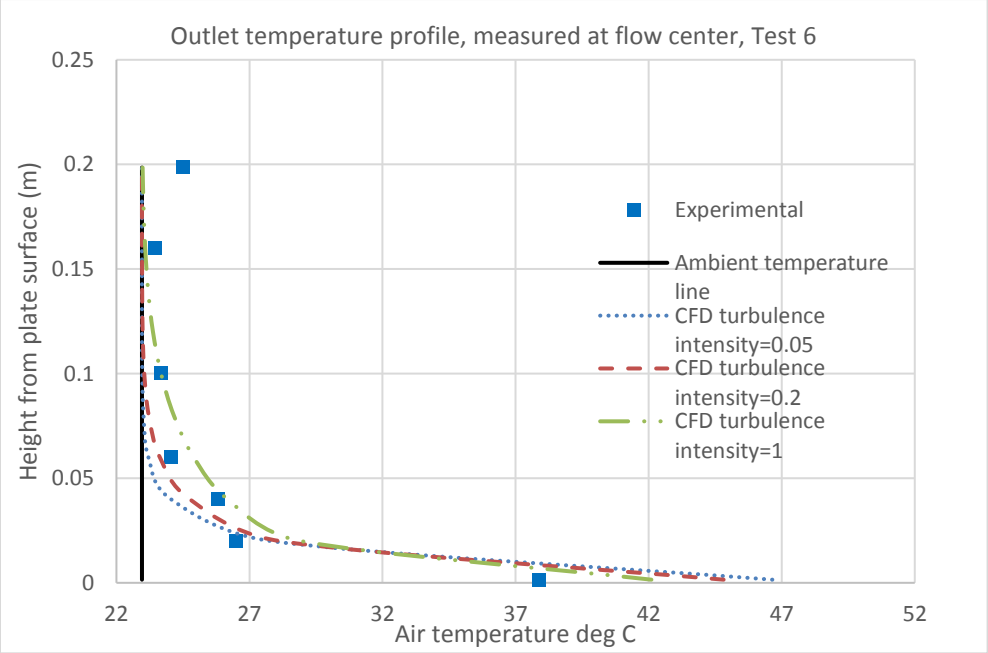

Figure 6.6.6. Temperature profile at the outlet, measured at the flow centre.

From evaluating between Figs. 6.6.4 and 6.6.6, it seems that an inlet turbulence intensity of 0.2 was the most conservative, but none of the inlet turbulence intensity values managed to fit in Figs. 6.6.3 and 6.6.5. This suggests the inlet turbulence intensity alone was not enough to account for the difference in heat rejection shown in Fig. 6.7.1. Other factors such as the swirl of the fan, and whether the extraction pressure across the rectangular duct was even due to the fan being circular was not considered in the refined CFD model.

6.7 Effects of turbulence intensity in the refined CFD

Due to the disagreement between the first set of refined CFD results using the default inlet turbulence intensity value of 0.05 and the experimental data, other inlet turbulence intensity values of 0.2 and 1 were also modelled to determine whether this would increase the amount of heat rejection. The heating foil power plot from Fig. 6.1.2 was compared with the heat rejection plot with different inlet turbulence intensities corresponding to the same experimental condition (ambient temperature and inner condenser temperature). All refined CFD results and the heating foil power are shown in Fig. 6.7.1 below.

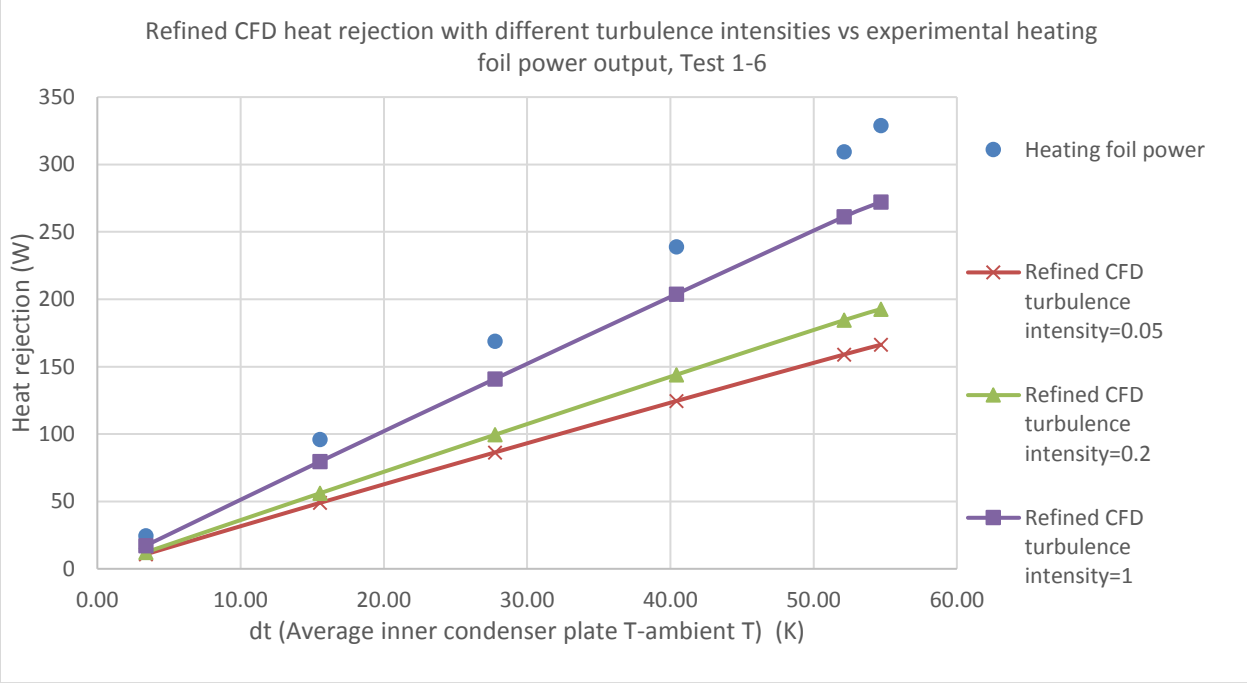

Figure 6.7.1. Experimental heating foil power vs CFD heat rejection for the same conditions (ambient temperature and inner condenser temperature), assuming all the heat to the heating foil is being rejected by the airflow.

To evaluate the heat rejection per volume of aluminium used, the linear trend line constants were obtained, shown in Table 6.7.1. Because the trend lines are linear, the heat rejection per volume of aluminium also increases linearly with temperature difference, therefore the unit can be converted to ($kW/(m^3K)$). This result is compared with Section 4.5.3 using Gorrie's experimental condition of ambient temperature=18.33°C, inner condenser temperature=29.81°C, which gave a result of 39.46W and $20.14kW.m^{-3}$. This compared well with the refined CFD value for inlet turbulence intensity of 0.2 in Table 6.7.1, with the interpolated value of $20.69kW.m^{-3}$. However, in Section 4.5.3 the transitional duct was not modelled, and the coarser mesh setting was used instead of the normal setting in this refined CFD study. This showed that despite these modelling differences, the CFD results were predicting relatively close to each other, except for extremely high inlet turbulence intensity values past 0.2. A turbulence intensity of 1 is an extreme case and should not reflect the experimental flow conditions.

At the highest level of inlet turbulence intensity of 1, the heat rejection value still did not match the experimental values. This suggests that there could either be heat loss in the rig that was not taken account of, as the experimental data only measures electrical power going into the heating foil. Also, it could be due to the underlying flow mechanisms that was not understood, as the flow was not visualised, which meant that the flow could be swirling or distributed in a way that leads to more heat being rejected. The inlet and outlet velocity profile was shown in Section 6.5, but it was only a time average representation of the flow, which cannot give information as to its dynamic behaviour.

Table 6.7.1. Deriving the heat rejection per volume of aluminium per temperature difference (average inner condenser plate temperature-ambient temperature).

	Gradient (W/K)	Constant (W)	Heat rejection under Test 17 condition of A. Gorrie (W)	Heat rejection per volume under Test 17 condition of A. Gorrie ($kW.m^{-3}$)	Heat rejection per volume per temperature ($kW.m^{-3}.K^{-1}$)
Refined CFD turbulence intensity=0.05	3.03	1.49	18.06 (interpolated)	18.06 (interpolated)	1.51
Refined CFD turbulence intensity=0.2	3.52	1.11	41.51 (interpolated)	20.69 (interpolated)	1.75
Refined CFD turbulence intensity=1	4.97	1.72	58.82 (interpolated)	29.32 (interpolated)	2.48
experimental heating foil	5.88	4.51	71.98 (interpolated)	35.88 (interpolated)	2.93

6.8 Flat plate heat transfer empirical correlation

Because there is uncertainty between the refined CFD and experimental results, and the heat rejection could not be determined from the airflow, there was a need to check with the empirical correlation in the literature. Section 2.12.6 mentioned a flat plate Nusslet correlation, which can be used to calculate convective heat transfer assuming heat transfer for a flat plate in an open space is similar to a ducted flat plate. Test 6 of the flat plate experiment would be used as the example input condition shown in Fig. 6.8.1. Because the outer condenser surface was not measured in the experiment, the value was interrogated from Test 6 of the refined CFD file instead.

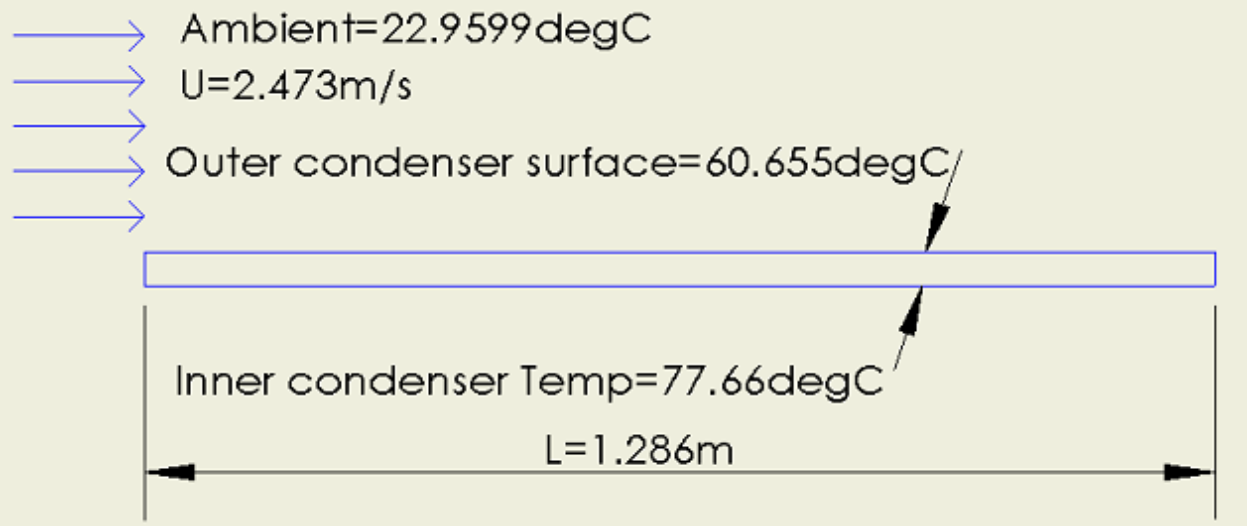

Figure 6.8.1. Determining the airflow heat rejection in Test 6, using the empirical correlation for an open flat plate.

Following workings in example 9.2 of [38] and assuming isothermal plate:

Film temperature of the air at the plate=(22.9599+60.655)/2=41.80°C

Air properties at 25.89°C: $\mu_{air} = 1.9154 \times 10^{-5} kg.(ms)^{-1}$, $\rho_{air} = 1.12255 kg.m^{-3}$, $Pr = 0.7034$, $k = 0.027389 W.(m.K)^{-1}$

Checking the Reynolds number:

$$Re_x = \frac{\rho_{air} x U_{max}}{\mu_{air}} = \frac{1.122558 kg.m^{-3} \times 1.286m \times 2.473 m.s^{-1}}{1.9154 \times 10^{-5} kg.(ms)^{-1}} = 1.86385 \times 10^5$$

Because this flow is considered laminar for an open flat plate, the following correlation is used:

$$\overline{Nu_L} = 0.664 {Re_x}^{0.5} Pr^{1/3} for\ isothermal\ plate\ and\ Re_x < 5 \times 10^5$$

$$\overline{Nu_L} = 254.94$$

$$\bar{h} = \frac{\overline{Nu_L} k}{L} = \frac{254.94 \times 0.027389 W.(m.K)^{-1}}{1.286m} = 5.4297 W.(m^2.K)^{-1}$$

$$q = \bar{h} A (T_{outer\ condenser} - T_{ambient})$$
$$= 5.4297 W.(m^2.K)^{-1} \times 1.286m \times 0.26m \times (60.655 - 22.9599)K = 68.434W$$

Comparing the refined CFD value at turbulence intensity of 0.05 and the experimental heat rejection value, which were 166.25W and 329W, the value from the empirical correlation was 100W lower than the refined CFD value at Test 6. Even if it is assumed that the outer condenser temperature was equal to the inner condenser of 77.66°C, this value would be 99.3W which is still short of the 166.25W from the refined CFD value. As to the reason this empirical result was lower than the refined CFD, this could be due to the critical Reynolds number; for a pipe or ducted flow, this is 2300, whereas for a flat plate in

open space this is 5×10^5. Because the critical Reynolds number for flat plate in open space is larger, it is harder for turbulent eddies to form, thus less heat transfers. This suggests that the assumption that flat plate heat transfer in an open space is similar to a ducted flat plate was not valid; therefore, it could not be proved whether the experimental or the refined CFD result at Test 6 was closer to the realistic value.

6.9 Flat plate summary

Through experimentation, it was found that there is always a linear correlation between heat rejection and *dt* (condenser temperature-ambient air temperature), but the refined CFD modelling has underestimated the heat rejection for a flat plate condenser by a factor of 2 (1.51 as to 2.93 $kW.m^{-3}.K^{-1}$). A study in Section 6.5 showed that the heat was mixed more evenly near the side wall in the experiment than what was predicted in the refined CFD model. Flow profiles at the inlet between the refined CFD model and experiment did not match due to the assumptions made regarding uniform inlet airflow when setting up the refined CFD model, as described in Section 6.5. At the outlet, the flow profiles were better matched, but the viscous effect was less obvious in the experimental profile. The overall flow rate calculated for the experimental inlet and outlet did not match, this could be due to the incorrect approach in measuring the static pressure by the pitot tube. As a result, it was not possible to calculate the experimental heat rejection using the method that was proposed in Section 4.6.4 regarding "Measuring heat rejection using the airflow".

After varying the turbulence intensity value in Section 6.7, it was found that turbulence intensity alone was not enough to account for this difference in heat rejection and there are some underlying flow mechanisms causing a higher amount of heat rejection from the condenser plate. Because the experiment was measuring electrical heating foil power, it was not known whether the losses as the heat gets transferred from the foil to the condenser. Literature correlation was used to calculate the heat rejection by a flat plate in an attempt to validate either the refined CFD or the experiment results, however there was also limitation in the correlation itself, as it was only applicable for an open flat plate and not ducted. Therefore, it could not be determined whether the refined CFD or the experimental result was closer to the ideal scenario (no heat loss and uniform flow).

In summary, heat rejection of the flat plate cannot be accurately due to complication in studying the flow mechanisms. It was assumed that the flow would be more predictable in the pin-fin study to come due to the flow straightening properties the fins would provide. Section 7 found that the difference between experiment and refined CFD heat rejection was significantly less at 25.6%, as the flow being was more confined to travel in a straight path by the presence of pins.

7 Results for Pin-fin condenser

7.1 Heating foil power output

Five experimental runs with different ambient and inner condenser plate temperatures were conducted with the same procedures described in Section 6.1. The refined CFD runs for the pin-fin model were conducted using the standard turbulence intensity=0.05, as it was found that turbulence intensity alone was inconclusive to account for the disagreement in heat rejection for the flat plate study.

More setups will be discussed in Section 7.2. From over plotting the experimental and refined CFD results in Fig. 7.1.2, it can be seen that the experimental heat rejection also follows a linear correlation. However, for the refined CFD, there were two outliers and it was uncertain whether Tests 2 and 3 or Tests 4 and 5 were the outlying pair (see Fig. 7.1.2). If Tests 2 and 3 were the outlying pair that would mean that the refined CFD predicts a heat rejection profile similar to the experimental data. If Tests 4 and 5 were the outlying pair then the refined CFD would predict a smaller heat rejection gradient, similar to the situation for the refined CFD in the flat plate analysis. Further analysis was done in Section 7.3 to determine which pairs were the outliers.

	Average ambient T (degC)	Average inner condenser (degC)	Condenser-Ambient (degC)	Measured heating foil power (W)	CFD
Test 1	19.88	24.36	4.48	121.00	93.37
Test 2	20.16	29.00	8.84	236.40	176.38
Test 3	20.08	33.70	13.62	358.80	247.48
Test 4	20.21	38.40	18.18	476.20	448.15
Test 5	16.31	41.52	25.22	657.40	678.60

Figure 7.1.1. Experimental and refined CFD summary of the pin-fin condenser. Results were plotted in Fig. 7.1.2.

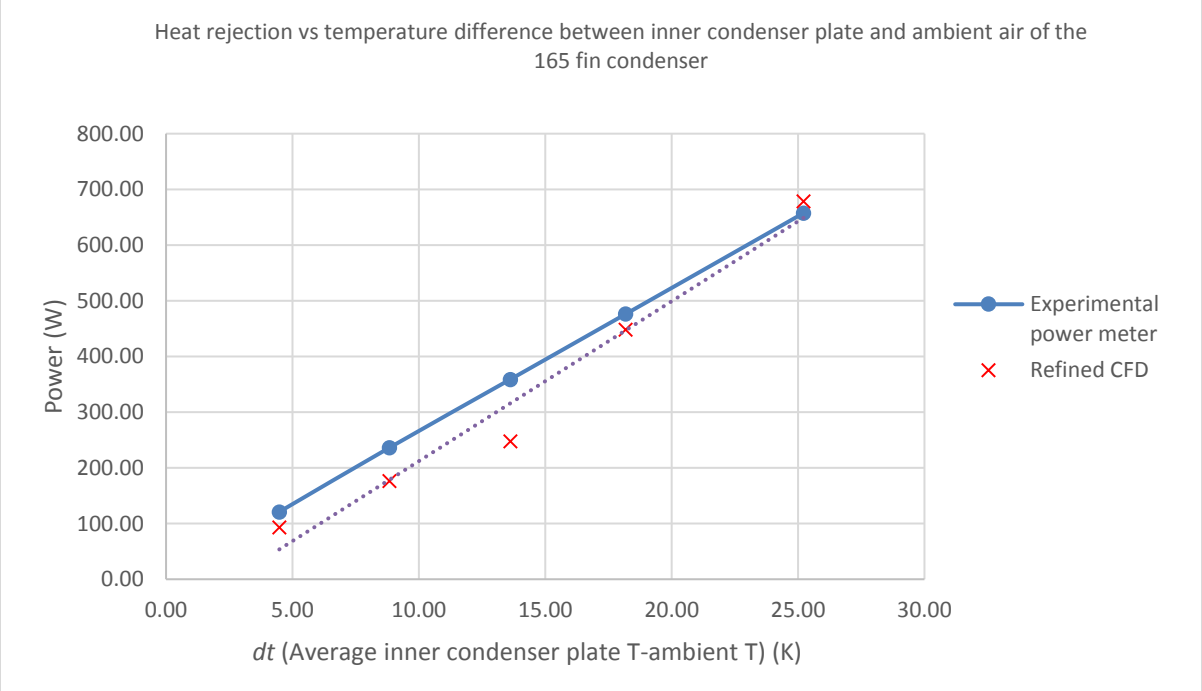

Figure 7.1.2. Experimental and refined CFD heating foil power/heat rejection plot.

A summary table of different heat rejection quantities of the pin-fin condenser was added in Table 7.1.1. It contains results that were mentioned in later chapters of Section 7 with the different CFD studies.

Table 7.1.1. Summary of the heat rejection per volume and per temperature values for the pin-fin condenser.

	Gradient (W/K)	Constant (W)	Heat rejection under Test 17 condition of A. Gorrie (W)	Heat rejection per volume under Test 17 condition of A. Gorrie ($kW.m^{-3}$)	Heat rejection per volume per temperature ($kW.m^{-3}.K^{-1}$)
Table 4.5.3 simplified	_____	_____	338.94	66.46	5.79
Experimental	25.83	6.66	303.14	69.76 (interpolated)	5.94
Refined CFD Test 1-5	28.70	-74.96	254.54	58.58 (interpolated)	6.61
Refined CFD Test 1-3 + 2 auxiliary points	19.22	0.812	221.4	50.95 (interpolated)	4.42
Simplified model, section 7.7, Fig. 7.7.1	29.14	-11.08	323.47	74.44 (interpolated)	6.71

7.2 Temperature profile of the inner condenser plate

Temperature measurements were collected in the same locations from the inlet as in Section 6.2 and also illustrated in Fig. 7.2.2, but the temperature profiles had a more dynamic characteristic due to heat rejection concentrated near the pins. Also, there are other interactions, such as the air getting hotter as it travels further into the pins. Therefore, the current plot in Fig. 7.2.1 does not have enough resolution to capture all the fluctuations due to the thermocouple locations of T1-T9, which were not situated equally away from the closest pin, as shown in Fig. 7.2.2. However, this was enough to determine the average plate temperature with reasonable accuracy for the refined CFD modelling. The general characteristic is that the temperature gets hotter as it gets further down the condenser, and unlike the flat plate condenser, the inner condenser temperature did not drop after T7. This was because, despite the presence of a swirl near the outlet, the air was hot enough that the swirl made little difference for a cooling effect on the condenser plate.

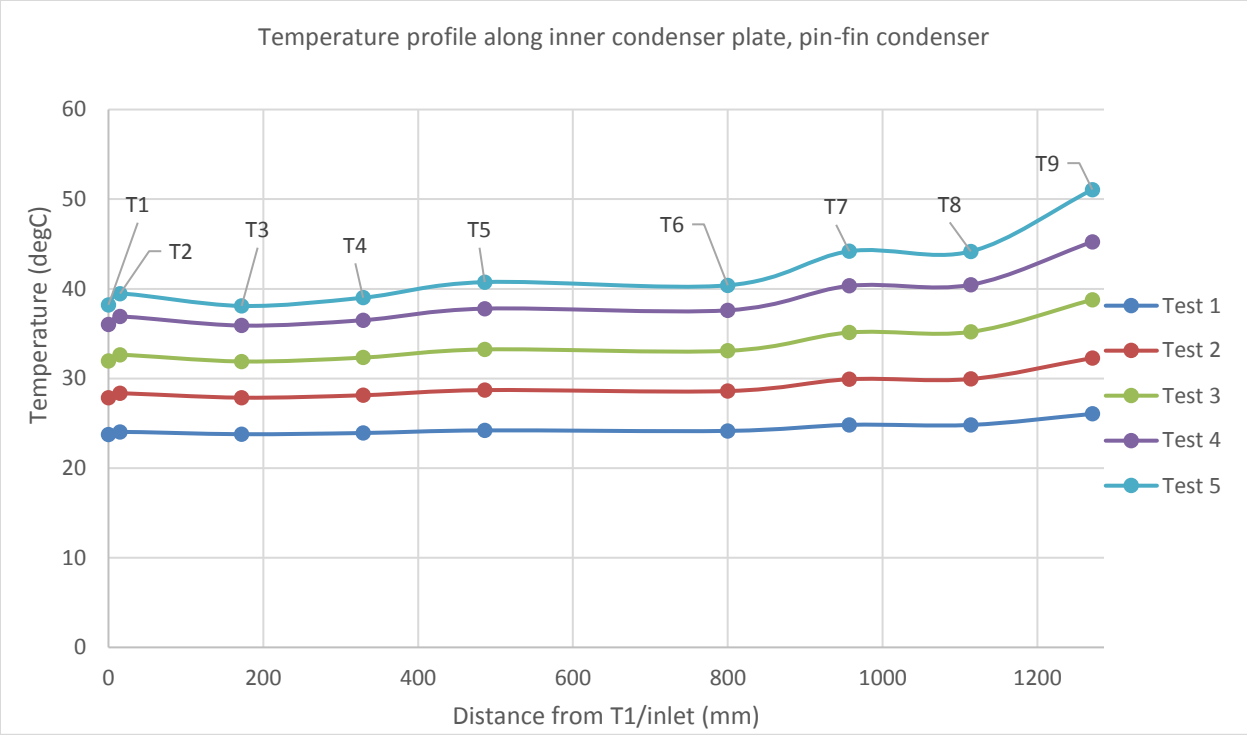

Figure 7.2.1. Experimental temperature profile along inner condenser surface for Test 1-5.

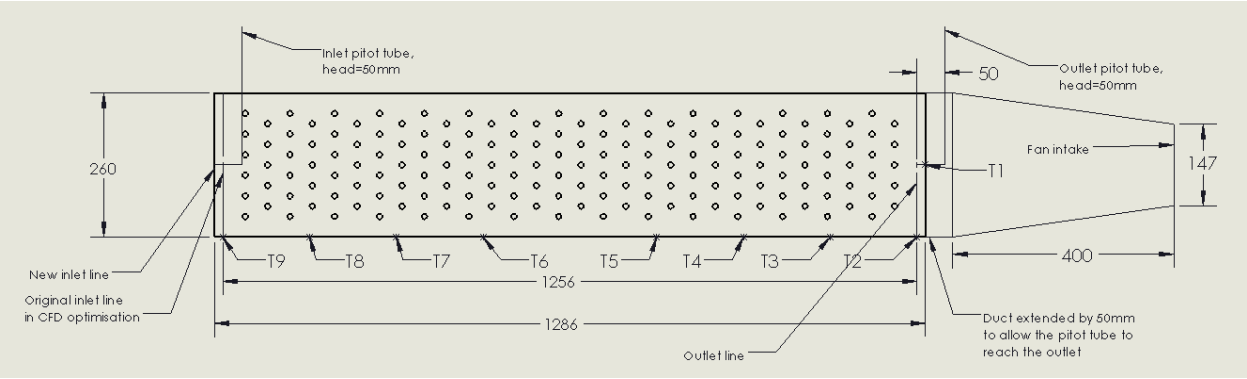

Figure 7.2.2. Thermocouple locations in relation to the pins.

7.3 Refined CFD setup for the pin-fin condenser

A refined CFD model was also built to replicate the geometry of the pin-fin rig used in the experiment, as well as the external conditions experienced on each experimental run. This was then compared with the experimental data, as shown in Fig. 7.1.2. The purpose of this was also to determine whether the refined CFD model was sufficient in predicting the experimental heat rejection, so that in the future, CFD can be used to predict heat rejection without the need for experimentation.

The coarse mesh setting on COMSOL was used, with the setting shown in Tables 7.3.1 and 7.3.2. This resulted in the meshed geometry in Fig. 7.3.1, containing 8.6 million elements and a computing time of three days, 56GB of ram for each run. Five CFD runs were required in total to compare the corresponding experimental runs.

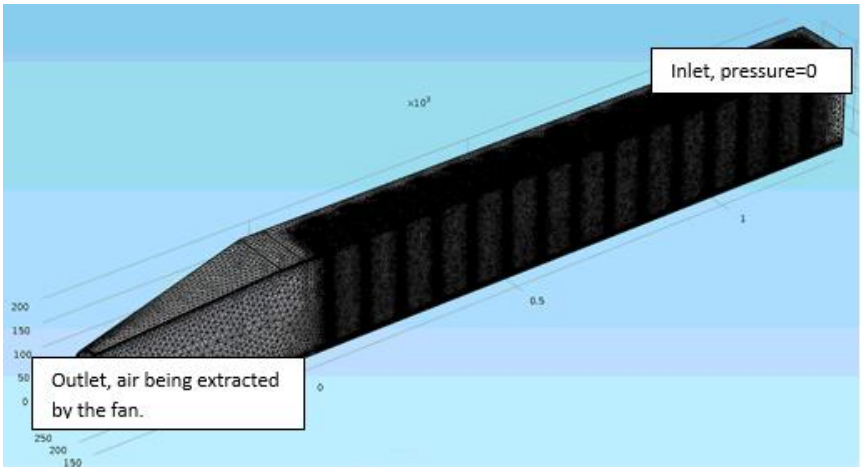

Figure 7.3.1. Meshed pin-fin condenser model for the refined CFD analysis.

Table 7.3.1. Mesh settings for the refined CFD model in each domain. Note the 1mm minimum element size refinement applies to all domains.

Mesh size settings	**Air domain**	**Pin-fins**	**Base plate**
Max element size (mm)	175	175	175
Min element size (mm)	1	1	1
Max element growth rate	1.5	1.5	1.5
Curvature factor	0.6	0.6	0.6
Resolution of narrow regions	0.5	0.5	0.5

Table 7.3.2. Mesh settings for wall boundary layers in the refined CFD model.

Boundary layer properties	Value
Number of boundary layers	5
Boundary layer stretching factor	1.2
Thickness of the first layer	Automatic
Thickness adjustment factor	2.5

The inner condenser temperature profiles in Fig. 7.2.1 were all correlated with a 2nd-degree polynomial; an example of such is shown in Fig. 7.3.2 and inputted on to COMSOL using the same method in Fig. 6.4.5. It was unnecessary to use a 6th-degree polynomial as in Section 6.4 for the flat plate, because it does not have enough resolution to capture the exact trend, as discussed in Section 7.2. The modelling approach was similar to the flat plate in Section 6.4, but there was increased computational complexity of the flow and thus a higher computational time.

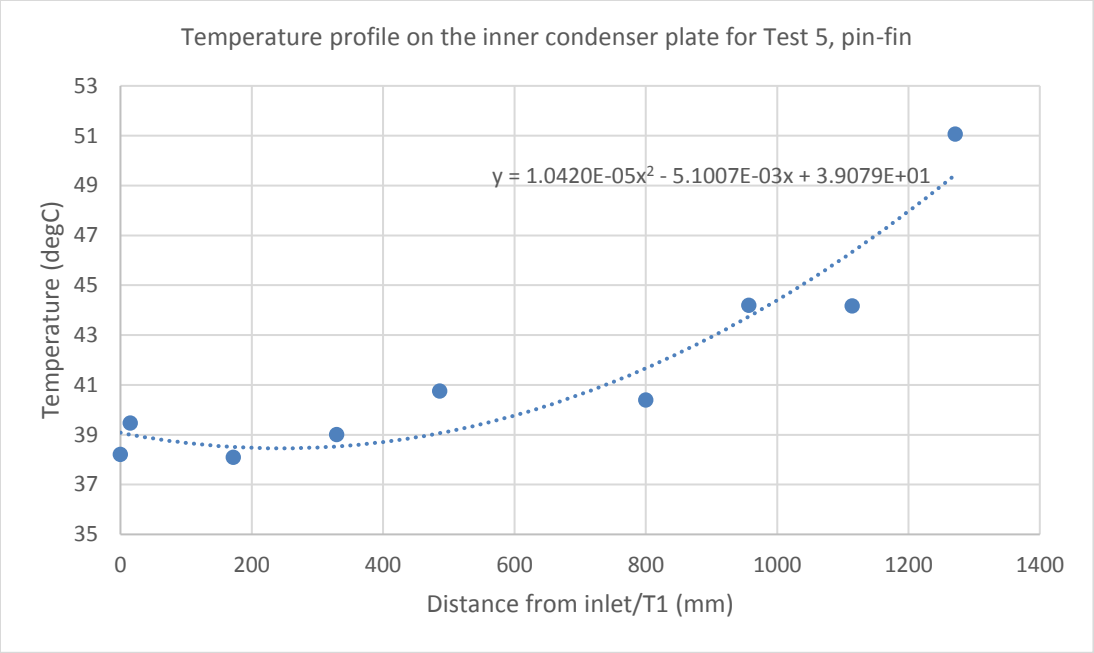

Figure 7.3.2. Characteristic polynomial of the inner condenser plate in Test 5, pin-fin condenser.

To determine the outlying pair in the refined CFD study in Fig. 7.1.2, two additional auxiliary points were modelled at *dt*=17 and 23K using the same refined CFD model. The inner condenser temperature and ambient temperature of these auxiliary points were not based on any experimental runs, so the ambient temperature was assigned to be the same as Test 3, and the inner condenser temperatures were 17K and 23K greater than the ambient temperature.

Looking at Fig. 7.3.3, the auxiliary study showed that Tests 4 and 5 were the outliers and that the refined CFD model should predict a lower heat rejection than the experiment. This was the same situation as in the flat plate experiment, where the refined CFD model predicts only a half of the experimental heat rejection. In the case of the pin-fin, looking at Fig. 7.3.3, the difference is less than 25.6% of the experimental heat rejection, assuming that Tests 4 and 5 were the outliers.

Some reasons why the refined CFD model predicts a lower heat rejection value than the experimental data:

1. In the experimental data, the heating foil power was assumed to be fully rejected by the airflow, not accounting for any losses on the way to the condenser plate.
2. Section 7.5 shows that the air was more thermally mixed in the experiment than what the refined CFD model predicts, particularly in the near wall region (see Figs. 7.5.2 and 7.5.4). This resulted in more heat being rejected. Section 6.7 discussed the possibility of unknown flow dynamics that might have caused more heat in being rejected; this may also apply to the pin-fin condenser.

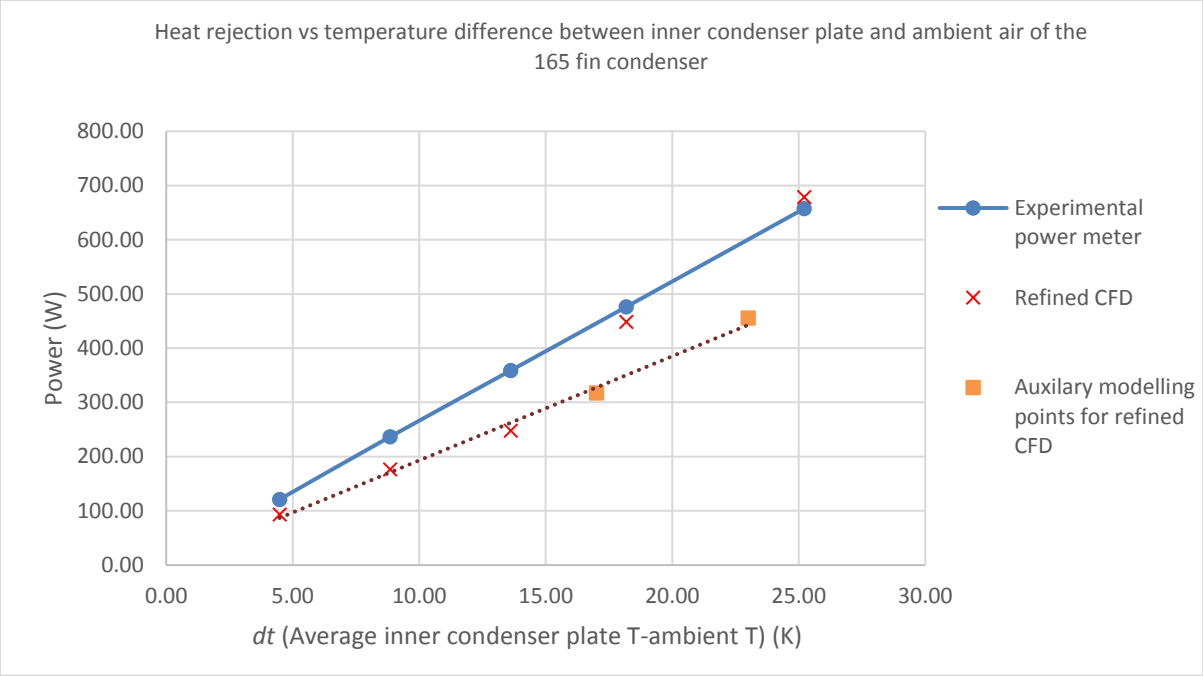

Figure 7.3.3. Overplotting the two auxiliary points with dt=17 and 23K to determine the outliers from the refined CFD study.

The error for these two outliers could also be due to how the heat rejection was calculated on COMSOL. To interrogate for the heat rejection from the COMSOL file, the surface integral energy sums were determined at the inlet and outlet, and then subtracted using the approach from Section 4.2.1:

$$\dot{Q} = C_p \left(\sum_{0}^{mesh_{i=n1}} \rho_{i\ outlet} v_{i\ outlet} T_{i\ outlet}\ A_{i\ mesh} - \sum_{0}^{mesh_{i=n2}} \rho_{i\ inlet} v_{i\ inlet} T_{i\ inlet}\ A_{i\ mesh} \right) (W)$$

For example, in Test 5 of the refined CFD model, for the pin-fin condenser, the inlet and outlet sum were 19434.4 and 19773.7W. To give the heat rejection, the outlet sum was subtracted from the inlet sum, which gave 339.3W. Then this was multiplied by 2 because the refined CFD model only models half of the rig, which gave 678.6W.

The problem with this is that when the two large sums are subtracted to give a small product (heat rejection), any precision error in the large sums will affect the product significantly. Because the product was only 339.3/19773.7=1.7% relative to the outlet sum, and due to the more complex nature of the flow compared to the flat plate study, it is easy for errors to be propagated.

Another issue was the four inverted elements found on the refined CFD model, which caused the minimum element quality to be negative as shown in Fig. 7.3.4. An inverted element occurs when the element is skewed to a point where it becomes an hourglass shape, as shown in Fig.7.3.5. This may have contributed to the outliers in Tests 4 and 5; looking at Fig. 7.3.3, Tests 1 to 3 of the refined CFD run and the two auxiliary modelling points do not form a perfectly straight line, suggesting the inverted elements may have affected all the CFD results.

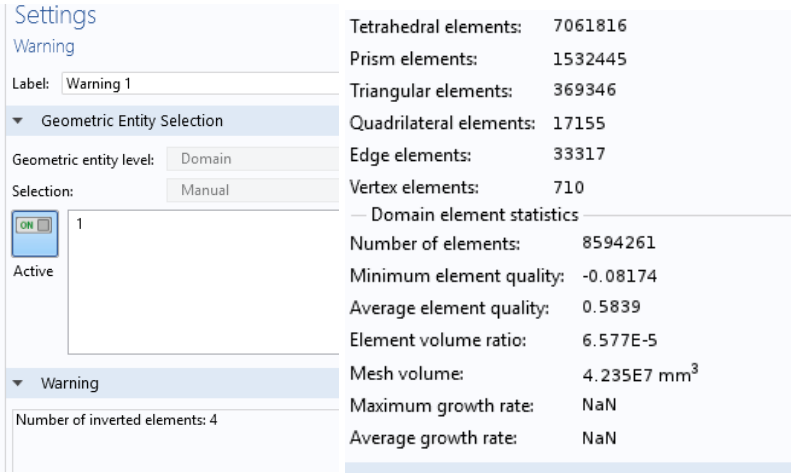

Figure 7.3.4. Mesh statistic for the refined CFD pin fin model. Note the negative minimum element quality due to the inverted element issue.

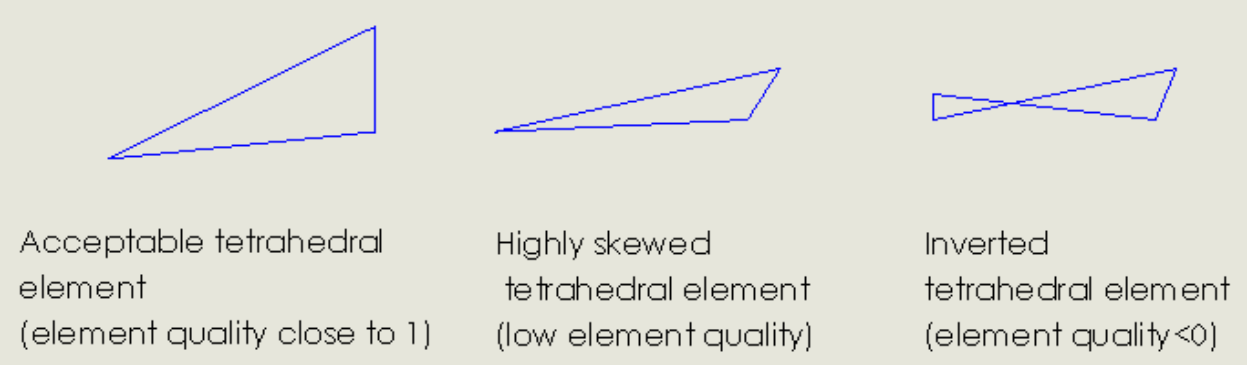

Figure 7.3.5. Mesh skewness and its relation to element quality, note the inverted element giving a negative element quality.

After deciding that the refined CFD model for Tests 4 and 5 were outliers, the difference between the experimental data and the new refined CFD trend line was 25.6%. This difference would have come from overestimating the heat rejection by measuring the heating foil power, and also from unknown flow mechanics that had increased the heat rejection, for both the flat plate and the pin-fin experiment. Without obtaining heat rejection from the airflow, this cannot be fully confirmed.

This meant that for the purposes of using CFD to predict the actual heat rejection by the airflow, for a worst case scenario, the CFD would be 25.6% from the true value. It is expected that the true error should be lower than this value, if heat rejection can be measured directly from the airflow. The outcome of this suggests that CFD is sufficient for predicting heat rejection in the pin-fin condenser with some amount of uncertainty, which can still be applied to other potential pin-fin condenser designs that were not considered in this research.

Also, to determine whether the computational time could be decreased, the simplified model approach from Section 4.5 was tested. It was found that this fitted well with the experimental data and gave a straight trend, but was also found to overpredict the actual heat rejection. Results and discussion for this study are in Section 7.7.

7.4 Velocity profile of the rectangular duct

The same procedures were followed as per Section 6.5 to collect the experimental inlet and outlet velocity profile. The same height and width convention was used in Figs. 7.4.2 to 7.4.5 as per the description in Fig. 7.4.1.

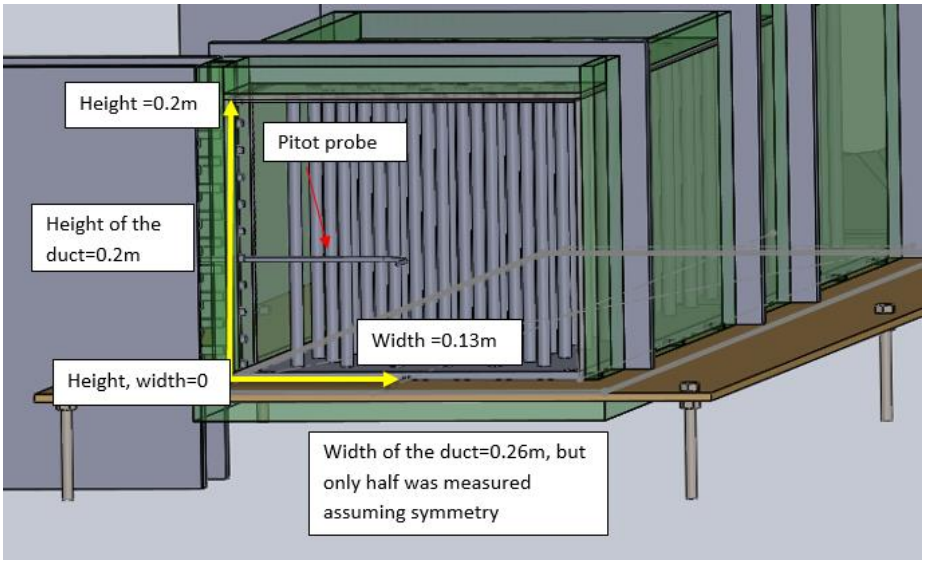

Figure 7.4.1. Description of the duct height and width corresponding to the air velocity profile plots.

At the inlet shown in Fig. 7.4.2 (left), a similar situation with the flow entry behaviour, as illustrated in Fig. 6.5.3, caused the experimental inlet velocity profile to be similar to Fig. 6.5.2 (left). This is because, in the refined CFD model, it assumes only the air entering within the rectangular boundary, the pressure drop effect was already induced at the front of the pin array, which caused this saddle shape profile shown in Fig. 7.4.2 (right). In the overhang areas (refer to Fig. 4.5.2), the air velocity predicted by the refined CFD model was much higher than what was measured in the experiment, because there was no obstacles slowing down the flow. This could also be one of the flaws in the design, as some of the airflow was not contributing to the heat rejection. More heat rejection can be achieved if the airflow was distributed evenly.

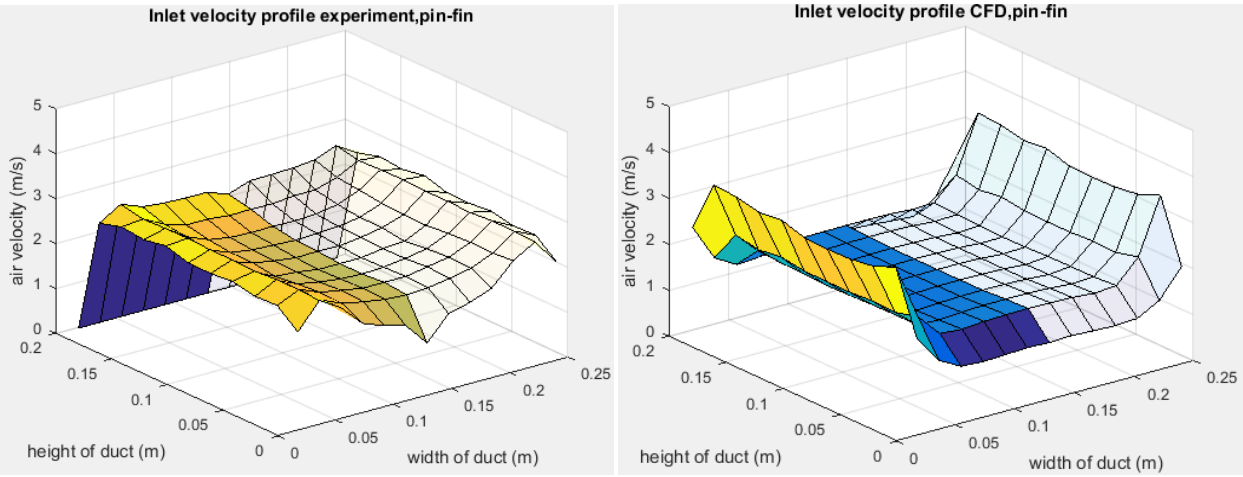

Figure 7.4.2. Experimental and CFD inlet air velocity profile; the solid half represents the half that was measured while the other half was mirrored assuming symmetry. Note that air velocities were not measured at the wall and the refined CFD only shows the same location that was measured in the experiment.

At the height of 198.5mm, for the experimental inlet profile in 7.4.2, air velocities on this level were all measured to be zero by the pitot tube. From checking with the DAQ measurement of pressure difference inside the pitot tube, it was found that this pressure difference was negative and therefore the pitot tube gave a zero air velocity reading. This suggests that the velocity at 198.5mm was not zero, but that there was flow going outwards from the inlet. For the flat plate inlet velocity measurements, this problem did not occur and it was not well understood why this occurred for the pin-fin rig. To identify this problem, the PIV or the dye method could be used to visualise the flow at the inlet.

The error ranged from 1.25 to -2.25m/s for the inlet; according to Fig. 7.4.3, this was due to the flow entry condition assumed in the refined CFD was different from in the experiment, as shown in Fig. 6.5.3. Also, because the airflow was allowed to enter from around the three side walls, the pressure drop distribution across the inlet due to the pin-array was more evenly spread in the experimental velocity profile, as seen in Fig. 7.4.2 (left).

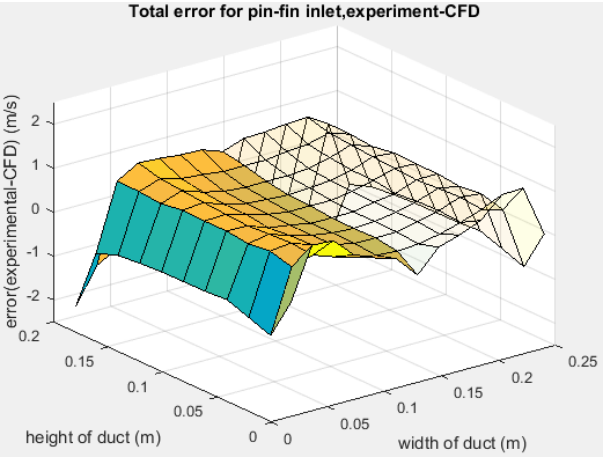

Figure 7.4.3. Total error between the experimental and the refined CFD data for the inlet of the pin-fin rig.

At the outlet, the flow in the experiment had time to transition to the flow predicted by the refined CFD model, which captured the slowing effects due to the positions of the pin-fins (shown in Fig. 7.4.4). This resulted in a lower absolute error than the inlet shown in Fig. 7.4.5. More measurements would be needed to remove the sharp edges in the plot, but this is sufficient to show the refined CFD model is valid. The experimental heat rejection value cannot be evaluated using the integral approach described in Section 4.6.14 without giving a negative value. This was again due to the experimental inlet and outlet flow rate not balancing. The refined CFD flow rate values (Fig. 7.4.6) also did not match, which could be due to the sharp edges in the plot, giving a coarse resolution when integrated for flow rate.

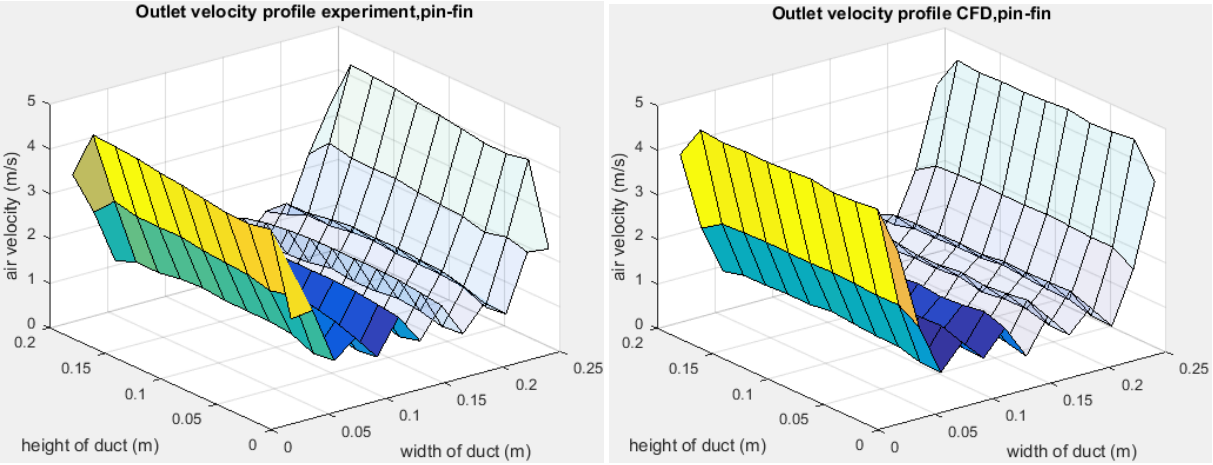

Figure 7.4.4. Experimental and CFD outlet air velocity profile; the solid half represents the half that was measured while the other half was mirrored assuming symmetry. Note that air velocities were not measured at the wall and the refined CFD only shows the same location that was measured in the experiment.

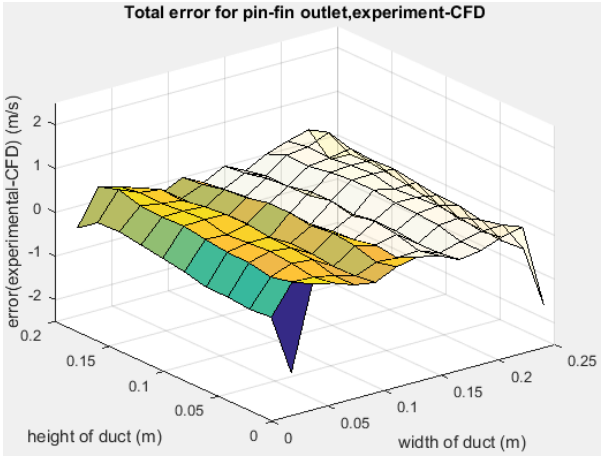

Figure 7.4.5. Total error between the experimental and the refined CFD data for the outlet of the pin-fin rig.

	Experiment from grid (m^3/s)	CFD from grid (m^3/s)
Inlet	0.1073	0.0983
Outlet	0.0955	0.103

Figure 7.4.6. Flow rate obtained from integrating the velocity profile plot, with the inlet and outlet flow rate not matching.

7.5 Experimental temperature profile along rectangular cross-sections

Temperature measurements gathered at the same locations are shown in Fig. 6.6.1, for the inlet and outlet during Test 5 of the pin-fin experiment. The measurement for 547mm from the inlet and the flow centre had to be shifted by 18.57mm to avoid collision. All temperature measurements were standardised using the method mentioned in Section 6.6. At the inlet, there was a similar problem with the measured temperature higher than the ambient air temperature. Because the measurements were always higher and not lower than the ambient air, it also occurred in Fig. 6.6.2; the assumption that the error came from thermocouple accuracy can be rejected. This was most likely due to the pre-heating of air from the rig as it enters the inlet, and is most noticeable near the plate surface. The air near the side wall was hotter, which could be due to the side wall emitting some of the heat it had absorbed from being in contact with the heating plate.

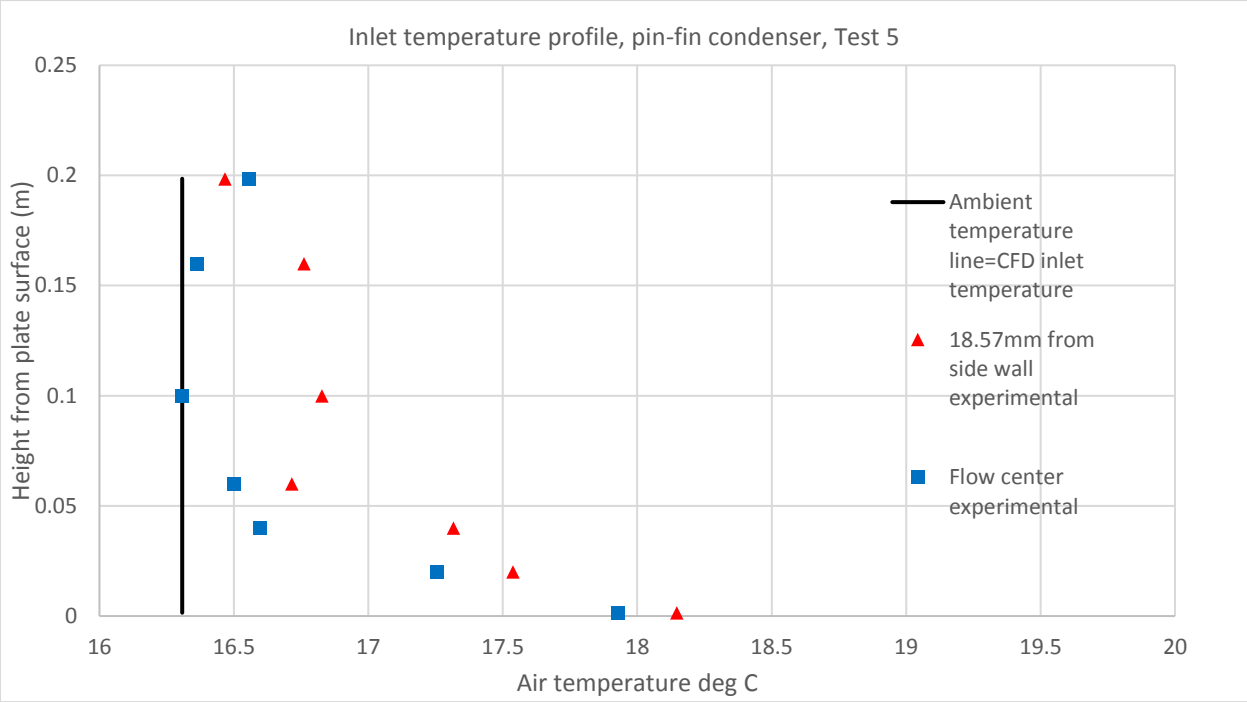

Figure 7.5.1. Temperature profile of the inlet for the pin-fin condenser.

For the profile at 547mm from the inlet, 18.57mm from the side wall shown in Fig. 7.5.2, the refined CFD model prediction was lower than the experimental except near the plate surface. This problem was also seen in Section 6.6 when all three refined CFD models with different inlet turbulence intensities predicted a stronger viscous effect from the side wall, thus lowering heat transfer onto the free stream airflow (refer to Figs. 6.6.3 and 6.6.5).

However, from Figs. 7.5.2 to 7.5.5, the experimental temperature measurement at 198.5mm was not greater than the measurement at 160mm, which was observed consistently from Figs. 6.6.3 to 6.6.6 for the flat plate study. It was thought that this was due to the heat emission from the roof in the flat plate experiment, but because the air stream was hotter in the pin-fin experiment from flowing past the pin array, the heat emission from the roof was less significant. Also, unlike in the flat plate study, the

temperature near the roof was no longer ambient temperature as there was a higher heat transfer due to the presence of 200mm pins.

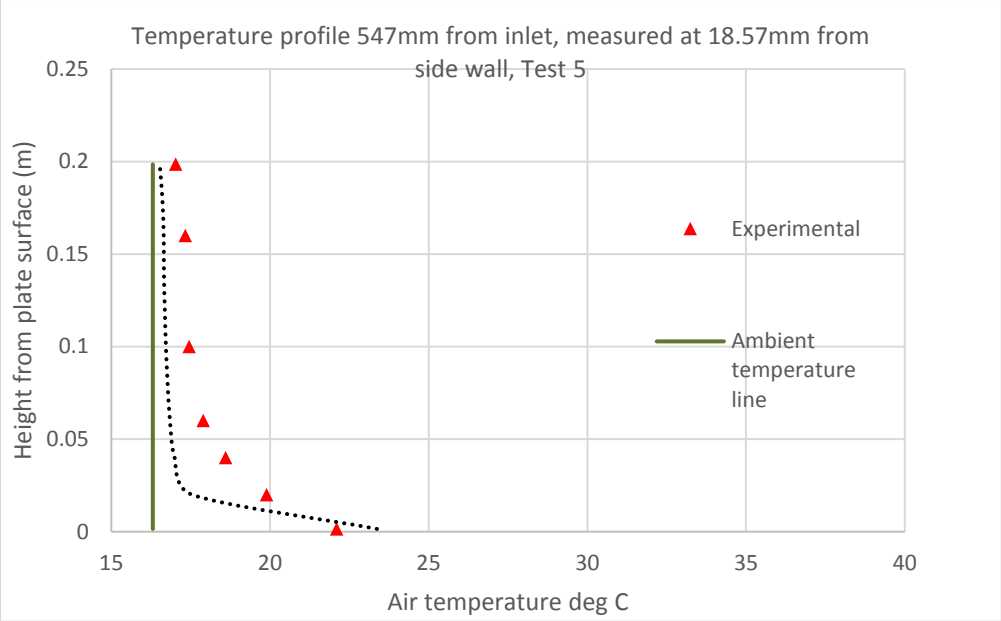

Figure 7.5.2. Temperature profile at 547mm from the inlet, measured at 18.57mm from side wall, pin-fin condenser.

The profile for 547mm from the inlet shown in Fig. 7.5.3 had to be shifted by 18.57mm from the flow centre due to collision with the pins. Due to the difficulty in manoeuvring between the pin array to get to the corresponding measuring location, the tip of the thermocouple wire may have been bent, resulting in positional error of ±5mm. These positional error can become significant if the thermocouple wire was deflected closer to one of the pins than it was supposed to. As seen in Fig. 7.5.3, the third and fourth experiment measurements from the plate surface might have been a result of the thermocouple wire deflecting closer to one of the pins. Other experimental measurement points matched closely, points 6 and 7 were off by approximately 1°C from the refined CFD, which could again be due to positional error in the experiment.

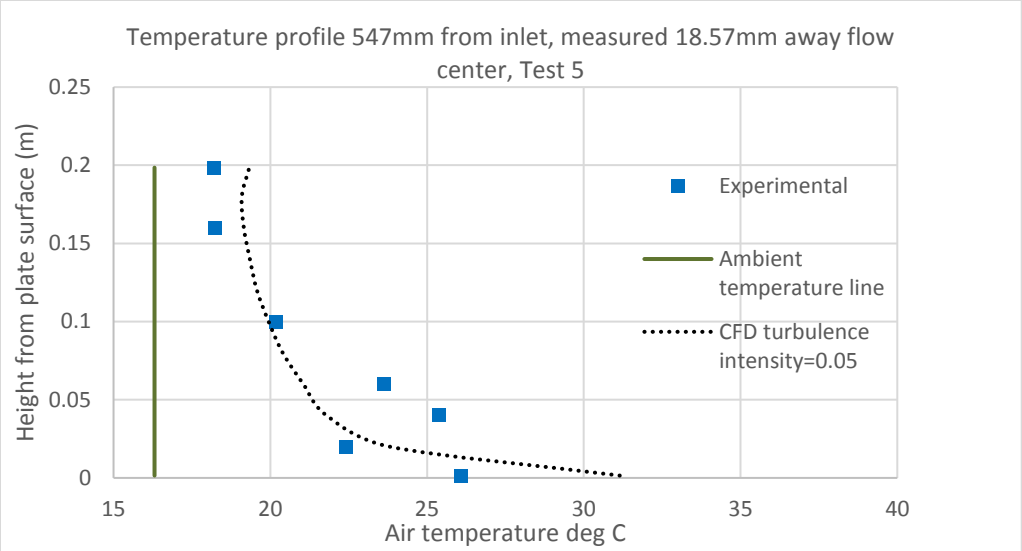

Figure 7.5.3. Temperature profile at 547mm from the inlet, measured at 18.57mm away from flow centre, pin-fin condenser.

At the outlet, 18.57mm from the side wall, Fig. 7.5.4 showed that the refined CFD model again predicts less heat transfer onto the mainstream airflow due to the stronger viscous effect, similar to the situation in Fig. 7.5.2. For the temperature profile at the flow centre of the outlet in Fig. 7.5.5, the refined CFD prediction was much closer to the experimental measurements than any previous plots. This was due to the consistency in air velocity plot shown in Fig. 7.4.4, where both profiles were nearly identical. Unlike at the outlet for the flat plate study in Fig. 6.6.5, where there was still some disagreement, as the refined CFD model predicted a sharper parabolic profile than the experimental data.

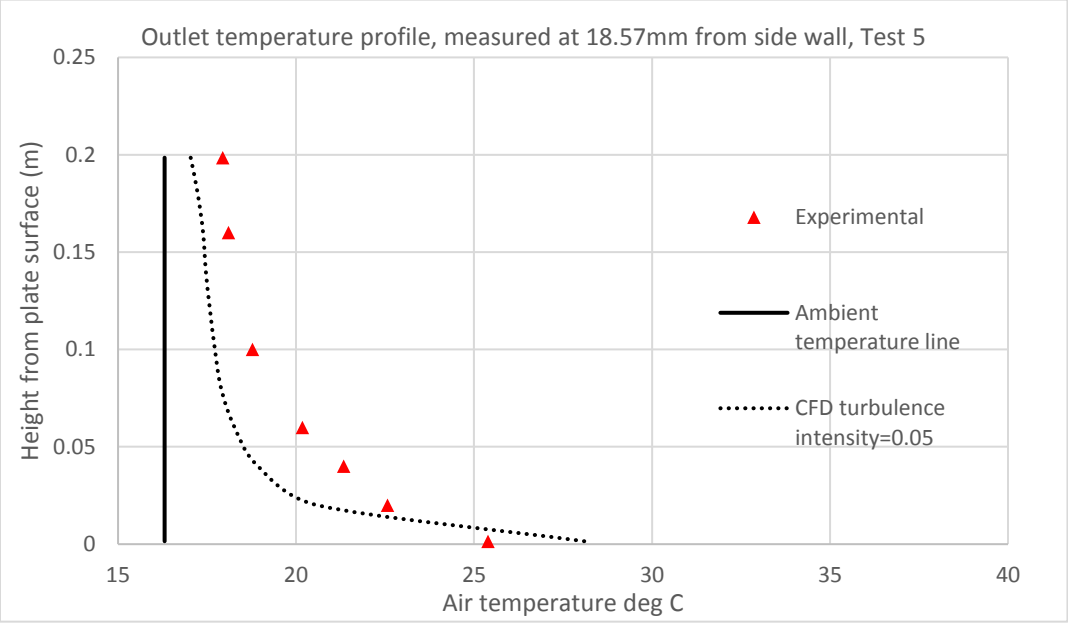

Figure 7.5.4. Temperature profile at the outlet, measured at 18.57mm away from flow centre, pin-fin condenser.

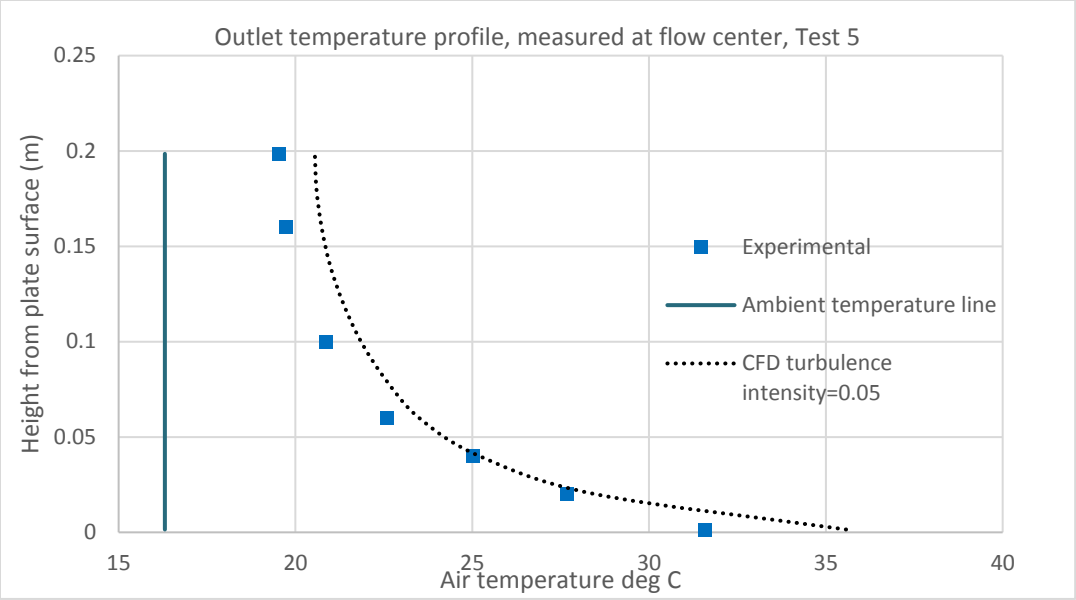

Figure 7.5.5. Temperature profile at the outlet, measured at flow centre, pin-fin condenser.

7.6 Temperature profile on selected pins

To determine whether the thermal grease between the condenser plate and pins had an effect on the amount of heat transfer, the temperature profile on the selected pins were compared with the refined CFD model for Test 5 (location is shown in Fig. 7.6.1). During the measurement, four thermocouples were attached and spaced 20mm apart, as illustrated in Fig. 7.6.3. Each measurement measured all four thermocouples for 30 seconds and averaged. The results in Fig. 7.6.4 show that the experimental temperature trends match the refined CFD model, with the back fin being 3K hotter at 0.06m. This could be due to the tape used for fixing the thermocouples insulating the heat, resulting in a higher local temperature. Overall, it can be concluded that the thermal grease did not have an effect on plate to pin-fins heat transfer.

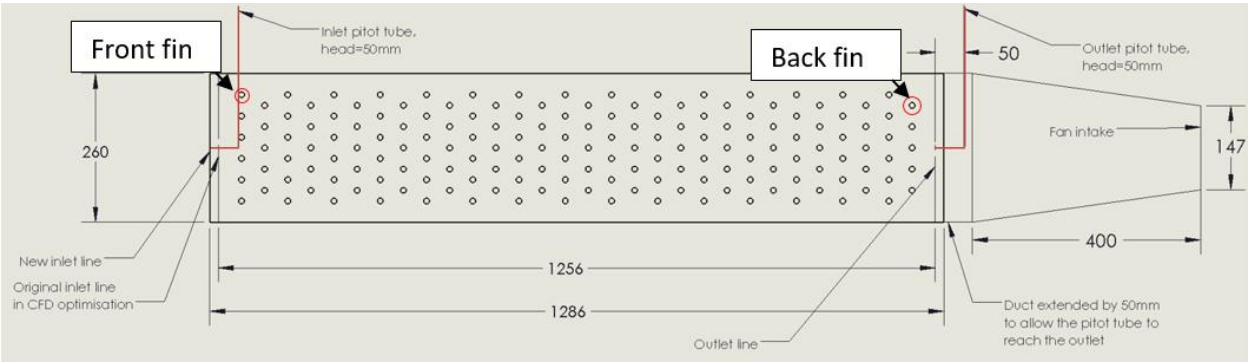

Figure 7.6.1. Location of the selected front and back pin on the rig.

Figure 7.6.2. Fastening the four thermocouples onto the back pin.

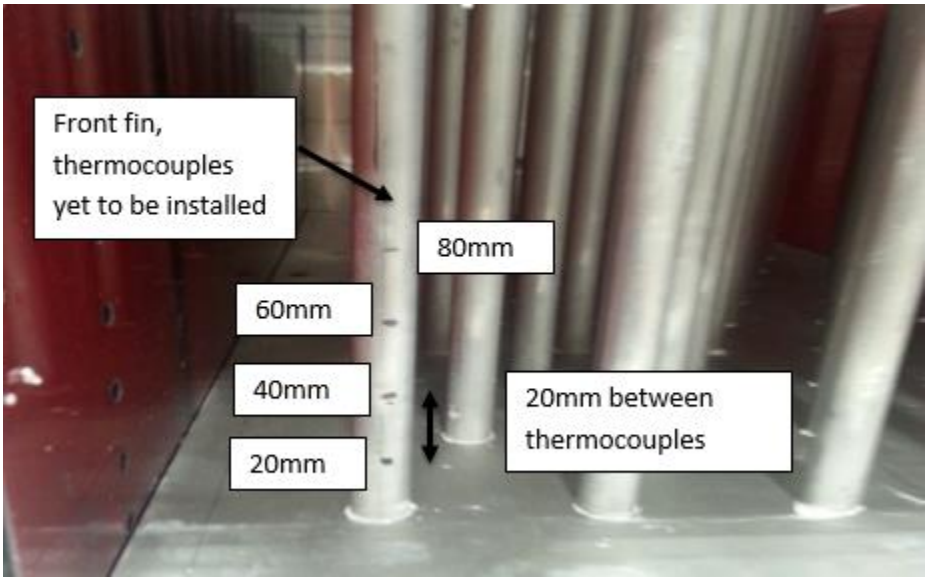

Figure 7.6.3. Placement location of the four thermocouples on the front and back pin.

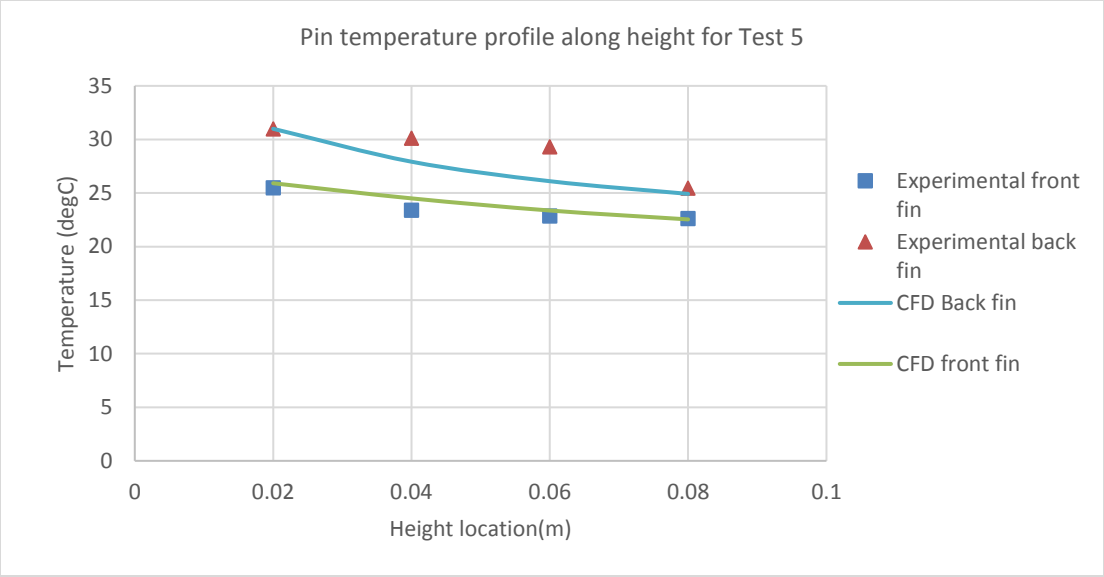

Figure 7.6.4. Location of the selected front and back pin on the rig.

7.7 Remodelling using the simplified model from Section 4.5

Due to the outliers in the refined CFD model shown in Fig. 7.1.2, the conclusion that despite larger models, they are able to mimic the actual experimental situation in more detail than the simplified model. This may allow for more errors to be propagated due to the higher complexity in the modelled airflow and the mesh size used. Therefore, the simplified model from Section 4.5 was used to replicate Test 1-5. The modelling approach as per Section 4.5, with the condenser plate lengthened by 30mm and the flow changed to extract instead of inflow.

The model required 13 hours to run with each taking 30GB of memory; it was found that this produced a linear correlation as would be expected, shown in Fig. 7.7.1. Despite fitting closely with the experimental data, the simplified model does overestimate heat rejection as it does not take into account the viscous loss from the side wall and the transitional duct. Also, the experimental data itself was an overestimation on the heat rejection, as it assumes all the heat from the heat foil reaches the condenser and the pins, neglecting any heat loss in the process. In Section 8.4 the overhang issue was discussed, illustrated in Figs. 8.5.1 and 8.5.2, showing that the airflow on the pin was higher on the simplified CFD model than in the refined CFD model, which would contribute to a higher heat rejection seen in the simplified model.

The main advantages of using the simplified model were its lower computational time and stability, and unlike the refined CFD model it did not produce any outliers. This can be useful for general optimisation, but for accurately determining heat rejection, the mesh on the refined CFD model will have to be refined, particularly in the inlet and outlet region so that the surface integral sum can be determined more accurately.

In terms of heat rejection per volume of material per temperature difference, this was calculated to be 6.71 $kW.m^{-3}.K^{-1}$, as presented in Table 7.1.1. This was higher than the experimental and refined CFD value due to its overestimated heat rejection.

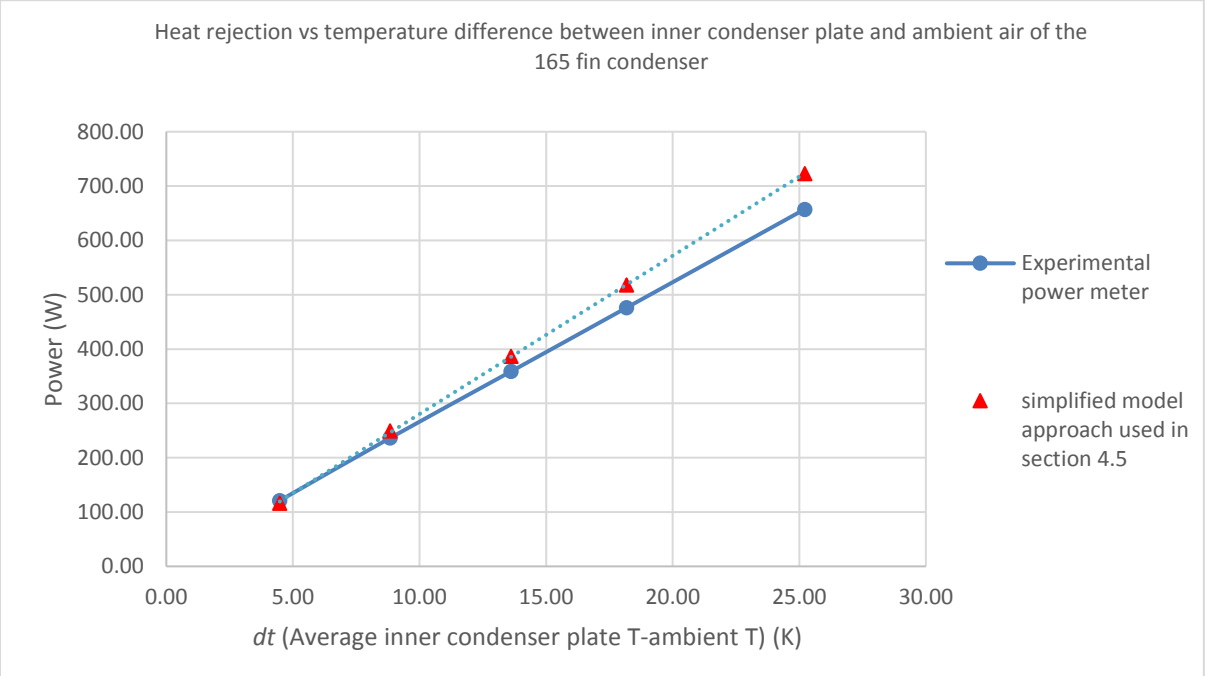

Figure 7.7.1. Remodelling of the pin-fin condenser using the simplified approach adopted in Section 4.5.

7.8 Pin-fin condenser summary

Through experimentation, it was validated that there was a linear relationship between heat rejection and *dt* (condenser temperature-ambient air temperature). There was uncertainty as to how much of the experimental heating foil power was rejected by the airflow and how much was due to heat loss, so it was difficult to know whether the refined CFD model was close to the actual solution. Also, the refined CFD model contains inverted elements which may have contributed to the two outliers in Tests 4 and 5. Note that the refined CFD Tests 1-3 and the two auxiliary CFD points in Fig. 7.3.3 did not form a perfectly straight line, which suggested that the inverted elements may have contributed to these CFD points but to a lesser degree.

The simplified model gave a linear correlation as expected, but it overestimated heat rejection as the model ignores the viscous effect from the side wall and predicts a higher airflow reaching the pin than the refined CFD model (see Figs. 8.5.1 and 8.5.2).

Other studies with the pin-fin condenser include the temperature profile analysis on selected locations inside the rig (Section 7.5), the temperature gradient along selected pins (Section 7.6) and also the air velocity profile at the inlet and outlet (Section 7.4). It was found that the heat was better mixed in the experiment than what was predicted by the refined CFD model, particularly when closer to the side wall (see Figs. 7.5.2 and 7.5.4). This showed that there are unknown airflow mechanics that are causing more heat transfer in the experiment. The temperature profile along the height of the selected pins matched

closely with the refined CFD model, suggesting that there is little thermal loss in heat transfer between the condenser plate and the pins. Looking at the air velocity profiles between what was predicted by the refined CFD model and measured, the same problem occurred as in the flat plate study, regarding the disagreement between the inlet air velocity profiles (see Fig. 7.4.2). This problem was illustrated in Fig. 6.5.2. Otherwise, the outlet velocity profiles matched closely, which showed that the pitot tube was sensitive enough to capture the velocity fluctuations behind and between the pins. Similar to the flat plate study, the overall flow rates at the inlet and outlet did not balance due to the error in static pressure measurements. This made evaluating the heat rejection using the method in Section 4.6.4 in "Measuring heat rejection using the airflow" not possible.

Overall, the 25.6% uncertainty between the experiment and refined CFD heat rejection in Fig. 7.3.3 was considered to be within a reasonable for the purpose of design validation.

8 Discussion

8.1 Heat rejection summary and validation of part 2 of CFD optimisation

In Table 8.1.1, a summary of the heat rejection findings from part 2 of the optimisation, experimentation and the CFD (if relevant) that was done after the experiment were included. Optimisation part 2 results for the 38, 228 and 300 fins condenser variant were also included to check that the experimental and refined CFD did also show that the 165 fins condenser was close to the optima and should perform better than these two other variants.

It was decided that all results should be converted to represent heat rejection per volume of aluminium per temperature difference, as it was identified that the correlation between heat rejection and *dt* was linear.

The result from the refined CFD heat rejection for the flat plate matched closely with the predicted result in Section 4.5.3, showing that the modification in rig geometry in the refined CFD study caused a small decrease in heat rejection. However, the experiment heat rejection value was almost twice that of the predicted and refined CFD value. This was caused by assuming that all the electrical heating foil power was rejected by the airflow, hence ignoring other heat loss and unknown airflow mechanisms. These loss mechanisms likely contributed to a higher heating foil power to maintain the same inner condenser temperature.

Table 8.1.1. Summary of heat rejection per volume of aluminium per temperature difference (inner condenser-ambient). No interpolation was needed by assuming heat rejection varies linearly with temperature difference.

	A	B	C	D	E
1	All test results converted to represent heat rejection per volume of material per temperature difference	Predicted heat rejection per volume of aluminium per temperature difference, optimisation part 2, simplified model (kW.(m^{-3}K))	Experimental heating foil power per volume of aluminium per temperature difference (kW.(m^{-3}K))	Refined CFD heat rejection per volume of aluminium per temperature difference, inlet turbulence intensity=0.05 (kW.(m^{-3}K))	Simplified CFD, Section 7.7 heat rejection per volume of aluminium per temperature difference (kW.(m^{-3}K))
2	Flat plate (manufactured)	**1.75**	**2.93**	**1.51**	Not modelled
3	38 fins, 200mm	**3.92**	Not tested	Not modelled	Not modelled
4	165 fins, 200mm (manufactured)	**5.61**	**5.94**	**4.42**(Fig. 7.3.3 with 2 auxiliary points)- **6.61** (Fig. 7.1.2 with outliers 4 and 5)	**6.71**
5	228 fins, 200mm	**5.67**	Not tested	Not modelled	Not modelled
6	300 fins, 200mm	**5.43**	Not tested	Not modelled	Not modelled

For the pin-fin results, the optimisation part 2 results matched closely with the simplified CFD in Section 7.7, as both used the simplified approach with only small changes in the pin diameter from 10mm to 9.5mm to match the rig that was manufactured. The experimental result also matched closely with

these two values, but the refined CFD study showed that there was uncertainty in the heat rejection due to the two outliers. Overall, the refined CFD predicted a value that was less than the experimental optimisation and simplified CFD results. It was thought that the experimental heating foil power did overestimate heat rejection due to measuring heating foil power instead of the experimental heat rejection by the airflow (which was not possible due to limitations in the measuring devices). However, unlike the flat plate study, where the difference between the experimental heating foil power and the refined CFD study was nearly doubled, this was 25.6% for the pin-fin study.

As to whether the optima found in optimisation part 2 was valid, because only one pin-fin condenser variant was constructed (165 fins, 200mm) and it cannot be confirmed certainly that the 228 fins, 200mm high variant was the optima. It was originally thought that if both the optimisation and refined CFD result were identical to the experimental results, then it can be concluded that this optima is correct.

However the amount of uncertainty between the refined CFD and experimental results was 25.6%. Also, comparing B5 and B6 with D4, the optimsation results for the 228 and 300 fins variants were within the range of the refined CFD for the 165 fins variant. This suggest that the 228 fins, 200mm may not be the optima, and the heat rejection performance between the 165, 228 and 300 fins condenser variant could be similar. However, if the same amount of uncertainty was scaled for the 228 and 300 fins variants using the optimization results, then the 228 fins variant should still be the optima.

Overall the heat rejection results on their own tentatively support the 228 fins variant as the optima, with a possibility that either the 165 or 300 fins variant may also perform adequately in terms of heat rejection per material usage. However, the optimisation did not account for manufacturing cost (see below in Section 8.4.5). As will be shown, the lower manufacturing cost of the 165 pins variant made it a more economical choice to be deployed in Tonga, while also being in the acceptable range of heat rejection performance with the other two variants.

8.2 Experimental and modelling findings

During the optimisation phase in Section 4.5, it was found that the key to finding the optimal number and height of the fins was balanced between conduction (amount of pins to transfer the heat from the plate) and convection (amount of airflow reaching the pins surface). For example, the 1650 fins variant did not allow sufficient air to pass through due to the pressure drop it induced on the fan, thus greatly reducing its heat rejection performance. Therefore, the 228 fins variant was found to be the optimal design in terms of heat rejection per volume of material used from the optimisation phase.

The discovery of a linear relationship describing heat rejection and temperature difference between the inner condenser plate and ambient air in the experiment made it convenient to correlate, as each experimental run started at a different ambient temperature.

The main finding from the flat plate experiment was that the refined CFD modelling has underestimated the heat rejection by a factor of two, 2.93 $kW.m^{-3}.K^{-1}$ in the experiment as to 1.51 $kW.m^{-3}.K^{-1}$ from the

refined CFD study. From the pin-fin condenser experiment, the heat rejection per volume per temperature difference values were 5.94 $kW.m^{-3}.K^{-1}$ from the experiment and 4.42-6.61 $kW.m^{-3}.K^{-1}$ from the refined CFD study. There was a level of uncertainty due to the presence of two outliers at refined CFD points 4 and 5. It was decided that this level of uncertainty was acceptable for estimating heat rejection of a condenser design using CFD, considering that the experimental result was within this uncertainty range.

The simplified CFD model was able to give a linear correlation and fitted closely with the experimental data, but it was considered to be an overestimation of the actual system as it was expected that the CFD model should be lower than the experimental values, due to the experimental values not taking into account the heat loss from the rig. The overestimation came from the simplified model neglecting the viscous effect from the side walls and the overhang issue causing a higher flow onto the pins, as discussed in Section 7.7.

An entire study on an outlet flow mixer design was done in Section 11.1; this was done as an attempt to look for ways to evenly mixed at the outlet. By doing so, only one temperature measurement will be needed along with the ambient temperature to determine heat rejection. It was found that the most basic design of a straight duct would require as much as 100 pipe diameters for temperature to be considered even. For the Kenics mixer, three or more mixer units were needed to be above 90% mixing effectiveness. The choice of the blade aspect ratio and air velocity made no difference in mixing effectiveness when the number of mixer blades is more than three as shown in Fig. 11.1.10. Though the Kenics mixer unit does induce a pressure drop which can be predicted by the correlation provided by [53]. To minimise the pressure drop without sacrificing mixing effectiveness, the aspect ratio of the blade must be longer. In the end, this concept was not implemented in this research due to space limitation and the manufacturing time required, but if constructed it will be able to evenly mixed the air temperature at the outlet.

In summary the main finding was that refined CFD results predicted outcomes within the experimental results, but there was a level of uncertainty due to measuring heating foil power instead of the heat rejected by the airflow. For the flat plate, the difference between the experimental and refined CFD prediction was nearly 50%, suggesting that the uncertainty likely arose from measuring heating foil power alone and also flow mechanisms inside the rig. The level of uncertainty was different between the flat plate and pin-fin study, suggesting the presence of additional heat loss mechanisms associated with the more unconstrained flow regime in the flat-plate situation. This issue is discussed in Section 8.3.

8.3 Explanations for differences between CFD and experimental data

From the experiment with the flat plate and pin-fin condenser, it can be concluded that the uncertainty in the flat plate experiment came from flow mechanisms inside the rectangular duct and any heat loss that resulted in more heat supplied by the heating foil. Turbulence intensity alone was not enough to explain for the uncertainty; even at an inlet turbulence intensity of 1, the CFD result still did not match the experimental heat rejection. This led to the hypothesis that the swirl profile generated by the axial

fan caused more heat to be rejected. The swirl effect would be more severe at the outlet as it was closest to the fan (see Fig 8.3.1 for description).

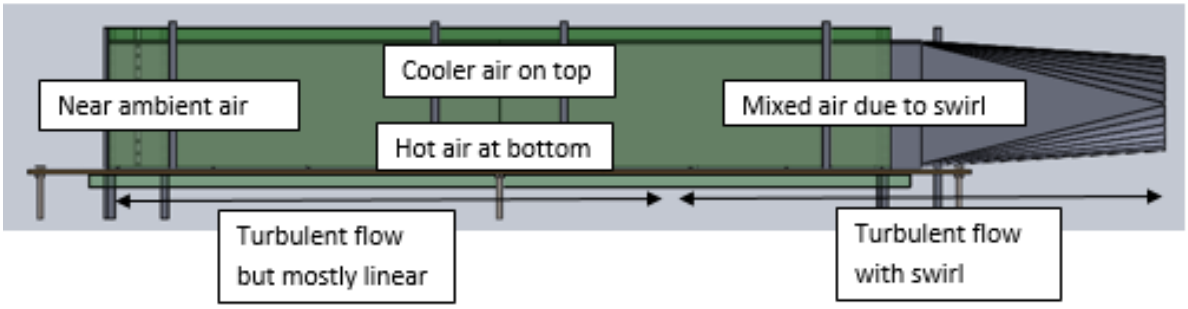

Figure 8.3.1. Flow behaviour inside the rig and at the outlet.

Flow visualisation using a tuft was done at the inlet and it was found that the flow was not stable in Fig. 8.3.2 with the tuft deflecting by 30°, suggesting that there was some level of turbulence intensity in the flow, but not more than 0.2. Also, the refined CFD model assumes that air enters the inlet uniformly, whereas the experimental profile showed that higher velocity was present at the side and top walls, due to the air being able to come behind the walls.

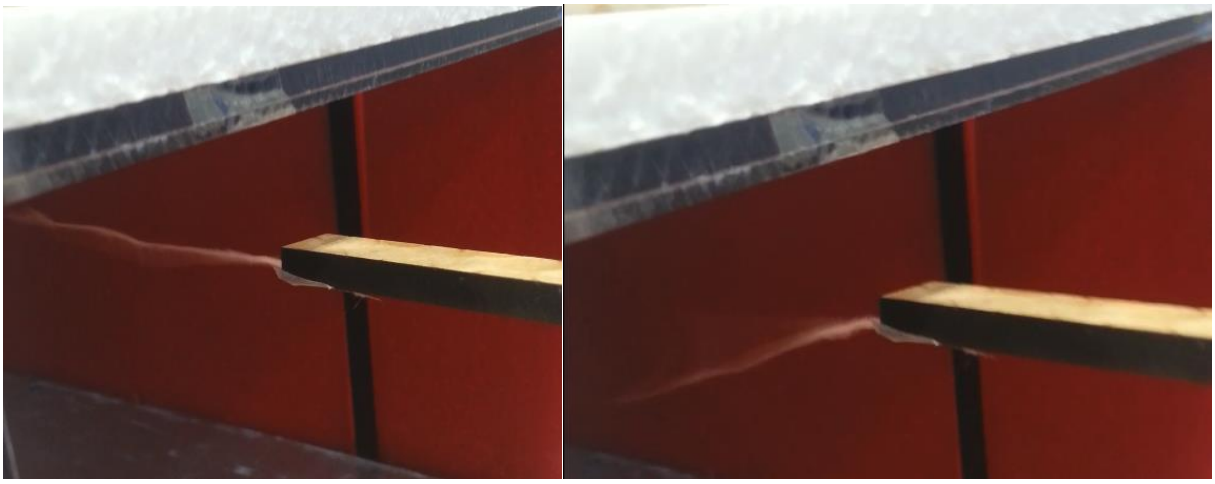

Figure 8.3.2. Flow visualisation at the inlet, where the tuft was deflected by 30°. Images are from two stills from a video, and show the extent of fluttering in the inlet airflow.

Other sources of error came from assuming that all the heat from the heating foil reaches the condenser plate. Some of the rig's heat loss would have came from the losses as the heat was being transferred from the heating foil to the condenser plate, as shown in Fig. 8.3.3.

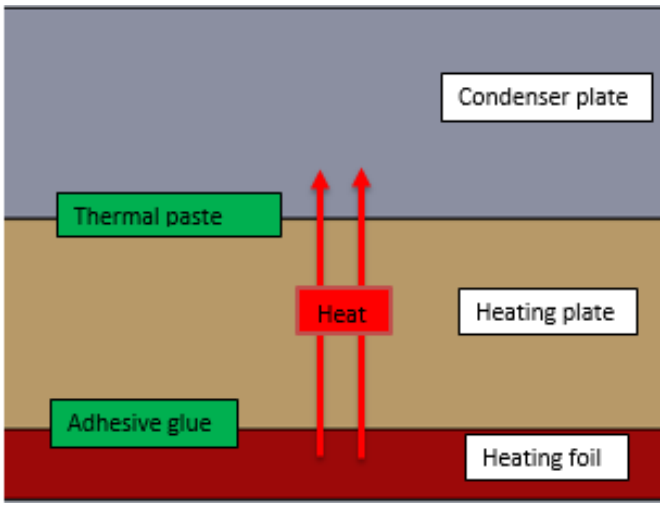

Figure 8.3.3. The path that the heat must travel along to get from the heating foil to the condenser plate.

Overall, the flow mechanics was shown to have a greater effect in the flat plate study than the pin-fin. By comparing the similarity between the experimental and refined CFD outlet velocity profiles from Figs 6.5.5 and 7.4.4, the experiment pin-fin airflow was shown to be more predictable than the flat plate. This is a somewhat counter-intuitive finding, in that the flow might be expected to be more complex in the finned arrangement. We believe that the explanation is that the fins constrain the flow, whereas the flat plate allows more flow paths for the air. Consequently, the experimental heating foil power was closer to the refined CFD prediction for the pin-fin than for the flat plate study.

8.4 Implications for deployment

8.4.1 The setup of the pin-fin condenser unit in Tonga

Despite uncertainties with the refined CFD study for the flat plate condenser, the pin-fin condenser is superior to the flat plate in terms of heat rejection per volume of aluminium used. Ultimately, this design would need to be implemented in Tonga. The fan was originally used to simulate natural convection, but it was found by Gorrie that without an active cooling system, the productivity decreased by 60% [1]. For this research, a new fan was used, and from power meter measurement the fan requires 38W of power to run. In an outdoor environment, this can be powered by a polycrystalline solar panel. Looking at the Komaes website, the KM(P) 60 model is able to provide 60W at STC (1000W.m^{-2}, 25°C). The dimensions of this panel are 690x680x35mm, which is small enough to be placed somewhere above the solar still, preferably above the condenser unit so that it is not in the way of the absorber while gaining maximum solar energy (see Fig. 8.4.1).

The condenser unit is installed on the solar still as shown in Fig. 8.4.2. Whether this condenser unit is robust enough to survive in an outdoor environment, especially close to the sea is an issue as it has only been tested indoors. More effort is needed to design a waterproof housing for the fan to avoid any damage to its electronics. For the main and transitional ducts, they would need to be made from a durable material that can resist rust/UV light and also be malleable enough to absorb thermal or physical shock. Such material could be painted sheet metal as it can be easily formed. The entire unit

should be cleaned regularly to avoid salt deposits from forming as it may decrease the life of the axial fan.

Other considerations are theft and any form of vandalism on the solar still, because aluminium is a valuable metal and can be sold to scrap collectors. To prevent such events from happening the condenser unit needs to be internally fastened to the solar still, and implement a locking device so that only the owner can access it.

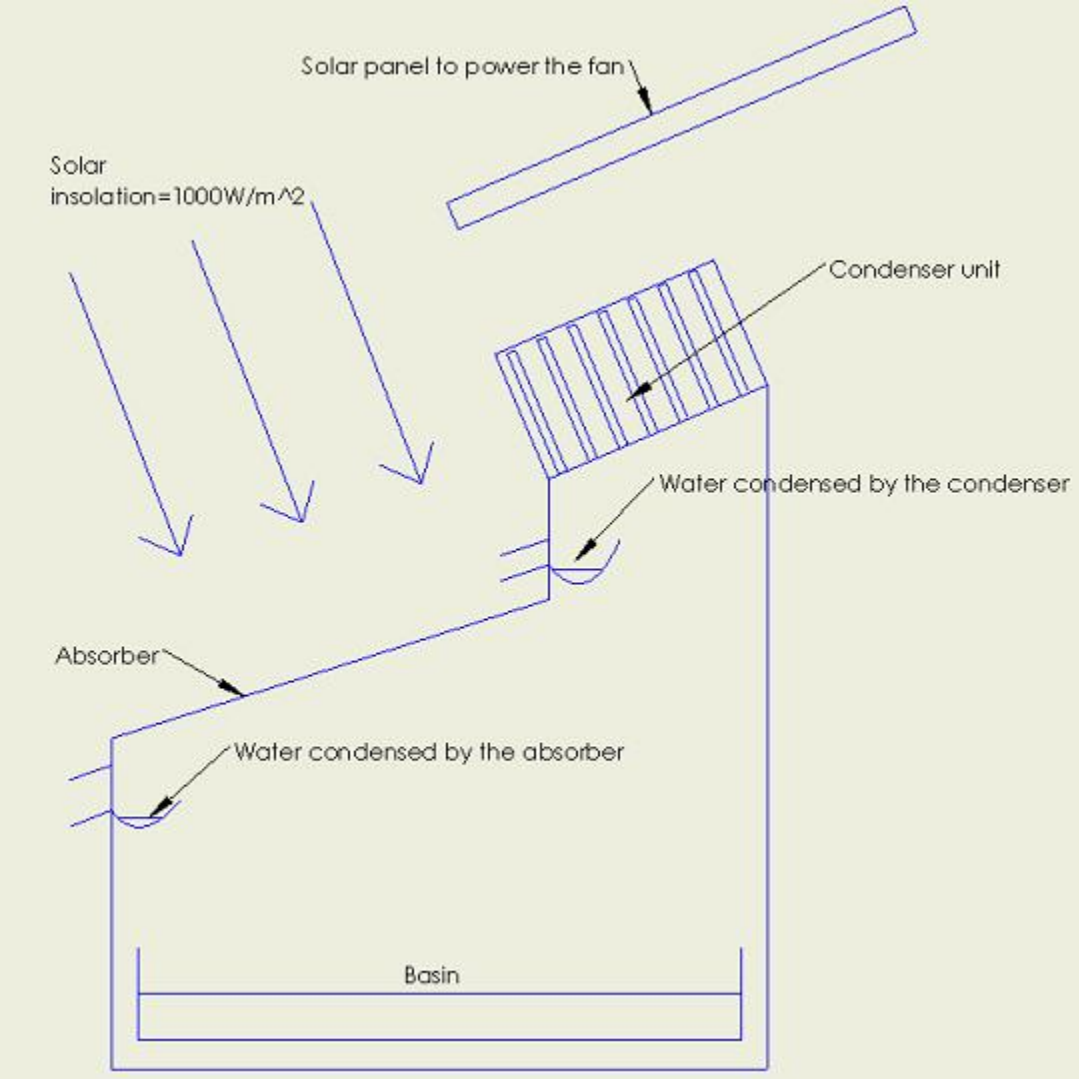

Figure 8.4.1. Placement of the solar panel with respect to the solar still to avoid blocking out the absorber.

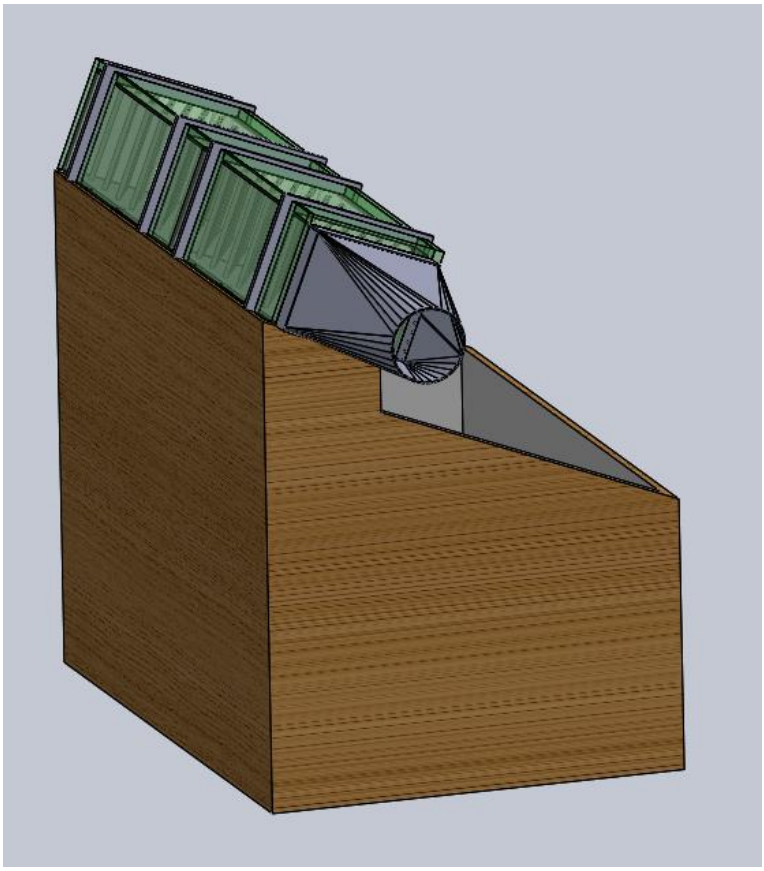

Figure 8.4.2. Installing the optimised condenser unit on to A. Gorrie's solar still. Note the duct will be made of sheet metal instead of Perspex for structural benefits.

8.4.2 Manufacturing considerations

Regarding manufacturing time, assuming automated mass production with only one person, the condenser unit alone would require 3.22 hours to construct if done in series. The process can be separated into three main streams, the pins (2.15 hours), the condenser plate (0.6 hours) and the duct (0.45 hours), as illustrated in Fig. 8.4.3. Assuming that the work stream can be done in parallel with minimal manual intervention, then this would only take 2.15 hours. Below, the time required and machine used for each manufacturing step is shown:

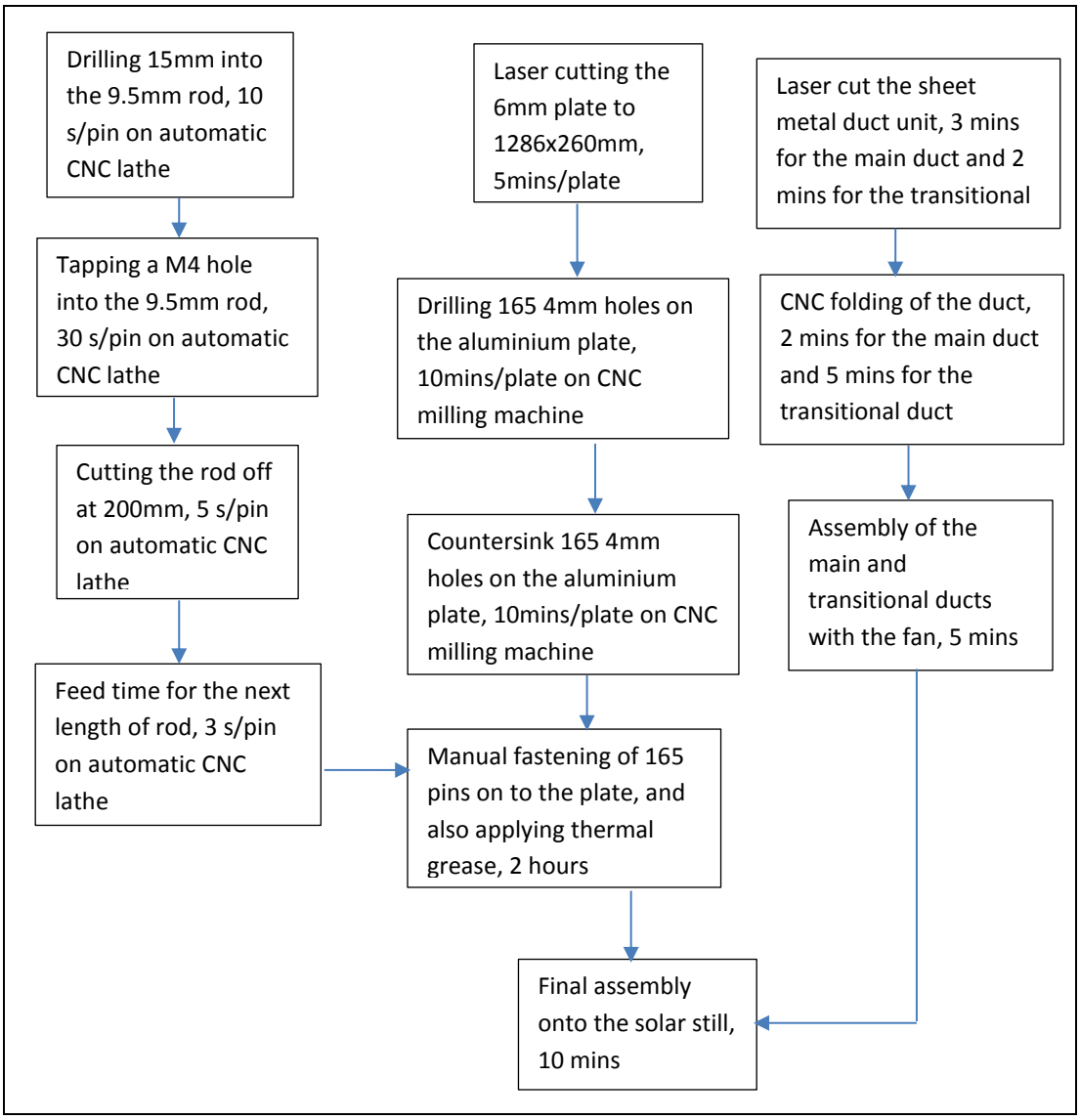

Figure 8.4.3. The work stream for manufacturing the condenser unit.

8.4.3 Estimated water gain

Heat rejection was the main focus in this research as the condenser was not implemented on Gorrie's solar still. Therefore, it is not known whether the optimised condenser design will make any meaningful gain in water production. Without experimental data, it is difficult to predict water production with solar still models like Dunkle's or Chilton-Coburn as they require experimental data inputs. Also, the design of Gorrie's rig is different to the single or double slope solar stills these models were intended for.

Because the pin-fin condenser is able to reject heat at 4.4 times the rate of the flat plate condenser (25.83 W/K as to 5.88 W/K from Table 7.1.1 and 6.7.1, 25.83/5.88=4.39), it will condense 4.4 times as much water. However, the problems with making this simple assumption are:

1. It is not known how much impact the higher heat transfer rate on the inner condenser surface will have on the temperature of the entire solar still. If this causes the solar still to be cooler,

then less water will evaporate. Despite the higher condensation rate at the inner condenser surface, if less water vapour forms then that means less water production.

2. There is also a convection mechanism for the water vapour, driven by temperature and internal pressure. From Dunkle's model, the rate of evaporation is determined by the evaporation term q_e, which is equal to $h_e(T_w - T_g)$. This h_e is related to [29]:

$$h_e = 16.273 \times 10^{-3} h_c \left(\frac{(P_w - P_g)}{T_w - T_g} \right) \; evaporative$$

$$h_c = 0.884 \left[T_w - T_g + \frac{(P_w - P_g) \times T_w}{268.9 \times 10^3 - P_w} \right]^{\frac{1}{3}} \; convective$$

Pressure can be correlated by [29]:

$$P(T) = exp\left[25.317 - \frac{5144}{T}\right] \quad T(283 - 363K)$$

If the heat rejection performance does affect the absorber and the basin water temperature, then there would be a difference in the evaporation and condensation rate. Without experimentation, it is unknown how much these temperature variables change between the flat plate and pin-fin condenser.

3. The efficiency of the water collection mechanics at the condenser is not known without conducting experiments. This efficiency is dependent upon factors such as the tilt angle of the condenser, the size of the water droplets that form and whether some portion of the water vapour escapes the solar still. At different temperatures, these interactions may be different and applying a single efficiency value may not be enough.

Without experimentation, it is difficult to predict the water production rate. For the general purposes of comparison in the remainder of this research, it will be assumed that the pin-fin condenser will produce 4.4 as much as the flat plate condenser. To give a rough estimate, in Gorrie's Test 17, 2.377kg of water was collected in 20 hours, which is equal to 3.3×10^{-5} kg/s. This would mean that with the pin-fin condenser, the water production rate would be 14.52×10^{-5} kg/s. Note that in Gorrie's experiment the fan used was different and the airflow was not ducted.

8.4.4 Payoff period for the pin-fin condenser over the flat plate

To decide whether the increased water production rate by the pin-fin condenser is worth the cost of manufacturing it, a costing analysis was conducted. It was estimated in Table 8.4.1 that $755 was needed to manufacture the pin-fin condenser unit; without the pins and with just the flat plate condenser this cost would be $432, which includes the fan and ducting unit as well. Considering a location in Tonga, where there is no tap water and the cost of a 1.5L bottle of water in Tonga is $2.07 T=$1.36NZD, which equates to 90c/kg. Without assuming travel costs, the estimated water production rate of the pin-fin condenser is 14.52×10^{-5} kg/s, while for the flat plate condenser it is 3.3×10^{-5} kg/s. This equates to 12.54kg and 2.85kg of water per day; therefore, the gain in water production by the pin-fin condenser over the flat plate condenser is 9.69kg per day. This means that $8.72 is saved every day by using the pin-fin instead of the flat plate condenser. Because the pin-fin condenser is $323 more

expensive to make than the flat plate condenser, it would take 37 days for the pin-fin condenser to be paid off, assuming the labour of assembling the pin-fin condenser is free.

Another scenario is on an island further away from any town in Tonga, and the water must be delivered by boat; the cost must now include petrol. For a small 100hp powerboat, the petrol consumption is 34L/hour. Petrol is $2.13/L, assuming the boat travels at a constant speed of 40kph, the cost per distance travel is $1.8/km. Typically these boat can carry 4 passengers=320kg, 320kg of water=$288 if purchased from bottled water. Therefore, the formula for the cost of water depends on two variables, the mass of water and the distance it needs to travel:

$$cost\ (NZD) = 0.9M + 1.8D, where\ M\ is\ the\ mass\ of\ water\ in\ kg, D\ is\ the\ distance\ travel\ by\ boat$$

In Tonga the furthest island away from any towns is about 70Km (see Fig. 8.4.4). This would mean the cost equation becomes:

$$cost\ (NZD) = 0.9M + 126$$

If carrying the maximum possible amount of 320kg of water, travelling to one of these islands would make the total rate $1.29/kg of water.

Deploying the pin-fin condenser in this remote island would save $12.50 per day per solar still. The payback period of the pin-fin condenser is 26 days, as the pin-fin condenser is $323 more expensive to make than the flat plate condenser.

Table 8.4.1. Cost to manufacture a single condenser unit. Assumes 165 fins and variants.

Item	***Amount***	***Costs***	***Comments***
1 piece of aluminum plate 1286x260x6	*1@$172.70 each (Ulrich)*	*$172.70*	
9.5mm aluminum round bar	*$18.40 per length (1 length=5m) 165×200mm=33m=6.6lengths =$121.44 (Ulrich)*	*$121.44*	*(1) This cost is expected to scale linearly with number of fins.*
CNC turning, tapping drilling, cutting and countersunk	*3.22 hours of machining time @$60/hour*	*$193.20*	*See note (1)*
0.95mm Sheet metal	*1.35m^2=10.422kg=$6.25 @$600/tonne*	*$6.25*	
M4 Counter sunk screws	*300 countersunk screws @$15*	*$8.25*	*See note (1)*
Waterproof paint	*$15 per can*	*$15*	
Centrifugal fan	*$238 (Fantech)*	*$238*	
Total cost		***$754.84***	

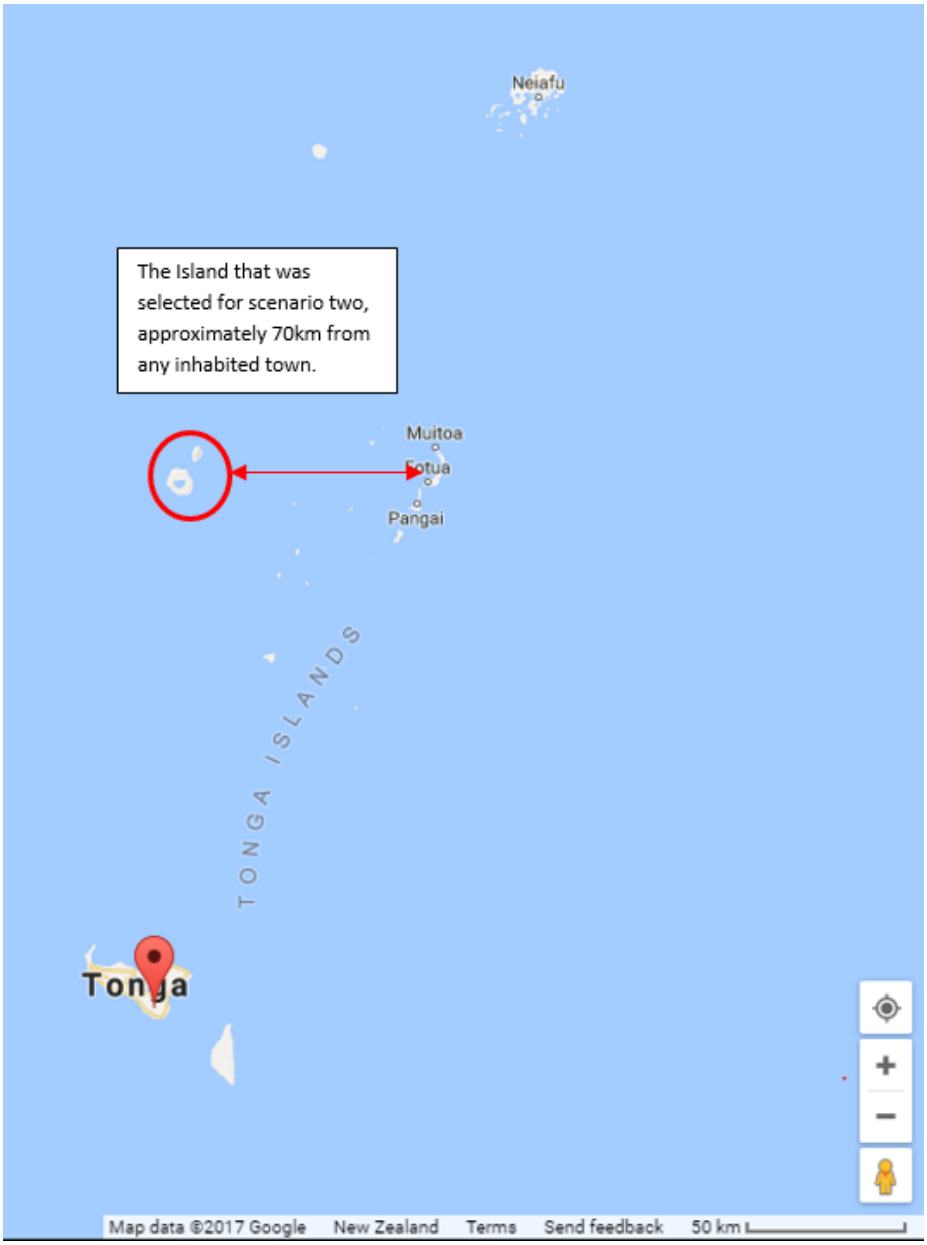

Figure 8.4.4. Map of Tonga and its islands.

8.4.5 Estimated gain of the 228 and 300 fins variant

From assuming that scaling the optimisation results for the 228 and 300 fins variant to estimate the experimental heat rejection was valid, it was found that the these variants rejects 5.15 and 5.90 times more heat than the flat plate condenser respectively. This equates to a water production rate of 17×10^{-5} kg/s and 19.47×10^{-5} kg/s per day.

The estimated cost of building the 228 and 300 fins variant were $854.61 and $962.2 resp., with cost increase due to longer manufacture time and more round bars needed to make the pins.

For the first case in Section 8.4.4 when travelling cost was required to deliver the water was not considered, the cost saving per day for these variants are $10.64 and $12.57 per day resp. over the flat plate condenser. Thus, the payoff times are 40 and 43 days, for the 165 fins variant this was 37 days.

In the second case when travelling cost was also considered, the cost saving per day for these variants were calculated to be $15.25 and $18.01 per day resp. over the flat plate condenser. Payback period were determined to be 28 and 30 days resp., this was 26 days for the 165 fins variant.

This section answered which variants was the optima due to uncertainty in Section 8.1 as the heat rejection results of the three variants were close. From the optimisation part 2 the 228 fins variant was determined to be the optima in terms of heat rejection per volume of material use. But if manufacturing cost was to be added then the 165 fins variant would be the best candidate followed by the 228 fins to be deployed in Tonga. The 300 fin design is excluded because it has poorer heat rejection per material volume (even though it has better total heat rejection), and is more expensive to manufacture.

We therefore conclude that the optimal design, taking into account heat transfer performance and manufacturing economics, is 165 fins, followed by 228 fins.

8.5 Limitations of the current research

This research only considers four pin geometries, with the pin size fixed at 10mm diameter, as stated in Section 4.1. After a basic optimisation process in Section 4.4 to determine the best pin geometry and layout, it is not known whether other geometries would perform better at different pin sizes. Rectangular and elliptical pins also have an extra variable due to their geometry, which makes the optimisation process more complex. A summary of the limitations for the optimisation stage are:

1. A limited number of pin geometries were considered; other pin shapes, such as triangular, were not studied.
2. Only a single size of pin was considered, which was 10mm (but 9.5mm was manufactured).
3. The height of the pin was fixed at 200mm. From Section 4.5 it was shown that the optimum could exist >200mm, but this would mean the duct would need to be changed.
4. In Section 4.4, when deciding on the best geometry and layout, only a limited number of combinations were attempted, with the height of the pin fixed at 100mm.
5. If the flow rate of the fan changes, then the optima will also change.
6. Very coarse mesh was used in Section 4.4, which caused the solution not to fully converge, as shown when the heat rejection values in Table 4.4.1 are even lower than a flat plate condenser. This may have caused a wrong decision to be made as to the optimal pin geometry and layout (inline vs staggered). But due to construction limitations, it is difficult to manufacture elliptical pins, or even making sure that the square/rectangular pins are aligned with the plate. Therefore, the circular pins were the only reasonable choice, with support from the literature that it performs better than other geometries for most scenarios.

Regarding the CFD model used, the k-epsilon model was used due to its stability in convergence and its low memory requirements, which was better suited for optimisation as precision was not needed. In the CFD optimisation and in the refined CFD modelling, the limitations experienced were:

1. The boundary layer was not computed but instead approximated using a wall function on COMSOL. Therefore the velocity at the wall is non-zero. It was not known if modelling the boundary layer would change the current heat rejection values. However, if the refined CFD studies were to be more accurate, then the SST model would have to be used, which requires an initial solution from the k-epsilon model and more internal memory. Currently, 56GB of ram is needed for the refined CFD model of the pin-fin rig.
2. In the refined CFD for the pin-fin condenser, there were four inverted elements found. This resulted in two possible outlying pairs in Fig. 7.1.2; it was only after modelling the two auxiliary points in Fig. 7.3.3 that Tests 4 and 5 became the outliers. However, even after ignoring the outlier points, the remaining point did not form a straight line, suggesting that the inverted elements may have contributed to this error.
3. Section 7.3 suggested that the current approach of interrogating the heat rejection from the refined CFD COMSOL files could generate large errors. This was due to subtracting the two larger sums, inlet and outlet energy to give a product (heat rejection) that was an order of magnitude or two smaller.
4. The simplified model did fit relatively close to the experimental results of the pin-fin condenser. Note that the experimental result may be an overestimation of the heat rejection by the condenser as it measured the heating foil power. The simplified model may also be overestimating more than the experimental value as it does not take account of the pressure loss by the transitional duct and the viscous effect from the side walls. Also, the simplified model does not take into account the overhang region (see Fig. 8.5.1). Because it is easier for the air to travel through this region than through the pin array, therefore the airflow experienced on the pins in reality is lower than what is shown in the simplified model (see Fig. 8.5.2).

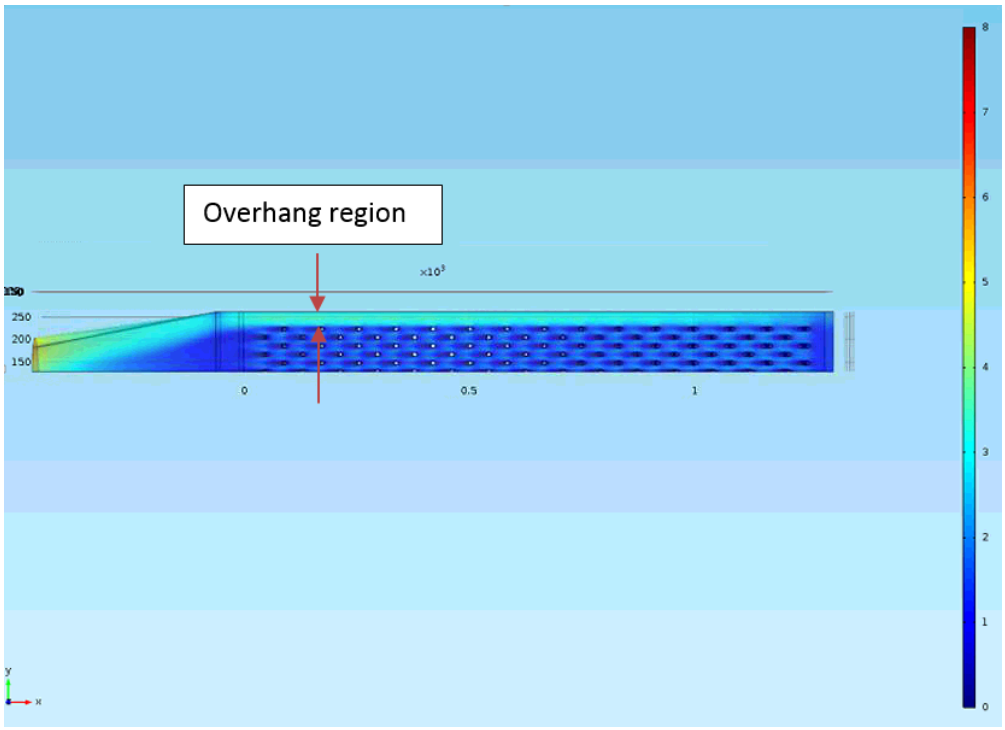

Figure 8.5.1. Airflow distribution for the refined CFD of the pin-fin condenser; airflow is higher in the overhang region.

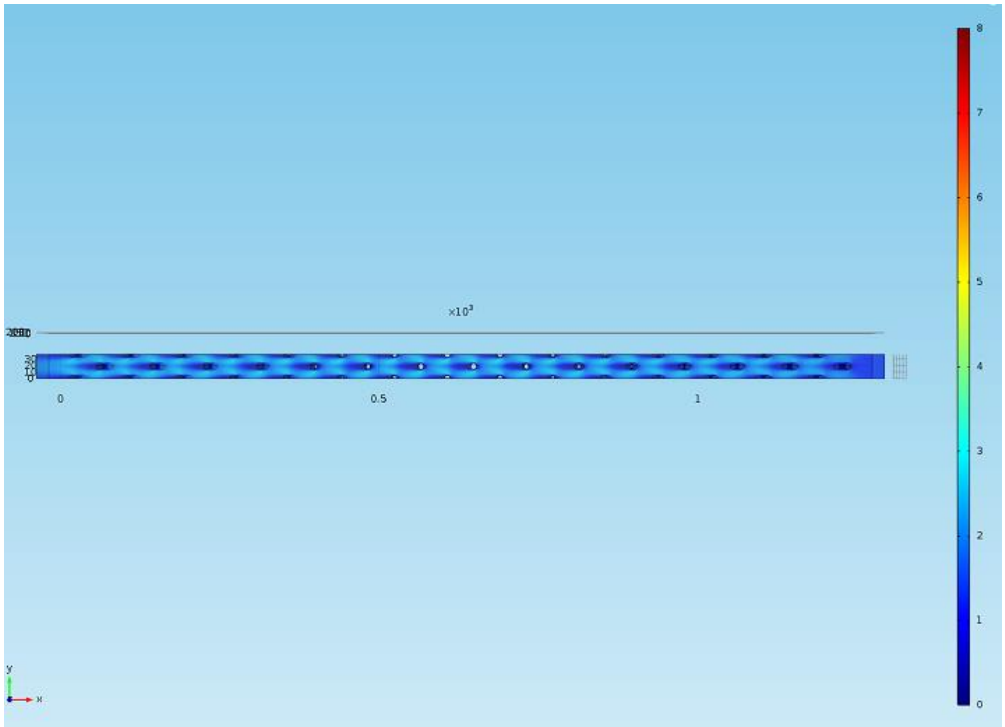

Figure 8.5.2. Airflow distribution for a simplified model of the pin-fin condenser; airflow experienced by the pins is higher than in Fig. 8.5.1.

5. The overhang region does contribute to a loss of heat rejection opportunity for the fins. This flaw was due to the layout algorithm set in Section 4.1 that the first pin must start at D_x and

D_y. To ensure the maximum possible amount of airflow reaches the pins, the layout algorithm should be changed so that the pins can spread more evenly along the plate.

In the data acquisition process, the heat rejection could not be determined using the integral approach described in Section 4.6.4 as the inlet and outlet flow rate did not balanced. Without this heat rejection value from the integral approach, it had to be assumed that the condenser rejects all the heat from the heating foil. This caused the heating foil power to be approximately 50% larger than the refined CFD heat rejection value for the flat plate study (standard inlet turbulence intensity=0.05), and 25.6% larger in the pin-fin study. Other limitations with the air velocity measurement was that the probe was too thick to measure flow at the boundary layer (probe diameter=3mm). Whether this would make a significant difference in calculating the integral heat rejection value is unknown.

All experimental measurements, air velocity, internal air temperature, inner condenser temperatures (T1-T9) and ambient temperature were measured over a period and averaged. This was due to the fluctuation in the system, which was caused by the constantly changing ambient temperature and the PID controller trying to maintain the same inner condenser temperature. When averaging and processing these measurements, some assumptions were made, such as the temperature profile measurements. Because the ambient temperatures were different for all 42 internal air measurements due to only one measurement being taken at a time, it was decided that the temperature difference between the internal air and the ambient temperature measurements were considered instead. This value was then added back to the overall averaged ambient temperature to give a steady-state representation of the temperature profile inside the duct, as implemented in Sections 6.6 and 7.5.

The main problem with comparing this averaged experimental result against the CFD is that the CFD assumes a steady-state condition. It is not known whether the amount of fluctuation when collecting time averaged experimental data was significant enough to generate errors. If there are enough data acquisition channels available and the power meter is able to display power instead of accumulative energy, then only one second of measurement is needed. Then this measurement can be inputted directly onto the refined CFD model and compared directly, eliminating any need for averaging, and standardising of the experimental data. It is also not known whether having 42 thermocouple probes inside the rig at the same time would affect the airflow.

8.6 Implications for future research

This research focused on optimising heat rejection of the geometric design of the external condenser surface. If future research were to be done on this pin-fin condenser unit, the main priorities could be:

1. Obtain more powerful computing facilities so that a finer mesh can be used on the refined model for the pin-fin condenser.
2. Alternatively, seek ways to simplify the model while also taking account of the viscous effect from the wall and the pressure drop of the transitional duct.
3. Remove the overhang region (see Figure 8.5.1) by redistributing the pins more evenly, so that a higher heat rejection value can be achieved.

4. Attempt the optimisation with other different circular pin sizes. Note that changing to non-circular pin geometries makes it difficult to manufacture. It was found that the pins near the outlet are hotter due to the heating of the passing air by the pins at the front, as shown in Fig. 8.6.1. This means that the pins at the back are not rejecting as much heat as the pins at the front; the scope for future research can look at shortening the back pins to increase the heat rejection per volume of material value. One idea would be a stepped pin-fin condenser design, as shown in Fig. 8.6.2.

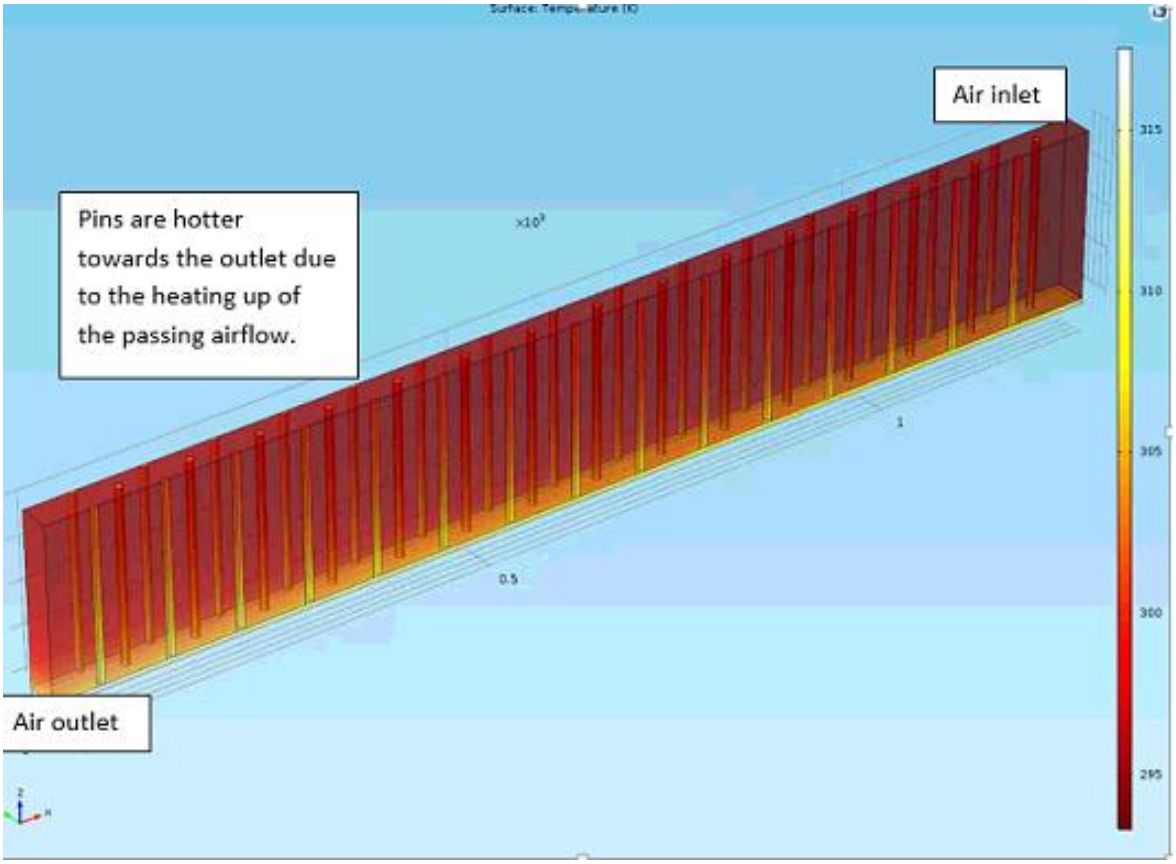

Figure 8.6.1. Temperature distribution of the pin-fins; note the hotter pins near the outlet.

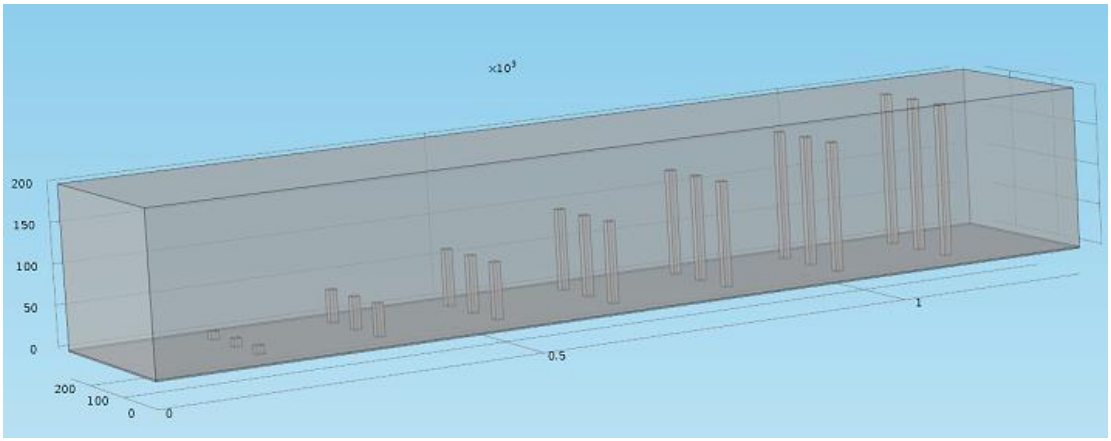

Figure 8.6.2. The stepped pin-fin design that could be looked at to reduce unnecessary aluminium usage.

5. A better means of measuring the flow rate and average temperature at the outlet would be desirable. It was difficult to calculate heat rejection using the integral approach with the air velocity and temperature. If this is possible that would mean only three measurements are needed to evaluate heat rejection, ambient temperature, flow rate and average temperature at the outlet. A concept of adding a control volume after the outlet is introduced in Fig. 8.6.3; the role of this control volume is to allow the heat and the airflow to mix evenly after the initial air volume is replaced. Then the flow rate can be measured at the outlet of the control volume. This outlet must be placed somewhere that would allow enough time for the air to mix evenly. The heat rejection will simply be:

$$\dot{Q} = \dot{m}_{Outlet\ control\ volume} C_p (T_{Outlet\ control\ volume} - T_{Inlet})\ (W)$$
$$C_p\ of\ air = 1.005kJ.(kg.K)^{-1}\ Specfic\ heat\ capacity\ of\ air$$

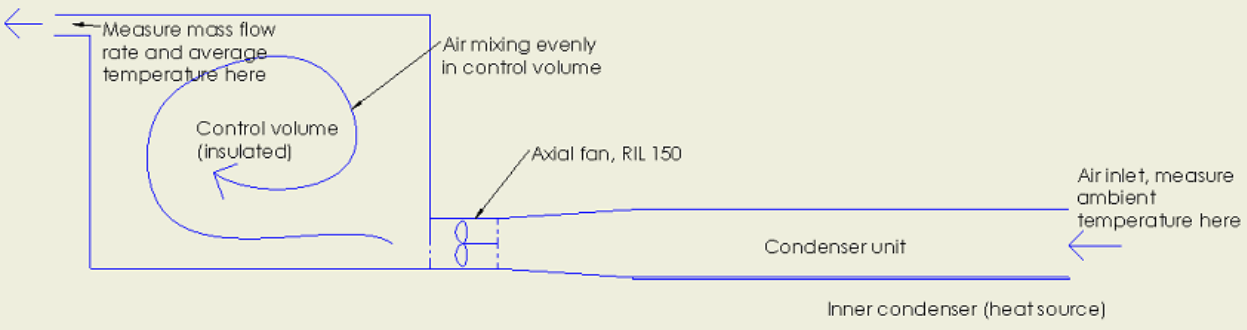

Figure 8.6.3. The control volume concept to allow the air to mix evenly, so that the heat rejection can easily be calculated.

6. Due to the difference between experimental and refined CFD inlet air velocity profile, as discovered in Sections 6.5 and 7.4, this could have contributed to the disagreement in heat rejection for the flat plate condenser experiment. For future research scope, the rig could be modified so that the inlet is lengthened to allow time for the flow to transition. From calculations, the length of duct required for the flow to develop fully is:

$$L_e = 1.6D_e \left(\frac{\rho_{air} D_e U_{max}}{\mu_{air}}\right)^{1/4} for\ 2300 < Re < 10^7$$

Assuming the average inlet velocity is 2.4m.s^{-1}, the entrance length is 4.89m. Therefore, 5m of duct is needed before the inlet to allow the flow to be fully developed before reaching the inlet. A reason this was not done in this research was due to space restrictions in the lab, and would not be practical to install a condenser unit this long on the solar still. Another way to improve the flow without lengthening the rig significantly is by adding bell mouths at the inlet. This will allow the flow to enter the duct more smoothly.

7. Gorrie identified the need to increase the available evaporative surface area to increase water production rate for a solar still [1]. Consequently a new concept is proposed as shown in Fig. 8.6.4. This concept works by implementing a pump and a nozzle to spray seawater particles inside the solar still, because of the great increase in evaporative surface of the seawater particles, it may increase evaporation rate and thus water production. However, it is unknown whether the cost and electricity of implementing a pump are worthwhile for additional water production.

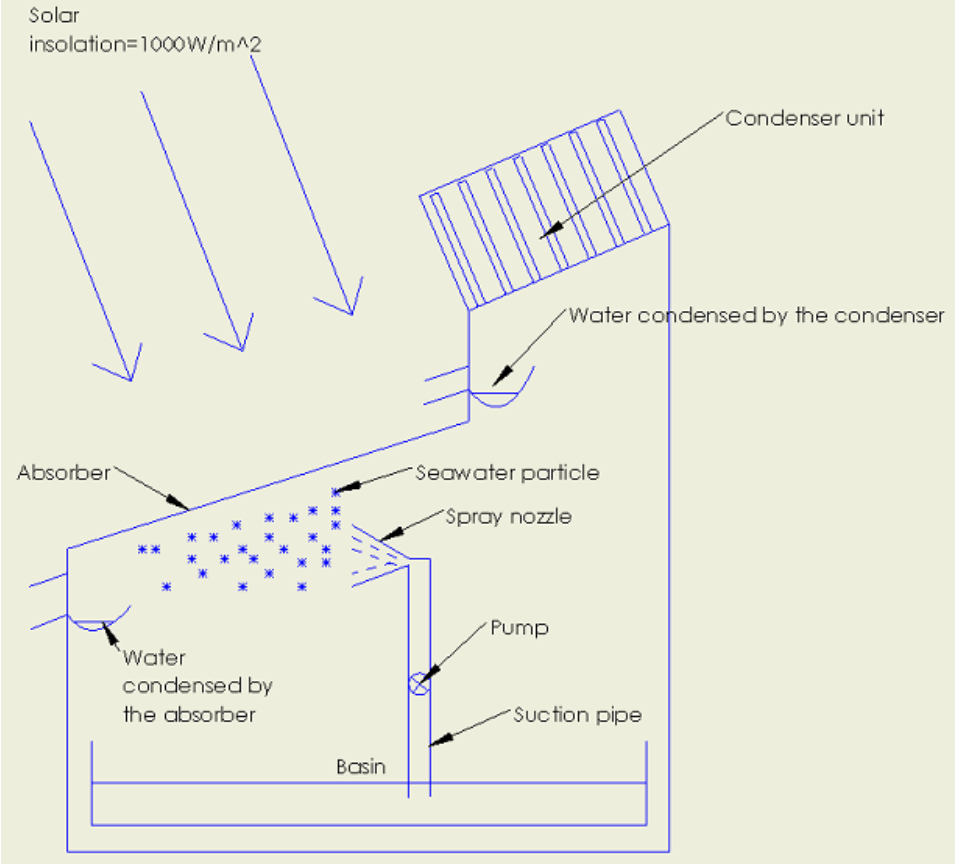

Figure 8.6.4. The spray concept to increase evaporative rate and water production.

9 Conclusions

This work makes several contributions. The first contribution was optimising the heat rejection of the condenser in terms of the volume of aluminium used. This concept was formed as A. Gorrie's proposed concept of the pin-fin condenser in Fig. 2.11.1 to increase heat rejection. A second component was added to this scope that the optimised condenser should minimise the use of aluminium. This was to accommodate the context that this condenser and solar still unit would be deployed in Tonga, where aluminium is scarce. In the literature, it was found that similar work looking at optimising heat rejection per volume of material was done in [17] and [18]. However, the limitations of those works were that heat rejection per volume of material was looked at only from an analytical approach in [17], and also the lack of experimental validation in both [17] and [18]. There was no literature that looked at the viability of using a pin-fin condenser on the solar still to increase water production, but there was literature regarding heat sink design, layout and pressure loss but they were all tailored for their particular situations.

The second contribution came during the experimental phase when a new method of measuring the heat rejection using the airflow was studied, due to the failure of the integral method proposed in Section 4.6.6. If this was achievable, then only one measurement is needed for the outlet flow rate and temperature to determine heat rejection. To do this, the literature review and CFD analysis were done on a Kenics mixer, where it was found that despite the mixer being able to mix thermally stratified air evenly, as shown in Section 11.1.2, but the pressure loss associated with these mixer units would change the original optimisation problem. Therefore, this concept was not taken further as it was considered not suitable. However, there was a contribution made as it was found that there was no literature that looked at using the Kenics mixer to mix thermally stratified air. Most literature only looked at using the mixer for chemical mixing applications.

The main outcome of this research was determining the optimal circular pin-condenser candidate. In terms of only heat rejection per volume of aluminium, this was found to be the 228 pins with each pin at 200mm high. After adding in manufacturing consideration, the 165 fins x 200mm variant was more economical to be deployed in Tonga while having a similar heat rejection per volume performance to the 228 and 300 fins variant.

Another outcome was determining that CFD can be used to predict heat rejection of pin-fin condensers within 25.6% of the experimental measurements. If heat rejection can be measured from the airflow this uncertainty is expected to be less. An implication for this outcome is that CFD could be used in the future to predict heat rejection for another condenser design without experimentation.

Also this work predicted water productivity and viability of deployment of a solar still in Tonga. It was estimated that because the heat rejection of the 165 pins, 200mm condenser was 4.4 times greater than the flat plate condenser, proportionally more water would be collected. This makes the payoff period from upgrading to the 165 pins, 200mm condenser from the flat plate would be about 26-37 days depending on whether it is located in mainland Tonga or on an island 70km away. The cost of water was calculated based on buying bottled water in Tonga and assuming no access to tap water.

10 References

1. Gorrie, A., Pons, D., Docherty, P., Maples, D., *OPTIMISATION OF SOLAR DESALINATION PROCESS, An investigation of the critical parameters affecting solar still water production in the context of a developing country*, in *Mechanical Engineering*. 2016, University of Canterbury: Christchuch, New Zealand. p. 234.
2. Baskaya, S., Sivrioglu, M., and Ozek, M., *Parametric study of natural convection heat transfer from horizontal rectangular fin arrays.* International Journal of Thermal Sciences, 2000. **39**(8): p. 797-805.
3. Sahiti, N., Lemouedda, A., Stojkovic, D., Durst, F., and Franz, E., *Performance comparison of pin fin in-duct flow arrays with various pin cross-sections.* Applied Thermal Engineering, 2006. **26**(11-12): p. 1176-1192 DOI: 10.1016/j.applthermaleng.2005.10.042.
4. Yang, K.S., Chu, W.H., Chen, I.Y., and Wang, C.C., *A comparative study of the airside performance of heat sinks having pin fin configurations.* International Journal of Heat and Mass Transfer, 2007. **50**(23-24): p. 4661-4667 DOI: 10.1016/j.ijheatmasstransfer.2007.03.006.
5. Matsumoto, R., Kikkawa, S., Senda, M., and Suzuki, M., *Heat transfer characteristics of an endwall with single row of oblique pin fins.* JSME International Journal, Series B: Fluids and Thermal Engineering, 2001. **44**(4): p. 599-607 DOI: 10.1299/jsmeb.44.599.
6. VanFossen, G.J., *Heat-Transfer Coefficients for Staggered Arrays of Short Pin Fins.* Journal of Engineering for Power, 1982. **104**(2): p. 268-274 DOI: 10.1115/1.3227275.
7. Islam, M.D., Oyakawa, K., and Kubo, I., *Investigation of heat transfer and fluid flow behavior between straight and inclined fins in tall duct.* Applied Thermal Engineering, 2012. **49**: p. 118-123 DOI: 10.1016/j.applthermaleng.2011.07.044.
8. Huang, R.T., Sheu, W.J., and Wang, C.C., *Orientation effect on natural convective performance of square pin fin heat sinks.* International Journal of Heat and Mass Transfer, 2008. **51**(9-10): p. 2368-2376 DOI: 10.1016/j.ijheatmasstransfer.2007.08.014.
9. Ozturk, E. and Tari, I. *CFD analyses of heat sinks for CPU cooling with fluent*. in *ASME/Pacific Rim Technical Conference and Exhibition on Integration and Packaging of MEMS, NEMS, and Electronic Systems: Advances in Electronic Packaging 2005, July 17, 2005 - July 22, 2005*. 2006. San Francisco, CA, United states: American Society of Mechanical Engineers.
10. Jeng, T.M. and Tzeng, S.C., *Pressure drop and heat transfer of square pin-fin arrays in in-line and staggered arrangements.* International Journal of Heat and Mass Transfer, 2007. **50**(11-12): p. 2364-2375 DOI: 10.1016/j.ijheatmasstransfer.2006.10.028.
11. Şara, O.N., *Performance analysis of rectangular ducts with staggered square pin fins.* Energy Conversion and Management, 2003. **44**(11): p. 1787-1803 DOI: 10.1016/S0196-8904(02)00185-1.
12. Armstrong, J. and Winstanley, D., *REVIEW OF STAGGERED ARRAY PIN FIN HEAT TRANSFER FOR TURBINE COOLING APPLICATIONS.* Journal of Turbomachinery, 1988. **110**(1): p. 94-103.
13. Axtmann, M., Poser, R., von Wolfersdorf, J., and Bouchez, M., *Endwall heat transfer and pressure loss measurements in staggered arrays of adiabatic pin fins.* Applied Thermal Engineering, 2016. **103**: p. 1048-1056 DOI: http://dx.doi.org/10.1016/j.applthermaleng.2016.04.066.
14. Uzol, O. and Camci, C., *Heat transfer, pressure loss and flow field measurements downstream of staggered two-row circular and elliptical pin fin arrays.* Journal of Heat Transfer, 2005. **127**(5): p. 458-471 DOI: 10.1115/1.1860563.

15. Tahat, M., Kodah, Z.H., Jarrah, B.A., and Probert, S.D., *Heat transfers from pin-fin arrays experiencing forced convection.* Applied Energy, 2000. **67**(4): p. 419-442 DOI: 10.1016/S0306-2619(00)00032-5.
16. Bergman, T.L., Incropera, F.P., DeWitt, D.P., and Lavine, A.S., *Fundamentals of Heat and Mass Transfer*. 2011: Wiley. ISBN: 9780470501979.
17. Bahadur, R. and Bar-Cohen, A. *Analysis and design of a least material orthotropic pin fin heat sinks*. in *10th Intersociety Conference on Thermal and Thermomechanical Phenomena and Emerging Technologies in Electronic Systems, ITherm 2006, May 30, 2006 - June 2, 2006*. 2006. San Diego, CA, United states: Institute of Electrical and Electronics Engineers Inc.
18. Yang, A., Chen, L., Xie, Z., Feng, H., and Sun, F., *Constructal heat transfer rate maximization for cylindrical pin-fin heat sinks.* Applied Thermal Engineering, 2016. **108**: p. 427-435 DOI: https://doi.org/10.1016/j.applthermaleng.2016.07.150.
19. Shuttleworth, W.J., *Putting the 'vap' into evaporation.* Hydrology and Earth System Sciences, 2007. **11**(1): p. 210-244 DOI: 10.1029/2002JD003119.
20. Billy, U.A., Utah, E.U., and Akpan, U.E., *ESTIMATION OF EVAPORATION RATE IN UYO, NIGERIA USING THE MODIFIED PENMAN EQUATION* Canadian Journal of Pure and Applied Sciences, 2013. **7**(1): p. 2277-2281.
21. Khalifa, A.J.N. and Hamood, A.M., *Performance correlations for basin type solar stills.* Desalination, 2009. **249**(1): p. 24-28 DOI: http://dx.doi.org/10.1016/j.desal.2009.06.011.
22. Nafey, A.S., Abdelkader, M., Abdelmotalip, A., and Mabrouk, A.A., *Parameters affecting solar still productivity.* Energy Conversion and Management, 2000. **41**(16): p. 1797-1809 DOI: http://dx.doi.org/10.1016/S0196-8904(99)00188-0.
23. Laribi, B., Wauters, P., and Aichouni, M. *Experimental study of aerodynamic behavior downstream of three flow conditioners*. in *Proceedings of the 2002 ASME Joint U.S.-European Fluids Engineering Conference*. 2002. Montreal, Que.
24. Laribi, B., Wauters, P., and Aichouni, M., *Comparative study of aerodynamic behaviour of three flow conditioners.* European Journal of Mechanical and Environmental Engineering, 2003. **48**(1): p. 21-30.
25. Laws, E.M. and Ouazzane, A.K., *A preliminary study into the effect of length on the performance of the Etoile flow straightener.* Flow Measurement and Instrumentation, 1995. **6**(3): p. 225-233 DOI: 10.1016/0955-5986(95)00011-A.
26. Han, S. *Three-dimensional numerical model to evaluate the suspended solid removal in surface flow constructed wetland*. 2014.
27. Xiao, G., Wang, X., Ni, M., Wang, F., Zhu, W., Luo, Z., and Cen, K., *A review on solar stills for brine desalination.* Applied Energy, 2013. **103**: p. 642-652 DOI: http://dx.doi.org/10.1016/j.apenergy.2012.10.029.
28. Duffie, J.A. and Beckman, W.A., *Solar Engineering of Thermal Processes*. 2013: Wiley. ISBN: 9781118418123.
29. Setoodeh, N., Rahimi, R., and Ameri, A., *Modeling and determination of heat transfer coefficient in a basin solar still using CFD.* Desalination, 2011. **268**(1-3): p. 103-110 DOI: 10.1016/j.desal.2010.10.004.
30. Khalifa, A.J.N., *On the effect of cover tilt angle of the simple solar still on its productivity in different seasons and latitudes.* Energy Conversion and Management, 2011. **52**(1): p. 431-436 DOI: https://doi.org/10.1016/j.enconman.2010.07.018.
31. Shawaqfeh, A.T. and Farid, M.M., *New development in the theory of heat and mass transfer in solar stills.* Solar Energy, 1995. **55**(6): p. 527-535 DOI: 10.1016/0038-092X(95)00069-4.

32. Muhammad Shakaib, M.A.K., *Modeling of Fluid Flow and Temperature Profiles in Solar Stills Using CFD*, N.U.o.E.a.T. Department of Mechanical Engineering, Karachi Pakistan, Editor. 2015. p. 272-276.
33. Akash, B.A., Mohsen, M.S., and Nayfeh, W., *Experimental study of the basin type solar still under local climate conditions.* Energy Conversion and Management, 2000. **41**(9): p. 883-890 DOI: http://dx.doi.org/10.1016/S0196-8904(99)00158-2.
34. Tu, J., Guan, H.Y., and Liu, C., *COMPUTATION FLUID DYNAMICS, A Practical Approach*. 2008: ELSEVIER. ISBN: 978-0-7506-8563-490000.
35. Parry, J., Bornoff, R.B., Stehouwer, P., Driessen, L.T., and Stinstra, E., *Simulation-based design optimization methodologies applied to CFD.* IEEE Transactions on Components and Packaging Technologies, 2004. **27**(2): p. 391-397 DOI: 10.1109/TCAPT.2004.828554.
36. Russo, F. and Basse, N.T., *Scaling of turbulence intensity for low-speed flow in smooth pipes.* Flow Measurement and Instrumentation, 2016. **52**: p. 101-114 DOI: 10.1016/j.flowmeasinst.2016.09.012.
37. White, F.M., *Fluid Mechanics*. 1986: McGraw Hill Book Company. ISBN: 9780070696730.
38. *MPE 635: Electronics Cooling, Part B: Heat Transfer Principals in Electronics Cooling*. Available from: http://www.pathways.cu.edu.eg/ec/Text-PDF/Part%20B-9.pdf.
39. Bahrami, M. *Forced Convection Heat Transfer ENSC 388 (F09)*. [cited 2017 31/8]; Available from: http://www.sfu.ca/~mbahrami/ENSC%20388/Notes/Forced%20Convection.pdf.
40. Nostell, P., Roos, A., and Karlsson, B., *Optical and mechanical properties of sol-gel antireflective films for solar energy applications.* Thin Solid Films, 1999. **351**(1–2): p. 170-175 DOI: http://dx.doi.org/10.1016/S0040-6090(99)00257-6.
41. Giovannetti, F., Foste, S., Ehrmann, N., and Rockendorf, G., *High transmittance, low emissivity glass covers for flat plate collectors: Applications and performance.* Solar Energy, 2014. **104**: p. 52-59 DOI: 10.1016/j.solener.2013.10.006.
42. Kumar, A., Siddhanta, S., and Barshilia, H.C., *Extraordinary high broadband specular transmittance of sodalime glass substrate by vapor phase etching.* Solar Energy, 2016. **129**: p. 147-155 DOI: http://dx.doi.org/10.1016/j.solener.2016.01.044.
43. Goodyear, J.K. and Lindberg, V.L., *LOW ABSORPTION FLOAT GLASS FOR BACK SURFACE SOLAR REFLECTORS.* Solar energy materials, 1980. **3**(1-2): p. 57-67.
44. Zhao, Q. and Burnside, B.M., *Dropwise condensation of steam on ion implanted condenser surfaces.* Heat recovery systems & CHP, 1994. **14**(5): p. 525-534 DOI: 10.1016/0890-4332(94)90055-8.
45. Rausch, M.H., Leipertz, A., and Froba, A.P., *Dropwise condensation of steam on ion implanted titanium surfaces.* International Journal of Heat and Mass Transfer, 2010. **53**(1-3): p. 423-430 DOI: 10.1016/j.ijheatmasstransfer.2009.09.014.
46. Ma, X., Chen, J., Xu, D., Lin, J., Ren, C., and Long, Z., *Influence of processing conditions of polymer film on dropwise condensation heat transfer.* International Journal of Heat and Mass Transfer, 2002. **45**(16): p. 3405-3411 DOI: http://dx.doi.org/10.1016/S0017-9310(02)00059-5.
47. Haraguchi, T., Shimada, R., Kumagai, S., and Takeyama, T., *Effect of polyvinylidene chloride coating thickness of promotion of dropwise steam condensation.* International Journal of Heat and Mass Transfer, 1991. **34**(12): p. 3047-3054 DOI: 10.1016/0017-9310(91)90074-O.
48. Coroneo, M., Montante, G., and Paglianti, A., *Computational fluid dynamics modeling of corrugated static mixers for turbulent applications.* Industrial and Engineering Chemistry Research, 2012. **51**(49): p. 15986-15996 DOI: 10.1021/ie300398z.
49. *How to Identify and Eliminate Air Stratification Problems with Properly Designed HVAC Mixing Systems*. Blender Products, Inc: 5010 Cook Street, Denver.

50. Meijer, H.E.H., Singh, M.K., and Anderson, P.D., *On the performance of static mixers: A quantitative comparison.* Progress in Polymer Science, 2012. **37**(10): p. 1333-1349 DOI: http://dx.doi.org/10.1016/j.progpolymsci.2011.12.004.
51. Galaktionov, O.S., Anderson, P.D., Peters, G.W.M., and Meijer, H.E.H., *Analysis and Optimization of Kenics Static Mixers.* International Polymer Processing, 2003. **18**(2): p. 138-150 DOI: 10.3139/217.1732.
52. Chen, G.H. and Liu, Z.L. *Numerical research of pressure drop in kenics static mixer*. in *4th International Conference on Manufacturing Science and Engineering, ICMSE 2013, March 30, 2013 - March 31, 2013*. 2013. Dalian, China: Trans Tech Publications Ltd.
53. Song, H.-S. and Han, S.P., *A general correlation for pressure drop in a Kenics static mixer.* Chemical Engineering Science, 2005. **60**(21): p. 5696-5704 DOI: 10.1016/j.ces.2005.04.084.
54. Thakur, R.K., Vial, C., Nigam, K.D.P., Nauman, E.B., and Djelveh, G., *Static Mixers in the Process Industries—A Review.* Chemical Engineering Research and Design. **81**(7): p. 787-826 DOI: 10.1205/026387603322302968.
55. Meng, H., Wang, F., Yu, Y., Song, M., and Wu, J., *A numerical study of mixing performance of high-viscosity fluid in novel static mixers with multitwisted leaves.* Industrial and Engineering Chemistry Research, 2014. **53**(10): p. 4084-4095 DOI: 10.1021/ie402970v.
56. *Turbulence intensity*. 29/10/2017]; Available from: https://www.cfd-online.com/Wiki/Turbulence_intensity.

11 Appendix

11.1 Thermal stratification problem and mixer study

This part of the study was to look at ways to evenly mix the heat at the fan inlet (or air outlet in Section 6.4), so that when calculating for heat rejection using the integral method, only one temperature measurement is needed instead of using the integral method and measuring all 88 points at the rectangular outlet. However, this concept was not adopted at the end, as the findings below showed that it would require additional manufacturing time and could change the initial optimisation problem. In Section 8.5, Fig. 8.5.3 there is a better concept that looks at using a control volume to evenly mixing the heat as well as the flow rate.

In Fig. 11.1.1 shows how the heat is distributed at the rectangular outlet and fan inlet, the portion in white shows that it is hotter than the surface averaged of the outlet, evaluated to be 288.15K.

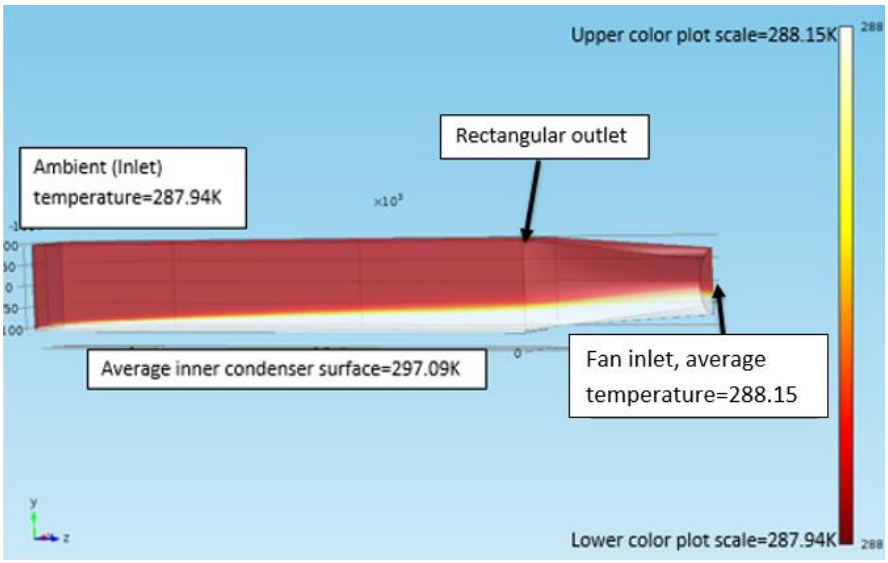

Figure 11.1.1. Thermal stratification at the fan inlet, as illustrated from one of the refined CFD runs for Test 6 in the flat plate experiment.

The level of stratification is shown numerically in Fig. 11.1.2, there is a steep change in temperature at the fan inlet between y=0-50mm, where it transitioned from 290.4K to the ambient temperature (287.94K). The rest of the fan inlet was at ambient temperature from y=50-147, which shows that the stratification is significant to be considered thermally uniform.

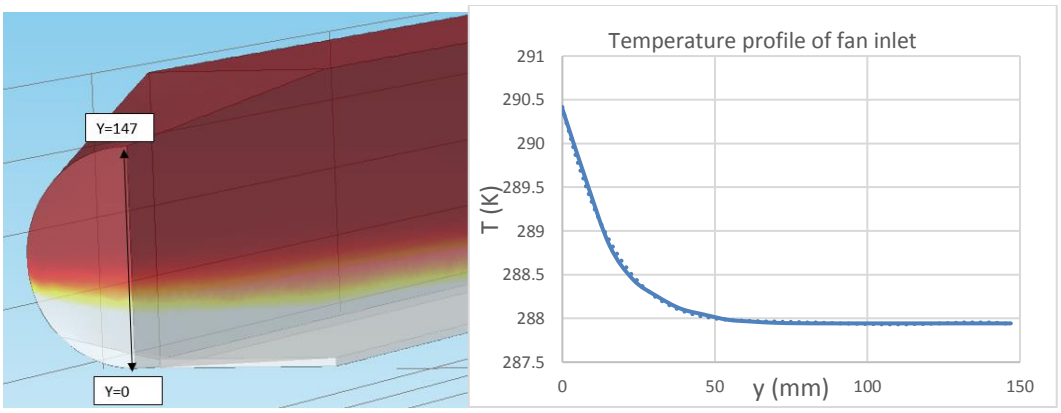

Figure 11.1.2. Temperature profile of the fan inlet of Test 6, which shows a steep change in temperature from y=0-50mm.

11.1.1 Straight pipe mixing

First form of mixing that was looked at was adding a length of straight pipe between the fan and the fan inlet as shown in Fig. 11.1.3. The diameter will remain the same at 147mm, while a 2D parametric CFD analysis was used to determine at what length the flow is thermally mixed before reaching the fan. From literature review, it was found that 100 diameters is needed [48].

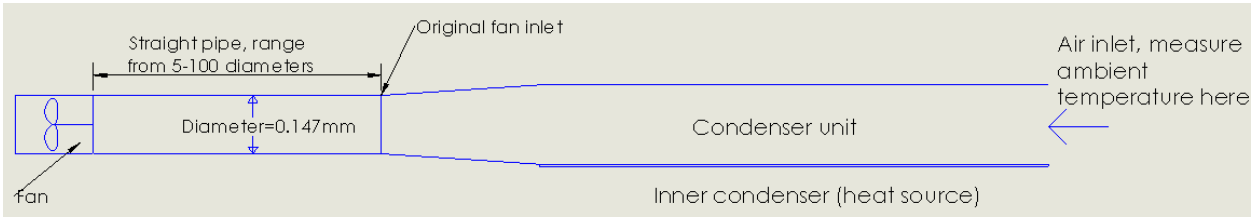

Figure 11.1.3. Concept of the straight pipe to eliminate thermal stratification at the fan inlet.

At the fan inlet of the CFD analysis, the temperature profile of Fig. 11.1.2 was inputed, as well as a flow velocity of 7m/s (see Fig. 11.1.5), as this was the fan inlet (air outlet) velocity in the refined CFD for flat plate Test 6. A summary of the inputs and variables on the CFD is illustrated in Fig. 11.1.4.

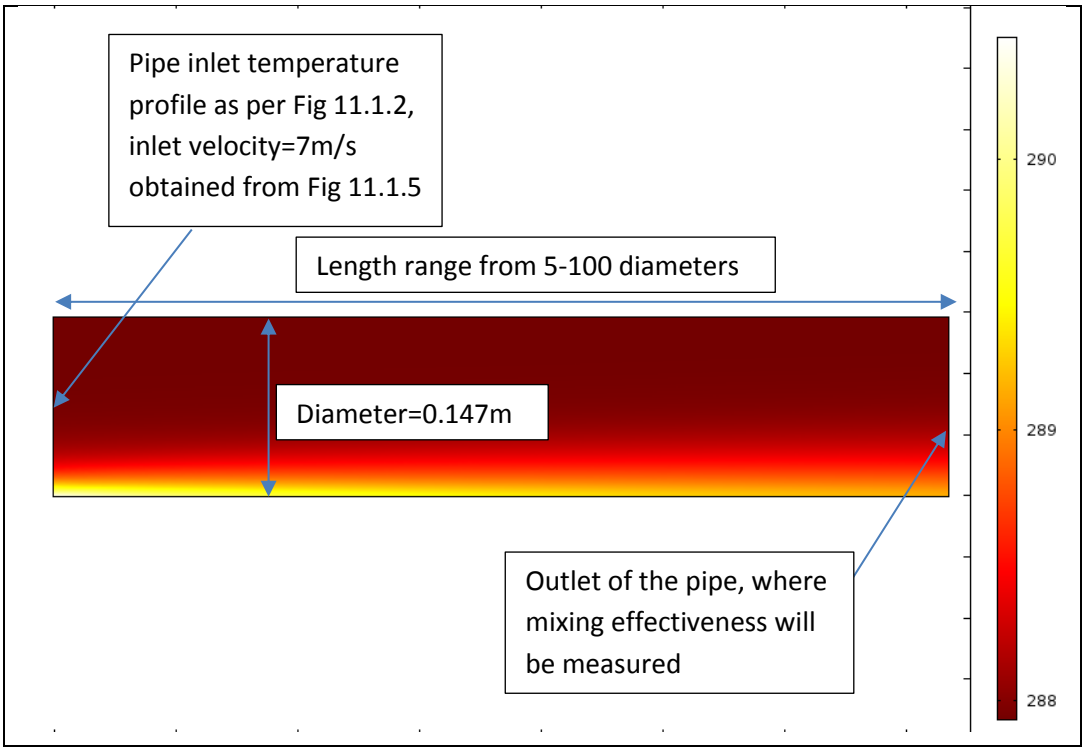

Figure 11.1.4. Straight pipe mixing CFD analysis to validate that 100 pipe diameter is enough for complete mixing from [48]

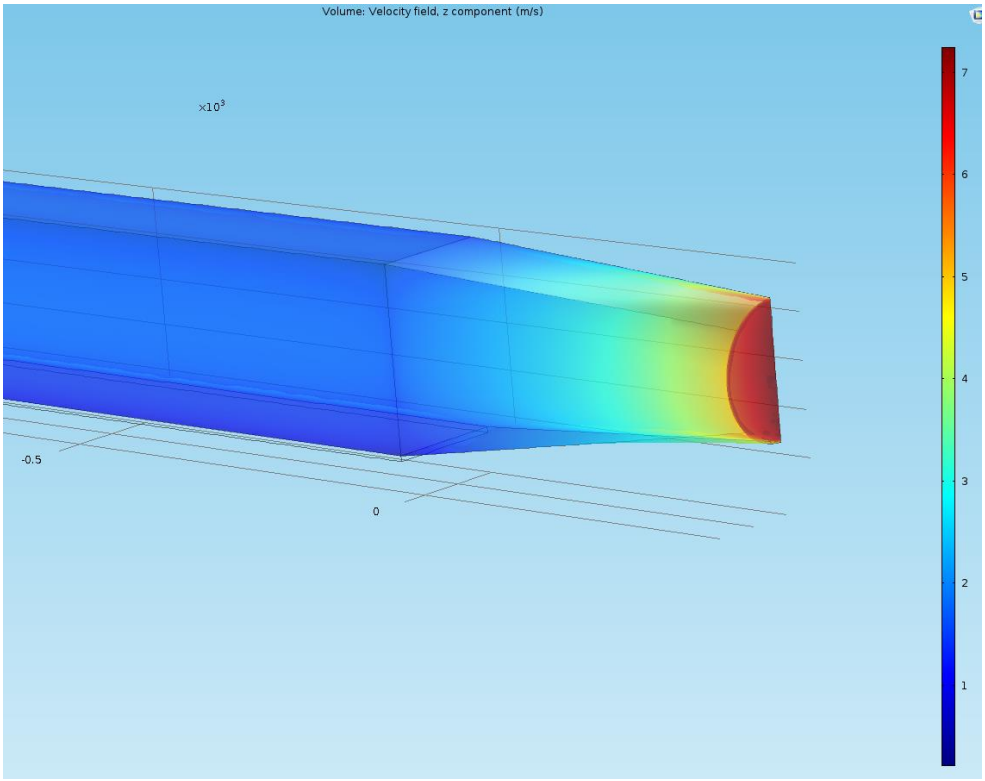

Figure 11.1.5. Air velocity at the fan inlet (air outlet)=7 m/s.

To evaluate how well the length of pipe has mixed the airflow, the following formula is used:

$$Mixing\ effectiveness = 1 - \frac{Temperature\ range\ at\ the\ outlet}{Temperature\ range\ at\ the\ inlet}$$

Temperature range can be determine using the surface maximum and minimum function on COMSOL. From this, Fig. 11.1.6 showed that at 100 diameter the airflow is 95% mixed. This would imply that the length of straight pipe to be greater than 14.7m, which is not feasible to be installed due to indoor space limitation. Therefore, this concept of straight pipe mixing was rejected.

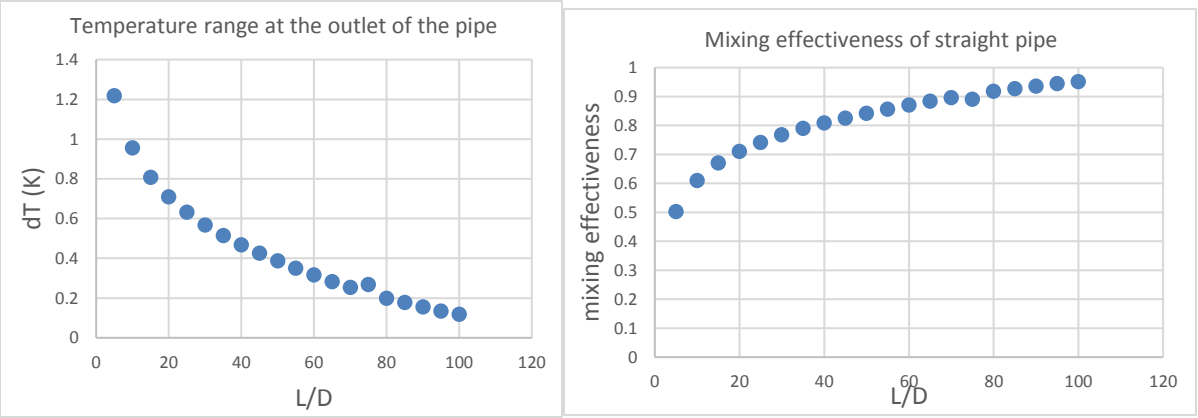

Figure 11.1.6. Temperature homogeneity at the pipe outlet.

11.1.2 Kenics mixer CFD study

Because of space limitation, a more compact design was needed to thermally mix the stratified flow. Kenics mixers variant were looked at in the literature review, with one reporting that the Kenics RL 140° was found to have the most efficient mixing [51].

A full 3D CFD study was conducted in two stages. The first stage looked at comparing the CFD result with the literature correlation in [53], this work has no originality as it has already been done by the [53]. But the purpose of doing so is to validate whether the CFD model on COMSOL predicts pressure drop reliably.

The second study looked at adding an arbitrary temperature stratification example, shown in Fig. 11.1.8. Then by modifying the model from the first CFD study, the mixing capability of different Kenics mixer variants was compared. This study is adding originality to this research as there was no work done on how different flow velocities (Reynolds number), aspect ratio and number of mixer blades affects thermal mixing.

For both studies, because the conventional Kenics blade angle is 180° and not 140°, the Kenics RL 180° was used instead. Because [53] commented that there was negligible difference in between the laminar and k-epsilon CFD results even at high Reynolds number (10^5), therefore the laminar model was used instead for faster convergence time.

Pressure loss study

The study by [53] derived the master curve for describing pressure loss as a function of Reynolds number, aspect ratio of the mixer blades and the number of mixer units using CFD and dimensional analysis.

$$C_f AR^{2.04} = K\left({Re}/{AR^{2.15}}\right)^n \; K \; and \; n \; are \; fitting \; constants$$

$$AR = {L_e}/{D_e} \; L_e \; is \; the \; length \; of \; the \; Kenics \; unit$$

$$where \; C_f \; is \; the \; dimensionless \; friction \; factor = \frac{2\Delta P D_e}{\rho U^2 L_p}$$

$$L_p = number \; of \; mixer \; units \times L_e$$

$$K = \begin{cases} 320 & 0 < {Re}/{AR^{2.15}} < 100 \\ 32 & 100 < {Re}/{AR^{2.15}} < 1000 \\ 2.66 & 1000 < {Re}/{AR^{2.15}} \end{cases}$$

$$n = \begin{cases} -0.86 & 0 < {Re}/{AR^{2.15}} < 100 \\ -0.36 & 100 < {Re}/{AR^{2.15}} < 1000 \\ 0 & 1000 < {Re}/{AR^{2.15}} \end{cases}$$

To validate this the pressure loss was tabulated using the master curve and compared with the CFD for a number of inlet velocities and blade aspect ratio, while the number of mixer units was fixed at five. Below in Fig. 11.1.7 describes the CFD geometry and setup, and in Fig. 11.1.8 the definition of the blade geometry was shown.

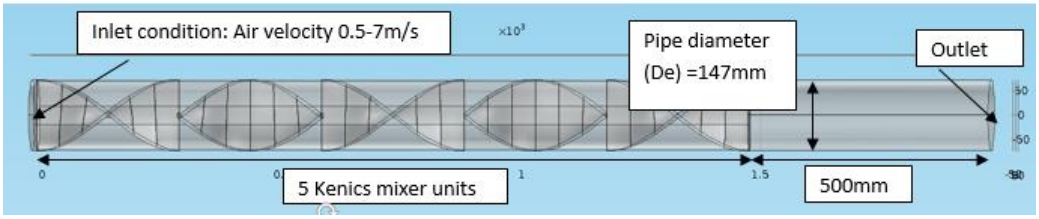

Figure 11.1.7. Layout of the Kenics mixer pressure drop CFD study.

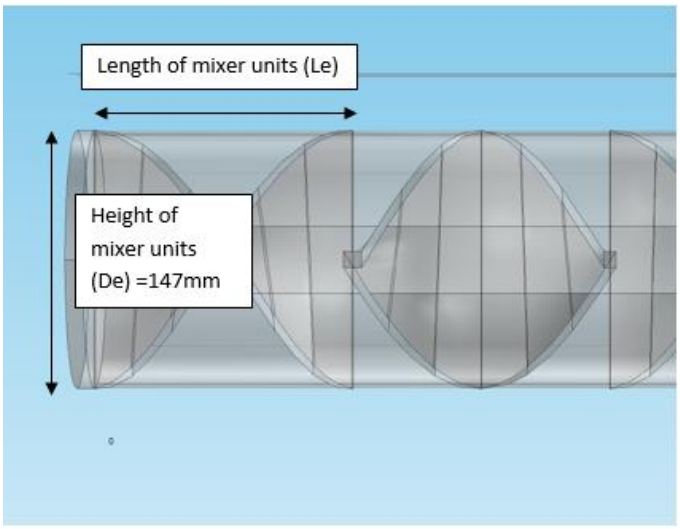

Figure 11.1.8. Definition of the mixer unit geometry, aspect ratio=Le/De.

In Fig. 11.1.9 shows the result of the literature master curve against the COMSOL parametric CFD study. It was found that the literature correlation predicts a lower pressure drop than the CFD particular at high velocities (high Reynolds number) and low aspect ratio. At low velocities and high aspect ratio the literature correlation predicts similar to the CFD, with the CFD still predicting a higher pressure loss. This could be due to that the coefficient K and n does not describe the correlation well enough using a single constant after $Re/_{AR^{2.15}}$ is greater than 1000. Therefore, the limitation of this study was found that neither the master curve nor the CFD is reliable at high velocity, low aspect ratio situations as no experimentation was done to validate. The current fan only has a static pressure of 215Pa from Fig. 4.3.8, so at low pressure loss region the correlation or the CFD should be valid. Due to the additional pressure loss from the five Kenics mixer units, the fan inlet velocity from Fig. 11.1.5 will no longer be 7m/s if this mixer unit was to be deployed on the flat plate condenser rig. This would change the original optimisation problem as it would reduce the overall flow rate, unless the aspect ratio of the mixer blade was to increase.

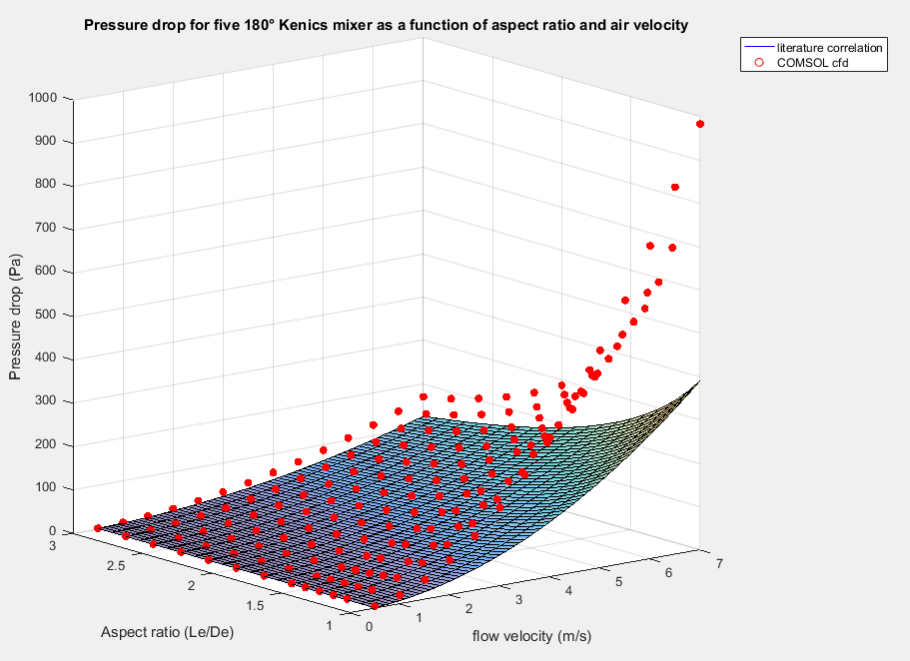

Figure 11.1.9. Comparison of the Kenics mixer pressure drop correlation by [53] against the COMSOL CFD parametric study.

Thermal mixing study

Despite disagreement in predicting pressure loss between the literature correlation and the CFD at high inlet velocities and low blade aspect ratio, it was found that the mixing effectiveness did not depend on inlet velocity, as shown in Fig. 11.1.11. This meant that for the remainder of the thermal mixing analysis, inlet velocity could be kept constant. The setup of the new parametric CFD study is shown below in Fig. 11.1.10 by defining an arbitrary thermal stratification scenario, which was a more severe case of thermal stratification than the one shown for the fan inlet in Fig. 11.1.2. The geometry was the same as from the pressure loss study, but the number of mixer units can vary from 1-5 as well.

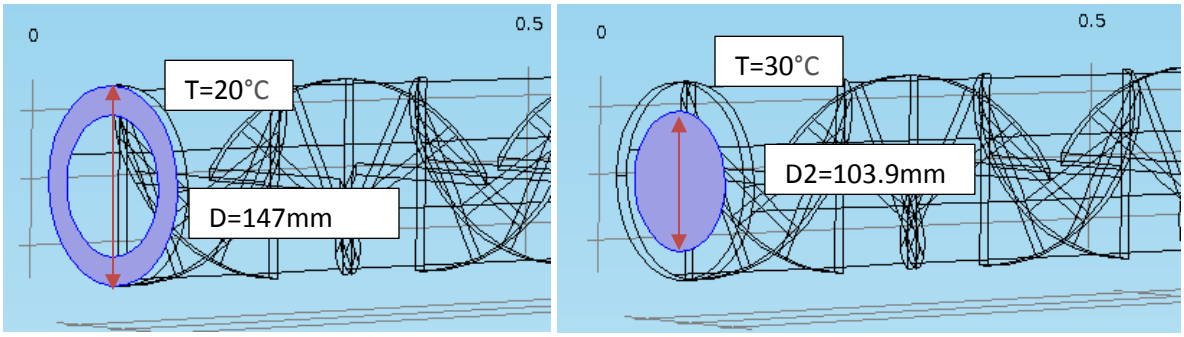

Figure 11.1.10. Temperature stratification input where both half of the inlet area were given a different inlet temperature, homogeneity performance would be based on the temperature difference at the outlet.

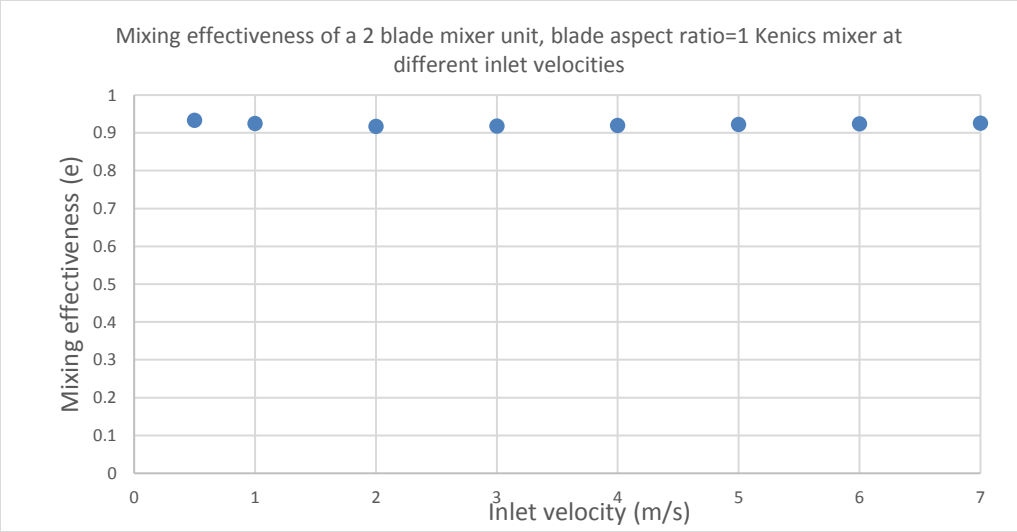

Figure 11.1.11. Mixing effectiveness of a Kenics mixer unit with two mixer blades, each with an aspect ratio of 1 against different inlet velocities.

Because it was found that the inlet velocity had no effect on the mixing effectiveness, the inlet velocity was fixed at 3m/s for the thermal mixing analysis with the different number of mixer units and blade aspect ratio, as shown in Fig. 11.1.12 below. It was shown that at a mixing effectiveness of about 95% can be achieved with three mixer units, at five mixer units this would be 99.5-99.8%. The aspect ratio of the blade was not a significant factor after the number of mixer units was greater than two.

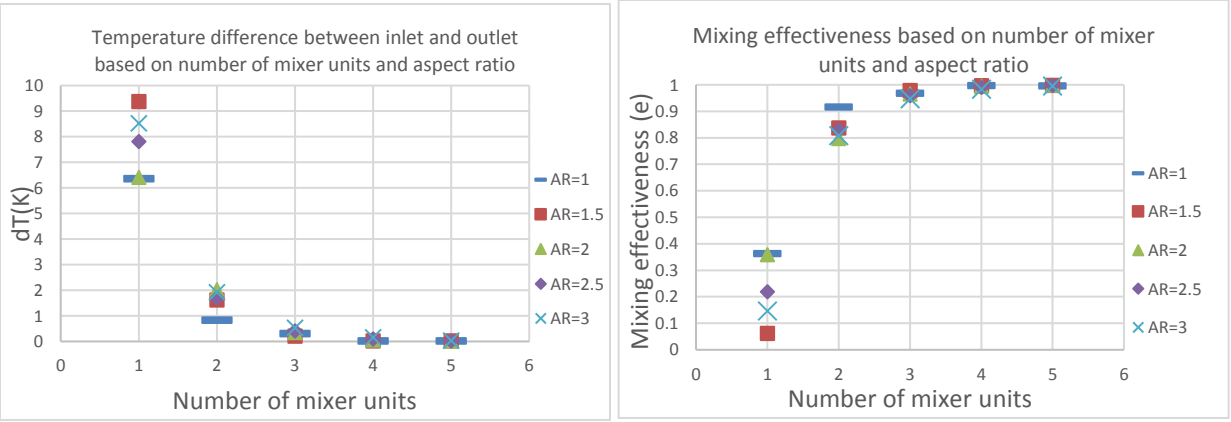

Figure 11.1.12. Temperature homogeneity at the outlet based on number of mixer units and mixer aspect ratio under constant inlet air velocity of 3m/s.

11.2 Specification of equipment and parts used in the rig

DIMENSIONS

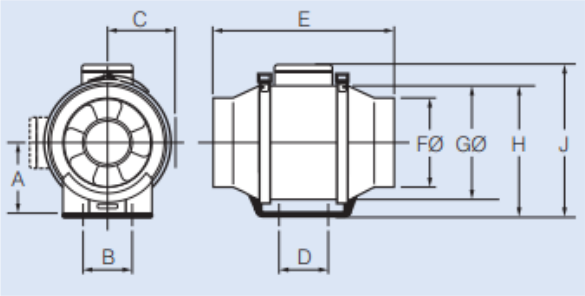

Model Number RIL-...	Dimensions, mm A	B	C	D	E	FØ	GØ	H	J
100	100	60	115	80	303	97	176	190	220
125	100	60	115	80	258	123	176	190	210
150	112	60	127	80	295	147	200	225	236
200	124	94	141	100	302	198	217	235	265

Figure 11.2.1. The dimension of the RIL-150 fan.

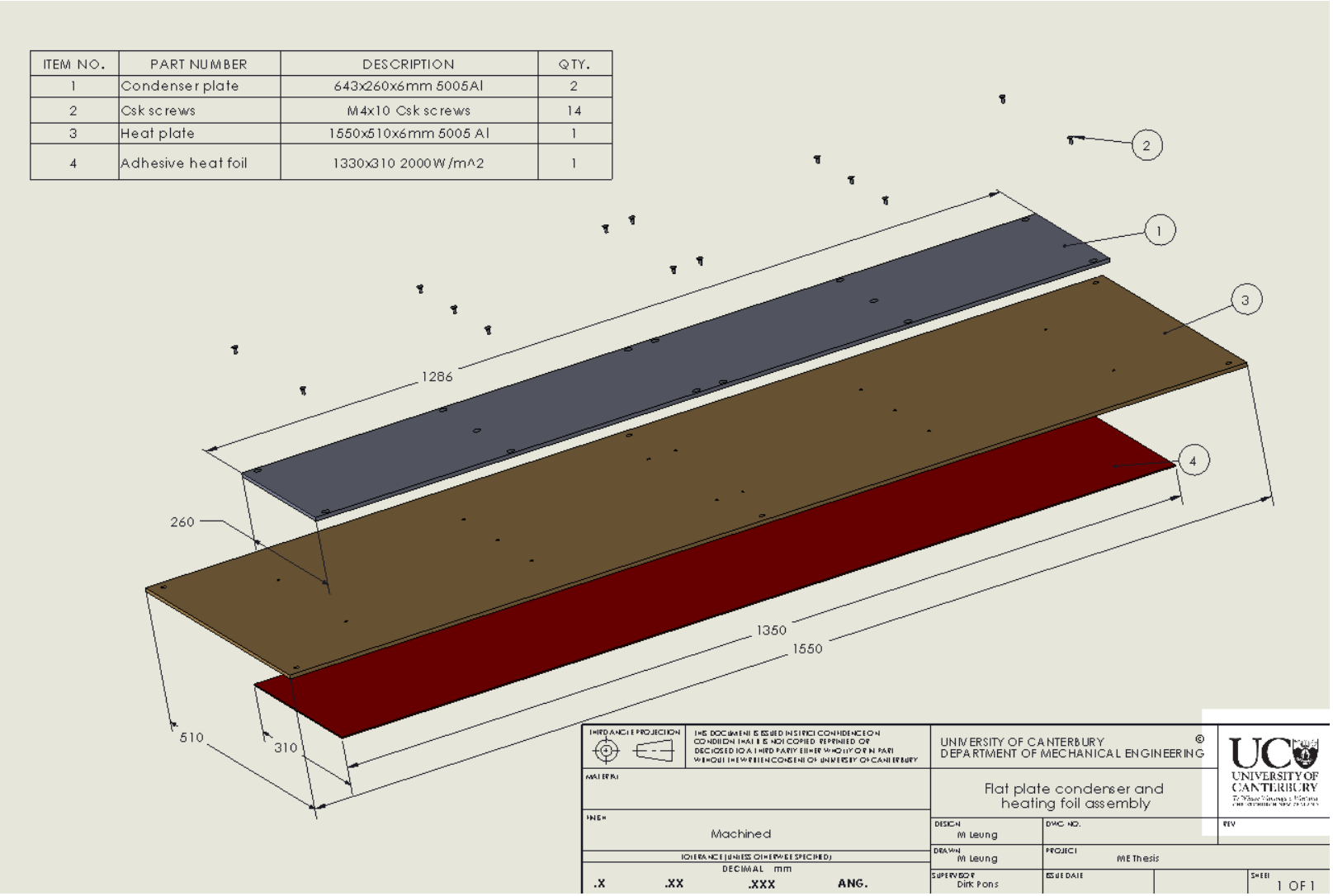

Figure 11.2.2. Installation of the heating module for the flat plate condenser.

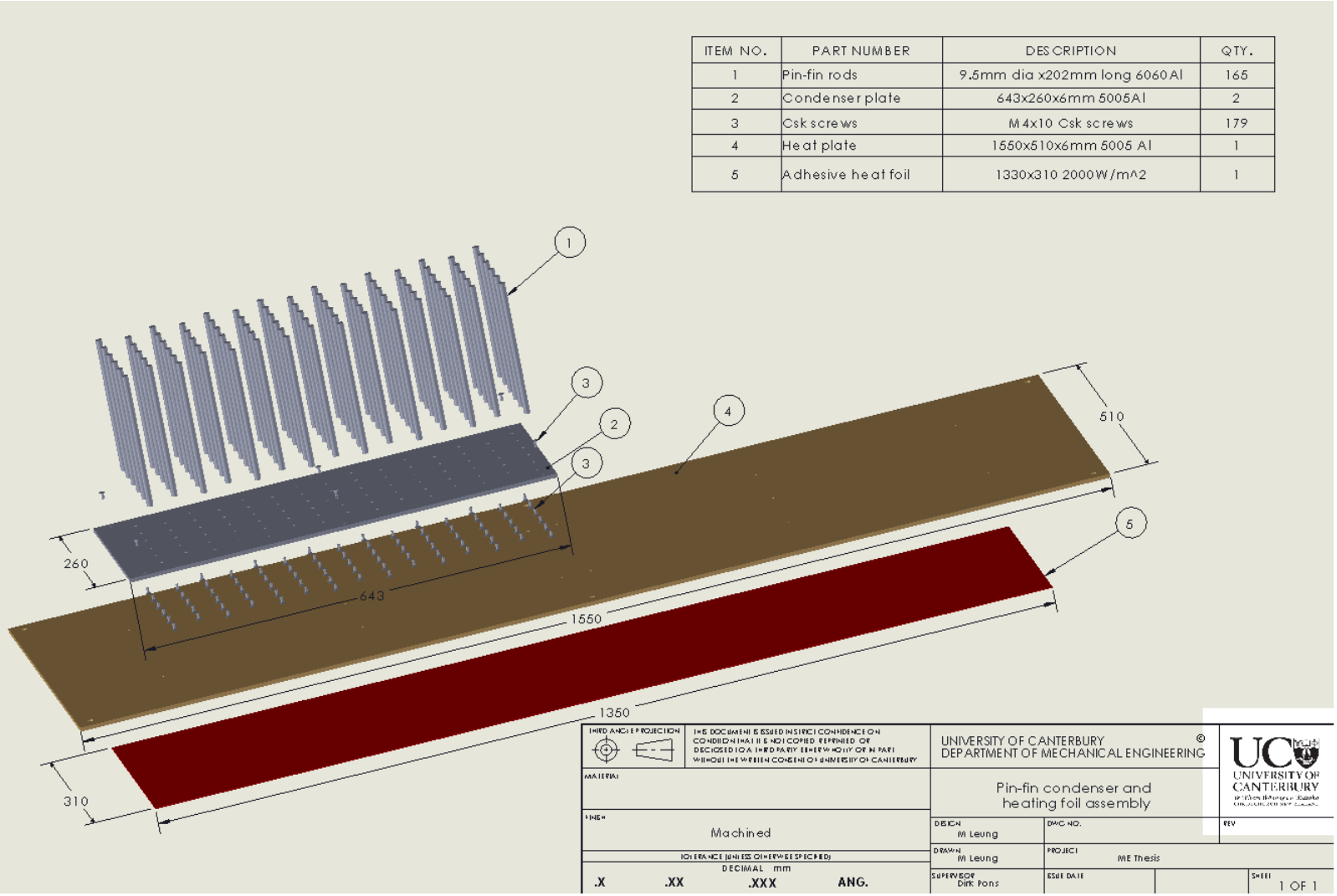

Figure 11.2.3. Installation of the heating module for the pin-fin condenser.

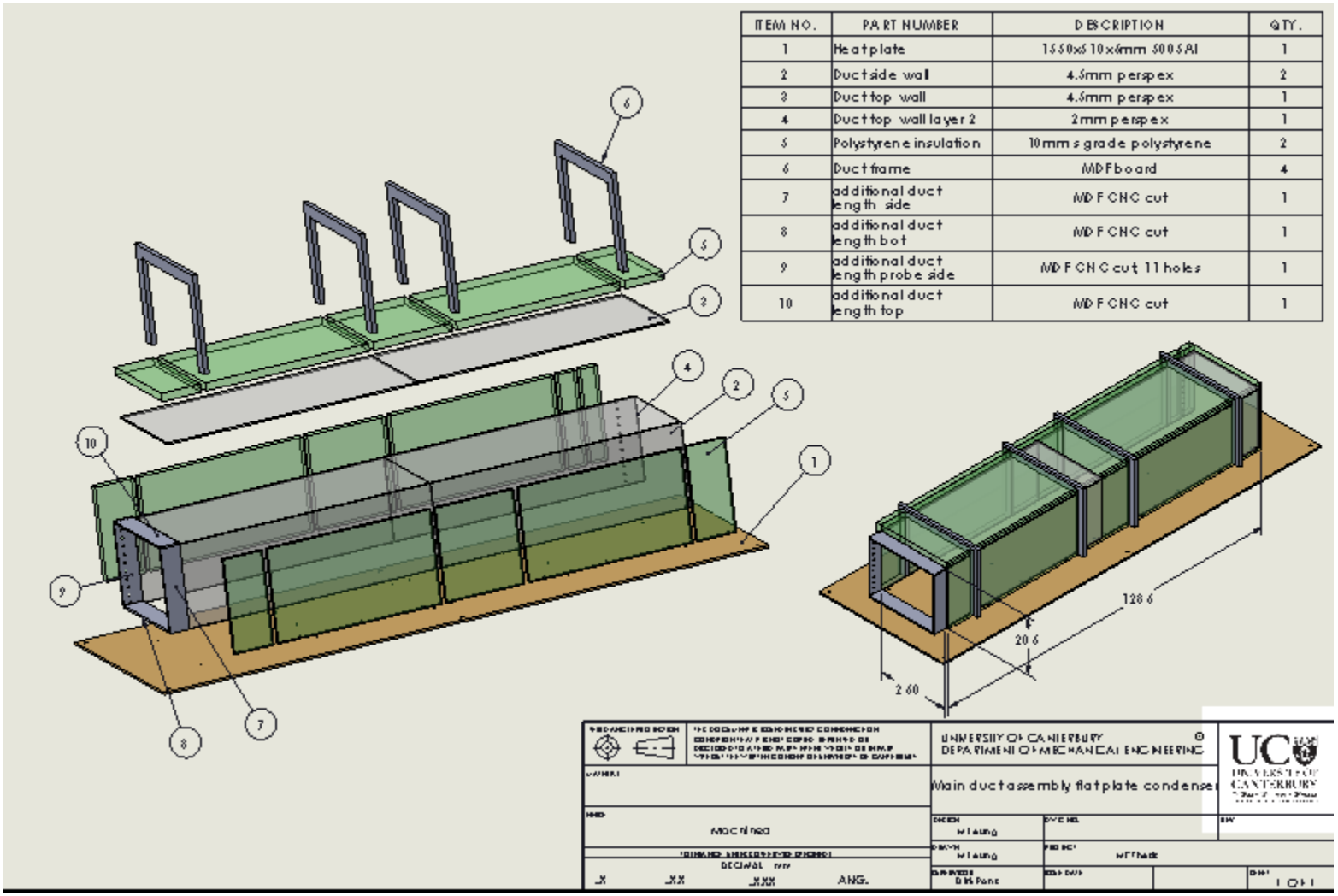

Figure 11.2.4. Installation of the main duct module for the flat plate condenser.

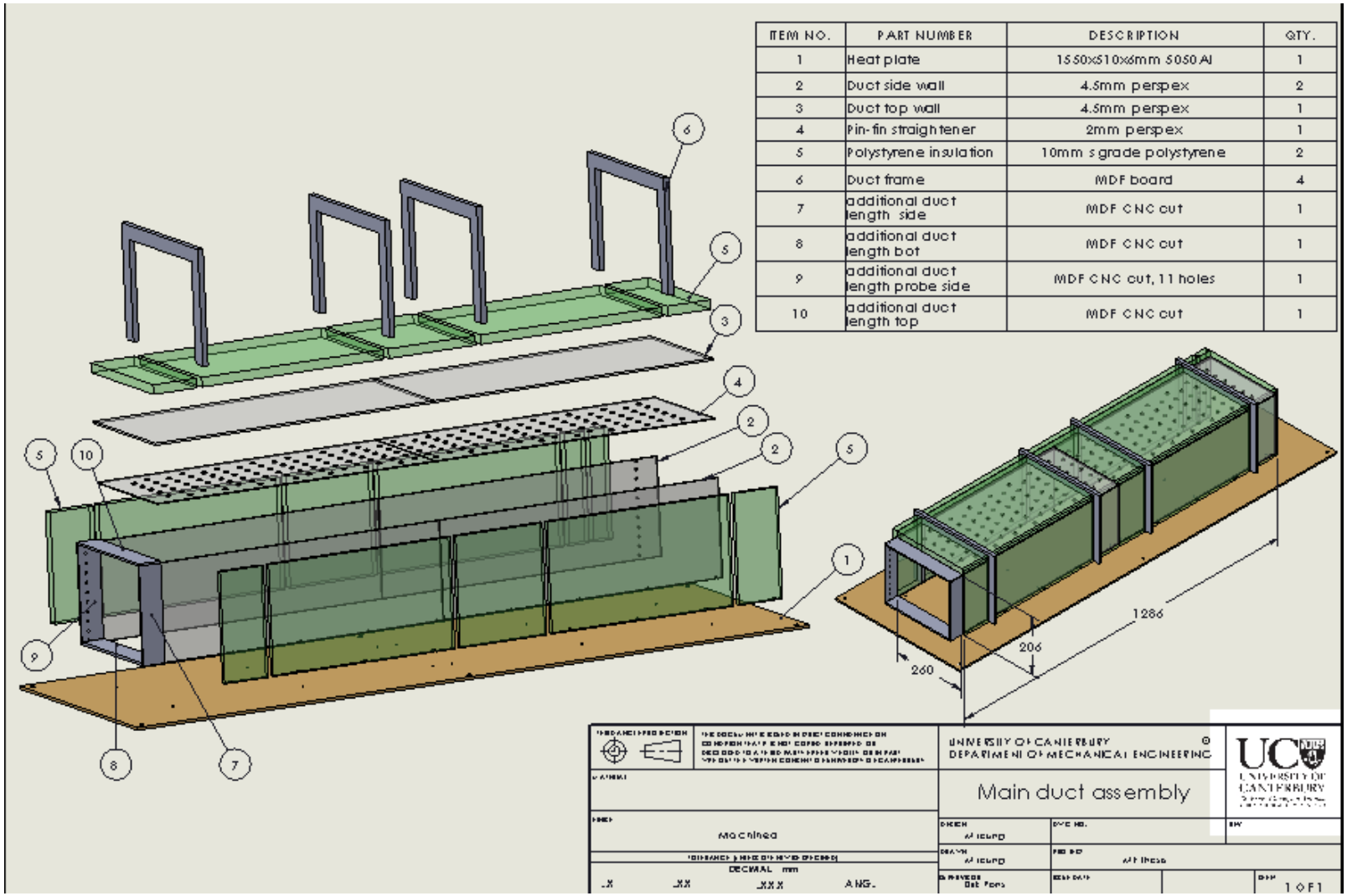

Figure 11.2.5. Installation of the main duct module for the pin-fin condenser.